

The Turbulent Very Wide-Gap Taylor-Couette Flow: Experimental Investigation

Von der Fakultät für Maschinenbau, Elektro- und Energiesysteme
der Brandenburgischen Technischen Universität Cottbus–Senftenberg
zur Erlangung des akademischen Grades

Doktor der Ingenieurwissenschaften

-Dr.-Ing.-

genehmigte Dissertation

vorgelegt von

M.Sc.

Mohammed Hussein Haytham Hamede

geboren am 02. Juli 1995 in Beirut, Libanon

Vorsitzender: Prof. Dr. rer. nat. Andreas Schröder

Gutachter: Prof. Dr.-Ing. Christoph Egbers

Gutachter: Prof. Dr. Innocent Mutabazi

Tag der mündlichen Prüfung: 12. Juni 2023

DOI: <https://doi.org/10.26127/BTUOpen-6445>

Zusammenfassung

Seit Jahrhunderten sind Wissenschaftler von dem einfachen geometrischen System der Flüssigkeitsströmung fasziniert, die zwischen zwei konzentrischen, unterschiedlich rotierenden Zylindern auftritt. Die sogenannte Taylor-Couette-Strömung (TC) wurde als ausgezeichnetes Modell zur Untersuchung von Scherströmungen an konkaven Oberflächen und als eines der beispielhaften Systeme der Flüssigkeitsphysik verwendet. Die differentielle Rotation der Zylinder kann bei bestimmten Strömungsparametern das Auftreten verschiedener faszinierender Strömungsmuster (z.B. Taylor-Wirbel) auslösen. Bei ausreichender Scherung erreicht die Strömung im Spalt einen Übergang zur Turbulenz und bewirkt einen effektiven Drehimpulstransport durch den Spalt, wobei die Größe dieses Transports eine Funktion der strömungstreibenden Parameter und der Geometrie des Systems ist. Bei noch höheren Schergeschwindigkeiten geht die turbulente Strömung vom klassischen turbulenten Zustand in den ultimativen Zustand über, was zu Änderungen des gesamten Strömungsverhaltens führt.

In dieser Arbeit wird eine experimentelle Untersuchung der turbulenten Taylor-Couette-Strömung in einer sehr breiten Spaltgeometrie mit einem Radiusverhältnis $\eta = 0.1$ durchgeführt. Das physikalische und dynamische Verhalten der Strömung wird in einer Geometrie untersucht, die bisher kaum untersucht wurde, was diese Studie einzigartig macht. Die Studie zielt darauf ab, die Auswirkungen der Krümmung auf die Taylor-Couette-Strömung zu verstehen, insbesondere in Fällen, in denen die Umfangslänge des inneren Zylinders kleiner ist als die Spaltbreite, was bei $\eta < 0.14$ der Fall ist. Als Strömungsmedium wurden verschiedene Flüssigkeiten mit unterschiedlichen kinematischen Viskositäten verwendet, was die Möglichkeit bot, die Strömung in einem breiten Bereich von Scher-Reynoldszahlen $530 \leq Re_s \leq 1.5 \times 10^5$ zu untersuchen. Darüber hinaus ermöglicht die unabhängige Steuerung der rotierenden Zylinder die Untersuchung der Strömung in den verschiedenen Rotationsregimen: gegenläufige, gleichsinnige und rein innere Zylinderrotation.

Dank des transparenten Außenzylinders wurde das Strömungsfeld mit Visualisierungstechniken in zwei verschiedenen Konfigurationen qualitativ untersucht. Bei der Untersuchung der verschiedenen Strömungsparameter wurden sowohl bekannte kohärente Strömungsmuster beobachtet, die zuvor in engeren TC-Strömungsgeometrien untersucht wurden, als auch neu beobachtete Muster, welche vermutlich nur für TC-Strömungen mit sehr großen Spalten existieren. Für eine detailliertere quantitative Studie wurde eine zeitaufgelöste Messung des Geschwindigkeitsfeldes mit der Hochgeschwindigkeits-Partikel-Image-Velocimetry-Technik durch die Endplatte des TC-Systems durchgeführt, wobei die Krümmung der Zylinderwand berücksichtigt wurde. Diese Messungen ermöglichen es, die radialen und azimutalen Geschwindigkeitskomponenten in der horizontalen 2D-Ebene zu erfassen. Um die axiale

Varianz der Strömung zu erfassen, wurde außerdem die Strömung an verschiedenen axialen Positionen gemessen, indem die axiale Position der horizontalen LASER-Schnittebene verändert wurde. Das aufgezeichnete Strömungsfeld wurde verwendet, um den Drehimpulstransport in Form der Quasi-Nusselt-Zahl zu berechnen. Die Ergebnisse zeigten ein Maximum des Drehimpulstransports für niedrige Gegenrotationsraten von $-0.011 \leq \mu_{max} \leq -0.0077$, das mit großräumigen Strukturen verbunden ist, die den gesamten Spalt ausfüllen. Darüber hinaus nimmt der Drehimpulstransport für Gegenrotationsraten größer als μ_{max} ab, bis er einen Minimalwert erreicht, um dann für höhere Gegenrotationsfälle wieder zuzunehmen. Das Raum-Zeit-Verhalten des turbulenten Strömungsfeldes für die Fälle mit hoher Gegenrotation zeigt die Existenz von neu beobachteten Mustern neben der äußeren Zylinderwand, die sich nach innen ausbreiten, den Drehimpulstransport verstärken und zu einem zweiten Maximum des Transports führen.

Für den rein rotierenden inneren Zylinder wurde die Skalierung des Impulstransports mit der Scherrate $Nu_\omega \sim Re_s^\alpha$ untersucht, und es zeigt sich ein Übergang der Skalierung zu $\alpha = -0.76$ für alle Strömungen mit $Re_s \geq 2.5 \times 10^4$. Diese neue Skalierung zeigt den Übergang der Strömung vom klassischen turbulenten Regime zum ultimativen Regime, wobei dieser Übergang von einer deutlichen Änderung des Strömungsverhaltens begleitet wird.

Als Versuch, die hydrodynamische Instabilität in linear stabilen Strömungen zu untersuchen, wird die Strömung im gleichsinnig rotierenden Regime und insbesondere im zentrifugal stabilen Regime ($\mu > +0.01$) untersucht. Die Strömungsvisualisierung zeigt das Vorhandensein von turbulenten Flecken, die die Strömung in der Region neben dem inneren Zylinder stören. Geschwindigkeitsmessungen bestätigen das Vorhandensein der gestörten Strömung in der Nähe des inneren Zylinders, was durch eine deutliche Abweichung der gemessenen Geschwindigkeitsprofile von denen, die durch laminare Strömung für Strömungen bis zu $\mu = +0.04$ vorhergesagt werden, unterstützt wird.

Abstract

For centuries, scientists have been intrigued by the straightforward geometric pattern of fluid flow that occurs between two concentric, differentially rotating cylinders. The so-called Taylor-Couette (TC) flow is used as a perfect model to investigate shear flow over concave surfaces and as one of the paradigmatic systems of the physics of fluids. The cylinders' differential rotation can trigger the appearance of different fascinating flow patterns (e.g., Taylor vortices) at specific flow parameters. For sufficient shear rate, the flow inside the gap achieves a transition to turbulence and causes an effective angular momentum transport through the gap, where the quantity of this transport is a function of the flow driving parameters and the geometry of the system. For further higher shear rates, the turbulent flow undergoes a transition from the classical turbulent state to the ultimate one, resulting in changes to the overall flow behavior.

In this thesis, an experimental investigation of the turbulent Taylor-Couette flow in a very wide gap geometry with a radius ratio $\eta = 0.1$ is performed. The physical and dynamical behavior of the flow is studied in a geometry that has rarely been investigated before the current study, which makes this study unique. The study aims to understand the effect of curvature on the Taylor-Couette flow, particularly in cases where the circumferential length of the inner cylinder is smaller than the gap width, which occurs when $\eta < 0.14$. Different fluids with different kinematic viscosities are used as working fluids, giving the opportunity to discover the flow in a broad range of shear Reynolds numbers $530 \leq Re_s \leq 1.5 \times 10^5$. Further, the independent control of the rotating cylinders allows us to study the flow in the different rotation regimes: counter-rotating, co-rotating, and purely inner cylinder rotating regimes.

Thanks to the transparent outer cylinder, the flow field has been qualitatively studied using visualization techniques in two different configurations. By probing the different flow parameters, familiar coherent flow patterns previously investigated in narrower TC flow geometries are investigated, in addition to newly observed patterns we assume only exist for very wide gap TC flows. For a more detailed quantitative study, a time-resolved velocity field measurement has been conducted using the High-speed Particle Image Velocimetry technique through the TC system end plate, taking into account the curvature of the cylinder wall. These measurements allow us to record the radial and azimuthal velocity components in the 2D horizontal plane. Furthermore, to scan the axial variance of the flow, the flow at different axial positions is measured, by changing the axial position of the horizontal laser sheet. The recorded flow field is used to compute the angular momentum transport in terms of the quasi-Nusselt number. The results show a maximum in angular momentum transport for low counter-rotating rates of $-0.011 \leq \mu_{max} \leq -0.0077$, which is associated with large-scale

structures that span the entire gap. Moreover, the angular momentum transport decreases for counter-rotation rates higher than μ_{max} until it reaches a minimum value and then tends to increase again for higher counter-rotation cases. The space-time behavior of the turbulent flow field for the high counter-rotating cases shows the existence of newly observed patterns next to the outer cylinder wall that propagate inward, enhancing the angular momentum transport and resulting in a second maximum in transport for higher counter-rotating rates.

For the pure rotating inner cylinder, the momentum transport scaling with the shear rate $Nu_\omega \sim Re_s^\alpha$ has been studied, and it shows a transition in scaling to $\alpha = -0.76$ for all flows with $Re_s \geq 2.5 \times 10^4$. This new scaling reveals the transition of the flow from the classical turbulent regime to the ultimate one, where this transition is accompanied by a clear change in the flow behavior.

As an attempt to study hydrodynamic instability in linearly stable flows, the flow in the co-rotating regime and particularly in the centrifugal stable regime ($\mu > +0.01$) is investigated. Flow visualization shows the existence of turbulent spots that disturb the flow in the region next to the inner cylinder. Velocity measurements confirm the presence of the disturbed flow near the inner cylinder, which is supported by a clear deviation of measured velocity profiles from those predicted by laminar flow for flows up to $\mu = +0.04$.

“Knowledge is a treasury, and the keys are the question, so ask, may God have mercy on you, for it is rewarded in knowledge four: the questioner, the speaker, the listener, and the lover of them” Imam Jaafar as-Sadiq (Peace be upon him)

Acknowledgements

‘He has not thanked God who has not thanked people’

I want to start by sincerely thanking my supervisor, Prof. Dr-Ing. Christoph Egbers, for his encouragement, guidance, and advice through all the stages of finishing this work, as well as the freedom he gave me to advance my scientific knowledge. Thank you for believing in me and giving me the opportunity to work at the Department of Aerodynamics and Fluid Mechanics and undertake my PhD under your supervision. Also, I like to thank Prof. Innocent Motabazi for the fruitful discussions we had and his willingness to become the second referee for my thesis.

Further, I would like to thank my group leader, Dr.-Ing. Sebastian Merbold for his infinite support, advice, and discussions through the years, without which this thesis could not have been developed as it was. I appreciate your generosity in providing me with any material that will help me grow not just scientifically but also personally. And it would be unjust not to acknowledge Sebastian outside the framework of being a great supporter and being there any time I needed him.

I genuinely appreciate the encouraging discussions I had with Prof. Dr. El-Sayed Zanoun, Prof. Dr. Uwe Harlander. I also want to express my gratitude to all of my former and present colleagues in the Department of Aerodynamics and Fluid Mechanics for the delightful and productive work atmosphere, the constructive scientific discussions, the great falafel evening, the wonderful conference travels and more: Costanza, Peter S., Gazi, Andreas, Tom, Antoine, Yarlaw, Vasyl, Vadim, Yann, Robin, Peter H, it was a great honor knowing you. I'd like to highlight the huge help from Stefan Richter in helping me cope in my first days in Cottbus, and I can't forget the time he spent accompanying me to the doctor several times. Stefan Rohark, thank you for all your technical support, and for helping me renovate my experiment. Silke, thank you for always responding quickly and being so kind in your assistance with administrative issues. Finally, I'd like to pay tribute to our colleague Andreas Stöckert, who unexpectedly passed away last year. I send my condolences and pray for peace for his spirit.

Here comes the part when words can no longer do justice. This part is dedicated to the most important people in my life, my family. Starting with the ones I owe everything in my life to, my father and mother, this thesis is primarily dedicated to you. Your faith, kindness, and unconditional love that you have been nourishing me with since childhood, paved the way toward where I am now. I hope that this work will make up for every hurtful moment we endured when saying our goodbyes at the airport or the happy moments that we couldn't share together. Baba, for your love, for every time you had to work very hard for us, and for the valuable discussions I had with you, this thesis is dedicated to you. Mama for your hard

work, love, sacrifice, and kindness; for the life-changing advice and for helping me be who I am now, this thesis is dedicated to you. Haytham and Nadia, I am truly blessed to have you as my parents, I love you both so much.

My wife Fatima, I want to sincerely thank you for your love, patience, and your endless support. My journey would have not been the same without you, I am so lucky for having you in my company throughout this journey in its ups and downs. I am so grateful for having you in my life. I love you so much, this thesis is dedicated to you.

To Hamza, Fatima, Saja, Yasser, and Mohammad Ali thank you for all the happy moments and laughter that we have shared together, I cherish every moment I have spent with you. I truly can't imagine a life without you being my siblings or more like my best friends. For the hours we spent daily on video calls, for all the moments we shared together, and for the infinite love we hold in between, this thesis is dedicated to you.

Finally, I gratefully acknowledge financial support from the German Research Foundation (DFG), which funded my stay during my time creating this thesis and working as a research assistant at the Department of Aerodynamics and Fluid Mechanics at the Brandenburg University of Technology Cottbus-Senftenberg.

Table of Contents

Title Page	i
Zusammenfassung	iii
Abstract	v
List of Figures	xv
List of Tables	xix
1 Introduction	1
1.1 Turbulence	1
1.2 Taylor-Couette (TC) flow	3
1.2.1 Historical Background	4
1.2.2 Current state of the art	5
1.2.2.1 Flow patterns	5
1.2.2.2 Angular Momentum Transport	5
1.2.2.3 General flow features	8
1.2.2.4 TC flow in the centrifugally stable regime	9
1.2.2.5 Curvature effect	11
1.3 Thesis Outline	11
2 Theoretical background and fundamentals	15
2.1 Fluid in motion	15
2.1.1 The continuity equation	15
2.1.2 The Navier-Stokes equation	16
2.1.3 Equation of motion in cylindrical coordinate system	16
2.2 Laminar Couette flow	17
2.3 Centrifugal instability	17
2.3.1 Rayleigh's stability criterion for non-viscous fluid	18
2.3.2 Linear stability analyses of the non-viscous fluid	19
2.4 Ekman Boundary layers	20
2.5 Angular Momentum Transport	21
2.6 Analogy of shear flows and Rayleigh-Bénard flow	22
2.7 Dimensionless Variables	23

TABLE OF CONTENTS

3	Experimental Setup, Measurement Technique, and Data Analysis methods	25
3.1	Experimental Setup	25
3.1.1	The top-view Taylor-Couette Cottbus (TvTCC) facility	26
3.1.1.1	TvTCC Geometry and Technical Details	27
3.1.1.2	TvTCC rotation control	30
3.1.1.3	Working fluids and Temperature control	30
3.2	Measurement Techniques	32
3.2.1	Flow Visualization	32
3.2.2	Torque measurement	35
3.2.3	Velocity measurement	35
3.2.3.1	PIV System	36
3.2.3.2	PIV Particles	37
3.2.3.3	Measurement procedure.	38
3.2.3.4	PIV measurements calibration.	39
3.2.3.5	PIV images post-processing	40
3.2.3.6	PIV error estimation	42
3.3	Data analysis methods	42
3.3.1	Statistical analysis	42
3.3.2	Spectral Analysis	44
3.3.2.1	The Fourier transform	44
3.3.2.2	Azimuthal energy co-spectra	45
3.3.3	Quadrant analysis	46
3.3.4	Dynamic Mode Decomposition (DMD)	46
4	Flow regimes in very wide gap TC flows with counter-rotating cylinders.	49
4.1	Experimental setup and visualization methods	49
4.2	Flow patterns	51
4.2.1	Laminar Taylor Vortex flow	51
4.2.2	Detached Taylor Vortex flow, Wavy Vortex Flow, and detached Wavy Vortex Flow	52
4.2.3	Turbulent Vortex flow	53
4.2.4	Turbulent Spots and Bursts	54
4.2.5	Axial Columnar Vortex	55
4.2.6	Helical Columnar Vortex	58
4.3	Regime diagram	58
4.4	Conclusion	60
5	The mean velocity field characteristics, and angular momentum transport.	61
5.1	Experimental set-up	62
5.2	Flow Field Features	65
5.2.1	Dependence of the flow structures on the rotation ratio.	65
5.2.2	Averaged velocity profiles	66
5.2.3	Neutral surface	70

5.2.4	Energy distribution	72
5.3	Angular momentum transport	74
5.3.1	The Nusselt number	74
5.3.2	Spatial and temporal behavior of the shear stress	79
5.3.3	Spatial spectral analysis	85
5.3.4	Quadrant analysis	87
5.4	Conclusion	89
6	Flow transition to the ultimate turbulent flow regime	93
6.1	Experimental setup and measurement procedure	94
6.2	Angular momentum scaling	95
6.3	Flow regimes and velocity profiles	96
6.4	Azimuthal energy spatial and temporal co-spectra	97
6.5	Dynamic Mode Decomposition (DMD)	102
6.6	Conclusion	104
7	The flow stability in the co-rotating regime.	105
7.1	Flow measurement methods	105
7.2	Flow visualization	106
7.3	Velocity Profiles	108
7.4	Conclusion	110
8	Conclusion	111
8.1	Open questions and future work	115
	References	117

List of Figures

1.1	Examples of turbulent dynamics.	2
1.2	Transition of laminar flow to turbulent flow, and a schematic figure for the Kolmogorov cascade theory of turbulence	3
2.1	Cartesian and cylindrical coordinates.	16
2.2	Schematic figures showing comparison between (a) Taylor-Couette, (b) Rayleigh-Bénard, and (c) Pipe flows.	22
3.1	Picture of the top-view Taylor-Couette Cottbus facility	28
3.2	CAD image for the upper part of the system	29
3.3	Inner and outer cylinder rotation velocity fluctuation	31
3.4	Regimes observed in flow between independently rotating cylinders at radius ratio $\eta = 0.883$	33
3.5	a) Sketch of the Taylor-Couette System with radius ratio $\eta = 0.1$, b) Images of meridional flow visualization	34
3.6	a) Sketch of the Taylor-Couette System with radius ratio $\eta = 0.1$, b) Images of the visualization setup	34
3.7	(a) PIV instantaneous image, b) the best fit of concentric circles through the cylinder points.	39
3.8	The PIV window in DaVis 10	39
3.9	Velocity vector calculation procedure used in DaVis 10	41
3.10	(a) The scale factor at the different heights, (b) the time and azimuthal averaged profile of the measured azimuthal velocity for a solid body rotation flow.	43
3.11	Schematic sketch describing the interpolation procedure	43
3.12	Example of the space-time subplot at a fixed radial position	44
4.1	Images of meridional flow visualization for Laminar Taylor Vortex flow	51
4.2	Images of meridional flow visualization for various Wavy Vortex flow situations	52
4.3	Sequence of meridional plane visualization of Turbulent Vortex flow	53
4.4	The Turbulent Spots	54
4.5	The Turbulent Bursts	55

LIST OF FIGURES

4.6	Sequence of meridional plane visualisation of Axial Columnar Vortex flow at $Re_s = 1650$, $\mu = -0.111$ for time steps: (a) 0.0 sec, (b) 0.2 sec, (c) 0.4 sec, (d) 0.6 sec, (e) 0.8 sec, (f) 1.0 sec, (g) 1.2 sec, (h) 1.4 sec. The inner cylinder wall is located at the right edge of the images, while the outer cylinder is located at the left edge.	55
4.7	The Axial Columnar Vortex	56
4.8	The Axial Columnar Vortex for higher Re_s flows.	57
4.9	Meridional visualization image and spatial-temporal behavior of the Helical Columnar Vortex for $Re_s = 1440$ and $\mu = -0.2$ at a location 5 mm away from the inner cylinder corresponding to $0.08d$	58
4.10	Regimes observed in flow between independently rotating cylinders at radius ratio $\eta = 0.1$	59
5.1	Left: Schematic of the TC apparatus with the PIV set-up, and the horizontal cross-section of the set-up with the horizontal laser sheet. Right: Mean Velocity field in the azimuthal-radial plane at mid-height for $\mu = -0.007$ and $Re_s = 6.1 \times 10^4$ obtained using PIV	62
5.2	The investigated parameter space in terms of Re_s and μ	64
5.3	Contour plots and velocity profiles showing the dependence of the normalized temporally and azimuthally averaged azimuthal and radial velocities.	65
5.4	Radial Profiles of spatially and temporally averaged angular velocity and momentum.	67
5.5	Radial Profiles of spatially and temporally averaged (t, ϕ, z) root-mean-square of (a) the radial velocity fluctuation multiplied by $2\pi r$, and (b) angular momentum fluctuation.	68
5.6	(a) Normalized radial gradient of angular velocity profiles as a function of μ , (b) normalized radial gradient of angular momentum profiles as a function of μ	69
5.7	(a) Normalized neutral surface \tilde{r}_n as function of the rotation ratio μ , (b) The radial position of the neutral surface at different heights.	70
5.8	Contour plots of the axially, azimuthally and temporally averaged, normalized energy as a function of \tilde{r} and μ at $Re_s = 6.1 \times 10^4$	72
5.9	Contour plots of the axially, azimuthally and temporally averaged, normalized energy as a function of \tilde{r} and μ at $Re_s = 1.31 \times 10^5$	73
5.10	(a) The quotient of the Nusselt number radial profiles over its average in the radial range, (b) The variation of the radial averaged Nusselt number Nu_ω^{Total} as a function of μ	75
5.11	(a) Radial averaged Nusselt number large-scale contribution (Nu_ω^{LSC}), (b) Radial averaged Nusselt number turbulent contribution (Nu_ω^{Turb}) as a function of μ	75
5.12	Contour plot showing the space-time diagram of $r^3(\omega u_r)/J_{lam}$ for 5 different radial positions, for $Re_s = 6.1 \times 10^4$. (a) $\mu = 0$, and (b) $\mu = -0.0077$	80
5.13	Contour plot showing the space-time diagram of $r^3(\omega u_r)/J_{lam}$ for 5 different radial positions, for $Re_s = 6.1 \times 10^4$. (a) $\mu = -0.015$, and (b) $\mu = -0.025$	81

5.14	Contour plot showing the space-time diagram of $r^3(\omega u_r)/J_{lam}$ for 5 different radial positions, for $Re_s = 6.1 \times 10^4$. (a) $\mu = -0.04$, and (b) $\mu = -0.06$	81
5.15	Contour plot showing the space-time diagram of $r^3(\omega u_r)/J_{lam}$ in the radial-time plane at a fixed azimuthal position $\phi = \pi/2$, for $Re_s = 6.1 \times 10^4$ for a) $\mu = -0.007$, and b) $\mu = -0.06$	82
5.16	Contour plot showing the space-time diagram of the radial velocity U_r in the azimuthal-time plane for 5 different radial positions for $Re_s = 6.1 \times 10^4$. (a) $\mu = -0.0077$, and (b) $\mu = -0.06$	82
5.17	The spatial two-point auto-correlation coefficient of the azimuthal velocity fluctuation for different rotation ratios, at a) $\tilde{r} = 0.2$ and b) $\tilde{r} = 0.8$	84
5.18	The pre-multiplied temporally averaged azimuthal energy co-spectra normalized by the area A_E below its graph. The profiles are shown for flows $Re_s = 6.1 \times 10^4$ at different heights. (a) $\mu = -0.007$ and $\tilde{r} = 0.6$, (b) $\mu = -0.007$ and $\tilde{r} = 0.9$, (c) $\mu = -0.06$ and $\tilde{r} = 0.6$, (d) $\mu = -0.06$ and $\tilde{r} = 0.6$	85
5.19	The pre-multiplied Temporally averaged azimuthal energy co-spectra for flow with $Re_s = 6.1 \times 10^4$ and different rotation ratios: a) $\mu = 0$, b) $\mu = -0.0077$, c) $\mu = -0.015$, d) $\mu = -0.025$, e) $\mu = -0.04$, and f) $\mu = -0.06$, at radial positions $\tilde{r} = 0.4, 0.5, 0.6, 0.7, 0.8, 0.9$	86
5.20	The Joint PDFs of radial velocity fluctuations u'_r and the angular velocity fluctuations ω' at different radial positions. For different rotation rates, (a) $\mu = 0$, (b) $\mu = -0.0077$, (c) $\mu = -0.025$, and (d) $\mu = -0.06$. For shear Reynolds number $Re_s = 6.1 \times 10^4$	88
6.1	The investigated parameter space in terms of Re_s and μ	94
6.2	(a) the radial averaged Nusselt number as a function of shear Reynolds number for $\mu = 0$, (b) the compensated Nusselt number $Nu_\omega Re_s^{-0.76}$ as function of shear Reynolds number	95
6.3	The radial profiles of spatially and temporally averaged (t, ϕ, z) normalized, (a) angular velocity $\tilde{\omega}$, (b) angular momentum \tilde{L}	96
6.4	Radial profiles of the of spatially and temporally averaged (t, ϕ, z) root-mean-square of the normalized radial velocity fluctuation $\tilde{U}_{rms}^r = U_{rms}^r/u_s$	96
6.5	The pre-multiplied Temporally averaged azimuthal energy co-spectra at the different radial positions and at the apparatus midheight for: (a) $Re_s = 10^4$, (b) $Re_s = 6 \times 10^4$, and (c) $Re_s = 1.5 \times 10^5$	98
6.6	The pre-multiplied Temporally averaged azimuthal energy co-spectra normalized by the area A_E below its graph. The profiles are shown for flows with different Re_s at : (a) $\tilde{r} = 0.4$, (b) $\tilde{r} = 0.6$, (c) $\tilde{r} = 0.9$	99
6.7	The pre-multiplied azimuthal energy temporal co-spectra for the measured velocity field at the apparatus midheight and different radial positions for flow with:(a) $Re_s = 10^4$, (b) $Re_s = 6 \times 10^4$, and (c) $Re_s = 1.5 \times 10^5$	101
6.8	Visualization of the DMD modes of the radial velocity component fluctuation for $Re_s = 10000$ and $\mu = 0$	102

LIST OF FIGURES

6.9	Visualization of the DMD modes of the radial velocity component fluctuation for $Re_s = 150000$ and $\mu = 0$	103
7.1	Meridional visualization image, and spatial-temporal behavior of the flow for $Re_s = 5 \times 10^4$ and $\mu = +0.01$ at a location 5 mm away from the inner cylinder.	106
7.2	Meridional visualization image, and spatial-temporal behavior of the flow for $Re_s = 5 \times 10^4$ and $\mu = +0.02$ at a location 5 mm away from the inner cylinder.	107
7.3	Meridional visualization image, and spatial-temporal behavior of the flow for $Re_s = 5 \times 10^4$ and $\mu = +0.03$ at a location 5 mm away from the inner cylinder.	108
7.4	Radial Profiles of spatially and temporally averaged (t, ϕ, z) normalized angular velocity $\tilde{\omega}$ for flows with rotation ratio $0.008 \leq \mu \leq 0.04$ for (a) $Re_s = 6 \times 10^4$, (b) $Re_s = 9 \times 10^4$	109
7.5	Radial Profiles of azimuthal and temporally averaged (t, ϕ) radial velocity (U_r) for $Re_s = 6 \times 10^4$ for (a) $\mu = +0.015$, (b) $\mu = +0.025$	109

List of Tables

2.1	Analogy of transport fluxes and dissipation rates in RB, TC and pipe flow. . .	22
3.1	Geometries built in the Top view Taylor-Couette Cottbus System	26
3.2	The maximum Reynolds number that can be reached by the TvTCC facility .	30
3.3	The fluid properties at different temperatures	31
3.4	VEO 640 Phantom camera resolution	37
3.5	PIV particles technical specifications	38
5.1	Scale factor at different heights	62

1

Introduction

1.1 Turbulence

The word “turbulence” is 10 letters long, but it has a big impact on our daily lives as it can be found everywhere around us. Some people associate turbulence with uncomfortable flights requiring fastened seat belts, but the reality is that it exists in many places, such as rivers, oceans, the atmosphere, smoke, car wheels, taps, car exhaust, and even inside our bodies where blood flows turbulently through arteries. Even more important, we rely on turbulence to mix the milk and sugar in our coffee mugs. Figure 1.1 provides examples of different turbulent flows.

What is turbulence? The word turbulence comes from the Latin word *Turba*, which means crowd, disorder, and confusion. In physics, turbulence refers to the irregular and apparently chaotic motion of a fluid. More than 500 years ago, Leonardo da Vinci studied this phenomenon and coined the term “turbolence” to describe such fluid flows. Over the last six centuries, physicists have tried to capture the essence of turbulence, but it appears to have been a difficult task, and it is still regarded as one of the most, if not the most, important unsolved problems today. The well-known physicist Sir Horace Lamb said the following: “I am an old man now, and when I die and go to heaven, there are two matters on which I hope for enlightenment. One is quantum electrodynamics, and the other is the turbulent motion of fluids. And about the former, I am rather optimistic”. From the definition of turbulence, where it was defined as a chaotic motion of a fluid, we can understand the problem of turbulence, which makes it impossible to precisely predict what is going to happen to any particular particle in the fluid.

Osborne Reynolds was one of many eminent scientists that studied the turbulence phenomena, and he identified the parameter UD/ν as a dimensionless group to distinguish the flows between laminar and turbulent. This parameter was named after the Reynolds number and is defined as: $Re = \frac{\rho UL}{\mu}$, where U and L are the flow characteristic velocity and length scale, respectively, ρ is the fluid density, and μ is the fluid viscosity. The flow



Figure 1.1: Examples of turbulent dynamics. From top left: water flow in a creek which encounters rapids (credits: jatin_kumar, flickr.com); smoke swirls of a cigarette; expansion of a milk spot in a coffee mug (credits: Connie_Ma, Flickr.com), at the bottom: vortex-shaped cloud formations (credits: Paul Chartier).

is defined as turbulent when the inertia forces sufficiently exceeded the viscous forces. For small values of Re , the velocity fluctuations are damped by the viscosity, so the fluid moves in a predictable direction without notable mixing between the different fluid layers. But when the Re exceeds a critical value, so that the velocity fluctuations are no longer damped by the viscosity, different flow instabilities arise in the flow and turn it turbulent. In 1922, Richardson gave one of the first views about turbulence, where he gave it a cascade picture. He mentioned that the turbulent flow is composed of eddies with different sizes, and due to the flow instability, the big size eddies break up into smaller eddies, and these smaller eddies break up into even smaller ones until they reach a size where they are damped by the molecular viscosity [1]. In 1941, three very important papers were published in Russia [2, 3, 4], where they held some important results of turbulence theory, and they had the signature of A. N. Kolmogorov. Kolmogorov added and quantified the picture of cascade with the so-called K41 theory [2]. Where the K41 theory states that the kinetic energy cascades from large scales to a smaller viscous scale where it is dissipated, as shown in figure 1.2.

As mentioned previously, turbulence exists in most fluid flows and is therefore of great interest in engineering studies. According to a study published in Bloomberg [5], about 10 % of the electricity generated annually is consumed in the process of overcoming the effects of turbulence. As a result, engineers have sought to study and model turbulent flow over various objects in everyday use, and then try to reduce its effect. For instance, the viscous drag on

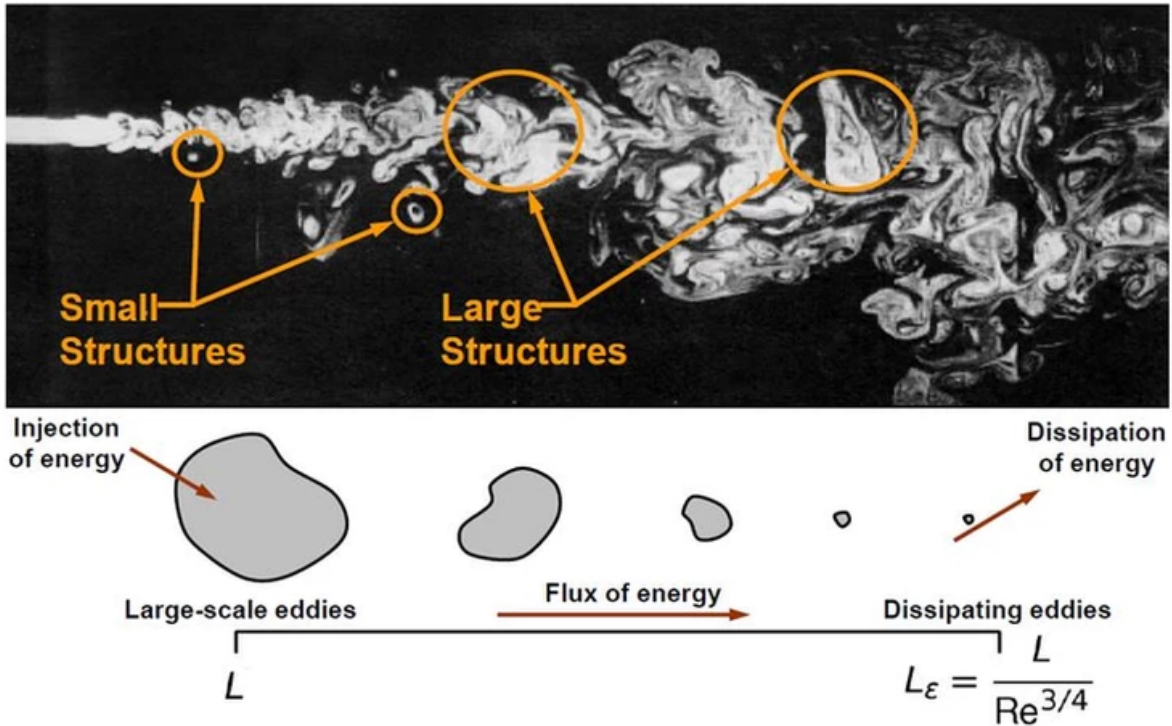


Figure 1.2: Top: transition from laminar to turbulent flow; the picture shows the existence of different sized structures in the turbulent flow. Bottom: A schematic for the Kolmogorov cascade theory of turbulence shows how the energy cascaded from the large scale to the dissipating scale, $L_E = L/Re^{3/4}$. The figure is adapted from: manchestercfd.co.uk.

a surface is much greater in turbulent flow than in laminar flow. Surface specifications are crucial in controlling drag, so engineers can study turbulent flow over these surfaces to achieve optimal design and reduce friction losses, resulting in lower energy consumption worldwide. This is one example that highlights the importance of studying and comprehending turbulence and its impact on our everyday lives. Moreover, the study of turbulent flow is essential in geophysical and astrophysical research, as the majority of studied flows are turbulent. In addition to inertia and viscosity, other factors, such as stratification [6] and magnetic fields [7] play important roles in the flow stability.

1.2 Taylor-Couette (TC) flow

Understanding the impacts of the various driving characteristics may help regulate turbulent flow, as was demonstrated in the preceding section, which emphasized the significance of researching this flow. For this reason, the scientist tried to study the turbulent flow using simple geometries in order to investigate the flow for the different driving parameters and study the effect of each. The Taylor-Couette (TC) system is one of these geometries. The flow in the gap between two concentric, independently rotating cylinders is named “Taylor-Couette flow”. The TC flow was used as one of the paradigmatic systems of the physics of fluids. Its simple and mathematically well-defined geometry, natural periodicity, and confinement of fluid volume lead to excellent conditions for experimental and numerical studies.

The flow in the gap in a Taylor-Couette system is primarily controlled by the rotation rates of the cylinders and the geometrical parameters. The main geometrical parameter of the system varies depending on the dimensions of both cylinders, and it is defined by the radius ratio $\eta = r_1/r_2$, the gap width $d = r_2 - r_1$, and the aspect ratio $\Gamma = L/d$, with r_1 the inner cylinder radius, r_2 outer cylinder radius, and L the apparatus length. The flow states in this system are mainly determined by the dimensionless Reynolds numbers $Re_1 = r_1\omega_1 d/\nu$ and $Re_2 = r_2\omega_2 d/\nu$ of the inner and outer cylinders, respectively, with ν is the kinematic viscosity of the fluid. In this study, in order to measure the shear induced by the cylinders' rotation on the flow, the shear Reynolds number introduced by [8] is used,

$$Re_s = \frac{2}{1+\eta} |\eta Re_2 - Re_1| = \frac{2r_1 r_2 d}{(r_1 + r_2)\nu} |\omega_2 - \omega_1|. \quad (1.1)$$

After defining the main flow parameters Re_1 and Re_2 , the flow inside the gap takes its shape. The flow global response can then be quantified in terms of the conserved angular momentum flux J_w [9]:

$$J^\omega = r^3 \left(\langle u_r \omega \rangle_{A(r),t} - \nu \partial_r \langle \omega \rangle_{A(r),t} \right), \quad (1.2)$$

with $\langle \dots \rangle_{A(r),t}$ denoting an average over a cylindrical surface and time t , u_r and ω denoting the radial and angular velocities, respectively.

1.2.1 Historical Background

Studying the flow of fluid caught between rotating concentric cylinders has its roots in more than 300 years of history [10], where the varied patterns that appear in these flows and their turbulent behavior stimulated physicists to study this kind of flow, which was named after that as ‘‘Taylor-Couette Flow’’ in more details. The journey started with Isaac Newtons, in 1687 he described the rotating motion of the fluid about a cylinder [11]. About one and a half centuries later, the pioneering theoretical fluid dynamicist George G. Stokes suggested that eddies would be produced if the inner cylinder were made to rotate too fast [12]. Stokes, when studying this flow, noted the difficulty in the boundary conditions at the walls of the cylinder. Later in 1881, Max Margules was the first person to propose constructing a rotating viscometer [13]. In 1888 Mallock conducted experiments to measure the water’s viscosity using two concentric outer and inner cylinders, with a rotating outer cylinder and inner cylinder suspended on a torsion fiber [14]. At the same time, Couette also announced the first experiments with his rotating cylinder viscometers [15], which are known today as ‘‘Couette viscometer’’. In 1923, the paper of G. I. Taylor was published [16], which was a key development in the study of fluid mechanics. The paper examines linear stability theory for cases of viscous flow confined between two rotating cylinders, with the flow studied for both co- and counter-rotating cylinders. In the 1950s, the great astrophysicist Chandrasekhar discussed the hydrodynamic stability of Taylor-Couette flow in his book *Hydrodynamic and Hydromagnetic Stability* [17], where this book increases the understanding of the TC flow. Until today, different experimental, numerical, and theoretical studies were conducted, and a lot of them are still in process. These studies investigate the flow in different geometries, for different rotation rates, and for different shearing intensities, and there is always something

new coming out of these studies, which always enhances our understanding of such kinds of flows.

1.2.2 Current state of the art

Various concepts and topics in fluid mechanics have been studied by the TC flow. The flow patterns [18, 19], angular momentum transport [20, 21, 22], the flow field features [23, 24], hydrodynamics instabilities [25], and other different topics. In the following section, the main findings from recent research on Taylor-Couette flow are presented.

1.2.2.1 Flow patterns

From the different scientific works studying the TC flow, several works were focusing on the existence of different flow states in the Taylor-Couette flow. The system's huge variety of flow states offers the possibility of studying the flow in its different phases, including laminar, turbulent, and the transition between these two phases [26, 27, 28, 20]. The different hydrodynamic instabilities that occur in the flow lead to the appearance of different coherent flow patterns [18, 29]. The changing of the driving parameters leads to a series of flow transitions; these flow transitions can be classified into different flows, like circular Couette flow, Taylor vortex flow, periodic nonaxisymmetric flow, wavy vortex flow, modulated wavy vortex flow, etc. [26, 30, 31, 32]. D. Coles [32] investigated, for a given Reynolds number, with a rotating inner cylinder and fixed outer cylinder, 25 different flow states, by probing the phase-space. Andereck et al. [33] studied for one single geometry ($\eta = 0.883$) the flow states for co-rotating cylinders. The previous studies were focusing on the wide gap TC geometries $\eta \geq 0.7$. While most of the work has been done on narrow gap TC flows, only a limited amount of research has been conducted on wide gap TC flows with $\eta \leq 0.5$. The effect of the end walls on the transitions between the Taylor and spiral vortices was studied numerically and experimentally by Altmeyer et al. [34] for $\eta = 0.5$ geometry. Moreover, Altmeyer et al. [35] studied numerically for the same geometry $\eta = 0.5$ the spiral structures in the TC flow. Also, the study of the counter-rotating regime for $\eta = 0.357$ has been carried out earlier in the experimental facility used in the present study [36] where also the visualization technique was used in order to investigate the existence of different flow patterns.

1.2.2.2 Angular Momentum Transport

The differential rotation between the inner and outer cylinders in the TC system drives the flow inside the gap through shear. This differential rotation causes a radial-dependent profile of the azimuthal velocity u_ϕ , and as a result, a radial-dependent profile of angular velocity ω and angular momentum L . This radial-dependent u_ϕ profile causes molecular and convective transport of the angular momentum through the gap. Different analyses were carried out to study the similarities between this flow and the Rayleigh–Bénard convection (RB) flow, the thermally driven flow heated from below and cooled from above [37, 38, 39, 40], where one of the fruits of these studies was to express the local transport quantities or the angular momentum transport in TC flow in analogy to the heat transport in RB flow in

1. Introduction

terms of the pseudo-Nusselt number $Nu_\omega = J^\omega/J_{lam}^\omega$, with $J_{lam}^\omega = 2\nu r_1^2 r_2^2 (\omega_1 - \omega_2)/(r_2^2 - r_1^2)$ the transport flux in laminar flow. The Nu_ω can be computed from the flow velocity field by calculating the angular momentum flux J^ω shown in equation 1.2. The Nu_ω is also directly connected in the TC system to the torque (T) induced on the inner cylinder in order to keep its rotation velocity constant when the angular momentum is transported through the gap. This torque can be presented in its dimensionless form and is defined as $G = T/2\pi l \rho \nu^2$, with ρ the fluid density, and then the pseudo-Nusselt number computes: $Nu_\omega = G/G_{lam}$, with $G_{lam} = r_1 r_2 Re_s d^{-2}$ the dimensionless torque for the laminar case.

Angular momentum transport dependence on the rotation ratio

The transported angular momentum through the gap shows a clear dependency on the kinematic of the system presented in terms of the rotation ratio (μ), where the Nu_ω attains different values for flows with the same Re_s and varied rotation ratio μ . For specific rotation ratio μ_{max} the angular momentum transport achieves maximum value. When talking about μ_{max} it is very important to distinguish between two sets of TC flow geometries: first, the very narrow gaps TC ($\eta \geq 0.91$) and the rotating plane Couette flow (RPC), and the second group is the TC flows with radius ratios $0.1 < \eta < 0.91$. Concerning the first group of geometries, it was reported the existence of two Nu_ω maxima at different rotation rates [41, 42, 43, 44]. The first maximum, or what they called “the broad peak”, was accompanied by the strengthening of the flow large-scale structures [41]. The second maximum, “the narrow peak”, was a consequence of shear instabilities. Moving to the second group of TC geometries, the broad peak was always found when the outer cylinder was set to rotate in the counter direction with respect to the inner cylinder, but the narrow peak was not observed in such TC flow geometries. For $\eta = 0.716$ Van Gils et al. [20] measured a maximum at $\mu_{max} = -0.33$, which confirmed the study of Poaletti et al. [45] for $\eta = 0.724$ with $\mu_{max} = -0.33$. For a wider gap $\eta = 0.5$, Merbold et al. [21] shows that the maximum occurs at $\mu_{max} = -0.2 \pm 0.02$ using direct torque measurements. For the same geometry, Froitzheim et al. [24] also investigated $\mu_{max} = -0.2$ using velocity field measurements. Froitzheim et al. [36] finally measured for a wide gap TC geometry $\eta = 0.357$ a maximum at $\mu_{max} = -0.123 \pm 0.03$ using the direct torque measurements. Ostilla-Mónico et al. [46] further confirmed the values of μ_{max} numerically by finding $\mu_{max} = -0.22$ for $\eta = 0.5$, and $\mu_{max} = -0.33$ for $\eta = 0.716$ and $\mu_{max} = -0.123 \pm 0.03$ for $\eta = 0.357$. They showed also that this maximum is connected to the formation of the turbulent Taylor vortices, which enhance the angular momentum transport. Where these measurements strongly support the prediction of Brauckmann and Eckhardt [47], where they discussed the enhanced Large-scale Circulation (LSC) role in transporting angular momentum. In conclusion, it is observed that the broad peak is observed in all studied TC geometries ($0.1 \leq \eta \leq 0.98$) up to now and in RPC flows, and it can be attributed to the same cause, the strengthening of large-scale structures.

Further, different attempts were made to drive a prediction for the position of μ_{max} related to the broad peak. Van Gils et al. [20] predict the so-called angle bisector hypothesis, which defines the rotation ratio of the torque maximum μ_b by :

$$\mu_b = \frac{-\eta}{\tan[\frac{\pi}{2} - \frac{1}{2}\arctan(\eta^{-1})]} \quad (1.3)$$

where they argued that the most unstable point in the parameter space is in an equidistant location between the Rayleigh stability line $\mu = \eta^2$ and $\mu = \infty$. The hypothesis correctly predicted the torque maximum for $\eta = 0.716$, but it deviates noticeably for $\eta = 0.5$, predicting $\mu_b = -0.309$, which is sufficiently different from $\mu_{max} = -0.2$. Another prediction was made by Brauckmann and Eckhardt [47], where they linked the location of the torque maximum to the onset of intermittency in the gap and the strengthening of the Taylor vortices, and they came back with the following:

$$\mu_p(\eta) = -\eta^2 \frac{(a(\eta)^2 - 2a(\eta) + 1)\eta + a(\eta)^2 - 1}{(2a(\eta) - 1)\eta + 1} \quad (1.4)$$

with $a(\eta)$ a factor that shows the extension of the Taylor vortices to the theoretical neutral line (the radial position in the gap where the azimuthal velocity). Brauckmann and Eckhardt [47] stated that for slight counter-rotation of the outer cylinder, the extension of the Taylor Vortices reaches the outer cylinder wall, so the vortices gain in strength and will cause a maximum angular momentum transport. The prediction yields $\mu_p(\eta = 0.5) = -0.191$ and $\mu_p(\eta = 0.71) = -0.344$ with very good agreement with the previously presented findings. It is worth mentioning that the position of the broad peak of the angular momentum transport changes slightly by varying the shearing of the system, but for high enough Re_s it reaches a fixed value. On the other side, Ezta et al. [42] show that the narrow peak position has a clear dependence on the driving rate.

The effective scaling of the angular momentum transport

Another topic discussed when studying the angular momentum transport in TC flow is the effective torque scaling with the shear rate, which can show the effect of the shearing on the flow global response. In order to focus on the effect of the flow driving forces expressed by Re_s , the flow for pure inner cylinder rotation $\mu = 0$ was typically assumed in the different studies, and a power-law ansatz of $Nu_\omega \sim Re_s^{\alpha-1}$ was formed. Wendt [48] found for three different geometries ($\eta = 0.68, 0.85$, and 0.935), the exponent $\alpha = 1.5$ for $4 \times 10^2 \leq Re_1 \leq 10^4$, and a transition of the exponent to $\alpha = 1.7$ for $Re_1 > 10^4$, where these results were calculated using direct torque measurements. In contrast to Wendt, Lathrop et al. [49] were not able to find a fixed scaling exponent, but they investigated experimentally for $\eta = 0.724$ a monotonic increase in the exponent from $\alpha = 1.23$ to $\alpha = 1.87$ for $8 \times 10^2 \leq Re_1 \leq 1.2 \times 10^6$. These results were further agreed by Lewis and Swinney [50] for the same geometry, after measuring the torque scaling with an order of magnitude higher accuracy compared to those reported by [49]. But for a very near geometry, van Gils et al. [20, 51] and Huisman et al. [52] found for $\eta = 0.716$ a nearly constant scaling of $\alpha = 1.78 \pm 0.06$ for a high Reynolds number. Further, for TC flow with $\eta = 0.5$, Merbold et al. [21] found an exponent of 1.62 for $3 \times 10^3 \leq Re_s \leq 8 \times 10^4$, and also investigated for shear rates beyond $Re_s = 10^5$ a transitional behavior on the scaling exponent, where its value increases to $\alpha = 0.75 \pm 0.03$. For further wider gaps Burin et al [53]

1. Introduction

calculated the angular momentum transport in TC flows with $\eta = 0.35$ using LDV velocity measurements and found $\alpha = 1.6 \pm 0.1$ for $2 \times 10^3 \leq Re_1 \leq 10^4$, and $\alpha = 1.77 \pm 0.07$ for $2 \times 10^4 \leq Re_1 \leq 2 \times 10^5$. Ostilla-Mónico et al. [23] linked the transitional behavior of the scaling exponent found in the presented investigations to the transition of the laminar boundary layer to turbulent ones. In other words, and in analogy to the Rayleigh–Bénard flow [54], the transition in the scaling exponent in the TC flow, indicates a transition to the "ultimate" regime where turbulence is fully developed in the bulk and the boundary layers [52, 55]. The transition to this ultimate regime occurs when the boundary layers are sheared strongly enough that they undergo shear instability and become turbulent [20, 55]. The transition can be characterized by effective scaling between the shear Reynolds number and the Nusselt number as $Nu_\omega \sim Re_s^{0.78 \pm 0.06}$, where, from the aforementioned results, it is observed that the scaling exponent is independent of the radius ratio, although the shear rate at which the transition takes place is dependent on the TC flow radius ratio.

1.2.2.3 General flow features

In the previous section, it is shown that as the flow shear strength increases and for a critical value of Re_s a transition in the torque scaling exponent occurs, where this transition was linked in analogy to the Rayleigh–Bénard flow to the transition from the classical turbulent regime to the ultimate turbulent regime [50, 52, 20, 21]. This transition from the classical regime to the ultimate regime is reflected in the general flow behavior. The flow velocity profiles in the gap can be separated into two boundary layers (first near the inner cylinder wall and second near the outer cylinder wall) and a bulk flow [56, 57]. In the classical regime, the bulk flow is turbulent, but the boundary layers are laminar and described by the Prandtl-Blasius theory [58, 59], in contrast to the ultimate regime, where both are turbulent. Further, it was found that the velocity profiles in the turbulent boundary layer in the ultimate regime depict a log-layer [60, 61, 62], so the velocity profiles have a logarithmic dependence on the distance to the wall. Such logarithmic profiles in the boundary layers were also found in the RB flow beyond the transition to the ultimate regime for the temperature mean [63, 55].

The flow velocity radial profiles were also studied in the bulk, where the angular velocity profile is of special interest when talking about angular momentum transport. It was found that when the bulk flow turns turbulent, the angular velocity profiles tend to have flat behavior in the bulk due to the effective mixing caused by the turbulence. By varying the rotation rate, the profiles get even more or less flat, and the gradient of these profiles in bulk varies as well. This behavior can be reflected in the angular momentum effective mixing in the bulk, so the more the profile is flat, the more angular momentum is transported. This was investigated for TC flows in different geometries ($\eta = 0.357, 0.5, 0.714, 0.833, \text{ and } 0.909$), where angular velocity profiles with a minimum gradient in the bulk are found for μ_{max} , the rotation ratio where a maximum of angular momentum transport occurs [46, 24, 36].

Another flow feature, which is more related to the flow kinematics defined by the rotation ratio, is the detachment of the neutral line. The neutral line is defined as the radial location in the gap where the azimuthal velocity component u_ϕ vanishes. The velocity profile, and particularly the azimuthal velocity (u_ϕ) profile, give access to finding the radial position of the

neutral surface by detecting the radial position where the mean azimuthal velocity changes its direction (sign). The study of the detachment of the neutral line gains a spectacular interest after the study of Brauckmann and Eckhardt [47], where they link the start of the neutral line detachment from the outer cylinder to the maximum of the angular momentum transport. Brauckmann and Eckhardt [47] argued that the Large-scale Circulations (e.g. Taylor Vortex Flow) seek to extend beyond the outer cylinder, but they are restricted by a rigid wall for $\mu > \mu_{max}$, and for μ_{max} where the detachment of the neutral surface starts, the rigid wall is replaced by a softer surface like the laminar boundary layer, so the Large-scale Circulations turned out to be less restricted and were able to extend and gain more strengthening and, as a result, effectively increase the momentum transport. This prediction was proved in different experimental works, where van Gills et al [20] found that the detachment of the neutral line from the outer cylinder started at μ_{max} for $\eta = 0.71$, the same for $\eta = 0.5$ by Froitzheim et al. [24]. Further, for $\mu < \mu_{max}$ and after the detachment of the neutral line, radial segregation inside the gap occurs, so the flow in the inner region is centrifugally unstable, while in the outer region it is stable due to the outer cylinder rotation stabilizing effect [17]. Furthermore, for $\mu > \mu_{max}$ the stabilized outer region experiences a penetrating intermittent burst, which destroys the LSC and leads to a drop in the angular momentum transport, as proposed by [47].

1.2.2.4 TC flow in the centrifugally stable regime

When both the inner and outer cylinders of a TC system rotate in the same direction, the flow inside the gap is considered to be in the co-rotating regime. But the flow in the co-rotating regime experiences another important segregation, where it is divided into centrifugally stable and centrifugally unstable parts. According to the Rayleigh criterion [64], when the angular momentum $L = r^2\omega$ increases radially with increasing r ($\omega_1 r_1^2 < \omega_2 r_2^2$) the flow is centrifugally stable, or in other words, the flow is centrifugally stable for rotation ratios $\mu > \eta^2$, and centrifugally unstable for $\mu < \eta^2$. It is clear that the flow in the second group is unstable due to centrifugal instability. However, the question has always been raised about the first group: is the flow completely laminar, or is there any other mechanism that could destabilize the flow apart from centrifugal instability? This question is of very special interest to astrophysical studies when studying the flows quasi-Keplerian regime, which is centrifugally stable. Such flows can be found in the accretion disks, which are astrophysical disks composed of gas and dust that rotate around a central object, like a star or a planet. The central objects of accretion disks are formed by the gravitational collapse of the disk matter. The rotation of these disks, even a very slight rotation, leads to angular momentum, which is strong enough to overcome the gravitational forces that are responsible for the formation of the disk's central object [65]. As a result, the orbiting matter needs to lose angular momentum to move radially toward the central object. From the observed accretion rates of the accretion disks, it is stated that the angular momentum transport cannot be due to the pure molecular viscosity [66, 67]. But unlike molecular viscosity, turbulence can efficiently transport angular momentum, letting the gravity forces become stronger than the outer-radial angular momentum component and collapsing matter to form the observed astrophysical bodies. So it was always the question of the

mechanism that destabilizes the flow and generates turbulence, as the rotating matter around the disk has a Keplerian velocity profile and the flow is centrifugally stable. Two possible instabilities have been proposed to account for destabilizing the Keplerian (centrifugally stable) flow: the magnetorotational instability and the subcritical hydrodynamic instability. In order to study the second proposition, the subcritical hydrodynamical instability, the TC system was suggested as a model to study the transport behavior in the accretion disks [8, 68, 69, 67], as the gas-dust region of the accretion disks can be approximated as a simple differentially rotating shear flow. In addition to the different control parameters used to characterize the TC flow in the counter-rotating regime, the community defines the parameter q [70, 71] with:

$$\frac{\omega_2}{\omega_1} = \mu = \eta^q. \quad (1.5)$$

The parameter q is defined just for the co-rotating regime. As discussed above, for $q > 2$, the flow is centrifugally unstable, while for $0 < q < 2$ the flow is centrifugally stable, and it is also known as the quasi-Keplerian regime. In the accretion disks, the keplerian azimuthal angular velocity profile $\omega(r) \propto r^{-3/2}$ [72], leads to $q = 3/2$. The key question now is: can the TC flow in the centrifugally stable regime ($0 < q < 2$) become unstable due to finite-size perturbations caused by a subcritical transition to turbulence? To answer this question, different numerical and experimental studies were done, investigating the centrifugally stable TC flow in different geometries. Ji et al. [70] studied experimentally the angular momentum transport in the quasi-Keplerian flow in a $\eta = 0.35$ and $\Gamma = 2.1$ TC apparatus. The experimental apparatus used in the study was designed in such a way that the top and bottom plates rotate independently of each other and from the system cylinders in order to reduce their effect on the flow. The flow was studied for $3 \times 10^5 \leq Re_s \leq 2 \times 10^6$, and it was found that the angular momentum transport is approximately equal to the molecular viscous transport, which means that no angular momentum transport due to turbulence exists in the quasi-Keplerian flow. Using different TC apparatus, Paoletti & Lathrop [45] and Paoletti et al. [71] measured the global torque as a function of the driving rate Re_s in a $\eta = 0.7245$ and $\Gamma = 11.47$ TC system. The end gaps of the system were attached to the outer cylinder, and the torque was measured in the central part of the inner cylinder, assuming that the system has a large enough aspect ratio and that the end plate effect can't affect the torque measurements in the center part. It was found from this study that for flow in the quasi-Keplerian regime and $Re_s \approx 7 \times 10^5$, the angular momentum transport is larger than the laminar viscous transport; these results are in contrast to those found by Ji et al. [70]. However, the argument was always about the end plates' effects and whether they are responsible for destabilizing or stabilizing the flow in the quasi-Keplerian regime. Numerically, Ostilla-Mónico et al. [73] investigated the flow in the quasi-Keplerian regime using periodic boundary conditions in the axial direction in order to prevent the effect of the end plates. The flow in their DNS was investigated for $\eta = 0.714$, $\Gamma = 2.094$, and a shear Reynolds number of up to 10^5 . In their simulations, they started with a turbulent flow and then started rotating the outer cylinder until the flow reached the quasi-Keplerian regime. They show that the angular momentum transport decreases by time down to a value corresponding to laminar flow when the flow reaches the quasi-Keplerian regime, and then they derive the same conclusion as in Ji et al. [70]. From the presented

studies, it is clear that the question is still open and not completely answered yet. Taking into account the studies mentioning that the TC flow is centrifugally stable in the quasi-Keplerian regime [70, 73, 74], these studies investigate the flow just up to $Re_s \approx 10^6$ in specific TC geometries, and so the subcritical transition to turbulence can't be excluded for higher shear Reynolds number flows and much wider-gap TC geometries.

1.2.2.5 Curvature effect

It is clear from what is presented in this section that the TC flow has some common behavior for different geometries with different radius ratios and some does not. The radius ratio η is directly related to the curvature effect, which also plays a very important role in TC flow. The curvature number $R_c = d/\sqrt{r_1 r_2}$ introduced by [8], measures the influence of curvature in terms of the geometrical mean of both the cylinder's radii and the gap width d . One of the examples that can explain the effect of the curvature is the Görtler instability. Where this instability can disturb the viscous boundary layers of flows over concave surfaces, streamwise-oriented counter-rotating vortices named Görtler vortices lead the flow through a transition to turbulence [75, 76]. As η approaches 1, the curvature effect vanishes and R_c becomes zero, where in this situation the TC flow becomes a rotating Plane Couette flow [41]. They also showed that, for $\eta < 0.9$, the asymmetry inside the gap increases and shows the difference between the inner gap region and the outer region, and the curvature effect becomes more important. This asymmetry inside the gap increases as η decreases. It is observed how μ_{max} is strongly related to the radius ratio; also, the effect of the radius ratio can be observed in the transition to the ultimate turbulent regime, so the flow for $\eta = 0.357$ reaches the transition for lower Re_s [36] compared to the flow for $\eta = 0.5$ [21, 24]. Further, Brauckmann et al [41] performed a numerical simulation for flows with radius ratios between 0.5 and 1, and they concluded that the dependence of the Nusselt number on the radius ratio is due to the radial partitioning of the flow.

1.3 Thesis Outline

Different concepts and topics in fluid mechanics have been studied in TC flow, but most of the previous studies have been conducted in narrow gap, less in wide gap, and rarely in very wide gap geometries. And after each of these studies, the common question always arises about the effect of the system curvature on the general flow behavior. In this thesis, these concepts are experimentally studied in a very wide gap Taylor-Couette geometry with a radius ratio $\eta = 0.1$, where the influence of the cylinder walls curvature on the flow behavior is anticipated to be very high. Throughout this thesis, the flow was investigated in the different rotation regimes in the range of $530 \leq Re_s \leq 1.5 \times 10^5$. The theoretical description of phenomena related to the investigation, the experimental setup, the measurement techniques, the formation of flow patterns, the angular momentum transport, the transition from one turbulent regime to another, and the flow field behavior are treated in different chapters, which will be described hereafter.

In chapter 2, the fundamental theory to describe the general flow motion in addition to the Taylor-Couette flow is presented. The contents shown are not original work but are mainly reported from textbooks and intended to provide the reader with a basic knowledge of the concepts that will be dealt with in the next chapters. The first section focuses on the basic equations controlling fluid motion in general and then how they can be used in a cylindrical coordinate system, which is the case in the current study. The rest of the sections are devoted to the fundamental theories and equations describing different events in the Taylor-Couette flow. Starting with the flow in its laminar situation, afterward describing two of the destabilizing mechanisms that can disturb the laminar flow, the centrifugal instability and the boundary effects. Furthermore, the global flow response characterized by angular momentum transport is discussed in this chapter. Moreover, the analogy between the sheared flow and the thermal-driven flow is shortly discussed then. Finally, the main dimensionless parameters used within this thesis are presented with a brief definition.

The experimental facility, measurement techniques, and data analysis methods used in this thesis are described in Chapter 3. First, the Top view Taylor-Couette facility is illustrated by describing in detail the main technical features, besides the facility's driving control system and the temperature monitoring procedure. The second section dealt with the measurement techniques used in this study. Starting with the flow visualization, the different devices used are explained, in addition to describing the two different configurations used in aligning the light source and the recording object. Moving to the direct torque measurements, after describing the torque sensor used, the integration of the sensor with the TC facility was explained. Then the velocity measurement technique with the use of the High-speed Particle Image Velocimetry (Hs-PIV) technique is discussed. The PIV system consists of a camera and a light source (laser), where each of these devices is explicitly described, in addition to the tracing particles used in our measurements. After describing the PIV system hardware, the technique's usage steps are expounded, from the measurement procedure to the PIV images post-processing. A big portion of this section was spent presenting the calibration method used, further validating it, and quantifying the possible measurement error. The third section focuses on the different data analysis techniques used to analyze the results of this thesis, where a brief overview of each method, in addition to the purpose of usage in this study, are presented.

The results of this thesis are presented in Chapter 4 consecutively. In this chapter, the different flow patterns that appear in the counter-rotating regime are presented in the range of $530 \leq Re_s \leq 1.5 \times 10^4$. After presenting the different details around the data measurement, the flow patterns are presented in both instantaneous flow images and space-time figures. To capture the coherent flow patterns, the global flow visualization, in addition to the visualization in the radial-axial plane is used. From the captured patterns, some of them were known and investigated previously in different TC flow geometries; another set was newly observed in this study, and we gave them names depending on their principle motion behavior. This chapter ends with a regime diagram summarizing the different investigated patterns in terms of the driving parameters.

For the same rotating regime and for $Re_s = 2 \times 10^4, 6.1 \times 10^4$, and 1.31×10^5 , the flow is studied quantitatively by measuring the radial and azimuthal velocities at different axial positions using Hs-PIV in Chapter 5. After describing the measurement procedure and the investigated parameters, the flow axial dependence is discussed. The measurements are done for different rotation ratios in the range : $-0.06 \leq \mu \leq 0$, allowing the study of the influence of the flow kinematics presented by the rotation ratio on the general flow behavior. To do so, the angular velocity and angular momentum mean radial profiles and gradient are compared for the different investigated parameters, followed by the analysis of the neutral surface position and the energy distribution. Furthermore, the angular momentum transport dependence on the rotation ratio is presented in terms of the quasi-Nusselt number for the three studied shear Reynolds number flows, where its behavior is further interpreted by studying the turbulent flow's spatial and temporal behavior and the spatial two-point auto-correlation. Finally, the quadrant analysis is used to characterize the trajectory and strength of the shear stress.

The transition of the flow from the classical to the ultimate regime is discussed in Chapter 6. The angular momentum transport is measured for different shearing rates $5 \times 10^3 \leq Re_s \leq 1.5 \times 10^5$ for flow with a stationary outer cylinder. Both the direct torque measurements and the height-dependent velocity measurements are used to quantify the momentum transport in this chapter. The scaling of the quasi-Nusselt number to the shear Reynolds number is then used to verify the transition to the ultimate rotating regime. The different factors that feature each of the investigated regimes in this chapter are discussed, first by a statistical analysis of the mean flow concerning the radial velocity and the angular velocity and momentum. Further, the azimuthal energy co-spectra is used to assess the structures' behavior at the different gap radial positions for both regimes. As a supplement to the spectral analysis, the flow dominant structure's growth/decay rate is analyzed using the Dynamic Mode Decomposition (DMD).

The flow stability in the co-rotating regime is studied in Chapter 7. The flow is investigated using both the flow visualization and the height-dependent velocity measurements. The flow dynamics in the radial-axial plane are analyzed. Furthermore, the mean flow statistics concerning the radial and azimuthal profiles are analyzed.

In the end of this thesis, a general conclusion is presented in Chapter 8, including a summary of the work presented and some suggestions for future works that may answer the open questions raised by the work's results.

The results of this thesis are mainly based on two published, and two submitted papers: (i) Experimental methods for investigating the formation of flow patterns in a very wide gap Taylor-Couette flow ($\eta= 0.1$), (Technisches messen 2023) [77]; (ii) Flow regimes in a very wide-gap Taylor-Couette flow with counter-rotating cylinders, (Philosophical Transactions A 2023) [19]; (iii) Experimental investigation of turbulent counter-rotating Taylor-Couette flows for radius ratio $\eta = 0.1$, (Journal of Fluid mechanics 2023) [78]; (iv) Transition to the ultimate Turbulent regime in a very wide gap Taylor-Couette flow ($\eta = 0.1$) with a stationary outer cylinder, (Europhysics letters 2023) [79].

2

Theoretical background and fundamentals

In this chapter, we will outline the underlying theory and equations describing the Taylor-Couette physical system, which is the subject of our investigation. In order to provide the reader with the theoretical foundation needed to comprehend the phenomena investigated in the laboratory experiments, the key equations defining fluid motion will be provided. The derivation of the equations is outside the scope of this thesis, which presents an experimental analysis of the flow. [26, 9] are recommended as further reading for those who are interested in more in-depth theoretical investigations.

2.1 Fluid in motion

2.1.1 The continuity equation

The fluid motion is described in a mathematical way by using different sets of fundamental equations. First, we will present the continuity equation, which is derived based on the law of conservation of mass [80], which works under the assumption that the inflow will be equal to the outflow for any fluid volume. The general form of the continuity equation is:

$$\frac{\partial \rho}{\partial t} + \nabla \cdot (\rho \vec{u}) = 0, \quad (2.1)$$

with ρ the fluid density and u the fluid velocity. For incompressible fluids, which is the case in the current study, where the fluid has a constant density, the continuity equation is defined as:

$$\nabla \cdot \vec{u} = 0. \quad (2.2)$$

2.1.2 The Navier-Stokes equation

The Navier-Stokes equations are equations that describe the motion of a viscous fluid and can be used to determine the velocity vector field that applies to a fluid, given some initial conditions. These equations are derived from the application of Newton's second law in combination with fluid stress (due to viscosity) and a pressure term. In addition, these equations can be derived from the basic conservation and continuity equations applied to the properties of fluids. The Navier-Stokes equation can be written as:

$$\rho \frac{\partial \vec{u}}{\partial t} + \nabla \vec{u} \cdot \vec{u} = -\nabla p + \rho g + \mu \Delta \vec{u} + F, \quad (2.3)$$

where \vec{u} is the fluid velocity, p is the fluid pressure, ρ is the fluid density, F is the external forces applied to the fluid, and μ is the fluid dynamic viscosity. The different terms correspond to the inertial, pressure, viscous, and external forces applied to the fluid.

2.1.3 Equation of motion in cylindrical coordinate system

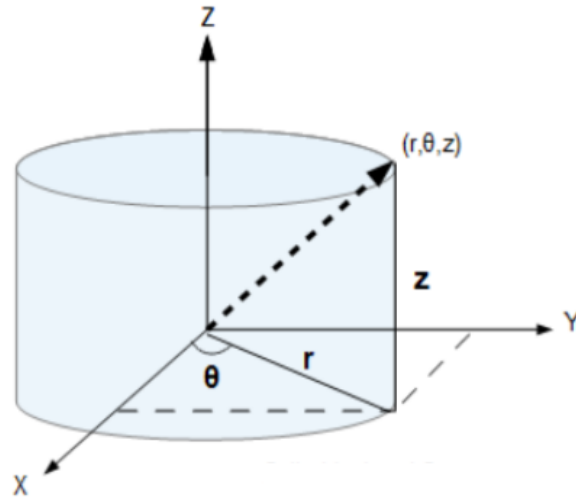


Figure 2.1: Cartesian and cylindrical coordinates.

In the current study, we are studying the flow between two concentric cylinders. So the motion of the flow is described in the cylindrical coordinate system instead of the Cartesian coordinate system, as shown in figure 2.1, so that the unit vectors are represented as:

$$\begin{aligned} e_r &= \cos(\phi)e_x + \sin(\phi)e_y, \\ e_\phi &= -\sin(\phi)e_x + \cos(\phi)e_y, \\ e_z &= e_z. \end{aligned} \quad (2.4)$$

In the cylindrical coordinates the Nabla and Laplace operator used in equation 2.3 is written as :

$$\nabla = \frac{\partial}{\partial r} + \frac{1}{r} \frac{\partial}{\partial \phi} + \frac{\partial}{\partial z}, \quad (2.5)$$

$$\nabla^2 = \frac{\partial^2}{\partial r^2} + \frac{1}{r} \frac{\partial}{\partial r} + \frac{1}{r^2} \frac{\partial^2}{\partial \phi^2} + \frac{\partial^2}{\partial z^2}. \quad (2.6)$$

And then the Navier-Stokes equation of an incompressible viscous fluid in cylindrical coordinates is written as:

$$\frac{\partial u_r}{\partial t} = -(\vec{u} \cdot \nabla) u_r + \frac{u_\phi^2}{r} - \frac{1}{\rho} \frac{\partial p}{\partial r} + \nu (\nabla^2 u_r - \frac{u_r}{r^2} - \frac{2}{r^2} \frac{\partial u_\phi}{\partial \phi}), \quad (2.7)$$

$$\frac{\partial u_\phi}{\partial t} = -(\vec{u} \cdot \nabla) u_\phi + \frac{u_\phi u_r}{r} - \frac{1}{\rho} \frac{\partial p}{\partial \phi} + \nu (\nabla^2 u_\phi - \frac{u_\phi}{r^2} - \frac{2}{r^2} \frac{\partial u_r}{\partial \phi}), \quad (2.8)$$

$$\frac{\partial u_z}{\partial t} = -(\vec{u} \cdot \nabla) u_z - \frac{1}{\rho} \frac{\partial p}{\partial z} + \nu (\nabla^2 u_z), \quad (2.9)$$

as well, the continuity equation

$$\frac{1}{r} \frac{\partial (r u_r)}{\partial r} + \frac{1}{r} \frac{\partial u_\phi}{\partial \phi} + \frac{\partial u_z}{\partial z} = 0. \quad (2.10)$$

2.2 Laminar Couette flow

The equations 2.7, 2.8, and 2.9 can be solved analytically in some special cases. When flow inside the gap is stationary and purely azimuthal and in the absence of any external forces, so $u_r = u_z = 0$ and the azimuthal velocity is a function of the radius r , or, in other words, if the flow is laminar [81], a laminar solution can be predicted. Another assumption should also be made to solve the laminar solution of the momentum equation: the velocity gradient in time, azimuthal and axial directions is equal to zero and there is only a gradient of the azimuthal velocity along the radial component. Based on the assumptions explained above, the solution of equation 2.7 is $\rho u_\phi^2 / r = \partial_r p$, where it means that the radial pressure gradient is in balance with the centrifugal force. The axial component from equation 2.9 vanishes. For equation 2.8 describing the azimuthal component, the equation is solved using the Eulerian ansatz $u_\phi(r) = r^n$. The angular velocity (ω) is defined by $\omega = u_\phi / r$, by substituting u_ϕ with ω and using the boundary conditions $\omega(r_1) = \omega_1$ and $\omega(r_2) = \omega_2$, the laminar Couette solution of the equation can be written as:

$$\omega_{lam} = \frac{r_2^2 \omega_2 - r_1^2 \omega_1}{r_2^2 - r_1^2} - \frac{r_1^2 r_2^2 (\omega_2 - \omega_1)}{r_2^2 r_1^2} \frac{1}{r^2} = A + \frac{B}{r^2}, \quad (2.11)$$

where in the case of $\omega_1 = \omega_2$, the flow is named solid body rotating flow.

2.3 Centrifugal instability

Beside the laminar stable flow state, the TC flow is founded to be disturbed and unstable, mainly due to the centrifugal instability. Such instability is often present for flows with curved streamlines (e.g., TC flow, flow in a curved channel and flow in a boundary layer on a concave wall). In the following, we will present two explanations of the centrifugal instability, one using the energy argument and the other using the linear stability analysis.

2.3.1 Rayleigh's stability criterion for non-viscous fluid

Considering a non-viscous fluid (i.e., Euler equations) in cylinder coordinates, the Euler equations in the cylindrical coordinates will be written as:

$$\begin{aligned}\frac{Du_r}{Dt} - \frac{u_\phi}{r} &= \frac{1}{\rho} \frac{\partial p}{\partial r}, \\ \frac{Du_\phi}{Dt} + \frac{u_r u_\phi}{r} &= -\frac{1}{\rho} \frac{1}{r} \frac{\partial p}{\partial \phi}, \\ \frac{Du_z}{Dt} &= -\frac{1}{\rho} \frac{\partial p}{\partial z},\end{aligned}\tag{2.12}$$

with

$$\frac{D}{Dt} = \frac{\partial}{\partial t} + u_r \frac{\partial}{\partial r} + \frac{u_\phi}{r} \frac{\partial}{\partial \phi} + u_z \frac{\partial}{\partial z}.\tag{2.13}$$

Assuming axisymmetric flow, so that $\partial/\partial\phi = 0$, then the equation above is reduced, where all the terms with $\partial/\partial\phi$ vanish.

One should note that the circulation for non-viscous flows is constant according to Kelvin's circulation theorem and will be given by

$$\Gamma = 2\pi r u_\phi = \text{constant},\tag{2.14}$$

Rayleigh [64] found from equation 2.14 and following the assumption presented above, that the ϕ -component of equations 2.12 can be written in the form of:

$$\frac{D(ru_\phi)}{Dt} = 0.\tag{2.15}$$

In the TC flow, the angular momentum and the angular velocity of the flow are defined as $L = u_\phi r$ and $\omega = u_\phi/r$ respectively. By the use of Equation 2.15 it can then be shown that the angular momentum L is conserved for all fluid particles.

Moreover, and by considering two fluid rings at the same axial positions, but at different radial positions, where both have the same mass:

$$2\pi r_1 dr_1 = 2\pi r_2 dr_2 = ds.\tag{2.16}$$

The energy of the two fluid rings at r_1 and r_2 at any time can be written as :

$$E_t = \frac{L_{r_1}^2}{r_1^2} + \frac{L_{r_2}^2}{r_2^2}.\tag{2.17}$$

If we then consider at time (t_1) the exchange of position of the two rings with equal masses and arbitrary radial positions, the difference in energy at ($t = t_0$) and ($t = t_1$) is presented as:

$$\begin{aligned}\Delta E = E_{t_1} - E_{t_0} &= \left[\left(\frac{L_{r_2}^2}{r_1^2} + \frac{L_{r_1}^2}{r_2^2} \right) - \left(\frac{L_{r_1}^2}{r_1^2} + \frac{L_{r_2}^2}{r_2^2} \right) \right] ds \\ &= (L_{r_2}^2 - L_{r_1}^2) \left(\frac{1}{r_1^2} - \frac{1}{r_2^2} \right) ds.\end{aligned}\tag{2.18}$$

The exchange of positions we suppose above can only occur when $(L_{r_1}^2 > L_{r_2}^2)$, otherwise there will be insufficient centrifugal force to drive the changes. Therefore, the Rayleigh criterion for Taylor-Couette flow stability can be written as

$$\frac{dL^2}{dr} > 0 \quad (2.19)$$

In the Taylor-Couette flow, the relation $(L_{r_1}^2 > L_{r_2}^2)$ can also be expressed in terms of the kinematic and the geometry of the TC system, presented in terms of the system radius ratio $\eta = r_1/r_2$ and the cylinders rotation ratio $\mu = \omega_2/\omega_1$, where 1 and 2 are related to the inner and outer cylinders, respectively. The Rayleigh's criterion can then be written as: for $\mu < \eta^2$ the flow is centrifugally unstable, and for $\mu > \eta^2$ the flow is centrifugally stable.

2.3.2 Linear stability analyses of the non-viscous fluid

For the same purpose, the Rayleigh stability criteria can be derived using the linear stability method [82, 83, 84]. The different variables of equation 2.12 are separated using the Reynolds decomposition to mean flow (U, P) and the perturbation (u', p') , with :

$$\begin{aligned} u &= U + u', \\ p &= P + p'. \end{aligned} \quad (2.20)$$

In the TC flow, the laminar base flow is given by : $U_r = U_z = 0$ and $U_\phi = \omega_{lam}/r = V(r)$. By substituting 2.20 to 2.12, and then substituting the base flow from the resultant equations and neglecting all the non-linear terms (they are assumed to be very small), the equation of fluctuation is obtained as:

$$\begin{aligned} \frac{\partial u'_r}{\partial t} + \frac{V(r)}{r} \left(\frac{\partial u'_r}{\partial \phi} - 2u'_\phi \right) &= -\frac{1}{\rho} \frac{\partial p'}{\partial r}, \\ \frac{\partial u'_\phi}{\partial t} + \left(\frac{dV(r)}{dr} + \frac{V(r)}{r} \right) u'_r + \frac{V(r)}{r} \frac{\partial u'_\phi}{\partial \phi} &= -\frac{1}{r\rho} \frac{\partial p'}{\partial \phi}, \\ \frac{\partial u'_z}{\partial t} + \frac{V(r)}{r} \frac{\partial u'_z}{\partial \phi} &= -\frac{1}{\rho} \frac{\partial p'}{\partial z}. \end{aligned} \quad (2.21)$$

Equation 2.23 reveal a plane wave solution in the form of:

$$(u'_r, u'_\phi, u'_z, p') = (u_r(r), u_\phi(r), u_z(r), p(r)) e^{i(\Omega t + m\phi + kz)}. \quad (2.22)$$

Substituting 2.22 in 2.23 reads:

$$\begin{aligned} i(\Omega + m \frac{V(r)}{r}) u'_r - \frac{2V(r)}{r} u'_\phi &= -\frac{1}{\rho} \frac{dp'}{dr}, \\ i(\Omega + m \frac{V(r)}{r}) u'_\phi - \left(\frac{V(r)}{r} + \frac{dV(r)}{dr} \right) u'_r &= -\frac{imp'}{r\rho}, \\ i(\Omega + m \frac{V(r)}{r}) u'_z &= -k \frac{p'}{\rho}. \end{aligned} \quad (2.23)$$

2. Theoretical background and fundamentals

The equation for the perturbed flows was derived in a lagrangian frame of reference, which allowed Drazin and Reid [82] to define the stability criteria for the TC flow under an axisymmetric perturbation, neglecting viscous effects, as:

$$\Psi = 2 \frac{\omega(r)}{r} \frac{d(r^2 \omega(r))}{dr} > 0. \quad (2.24)$$

This stability criterion was called as the Rayleigh discriminant, so for $\Psi < 0$ the flow becomes unstable and the perturbations grow exponentially. While for $\Psi > 0$ the perturbations are damped and as a result the instabilities decrease, and the flow stabilize. Kundo et al. [84] stated that this criterion demonstrated by Rayleigh is both necessary and sufficient for instability to occur. For TC flows, the equation 2.24 can be written in the same form shown in the previous section: for $\mu < \eta^2$ the flow is centrifugally unstable, and for $\mu > \eta^2$ the flow is centrifugally stable.

2.4 Ekman Boundary layers

In the TC system, where the flow rotates in a closed cavity, the question always arises about the effect of the boundary layers near the top and bottom plates. The so-called Ekman boundary layer is the layer between the flow and the solid boundary at which the no-slip condition applies, so the viscous forces are balanced with the pressure gradients and the Coriolis force. This balance can be represented in the momentum equation as:

$$2\vec{\Omega}u + \frac{1}{\rho}\nabla p = \nu\nabla^2 u \quad (2.25)$$

where the two terms on the left represent the pressure and Coriolis effects, and the right term represents the viscous effects. Then the thickness of the boundary layer is given by [85] as:

$$\delta_E k = \sqrt{\frac{\nu}{\Omega}}. \quad (2.26)$$

From the presented equation above a maximum thickness of $3mm$ is calculated for the parameters studied in this study, assuming that silicon oil ($\nu = 20mm^2/sec$) is the working fluid, which is the most viscous fluid used within this thesis, and assuming the minimum rotation speed used in the study.

The Ekman layer solution on a solid surface demonstrates that within the boundary layer, the three-way balance among the three forces represented in equation 2.25 results in a component of flow directed toward the lower pressure. Then, the friction forces can cause a flow around the low-pressure center to spiral inward [86]. In addition to the azimuthal velocity gradient near the apparatus end gap, the Ekman layers can also lead to the development of radial and axial velocity components. These velocity components can then lead to angular momentum transport within the fluid, creating a non-azimuthal circulation, although they have small values [87]. This non-azimuthal circulation can generate large horizontal vortices that may extend from the end plates to the apparatus mid-plane under some conditions [88]. Further, in order to avoid the effects of the end walls on the flow, the theoretical studies assumed infinitely long cylinders, while the numerical studies use periodic boundary conditions

at the axial extrema of the computational domain, and for the experimental studies, which is the case in the current study, relatively long cylinders compared to the gap between the cylinders are used.

2.5 Angular Momentum Transport

In this section, we will present briefly the theory of torque scaling and angular momentum current derived by Eckhardt et al. [9]. In order to illustrate the azimuthal current, Eckhardt et al. [9] averaged the equation 2.8 of u_ϕ over the cylindrical surface of height l and area $A(r) = 2\pi rl$, which is chosen to be co-axial to the Taylor-Couette system cylinders, with $r_1 \leq r \leq r_2$. The u_z component in the equation was eliminated using the continuity equation 2.11. Then [9] obtained:

$$0 = \partial_r(r^3[\langle u_r \omega \rangle_{A,t} - \nu \partial_r \langle \omega \rangle_{A,t}]). \quad (2.27)$$

Equation 2.27 shows that the quantity inside the brackets is independent on r , so its value doesn't change for any radial position in the gap between the outer and inner cylinders, and also that this quantity is independent in t, ϕ, z due to the averaging on these variables. This quantity was designated according to [9] as J^ω :

$$J^\omega = r^3[\langle u_r \omega \rangle_{A,t} - \nu \partial_r \langle \omega \rangle_{A,t}]. \quad (2.28)$$

which is the transverse current of azimuthal motion, constant over all radii, and transports angular velocity in the radial direction. Where the two elements contained in 2.28, $\langle u_r \omega \rangle$ and $\partial_r \langle \omega \rangle$ reflect the Reynolds stress and the viscous derivative of a mean flow, respectively. In addition, J^ω can be directly obtained by measuring the torque (T) applied either on the inner or outer cylinder walls to keep both cylinders rotating at a constant speed, with:

$$J^\omega = \frac{T}{2\pi L \rho_{fluid}}. \quad (2.29)$$

Moreover, [9] suggested the pseudo-Nusselt number Nu_ω to quantify the angular momentum transport in analogy to the Rayleigh-Bénard flow where heat transfer takes place through the flow. Eckhardt et al. [9] define the pseudo-Nusselt number Nu_ω in the TC flow as:

$$Nu_\omega = \frac{J^\omega}{J_{lam}^\omega}. \quad (2.30)$$

with J_{lam}^ω the angular momentum flux in the pure viscous transport case, where the flow is purely azimuthally, and the radial and axial velocity components vanish. J_{lam}^ω is defined as:

$$J_{lam}^\omega = 2\nu r_1^2 r_2^2 \frac{\omega_1 - \omega_2}{r_2^2 - r_1^2}. \quad (2.31)$$

The pseudo-Nusselt number Nu_ω measures the angular momentum overall transport in terms of the transferred amount in laminar flow, or, in other words, in terms of purely viscous transport. So by definition, the value of Nu_ω is equal to 1 in the laminar flow cases.

2.6 Analogy of shear flows and Rayleigh-Bénard flow

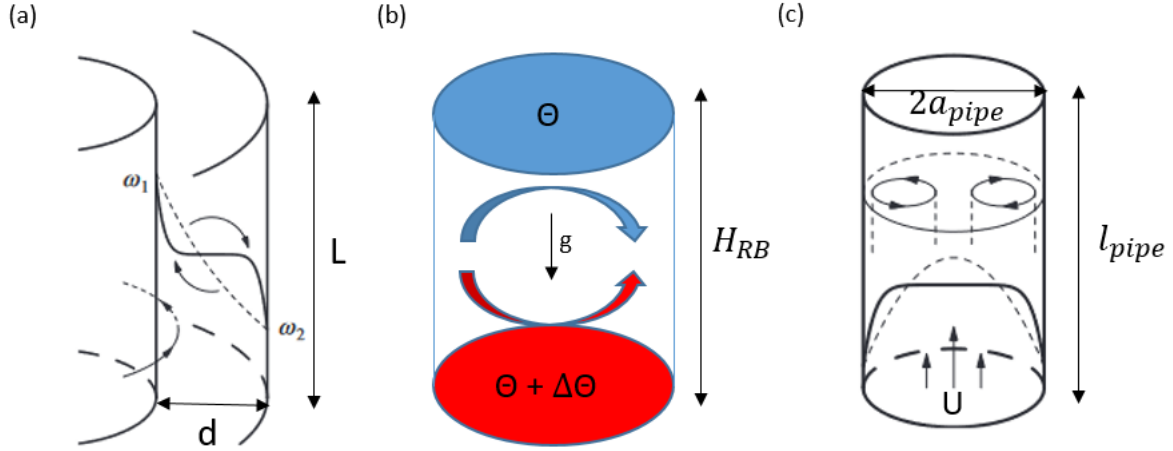


Figure 2.2: Schematic figures showing comparison between (a) Taylor-Couette, (b) Rayleigh-Bénard, and (c) Pipe flows, the figure is modified from [40].

Various attempts have been made to identify similarities between temperature-driven and shear flows. The Rayleigh-Bénard (RB) flow was commonly used as an example of a temperature-driven flow. The RB flow is described as the flow in a container heated from below and cooled from above, leading to thermal convection. On the other side, the TC and pipe flows were commonly used as examples for the shear flows, where the first is the shear flow confined between two cylinders and the second is the shear flow caused by the pressure gradient, respectively. For the three flows mentioned above, it was found to have a conserved global transport quantity J and a dissipation rate for the wind ϵ^W , where these quantities are exact consequences of the Navier-Stokes equations for the three flows. Both J and ϵ^W are strongly correlated so that J cannot achieve an increase without a non-zero dissipation rate of the wind.

Taylor-Couette	Rayleigh-Bénard	Pipe
$J^\omega = r^3 [\langle u_r \omega \rangle_{A,t} - \nu \partial_r \langle \omega \rangle_{A,t}]$	$J^\Theta = \langle u_z \Theta \rangle_{A,t} - \kappa \partial_z \langle \Theta \rangle_{A,t}$	$J^{u_z} = r^{-1} [\langle u_r u_z \rangle_{A,t} - \nu \partial_r \langle u_z \rangle_{A,t}]$
$\epsilon^W = \nu^3 d^{-4} \sigma^{-2} Ta (Nu_\omega - 1)$	$\epsilon^W = \nu^3 d^{-4} Pr^{-2} Ra (Nu_\Theta - 1)$	$\epsilon^W = U J_{lam}^{u_z} (Nu_{u_z} - 1)$

Table 2.1: Analogy of transport fluxes and dissipation rates in RB, TC and pipe flow.

Eckhardt et al. [40] investigated a similar expression for J and ϵ^w for the TC, RB and pipe flow. Starting with the TC flow where the angular velocity is the transported quantity, and it is transported by the velocity component in the radial direction. After averaging the ϕ -component of the Navier Stokes equation over the cylinders wall, [40] found J^ω and ϵ^W as shown in table 2.1, with $\sigma_{Pr} = 2^{-4} (1 + \eta)^4 \eta^{-2}$ the pseudo-Prandtl number which is a geometry dependent dimensionless number, and Ta the Taylor number, a dimensionless number linked to Re_s by : $Ta = \sigma_{Pr}^2 Re_s^2$. For the RB flow, the heat (Θ) is the transported quantity, and it is transported by the velocity component that has the direction of the thermal gradient. Eckhardt et al. [40] found J^Θ the heat flux and ϵ^W as shown in table 2.1, with $\langle \dots \rangle_{A,t}$ denoting the average over the planes parallel to the top and bottom planes and time,

$Ra = \alpha_{\ominus} g \Delta \Theta H_{RB}^4 / \kappa \nu$ denotes the Rayleigh number, $Pr = \nu / \kappa$ the prandtl number, g the gravitational acceleration, α_{\ominus} the thermal expansion coefficient, H_{RB} the container height, and $Nu_{\ominus} = J^{\ominus} / J_{lam}^{\ominus}$ the heat flux Nusselt number. The same analysis was conducted on the pipe flow, where by averaging the Navier-Stokes equation for the axial velocity (u_z) over co-axial cylinders, Eckhardt et al. [40] found J^{u_z} the axial velocity flux and ϵ^W as shown in table 2.1, with $\langle \dots \rangle_{A,t}$ denoting the average over the pipe walls and time, U the cross-section averaged velocity, $J_{lam}^{u_z}$ the axial velocity flux for laminar flow, and $Nu_{u_z} = J^{u_z} / J_{lam}^{u_z}$ the axial velocity flux Nusselt number.

The direct link between the conserved flux quantities and the wind dissipation rate shows an obvious similarity between these flows. Further similarities can be found between RB and TC flows, where for specific flow parameters, Bénard roles appear in RB flow, where these flow patterns enhance heat transfer [89], the same is true for TC flow, where Taylor vortices appear, which also enhance angular momentum transport [20, 24]. Moreover, for a sufficient shearing rate, the TC flow achieves a transition from the classical turbulent regime to the ultimate one in analogy to the RB flow [23]. Another analogy can be found between the pipe and TC flow, wherein both the transition for the flow to turbulence occurs once the lifetime of the localized turbulent events exceeds their decaying rates [90, 91, 92].

2.7 Dimensionless Variables

In order to reduce the number of parameters by choosing suitable scales, different dimensionless numbers were used throughout this thesis. Two groups of dimensionless numbers and parameters were used, one describing the geometry and the other the driving of the system and some physical properties. For the second group, the fundamental assumption is that the rotation speed of the inner cylinder $\omega_1 \neq 0$, and always has a positive value. For the outer cylinder rotation speed, ω_2 it can be zero, negative, or positive. The main dimensionless numbers that are frequently used in this study will be presented in this section, along with a brief description of each.

The system geometry is described by:

- **Radius ratio:** $\eta = r_1 / r_2$.
- **The curvature number:** $R_c = d / \sqrt{r_1 r_2}$ introduced by [8], measures the influence of curvature in terms of the geometrical mean of both cylinder's radii and the gap width d .
- **Aspect ratio:** $\Gamma = L / d$, with L the height of the apparatus, and $d = r_2 - r_1$ the gap width.

Further, the driving of the system and the global response are described by:

- **Rotation ratio:** $\mu = \omega_2 / \omega_1$, with $\omega_{1,2}$ the rotation ratio of the inner and outer cylinder, respectively.
- **Reynolds number:** Re is the most common dimensionless number used in fluid mechanics, and it describes the ratio between the inertia forces and the viscous forces, with ν the kinematic viscosity of the fluid.

2. Theoretical background and fundamentals

$$Re_{1,2} = \frac{r_{1,2}\omega_{1,2}d}{\nu}. \quad (2.32)$$

- **Shear Reynolds number.**: Re_s measures the shear between the cylinders, and it was introduced by Durbrulle et al. [8]:

$$Re_s = \frac{2}{1+\eta}|\eta Re_2 - Re_1| = \frac{2r_1r_2d}{(r_1+r_2)\nu}|\omega_2 - \omega_1|. \quad (2.33)$$

- **The pseudo-Nusselt number**: the global response of the flow to the different driving parameters is illustrated by Nu_ω , which quantifies the amount of angular transported compared to the angular momentum transport in the laminar case.

$$Nu_\omega = \frac{J^\omega}{J_{lam}^\omega}. \quad (2.34)$$

3

Experimental Setup, Measurement Technique, and Data Analysis methods

The main goal of this thesis is to investigate the flow in very wide-gap Taylor-Couette geometry flows using different measurement methods. To do so, the used experimental facility should be specially designed to be suitable for obtaining the goals of this study. In addition to the experimental setup, the measurement techniques and the data analysis methods used in this thesis are presented in this chapter. This chapter is organized as follows: In Section 3.1 the experimental setup is described in detail by presenting the technical details of the used TC system. In Section 3.2 the three used measurement techniques: flow visualization, direct torque measurement, and particle image velocimetry (PIV), are presented and discussed. Finally, in Section 3.3 the methods used to analyze the data of this study are presented.

The main results presented in sections 3.2.3.4 and 3.2.3.6, are part of the paper *Experimental methods for investigating the formation of flow patterns in a very wide gap Taylor-Couette flow ($\eta = 0.1$)*, by M. H. Hamede, S. Merbold and Ch. Egbers (2023), published in Tech. Mess. [77]. Note the text is mainly taken from the paper.

3.1 Experimental Setup

The idea of building a Taylor-Couette experiment started in 1888, when Mallock [14] and Couette [15] built their fluid viscometers using two concentric outer and inner cylinders. About half a century later, Wendt [48] built his TC experiment with three different radius ratios $\eta = 0.68, 0.85, 0.935$, and investigated the torque behavior in the flow. Further, different TC apparatuses are built with different designs and geometry for different purposes. The different TC experiments can be classified depending on their different features, like the apparatus geometry (radius ration and aspect ratio), optical access to the flow inside the gap, ability to apply direct torque measurements, maximum reachable shear Reynolds number, end plate condition, etc.

R_1 (mm)	$d=R_2 - R_1$ (mm)	$\eta = \frac{R_1}{R_2}$	$\Gamma = \frac{L}{d}$
7	63	0.1	11.1
14	56	0.2	12.5
25	45	0.36	15.6
35	35	0.5	20
50	20	0.71	35

Table 3.1: Geometries built in the Top view Taylor-Couette Cottbus System. With $R_2 = 70\text{mm}$ outer cylinder radius, $L = 700$ mm apparatus length.

Prigent et al. [93] built their very narrow gap apparatus with $\eta = 0.983$, the main feature of this facility is its very high aspect ratio, which helped in neglecting the effect of the end plates on the flow. Another very narrow gap apparatus was built by Revelet et al. [94] ($\eta = 0.92$), but with a smaller aspect ratio, where they measure the torque and the flow velocity. Further, Avila et al. [95] constructed their experiment with a changeable radius ratio $\eta = 0.71, 0.88, 0.98$ to investigate the subcritical transitions and the effect of boundary conditions. Another TC apparatus with a flexible radius ratio was built in the University of Twente [96] with $\eta = 0.72, 0.77, 0.83$, and 0.91 . This experiment has been used to investigate the bubbly and single-phase TC flow at high shear Reynolds numbers. For the purpose of investigating the flow in the quasi-Kaplerian regime, Shartmann et al [97, 98] constructed a relatively short annulus with a wide gap radius ratio $\eta = 0.35$, and independent end plates. Another TC apparatus with wide gap geometry was built in Cottbus with a radius ratio of $\eta = 0.5$ and aspect ratio $\Gamma = 20$. The so-called Turbulent Taylor-Couette Cottbus (TTCC) has the ability to reach relatively high shear Reynolds with precise torque measurements, independently controlling the top and bottom plates [21]. All the above-mentioned TC apparatus, in addition to the TC experiments constructed in Maryland [49, 50, 99] have a common feature, which is the transparent outer cylinder that allows optical access to the flow through the outer cylinder. Further, in order to have better optical access to the flow, the boiling Twente TC facility (BTTC) was built, which is in addition to the features of the first TC facility at Twente University, this apparatus has a transparent top plate, so the flow is fully optically accessible from the side and top [100].

3.1.1 The top-view Taylor-Couette Cottbus (TvTCC) facility

Due to the limitations of the Turbulent Taylor-Couette Cottbus facility from the standpoint of having a fixed radius ratio and optical access to the flow just from the sides, it was planned to build a new TC facility. The new facility should have different attributes: high rotation speeds of both cylinders to ensure reaching fully turbulent flows with a high shear Reynolds number for the different working fluids; a flexible radius ratio by having a changeable inner cylinder; both cylinders should rotate independently to realize different flow regimes (co- and counter-rotating regimes); optical access through the top and sides; and finally, the possibility of direct torque measurements to quantify the angular momentum transport.

3.1.1.1 TvTCC Geometry and Technical Details

While building and designing the TvTCC apparatus, different challenges were taken into account. The system cylinders, especially the inner cylinder, will rotate at a high speed with a maximum speed of about 2300 rpm, which can produce a lot of shaking throughout the whole system. In order to prevent these noises, the apparatus was built over a heavy weight table with a 4 mm thickness steel plate on the top surface. The apparatus base was then fixed to the table top surface from its four sides. In addition, the apparatus was built in the middle of four aluminum beams, so the apparatus' aluminum plate base connected these four beams, plus another aluminum plate above the system's upper plate connected these beams from the top. The existence of these beams helps to keep the whole apparatus exactly straight and concentric and reduces system vibration if it exists. These aluminum beams were plated with black in order to prevent any light reflection when using the optical measurements. The TvTCC system has a flexible geometry, so it can be used with different radius and aspect ratios. The different available geometries that can be used in the system are shown in table 3.1. The system has a very simple structure, so changing the inner cylinder and mounting and unmounting the system can be done in a short time.

The simple system structure is accompanied by precise technical details, as will be shown further. Starting from the bottom, the baseplate contains a drill hole containing a ball bearing, through which a driving shaft goes. A turntable is then attached to the top of the driving shaft. The TC system's aluminum bottom plate sits on the turntable, and it is screwed to it. The system bottom plate contains two drill holes: one is connected to a drain valve in order to fill and empty the gap, and the next is connected to a temperature sensor to measure the fluid temperature. This TC system is not temperature controlled, but by using the temperature sensor, the temperature is always monitored. In addition, the bottom plate contains two concentric grooves, the outer one for the outer cylinder to sit in and the inner one for its O-ring seal. Further, in its center, a circular hole for the inner cylinder bottom bearing takes place. As for the outer cylinder, two different outer cylinders were used in this study, one made of glass and the other of acrylic-glass. Both were transparent, allowing optical access from the sides. At the top and bottom of the cylinder, two flange rings take place; in addition to the fact that they were glued to the cylinder, an O-ring seal was placed between the flange and the cylinder to ensure no fluid leakage. The flange was placed with a relative displacement from the cylinder edges in order to fit into the top and bottom plates, and then the bottom flange was screwed to the bottom plate. The gap is then closed with a transparent acrylic top plate, which contains in its center a bearing seat, where the volume of the bearing seat is connected to the volume of the gap, and this volume is used as a buffer volume to ensure that the gap is fully filled with fluid and air bubbles don't exist. In addition, the seat has two holes in the side, closed with screws, and they can be used to fill the gap with fluid. As with the bottom plate, the top plate has two concentric grooves for the same purpose. The transparent top plate allows optical access to the flow from the top. Both the top and bottom plates are screwed to the outer cylinder, so they both rotate with the outer cylinder. Both end plates should be changed by using inner cylinders with different radii.

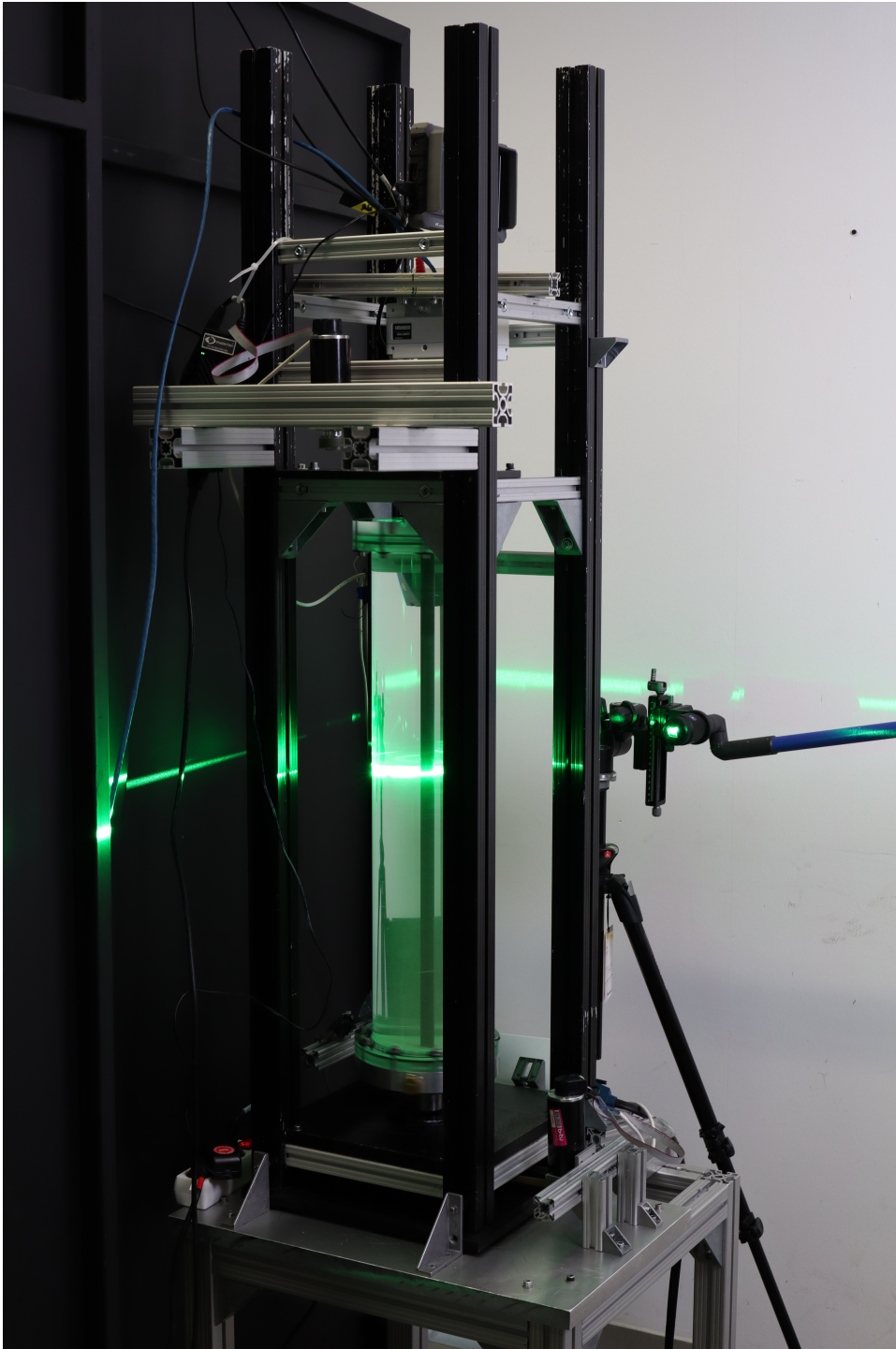


Figure 3.1: Picture showing the top-view Taylor-Couette Cottbus facility with the PIV setup. In the picture, you can see, in addition to the high-speed camera installed above the apparatus end plate, the laser head at the end of the guiding arm fixed on a scale plate, which is used to change the axial position of the horizontal laser sheet observed in the picture.

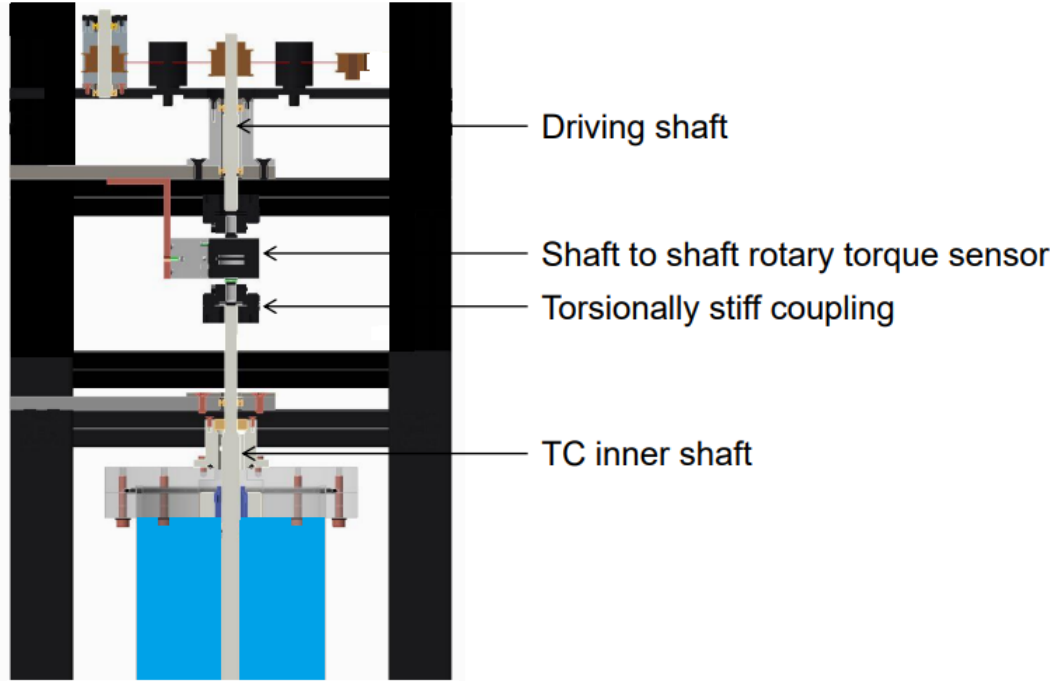


Figure 3.2: CAD image for the upper part of the system where the shaft-to-shaft torque sensor is connected to the inner cylinder

One of the main features of this apparatus is the flexible geometry, which is controlled by the radius of the inner cylinder. The inner cylinder is placed inside the outer cylinder, where it is seated in a deep groove ball bearing in the bottom plate and in the bearing seat on the top plate. For $\eta = 0.1$ geometry, the inner cylinder was produced from material steel C55, and it was coated with chemical/electrolytic corrosion protection, and a structure of silk matte against reflections. For the geometries with $\eta > 0.1$, the inner cylinder is built from aluminum anodized cylinders with different radius sizes depending on the radius ratio; these cylinders are mounted on the steel inner shaft with a radius $r = 7$ mm. For connecting the cylinder to the shaft, aluminum fittings and stainless steel trantorques are used to connect and seal the cylinder and the shaft, so no fluid can go between the cylinder and the shaft. Above the top plate, the inner shaft is parallelized to the whole system by a deep groove ball bearing. This bearing is placed in the middle of an aluminum plate that is fixed to the aluminum beams surrounding the system, where it helps in avoiding any inclination in the hole volume. In addition, the apparatus is designed to have a shaft-to-shaft torque sensor connected to the inner shaft, as shown in figure 3.2. The sensor is connected from one side to the inner cylinder and from the other side to a driving shaft using a torsionally stiff coupling. The driving shaft is seated against the stand with a deep groove ball bearing, and a gear is connected to the end of it. In order to transport the motion from the motor to the driving shaft, an arrangement of two gears, two pulleys, and a belt is used. This arrangement helps, in addition to transporting motion to the shaft, reduce any radial fluctuations.

The torque acting on the thin inner cylinder for the case of $\eta = 0.1$ is below the threshold for accurate measurement ($< 2 \times 10^{-5} Nm$) using the same sensor used in [101]. A second shaft-to-shaft torque sensor with higher sensibility (Lorenz DR-3000) was used, which has

3. Experimental Setup, Measurement Technique, and Data Analysis methods

$\eta = \frac{R_1}{R_2}$	0.1	0.2	0.36	0.5	0.71
max Re_1	1.06×10^5	1.88×10^5	2.7×10^5	2.95×10^5	2.41×10^5
(200 W motor) max Re_2	2.31×10^5	2.05×10^5	1.65×10^5	1.28×10^5	7.33×10^4
(75 W motor) max Re_2	4.61×10^4	4.1×10^4	3.3×10^4	2.56×10^4	1.46×10^4
max $Re_s(\mu = 0)$	1.93×10^5	3.14×10^5	4×10^5	3.93×10^5	2.8×10^5

Table 3.2: The maximum inner cylinder, outer cylinder, and shear Reynolds number with stationary outer cylinder flow that can be reached by the TvTCC facility, for the different geometries, assuming water at room temperature as a working fluid.

a measurement range ± 0.1 Nm and a measurement accuracy of 0.05%. Unfortunately, the torque sensor could only be used for a few experiments up to a shear Reynolds number of 7000; for further experiments, the sensor caused major problems in accuracy and did not give reliable results until it entirely broke.

3.1.1.2 TvTCC rotation control

For running the system, both the inner and outer cylinders are driven by DC motors, each independently. For the inner cylinder, a 200 W Maxon DC motor was used with a maximum speed of around 2300 rpm. For the outer cylinder, two different Maxon DC motors were used: a 200 W motor with a maximum speed of 500 rpm and a 75 W motor with a maximum speed of 100 rpm. The idea of using two motors is related to the desired rotation speed of the outer cylinder. For very low outer cylinder rotation speeds, the small motor has much fewer temporal fluctuations and gives a more stable rotation speed. The rotation speed of both cylinders is measured independently by light barriers. The TvTCC system is controlled by the software program LabVIEW. The cylinder's rotation speed was adjusted using two different methods. The first was by importing the desired cylinder velocity into the LabVIEW code, and then a PID controller is applied that uses the measured rotation speed. The second method was to adjust the motors' currents using the LabVIEW code until they reached the desired velocity. Also, the cylinder's rotation speed was measured using testo 470 tachometer, so by sticking a small reflective marker on the cylinder and then aiming a visible red beam at the reflective marker, we can read the cylinder's velocity. Table 3.2 shows the maximum Reynolds number for both cylinders that can be reached by the TvTCC facility, although a higher Reynolds number can be reached in the case of using less viscous fluids like M 0.65 silicone oil with $\nu = 0.65 \times 10^{-6}$. The rotational velocities of both cylinders have very low temporal fluctuations, with a maximum fluctuation for both cylinders of $\pm 0.3\%$ as shown in figure 3.3.

3.1.1.3 Working fluids and Temperature control

The TvTCC apparatus is not temperature controlled, but the temperature of the working fluid inside the gap can be monitored. The seals and the bearings integrated into the system are chosen to minimize the friction of the inner cylinder while rotating. In addition, a regular check was done for all system bearings, especially the ones in the top and bottom plates, and they were changed when necessary. A type K Thermocouple sensor ($-50 + 300^\circ C, \pm 1.5\%$)

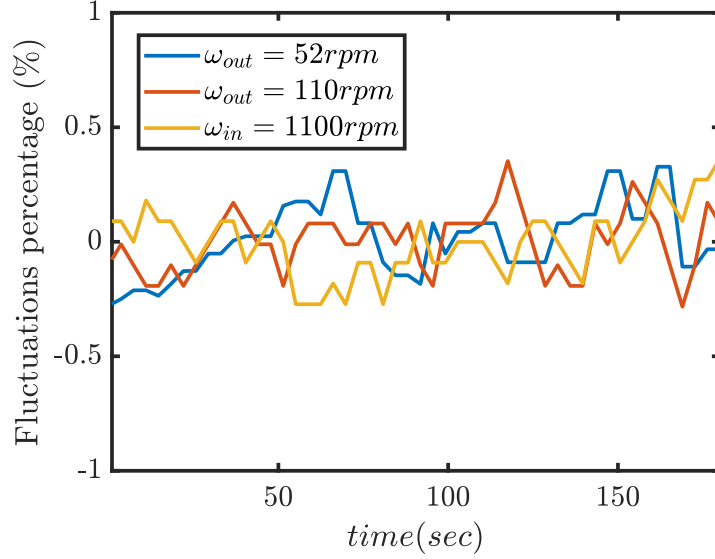


Figure 3.3: The percentage of the inner and outer cylinders' rotation velocity fluctuation as function of time, at different rotation speeds.

Temperature ($^{\circ}C$)	20	21	22	23	24	25	26
Kin. Viscosity (mm^2/sec)	1.0034	0.9795	0.9565	0.9344	0.9131	0.8926	0.8729
Density (g/cm^3)	0.9982	0.998	0.9978	0.9975	0.9973	0.997	0.9968

Table 3.3: The fluid properties: density and kinematic viscosity, for distilled water, which was used as one of the working fluids within this study, were measured and presented at different temperatures.

was used. The thermocouple tip was inserted into the bottom of the gap through the bottom plate, and it measures the fluid temperature there, assuming that the fluid temperature is homogeneous throughout the whole gap as the flow is fully turbulent, which causes effective mixing of the fluid. The temperature measurement is not possible when the outer cylinder is rotating, as the bottom plate, to which the sensor wire is connected, rotates with the cylinder. As a result, the temperature was measured for the pure inner cylinder, assuming that the main source of friction and heating up the fluid is in the inner cylinder bearings. In addition, the fluid temperature was measured before and after each PIV measurement set, and it shows a maximum $\Delta T = 2^{\circ}C$ for a 2-hour measurement set.

The main idea of monitoring the fluid temperature is to control the fluid properties (viscosity and density), as they are temperature-dependent, as shown in table 3.3 for the distilled water. In order to compensate for the rising fluid temperature, the velocity of the rotating cylinders is adjusted so that the dimensionless parameters (Re_s, μ) are guaranteed to be constant for every single measurement set. It was assumed that the temperature rises about $0.4^{\circ}C$ each 30 minutes, and then the rotation velocities of both cylinders were adjusted each 30 minutes in order to prevent any big change in Re_s and μ .

In addition to distilled water, different silicone oils with different viscosities were used in this study, which gives the opportunity to have different Re_s with the same driving power. As an example, for very low Reynolds numbers flows, these flows can be unreachable when using water, since the cylinders should rotate at very low velocities and the cylinder motors have a minimum

velocity to rotate the cylinders continuously without high-velocity fluctuations. In such a case, using high-viscosity fluids like M20 ($\nu = 20(mm^2/sec)$) can be a good option to reach the desired Re_s with higher cylinder rotation speeds. For flow visualization experiments and torque measurements, the M 5, 10, 20 silicone oils were used with $\nu(@25^\circ C) = 5.402, 10.34, 19.95$ respectively. The properties of these fluids at different temperatures were measured using a Stabinger viscosimeter with an integrated density measurement cell (Anton Paar, SVM 3000/G2, $\Delta\nu \pm 0.35\%$, $\Delta\rho \pm 0.0005g/cm^3$).

3.2 Measurement Techniques

In this section, the three different techniques used to investigate the flow qualitatively and quantitatively are described. Starting with the flow visualization, which was used for capturing and investigating the different observed flow patterns. In this study, two physical quantities were measured: the torque induced on the inner cylinder, and the flow velocity field in the $r - \phi$ plane. The first was measured using a torque sensor integrated into the TC apparatus, while the second was measured using Particle Image Velocimetry (PIV). In the following, the instrument used, the experimental configuration, and some basics about each of the three techniques are presented.

3.2.1 Flow Visualization

One of the main characteristics of the TC flows is the variety of flow patterns that appear in the flow. An additional factor that makes those who study the TC flow fortunate is the ability to have transparent experiment walls, which make the studied subject easily visualized. Over the years, visualization techniques were used to analyze the flow topology qualitatively for different fluid mechanics research; also, quantitative analyses were done using this technique, allowing deep insights into the fluid dynamics and its physical processes [102]. Flow visualization was used in different ways and for different purposes in experimental fluid mechanics studies. Starting from Reynolds [103] where he studied the laminar to turbulent transition in the pipe flow using dye. Coles [104] used to seed the fluid with aluminum flakes, and he investigated for Taylor-Couette flow at a given Reynolds number, with a rotating inner cylinder and fixed outer cylinder, detecting 25 different flow states by probing the phase-space. The flow visualization was also used as an art due to the fascinating patterns that appear in the flow [105]. Overviews about the visualization techniques and methods are given in [102, 106].

For the TC flow, the visualization of the flow produces fascinating patterns that vary due to different conditions, by changing the rotation rate of the cylinders and also by changing the aspect ratio of the apparatus. The changing of the driving parameters leads to a series of flow transitions. These flow transitions can be classified into different flows, like circular Couette flow, Taylor vortex flow, and periodic nonaxisymmetric flow, wavy vortex flow, modulated wavy vortex flow, etc. [16, 108]. Andereck et al. [33] studied for one single geometry ($\eta = 0.883$) the flow states for co-rotating cylinders, and then the same geometry is reported and depicted in his famous regime diagram for flow patterns shown in figure 3.4 [107]. In addition to the study of the flow structure, the visualization techniques were used

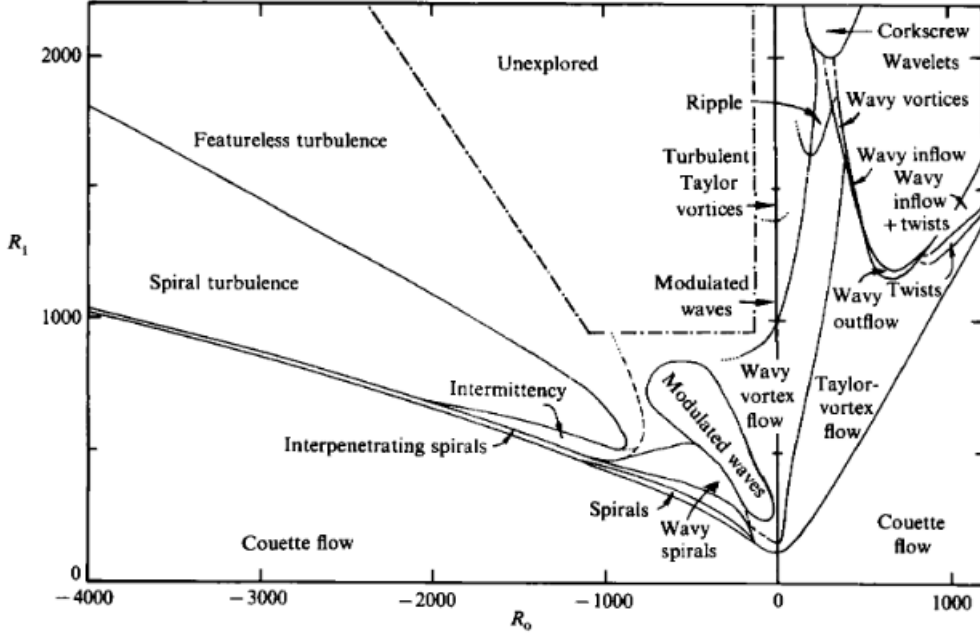


Figure 3.4: Regimes were observed in flow between independently rotating cylinders with a radius ratio $\eta = 0.883$, for different inner and outer cylinder Reynolds numbers (R_i and R_o respectively), and for co- and counter-rotating regimes. This figure is reproduced from [107]

for other purposes in TC flow, like flow stability and flow regimes, flow subcritical transitions [95, 109, 110], and studying the effect of the flow patterns on angular momentum transport [111, 112, 36].

In the current study, the purpose of using the visualization technique was to discover the flow patterns that exist in very wide gap Taylor-Couette geometry $\eta = 0.1$, as the flow in such geometry had not been investigated before the time of submitting this thesis. Also, the visualization data helps in selecting the flow parameters that should be measured using PIV, as it was not possible to cover all the different flow parameters by our measurements, as each set of PIV measurements is very time-consuming. For the visualization procedure, the TvTCC apparatus was filled with different working fluids with different viscosities in order to cover a wide range of flow parameters. To make the flow patterns visible, the flow was seeded with Kalliroscope particles, which are guanine flakes with a typical dimension of approximately $30 \times 6 \times 0.07 \mu\text{m}$. These particles have a very low Stokes number, and they follow the flow precisely. These flat particles collide with the local shear stress and reflect light depending on their orientation. The most light is reflected when the particle's long edge is directed toward the observer, and less when the sharp edge is directed toward the observer. Abcha et al. [113] showed experimentally a clear investigation of this behavior, where they showed a good agreement between the magnitude obtained from the light reflection of the radial velocity, which is aligned with the flow streamline, and the one obtained using numerical simulations of [114]. The volume fraction of Kalliroscope compared to the working fluid is kept at less than 10^{-4} . In addition to the particles, for some measurement sets, a blue dye was added to the fluid to reduce the fluid's transparency, increasing the contrast of the visualized images.

Two different visualization arrangements were used in this study. For the first arrangement, as shown in figure 3.5, two continuous lasers emitting a monochromatic beam at wavelength

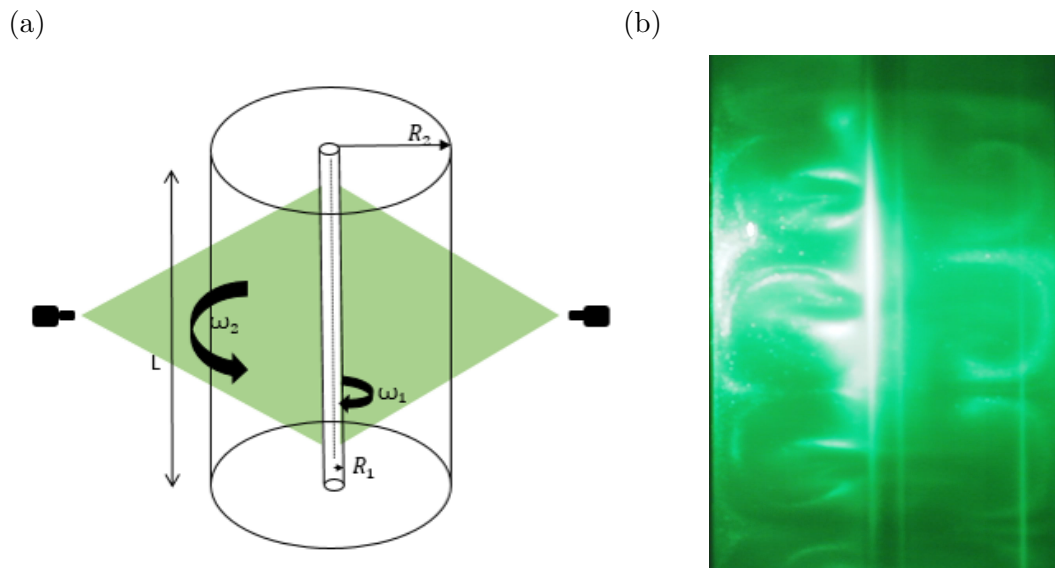


Figure 3.5: a) Sketch of the Taylor-Couette System with radius ratio $\eta = 0.1$, of radius R_1, R_2 rotating at angular velocities ω_1, ω_2 . In green, the LASER sheet for the use of flow visualization in the radial-axial (meridional) plane is indicated. b) Images of meridional flow visualization for $Re_s = 530$ and $\mu = -0.017$.

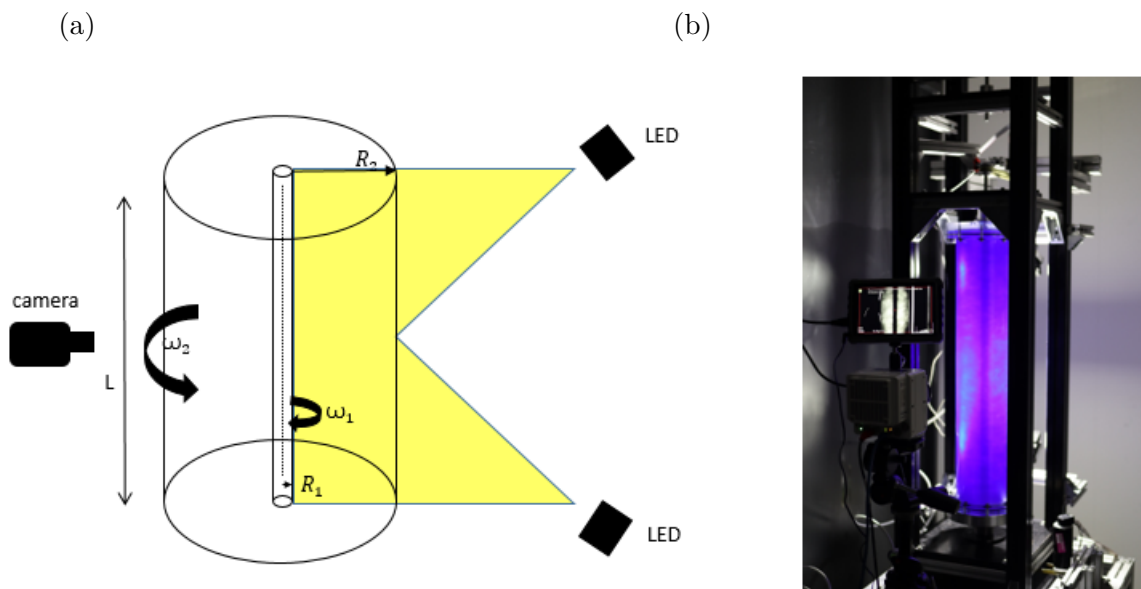


Figure 3.6: (a) Sketch of the Taylor-Couette System with radius ratio $\eta = 0.1$, of radius R_1, R_2 rotating at angular velocities ω_1, ω_2 . In yellow, the light is illuminated by the LEDs use for flow visualization. (b) Images of the visualization setup, showing the Phantom fast speed camera and the TVTCC apparatus.

532 nm (green beam), producing a quasi-2D laser sheet with a maximum thickness of 1 mm, were used. The lasers were placed exactly opposite each other, at the same distance from the outer cylinder. The laser sheet was aligned in the radial-axial (meridional) plane, and the laser sheet was tangent to the inner cylinder so that we prevented light reflection from the cylinder. The goal of this arrangement was to capture the flow patterns in the meridional plane through the whole gap (left and right of the inner cylinder), and in an axial range between $\pm 3d$ from the apparatus mid-height. For this arrangement, the flow was recorded using a Canon EOS 1100D camera with a frame rate of 25 fps. The camera was placed opposite the laser sheets. The second arrangement was done using two LED light sources, placed on one side, one at the top of the apparatus and the second at the bottom, as shown in figure 3.6. The LEDs were tilted and pointed toward the apparatus at midheight in order to illuminate the axially middle segment of the flow. The camera was placed in the opposite direction from the LED and aimed at the apparatus at mid-height. With this arrangement, we use the Phantom high-speed camera ($2560 \times 1600px$) the same used for PIV measurements, and an Optronis CR 300x2 high-speed camera ($1690 \times 1710px$).

3.2.2 Torque measurement

When talking about rotating cylinders or any rotating machinery, it is always important to monitor and keep an eye on the torque applied to the rotating object. In industry, torque measurement is used to quantify the resistance on the rotating machinery, where it is always important to reduce this torque and, as a result, reduce any energy lost. Rhe torque measurement was used widely and for a long time in the TC flow. Starting from Mallock [14, 115], and Couette [15] where they used to measure the torque applied on one of the TC cylinders in order to measure the fluid viscosity. Their method was based on fixing and suspending one of the cylinders to a single torsion spring, and by measuring the deflection of the spring, they could calculate the torque induced in the cylinder and, as a result, the viscosity of the fluid. For the same purpose, Wendt [116] and Taylor [26] also measured the torque using different methods. The recent studies investigating the TC flow used to measure the torque in order to quantify the angular momentum transport [21, 36]. In this study, we used the torque measurement for the same purpose, where a shaft-to-shaft torque sensor was used in order to measure the torque applied to the inner cylinder. The Lorenz DR-3000 torque sensor was used, which has a measurement range ± 0.1 Nm and a measurement accuracy of 0.05%. Unfortunately, the torque sensor could only be used for a few experiments up to a shear Reynolds number of 7000; for further experiments, the sensor caused major problems in accuracy and did not give reliable results until it entirely broke. The torque was measured for 180 seconds with a sampling rate of 10 Hz.

3.2.3 Velocity measurement

In this study, the main measured physical quantity is the flow velocity. The fluid inside the gap between the cylinders is affected by the rotation of the cylinders. The cylinder's shearing forces the fluid to move in different directions. The different shear intensities and directions

cause different flow motions, and one of the main goals of this study is to investigate the effect of the different shears on the flow.

In order to measure the flow velocity field, the PIV technique was used. The simple concept of PIV is that the flow is seeded with tiny particles that have the same density as the working fluid, so that barely any slip occurs between the particles and the fluid, and by measuring the particle velocities we can project these velocities onto the fluid. Further, these particles are subjected to laser light, and the illumination of the particles is recorded by an optical camera. The images captured by the camera are then processed using different particle tracing methods, and as a final result, the flow velocity field is constructed. In the current study, we used a planer laser sheet, so only two velocity components were measured. Using the so-called 2C-2D PIV we were able to measure the radial and azimuthal velocities at a fixed cylinder height. The PIV technique allows obtaining the flow velocity field by obtaining the displacement of the particles at a known time, so the velocity field magnitude and vector can be calculated in a direct way, in contrast to other measurement techniques like hot wire measurements or LDV measurement technique.

3.2.3.1 PIV System

The PIV system is basically composed of a camera and a laser. Also, a computer with a PIV post-processing algorithm is needed in order to save the PIV images and post-processed afterward. The PIV system used in the current study is a high-speed system, allowing for time-resolved velocity measurements. Below, a brief description of each of the PIV system parts is presented.

Laser

The Litron LDY.300 PIV was used; it is one of the LDY-PIV series lasers, which are dedicated configurations primarily for use as an illumination source for PIV. This laser system produces infrared laser light at 1053 nm using two CW Q-switched Nd:YLF DPSS laser resonators. Using an intra-cavity Harmonic Generation Assembly (HGA) the laser light is converted to visible green 527 nm laser light. The laser can be used in two modes: double-pulsed mode and single-pulsed mode. The system consists of a laser head and a separate power supply unit. The power supply has the laser system control, the power section, and the laser cooling section. For the idea of cooling, the power supply unit contains a water-to-air active chiller unit for the thermal management of the deionized water used to cool the laser diodes and the laser rods in the laser head during operation. The laser output beam goes through a cylindrical lens that spreads it into a 2D thin plane sheet with a thickness $< 1\text{mm}$ which ensures capturing the two-component two-dimensional (2C2D) flow without the third component perpendicular to the plane. The laser works in two modes: internal and triggering mode. For the measurements, the triggering mode was used. In addition, using the Litron Laser Control Software, it is possible to control the diode current and the repetition rate of the laser pulse, as well as turn on and off the system, pump, laser, and shutter.

Resolution (H × V)	Maximum Frame Rate - fPS
2560 × 1600	1490
2560 × 1440	1650
1536 × 1536	2350
1920 × 1080	2800
1280 × 1280	3260
512 × 512	14400
128 × 4	290000

Table 3.4: Example of the different maximum frame-rate for common resolutions for VEO 640 Phantom camera.

Camera

In this study, all our velocity measurements were carried out using a high-speed PIV system, so for this purpose, a Phantom VEO 640 high-speed camera was used. This camera captures images at $6Gpx/sec$ for a frame rate reaching 1400 frames per second (fps) at its full resolution of 2560×1600 px as shown in table 3.4. This camera has a 4 Mpx 35mm CMOS sensor, which strikes the perfect balance between increased image data and light sensitivity. This camera is available with different RAMs. In our study, first the 16 Gb RAM camera was used, so we were able to run and record measurements at its full resolution 2560×1600 px with 200fps for 10 seconds. For further and longer measurements, we used the 72 Gb RAM camera, which allows us to record up to 40 seconds.

The camera offers high flexibility by having interchangeable lens mounts. Choosing a suitable lens is a very important factor for PIV measurements, as it is responsible for controlling the PIV image quality. In addition, choosing the right lens can help reduce the optical distortion, and obtain the desired focus and aperture, all of which are key parameters for a good PIV image. For our measurements, we used the Nikon AF Nikkor lens with a focal length of 50 mm and a maximum aperture of f/1.4.

3.2.3.2 PIV Particles

For the PIV measurements, choosing the appropriate PIV particle is very important factor, as in reality using the PIV technique one measures the velocity of the tracer particle. Due to this fact, the chosen particle should be appropriate to the measured fluid velocity field, so by measuring the particle velocity, we ensure measuring the fluid velocity field. The dimensionless Stokes number is used in order to show the degree to which the particles faithfully follow the flow and their tendency to flow with the fluid. The Stokes number (St) is the characteristic response time of the fluid divided by the characteristic response time of the particle. A particle with a low Stokes number $St \ll 1$ is assumed to follow the fluid streamlines, and it is perfectly advected through the flow, while a particle with a large Stokes number $St > 1$ is dominated by its inertia and continues along its initial trajectory. Therefore, the PIV tracing particles should be small enough to minimize inertia and sedimentation effects, and the particles should be sufficiently light scattering and bright so that they can be captured by the PIV camera. For the PIV measurement conducted in the study, we seeded the working fluid with two different tracer particles. The silver-coated hollow-glass spheres from DANTEC

3. Experimental Setup, Measurement Technique, and Data Analysis methods

Particles technical specifications	Silver-coated hollow-glass	Fluorescent particles
Mean particle size (μm)	10	30
Particle shape	spherical	spherical
Density (g/cm^3)	1.4	1.17–1.20
Material	barosilicate glass	PMMA

Table 3.5: The used PIV particles technical specifications.

and fluorescent particles were used. The technical specifications of the particles are shown in table 3.5.

In order to ensure that the particles used for our measurements are suitable to be used as PIV tracer particles, the Stokes number of both particles was calculated with :

$$St = \left(\frac{\rho_p}{\rho} - 1\right) \frac{d_p^2 U_f}{18\mu d} \quad (3.1)$$

where ρ_p is the particle density, ρ is the working fluid density, d_p is the particle mean diameter size, and U_f and μ are the fluid velocity and viscosity respectively. For the silver-coated hollow-glass particles and assuming a maximum fluid speed of 2 m/sec, $St = 6.64 \times 10^{-5}$. For the Fluorescent particles and by assuming the same maximum speed, $St = 2.62 \times 10^{-4}$. It is clear that the Stokes number of both particles is $St \ll 1$, so we can be sure that these particles follow the flow.

3.2.3.3 Measurement procedure.

The PIV measurement procedure started with seeding the working fluid with tracer particles. The distilled water was used for all the PIV measurements, and 0.1 gram of particles were added to each 1 L of water. The gap between the cylinder and the top plate is then filled with the working fluid. It is important to ensure that the whole gap is filled with the working fluid and that no air bubbles exist, especially next to the top-plate. After filling the gap, the system is closed by the top plate, and the camera is installed above the top plate, where the camera lens is directed towards the gap. It was impossible to capture the whole gap due to some physical obstacles, so the camera was mounted at a selected height which allows capturing the radial-azimuthal flow in one-half of the gap. Further, the laser head was fixed on the top of a tripod, and the tripod was placed facing the side of the cylinders where the measurement will take place.

Before starting the measurements, the inner cylinder is set to rotate by linearly increasing its rotation rate up to a final predetermined value; the same is true for the outer cylinder. After a waiting time of about 10 minutes in order to ensure the flow reaches the desired state, the measurement starts. In this study, most of the measurements were done at different heights, with an axial difference of 5 or 4 mm between each height. The measurements start by placing the laser sheet at the top or bottom measured height, and then the laser head installed in the tripod is moved up or down by the value of the axial difference between each height until all the desired heights are measured. Here it is worth mentioning that the temperature of the system is monitored during the experiment, and the viscosity of the working fluid is assumed to be the viscosity of the working fluid at the measured temperature.

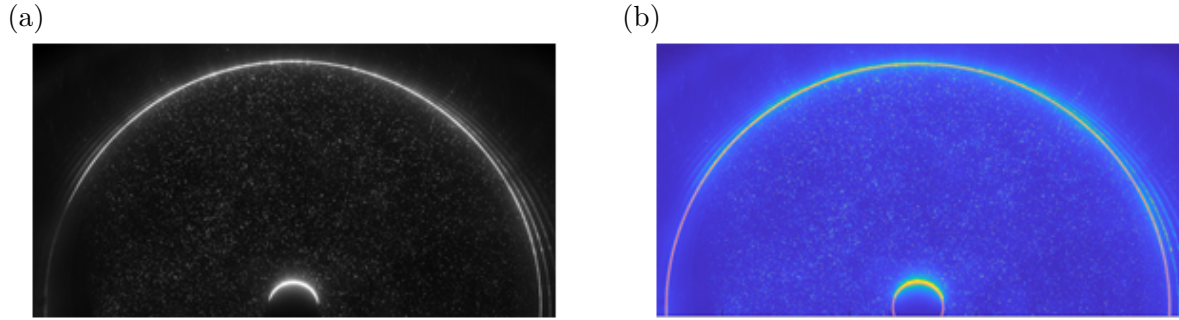


Figure 3.7: (a) Particle image Velocimetry instantaneous image showing the measured velocity field at the horizontal plane at a fixed axial position. (b) The red lines represent the best fit of concentric circles through the cylinder points. Height of horizontal plane: $z-L/2=40$ mm.

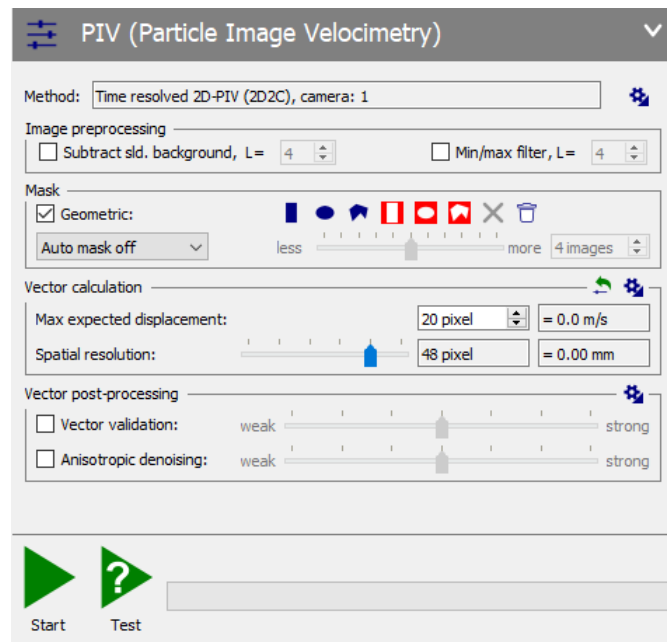


Figure 3.8: The PIV window in DaVis 10 where the different post-processing parameters are chosen

3.2.3.4 PIV measurements calibration.

In order to calibrate the PIV measurements, the use of a calibration target to do a regular calibration procedure is not possible, as the calibration target has to be placed inside the apparatus. This will generate a problem when removing the calibration target from the system, as it would need to disassemble the top plate and the camera placed above the top plate, which leads to losing the calibration after reassembling the apparatus again as it is not possible to replace them accurately in their previous positions due to the complexity of the facility.

For this reason, we detect the location of the inner and outer cylinders in image coordinates by fitting the system's coordinates to the illuminated walls in the images, and by doing so, we can detect the coordinates of the cylinder's center. Using the position of the centers of both cylinders, we can calibrate our measurements. Figure 3.7(a) shows an instantaneous PIV image. From this image, we can detect the light reflection from both the inner and outer cylinder walls. As the borders of the inner and outer cylinders are clear, we fit two concentric

circles through the IC and OC walls. Figure 3.7(b) shows in red the fitted concentric circles to the OC and IC, where the ratio of the fitted circle radius around the inner cylinder to the radius of the fitted circle around the outer cylinder is 0.1 which is equal to the real radius ratio of the facility ($\eta = 0.1$). Here we should mention that the PIV algorithm performed to the PIV images does all the calculations using image coordinates (unit in pixel), and the resulting velocities are also computed in image coordinates (units in px-displacement). In order to transform our output velocities to real coordinates (units in m and m/s), and after finding the image coordinates of the fitted concentric circles' center, we calculate the scale factor (mm/pixel) by determining the known gap width in image coordinates (unit in pixel). This can be done by drawing a line passing through the centers of both cylinders and crossing cylinder walls. Then the scale factor (mm/pixel) is defined as the ratio of the gap width in real units divided by the gap width in image units. The output velocities represent how many pixels the particle moved (which describes the fluid motion) between two consecutive images, so in order to have the velocities in real units, the output velocity was multiplied by the scale factor (mm/pixel) and then divided by Δt the time between two consecutive PIV images. This procedure was done for the different measured heights, so by adjusting the laser sheet height, the camera lens was refocused to capture the flow at the desired height with the highest possible resolution and clarity, and new spatial resolution was measured.

3.2.3.5 PIV images post-processing

In order to calculate the flow velocity field from the raw PIV images, the Data Acquisition and Visualization Software (DaVis) package from LaVision is used. For our measurements, the 2D-PIV(2D2C) software calculates the two vector components in the illumination plane. After recording the PIV images, using the DaVis software every single image is divided into small interrogation windows, where the size of the window is to be chosen by the user. The calculation of the velocity vector can go through multi-passes, starting with initial passes with a window size larger than the final passes, where the window size of these final passes represents the spatial resolution, as shown in figure 3.8. At the end, one velocity vector is calculated from each interrogation area. In addition, before calculating the velocity vector from the PIV images, a Mask option is available where every image can have a mask, which can mark a pixel or mask it out.

After dividing the images into small interrogation windows, the particle displacement (ds) at each interrogation window between two consecutive images at a known time interval (dt) is determined, and then the velocity of the particle is given by ds/dt. The calculation procedure of the particle movement (ds) is calculated by FFT-based cross-correlation of the two interrogation windows from the two consecutive images, following the procedure shown in figure 3.9.

The simple explanation of the FFT-based cross-correlation procedure presented in figure 3.9, is calculating the particles' displacement (ds) as follows: first, by defining the interrogation window at time t as $f(x)$ function, and the interrogation window at time $t + dt$ as $g(x)$ function, where the particles in $g(x)$ are shifted over some distance ΔX with respect to the same particle in $f(x)$. Then the correlation between the two functions is written as:

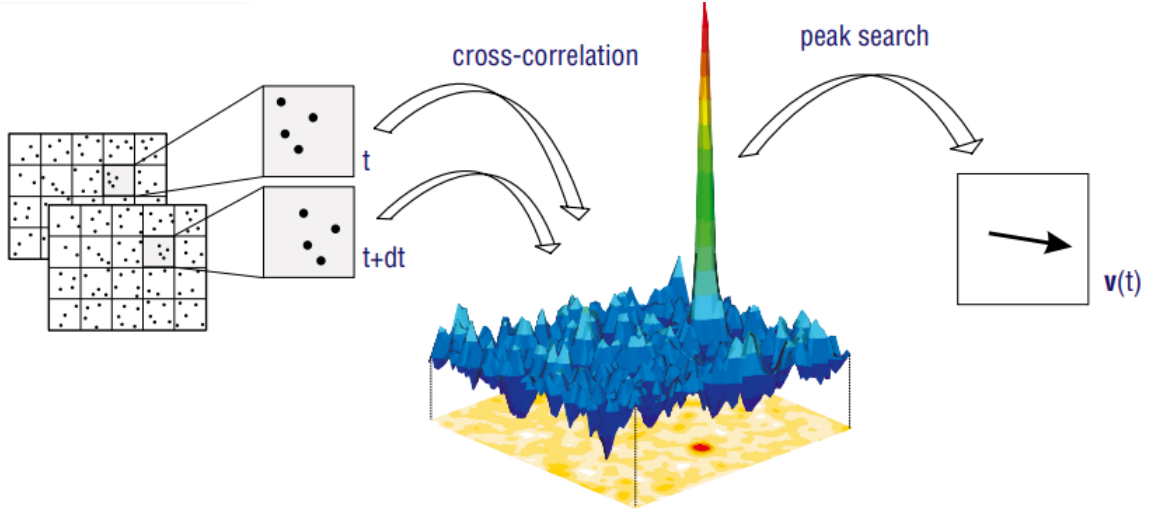


Figure 3.9: Velocity vector calculation procedure used in DaVis 10. From the left: the image is divided into small interrogation windows, then the displacement of the particles at one interrogation window is calculated from a Cross-correlation data processing procedure using an FFT algorithm, at the end we get the velocity vector with describes the fluid velocity at the selected interrogation window.

$$f \star g = C_{fg}(\Delta X) = \int_{-\infty}^{+\infty} f^*(x)g(x + \Delta x)dx. \quad (3.2)$$

By defining a wave number k , as a function of wavelength λ , the Fourier transform (\mathcal{F}) and the inverse Fourier transform (\mathcal{F}^{-1}), can be defined as :

$$H(k) = \mathcal{F}[h(x)] = \int_{-\infty}^{+\infty} h(x) \exp^{2\pi i k x} dx \quad (3.3)$$

$$h(x) = \mathcal{F}^{-1}[H(K)] = \int_{-\infty}^{+\infty} H(k) \exp^{-2\pi i k x} dk \quad (3.4)$$

Now, the correlation between the Fourier transform of $f(x)$ and $g(x)$ can be written as:

$$C_{fg}(\Delta X) = \int_{-\infty}^{+\infty} \mathcal{F}[f^*(x)]\mathcal{F}[g(x + \Delta x)]dx. = \dots = \mathcal{F}^{-1}[F^*(k)G(k)] \quad (3.5)$$

This is known as the correlation theory.

As explained above, the correlations are applied between the two-dimensional FFT of both interrogation areas. Then, by using a complex conjugate multiplication of the transforms, the cross-correlation is evaluated in the wave number domain, and then a back-transformation is done to have the cross-correlation in the physical domain. From the resulting correlation field, like the one shown in figure 3.9, we can determine the particle displacement (ds) from the maximum peak shown in the figure, which corresponds to the two-dimensional displacement of the particles in the interrogation area. For further detailed explanation and detailed equations, the reader is referred to [117].

Further, after calculating the velocity field vectors from the PIV images, a vector post-processing can be done. Whereby selecting different parameters the vector velocity data can pass through different filters that make the data smoother and smoother.

3.2.3.6 PIV error estimation

As shown above, the PIV measurements and then the PIV images post-processing go through different steps using different systems, which can increase the source of error associated with the final output velocity. The measurement quality is evaluated by the measurement errors. Within this study, two aspects of error are discussed. The first is the alignment of the camera with the laser sheet. The second is by using one of the features of the TC flow, where for a flow configuration with both inner and outer cylinders rotating at the same speed. The “solid-body rotation” flow velocity inside the gap is theoretically predicted, and then it can be compared to the measured velocities. Figure 3.10(a) shows that the scaling factors at different heights can be fitted to a linear line, which means that the scale factor is a function of height. Although at some height a small deviation from the linear line exists, with a maximum deviation of 0.3%. So it can be assumed that the camera is in good alignment with the laser sheet and that any other distortion of the optical path is negligible. Moreover, a measurement set was done over 21 different measured heights for a solid-body rotating flow configuration with $\omega_1 = \omega_2 = 31.3$ rpm. Figure 3.10(b) shows how the measured azimuthal velocities at the different heights have the same value and how they have a very good agreement with the theoretically predicted value. Although for the solid-body rotation, the radial component of the velocity should vanish, it is shown in figure 3.10(b) that u_r still exists with a maximum of 0.07mm/sec near the inner cylinder, which represents 0.2% of the mean azimuthal velocity at the same radial position, and a maximum of $\langle u_r \rangle = 0.8$ mm/sec next to the outer cylinder, which represents 0.4% of the mean azimuthal velocity. These values are still considered very low and negligible, and it can be concluded that the calibration method used is valid, and the measured velocities are accurate.

3.3 Data analysis methods

In this section, the methods used to analyze the measured velocity field within this study are described. A general overview of each method, in addition to the point of use of each in this study, is presented below.

3.3.1 Statistical analysis

Our measured velocities were mostly analyzed using statistical methods. But before discussing the analysis, it was crucial to set up our data matrices in a way that made such analyses possible. The output post-processed velocity data are first in Cartesian coordinates and are then converted to cylindrical coordinates using the calibration technique described in the preceding section. Yet, given that the velocities are dispersed almost arbitrarily with respect to the cylindrical coordinates, it is possible to locate velocities in a single row of a data matrix that correspond to various azimuthal and radial places. The velocity matrices were then

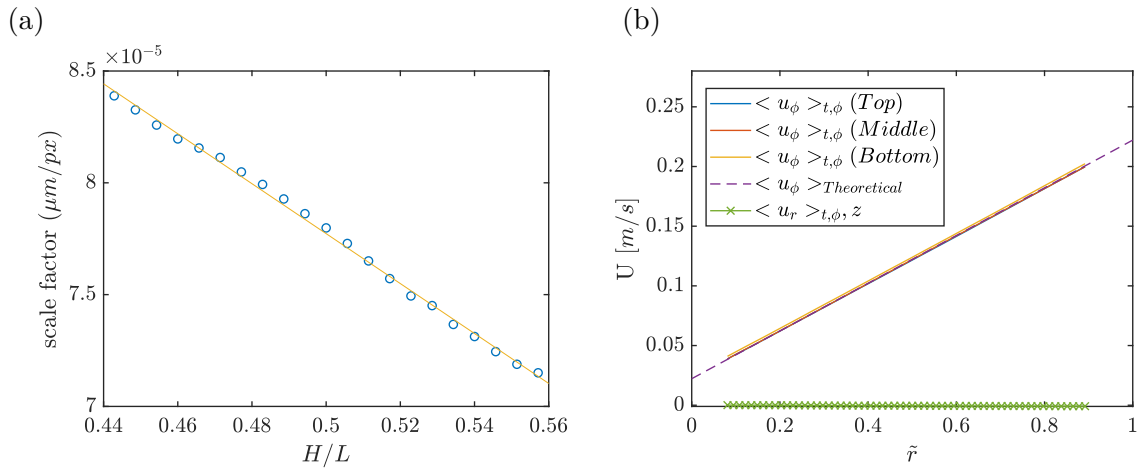


Figure 3.10: (a) The scale factor at the different heights for a measurement set of 21 heights around the apparatus mid-height, with an axial difference of 4 mm between each height. (b) The time and azimuthal averaged profiles of the measured azimuthal velocity at the three different heights are compared to the theoretically predicted velocity for a solid-body rotation ($w_i = w_o = 30.3\text{rpm}$); further, the time, azimuthal, and axial averaged profiles of the measured radial velocity are shown.

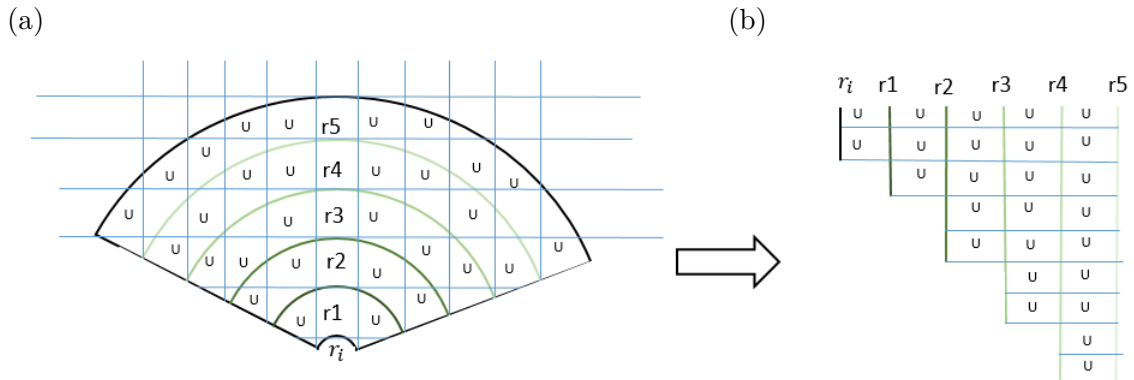


Figure 3.11: Schematic sketch describing the interpolation procedure. (a) The distribution of the velocities in x, y coordinates; (b) The distribution of the velocities after applying the 2D interpolation in r, ϕ coordinates, where the velocities at each column belong to fixed radial positions and different azimuthal positions.

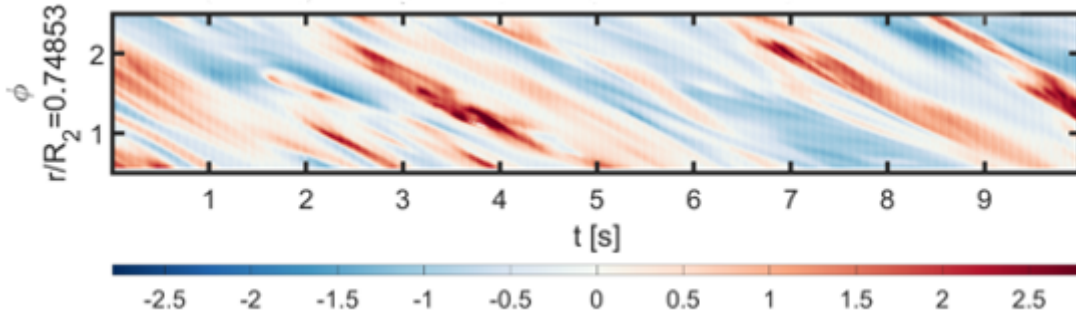


Figure 3.12: Example of the space-time subplot at a fixed radial position. The y-axis represents the azimuthal position and the x-axis time. The intensity of the presented quantity is described by the color map.

rearranged using a 2D interpolation technique such that the velocities for each instantaneous time at the same radial point are all in one column, as shown in figure 3.11. The velocities were distributed within the same azimuthal range for the different radial positions, but with different $\Delta\phi$ between the different data points. The reason for having a radial dependent $\Delta\phi$ returned to the fact that the arc length at the different radial positions is not the same, so it is clear that we will have a different number of data points in the different radial positions, and at the end, the number of data points at the radial position near the outer cylinder wall is ten times more than the ones in the radial position next to the inner cylinder wall. This may be problematic for statistical analysis, but the number of temporal samples (between 1400 and 8000 images) for each measurement set can compensate for this problem. As an output of the data matrix interpolation, we end up with a data set having four dimensions: radial position, azimuthal position, axial height, and time.

In addition to studying the mean and the standard deviation of this data with respect to the different dimensions, as will be shown in the results chapters, the data were analyzed using space-time plots. So the velocity data or any product between the different velocity components were shown in subplots describing the flow behavior at a fixed height and different azimuthal positions over time. As shown in figure 3.12, each subplot belongs to a fixed radial position. These plots are used to show the existence of patterns traveling through the flow and their characteristics.

3.3.2 Spectral Analysis

Once a wave-like behavior appears in a time series of data in physical space, frequency analysis in Fourier space is required to identify the properties and physical description of this wave.

3.3.2.1 The Fourier transform

The Fourier transform is a commonly used tool in fluid dynamics in order to analyze the measured data sets for different applications. The Fourier transform is used to transform the signal from the time domain to the frequency domain, while the inverse Fourier transform does the transformation in the opposite direction. The definition of the Fourier transform reads:

$$F(\omega) = \int_{-\infty}^{+\infty} f(t) \exp^{2\pi i \omega t} dt. \quad (3.6)$$

and the inverse Fourier transform is

$$f(t) = \int_{-\infty}^{+\infty} F(\omega) \exp^{-2\pi i \omega t} d\omega \quad (3.7)$$

Our data series have finite length, so the discrete Fourier transform was used, and in order to save the computation time the fast Fourier transform (FFT) is used, and it is defined as :

$$H(k) = \sum_{n=0}^{N-1} \exp^{-2\pi i \frac{kn}{N}} h(n) \quad (3.8)$$

The FFT is a transform gives complex results of spanning negative and positive frequencies (-Nyquist to +Nyquist). In order to analyze our results, we were not interested in the negative frequencies, so the single-side spectrum was used, which is throughout the negative frequencies. In this study, the single-side spectrum was used in order to measure the frequencies of the traveling patterns that appear in the flow. Also, it was used to identify the dominant frequencies in any data signal, so that we could figure out if there was any noise or external effect in our measured data sets.

3.3.2.2 Azimuthal energy co-spectra

In order to study the presence and scale of the different structures in the gap, the spatial energy co-spectra were used to analyze the length scale of the flow small-scale structures. The energy co-spectra were studied for the two velocity fluctuations (\acute{u}_r and \acute{u}_ϕ) a fixed axial height, and they are defined by:

$$\acute{u}(r, \phi, t) = U(r, \phi, t) - \langle U(r, \phi, t) \rangle_t \quad (3.9)$$

The energy co-spectra are calculated for the velocity fluctuations at different fixed radial positions and different azimuthal points $n_\phi = \{0, 1, 2, \dots, N - 1\}$, spaced by the arc length interval

$$\Delta s = \Delta \phi r. \quad (3.10)$$

The discrete spatial FFT ($\acute{U}_r(n_\phi)$ and $\acute{U}_\phi(n_\phi)$) of both velocity fluctuations (\acute{u}_r and \acute{u}_ϕ) are calculated based on equation 3.8. The spatial energy co-spectra $E_{r\phi}$ can be then computed using the algorithm presented by press et al. [118] as :

$$\begin{aligned} E_{r\phi}(k_\phi^0) &= \frac{1}{N^2} |\acute{U}_r^0 \cdot \acute{U}_\phi^0| \\ E_{r\phi}(k_\phi^{n_\phi}) &= \frac{1}{N^2} |\acute{U}_r^{n_\phi} \cdot \acute{U}_\phi^{n_\phi}| \\ E_{r\phi}(k_\phi^{\frac{N}{2}}) &= \frac{1}{N^2} |\acute{U}_r^{\frac{N}{2}} \cdot \acute{U}_\phi^{\frac{N}{2}}| \end{aligned} \quad (3.11)$$

for $n_\phi = [0]$, $n_\phi = [1, 2, \dots, (\frac{N}{2} - 1)]$ and $n_\phi = [\frac{N}{2}]$ respectively, and with the wave vector $k_\phi^{n_\phi} = n_\phi / \Delta s N$. By multiplying the energy spectra with the wave vector, we get the pre-multiplied energy co-spectra. Further, the temporal azimuthal energy co-spectra is calculated using the same procedure at different fixed radial positions and temporal points $n = \{0, 1, 2, \dots, N - 1\}$, spaced by the time step between each pair of consecutive PIV images.

3.3.3 Quadrant analysis

The quadrant analysis is a turbulence data-processing technique that is widely used. This simple technique is used principally in the investigation of turbulent shear flows. The quadrant analysis of the Reynolds shear stress that is used within this study was carried out first by Wallace et al. [119], where they tried to quantify the visual observation of Corino & Brodkey [120]. The quadrant analysis of the Reynold shear stress is based on classifying the velocity fluctuations with respect to their signs, ending with 4 categories: Q1(+u, +v), Q2(-u, +v), Q3(-u, -v), and Q4(-u, +v). The motions in the quadrants Q2 and Q4 are related to ejection and sweep events, while Q1 and Q3 are motions of outward and inward events.

3.3.4 Dynamic Mode Decomposition (DMD)

It is always important in fluid mechanics research to explore the existence of coherent patterns in the different studied flows. This is why the Dynamic Mode Decomposition (DMD) technique has gained big popularity in the fluid dynamics community since it was introduced [121]. DMD is a technique to extract spatio-temporal coherent patterns from high-dimensional fluids experimental and numerical data [122]. The DMD technique provides information about the flow dynamics, even the nonlinear ones [123]. For a review of the DMD literature, the reader is referred to [124] and [125]

For selected parameters, the time-resolved PIV data measured within this study were used in order to explore the existence of any coherent patterns. To construct a data structure for DMD, the data is typically collected from a dynamical system, which can be presented in a sequential set of data vectors $\{V_0, V_1, \dots, V_k\}$, where each data vector represents the velocity data at an instant in time. In the current study, the output velocity at one height is represented as $V = V(x, y, t)$ with dimensions $m \times n \times k$. Then, to build a sequential set of data vectors, the velocity matrix was transformed into a 2D matrix, where the first dimension represents space and the second is time, as shown in 3.12.

$$V = \begin{pmatrix} v(x_1, y_1, t_0) & v(x_1, y_1, t_1) & \dots & v(x_1, y_1, t_k) \\ \vdots & \vdots & & \vdots \\ v(x_1, y_n, t_0) & v(x_1, y_n, t_1) & \dots & v(x_1, y_n, t_k) \\ v(x_2, y_1, t_0) & v(x_2, y_1, t_1) & \dots & v(x_2, y_1, t_k) \\ \vdots & \vdots & & \vdots \\ v(x_2, y_n, t_0) & v(x_2, y_n, t_1) & \dots & v(x_2, y_n, t_k) \\ \vdots & \vdots & & \vdots \\ v(x_m, y_1, t_0) & v(x_m, y_1, t_1) & \dots & v(x_m, y_1, t_k) \\ \vdots & \vdots & & \vdots \\ v(x_m, y_n, t_0) & v(x_m, y_n, t_1) & \dots & v(x_m, y_n, t_k) \end{pmatrix} \quad (3.12)$$

The DMD is defined in terms of $(m \times n) \times k$ data matrices, where the k snapshots are arranged in two matrices:

$$V = \begin{pmatrix} | & | & & | \\ v_1 & v_2 & \dots & v_{k-1} \\ | & | & & | \end{pmatrix} \quad (3.13)$$

$$\dot{V} = \begin{pmatrix} | & | & & | \\ \dot{v}_1 & \dot{v}_2 & \dots & \dot{v}_{k-1} \\ | & | & & | \end{pmatrix} \quad (3.14)$$

where in our case here, $x_k = v_{k-1}$ and $\hat{x}_k = v_k$, and we assume that

$$\hat{x}_k = \hat{A}x_k \quad (3.15)$$

with \hat{A} an unknown matrix. Using the Exact DMD algorithm presented by Tu et al. [126], a operator is defined with:

$$A \triangleq \dot{X}X^+ \quad (3.16)$$

with X^+ the pseudo-inverse of X , and the dynamic mode decomposition of (V, \dot{V}) is given by the eigen decomposition of A , with the eigenvectors and eigenvalues of A being the DMD modes and eigenvalues respectively. The DMD modes are spatial fields that often identify coherent structures in the flow, while the eigenvalues define the oscillation frequencies and the growth/decay value for each mode.

4

Flow regimes in a very wide-gap Taylor-Couette flow with a counter-rotating cylinder.

In this chapter, we present and discuss the different flow patterns and regimes observed in a very wide gap Taylor-Couette flow ($\eta = 0.1$). The flow is investigated up to the shear Reynolds number $Re_s = 15 \times 10^3$, using visualization methods. The visualization work is limited to the centrifugally unstable cases, where, in addition to the inner cylinder rotation, the outer cylinder is either static or rotating in the counter direction. Different open questions arose before this work: Do the classical patterns that appear in the narrower gap TC flow geometries like the Taylor vortices (TV), Wave Taylor vortices (WTV), and others appear in the very wide gap TC flow geometry, and on the other hand, are there any patterns unique to this geometry? All these questions and more are answered in this chapter.

This chapter is organized as follows: in Section 4.1 the experimental setup and the visualization technique used are described. Section 4.2 presents the various observed patterns as instantaneous images and analyzes the spatial and time behavior of some of the observed structures. In Section 4.3 we present a flow-regime diagram that summarizes all the patterns observed. And this chapter ended with a conclusion in Section 4.4.

The main results presented in this chapter are part of the paper *Flow regimes in a very wide-gap Taylor-Couette flow with counter-rotating cylinders* by S. Merbold, M. H. Hamede, A. Froitzheim and Ch. Egbers (2023), published in *Phil. Trans. A* [19].

4.1 Experimental setup and visualization methods

The Top view TC Cottbus (TvTCC) experimental facility is used. As was described in Chapter 3 this TC facility has a transparent outer cylinder, which allows a deep sight inside the gap for the dynamics of the flow. An inner cylinder with radius $r_1 = 0.007$ m is used, leading

4. Flow regimes in very wide gap TC flows with counter-rotating cylinders.

to a radius ratio of $\eta = 0.1$ and gap width $d = 0.063$ m. During the rotation of the inner cylinder, a radial run-out is observed, where the maximum is measured at the cylinder's mid-height with $r_{ro} = 0.5$ mm. When comparing the maximum value of r_{ro} to the inner cylinder circumference, this is ≈ 0.011 , thus, it is assumed that the wall-normal forces are negligible. Further, the effect of the radial run-out on the driven shear is checked. First, estimate laminar torques $T_{lam} = R_1 R_2 Re_S d^{-2} 2\rho\nu^2$ [21] for the maximum shear Reynolds numbers investigated in this chapter $Re_s = 1.5 \times 10^4$: $T_{lam}(Re_S = 15000) = 3 \times 10^{-3}$ Nm, the radial run-out measured in wall units $r^+ = r_{ro}/y^* = r_{ro}\nu^{-1}\rho^{-1/2}\tau_w^{1/2}$, where $\tau_w = T/(2\pi LR_1^2)$ is the wall shear stress, computes to be $r^+(Re_w = 15000) = 3$. So we assume this uncertainty to be of an acceptable value.

For the small Re_s flows where the rotation speed of the outer cylinder (ω_2) doesn't exceed 25 rpm a 75 W Maxon DC motor is used to drive the cylinder, while for higher speeds, a 200 W Maxon DC motor is used. The idea of using two motors is that for low speeds, a small motor have less rotation velocity fluctuation, and therefore the rotation speed is mostly constant through time. The M20 silicone oil is used as a working fluid with kinematic viscosity $\nu = 21.87 \pm 0.07 \times 10^{-6} m^2/s$ (at $20^\circ C$). The temperature of the fluid is monitored using a thermocouple-type k sensor, but the data recording process was short in time, lasting less than 15 minutes for every single parameter, so we observed that the temperature difference between the moment of running the system on until it runs off is negligible.

The visualization technique is used in order to understand the global flow structures in the turbulent TC flow, where such a technique gives the possibility to observe the different flow regimes and their dependence on the different driving parameters like the rotation ratio and the shear Reynolds number. In addition, the transition of the flow from laminar to turbulent can be figured out using the visualization technique. To do so, the flow was seeded with kalliroscope particles, which are tiny gaunin flakes with dimensions of approximately $30 \times 6 \times 0.07 \mu m$, with Stokes number: $St = (\frac{\rho_p}{\rho} - 1)d_p^2 u_s / (18\mu d) \approx 1.4 \times 10^{-5}$, assuming a maximum speed of $1m/s$, and silicon oil as a working fluid, so $St \ll 1$ which means that they follow the flow precisely. In addition to the tracer particles, a colored dye was added to the flow in order to reduce the transparency of the fluid and increase the contrast of the visualization image. It is worth mentioning here that the amount of added dye and particles doesn't have any significant effect on the fluid properties. Two different flow visualization arrangements are used in this chapter, as described in Chapter 3.

The running path of the system is important when studying the flow patterns. Arias-Martinez et al. [127] show that the path of accelerating and decelerating the cylinders can influence the resulting flow structures. The same path is used in all cases for running the system: first, the inner cylinder is spun up until it reaches the desired Re_s in a minimum increment of 2.3 rpm with a static outer cylinder, then the outer cylinder is set to rotate in the selected direction with a minimum increment of 0.5 rpm using the 70 W motor and 2 rpm using the 200 W motor until it reaches the rotation speed required to obtain a specific rotation ratio, finally, the rotation of the inner cylinder is modified to keep $Re_s = cnst$. The system is accelerated to the given set Re_s and rotation ratio, and then the flow state needs time in order to rise up. The large eddy turnover time, $t_L = d/u_{r,z}$ is used in order to assume

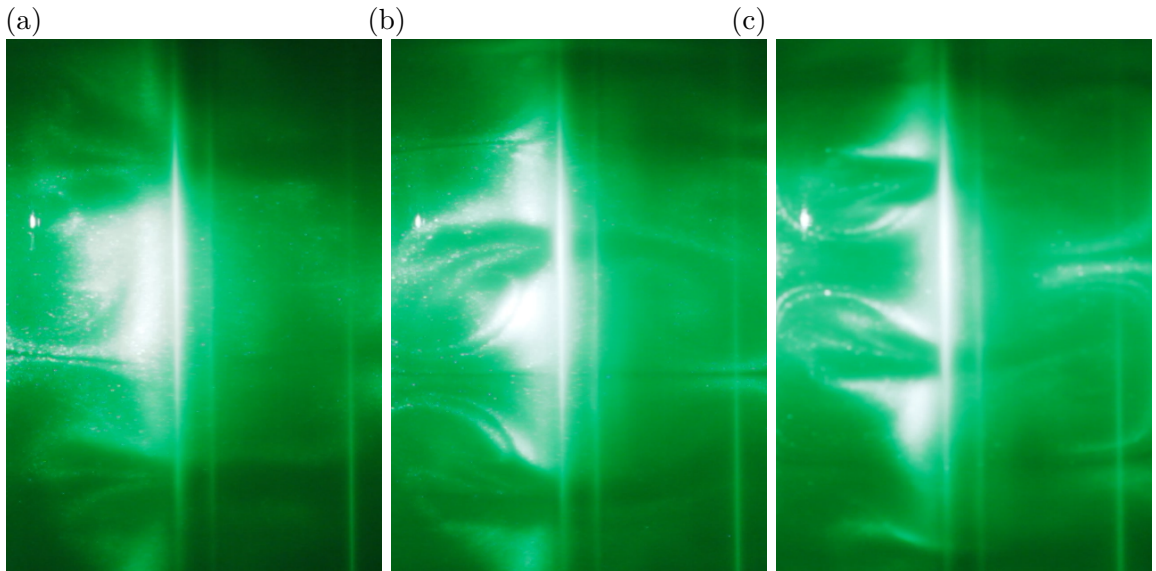


Figure 4.1: Images of meridional flow visualization for various flow situations, for $Re_s = 530$: (a) $\mu = 0.036$ laminar Taylor-Vortex flow, (b) $\mu = 0$ irregular laminar TVF, (c) $\mu = -0.007$ laminar TVF

the needed waiting time, where here $u_{r,z}$ is the velocity of the secondary flow. Although an exact measurement of this speed is not possible, preliminary observations are used, and the secondary flow is estimated to be 1 % of the driving velocity u_ϕ . Although the secondary flow can be much stronger, this assumption is used as a critical lower value to determine the waiting time. From this approximation, t_L varies from 2.4 seconds (for the highest velocities) up to 89 seconds (for the lowest velocities). To ensure a stabilized flow for all the visualized parameters, we wait up to 2 minutes, which we observe to be enough in all cases.

To present and analyze the global and meridional visualization results, snapshots at different instantaneous times are used. In addition, and in order to study the temporal behavior of the flow, the light intensity change I along an axial line at a certain azimuthal (for global visualization) or radial (meridional visualization) is analyzed, and after that the fluctuation of light intensity $I'(z, t) = I(z, t) - \bar{I}(z)$ is computed, which is then plotted in a space-time plot to show the temporal evolution of the flow patterns.

4.2 Flow patterns

In this section, we looked inside the very wide gap TC flow with a radius ratio of $\eta = 0.1$ and a shear Reynolds number ranging from 5×10^2 to 1.5×10^4 for pure-rotating inner cylinders and counter-rotating cylinders, respectively. The results will be presented in relation to flows with rotation ratios varying from $-0.125 \leq \mu \leq 0$. After the system is accelerated to reach the desired rotation ratios and shear Reynolds numbers and after a waiting time of two minutes to saturate the flow state as mentioned in the previous section, the patterns are observed.

4.2.1 Laminar Taylor Vortex flow

Starting with the minimum investigated shear Reynolds number, $Re_s = 530$, and for the case of pure inner cylinder rotation, $\mu = 0$, large-scale toroidal vortices exist that fulfill the entire

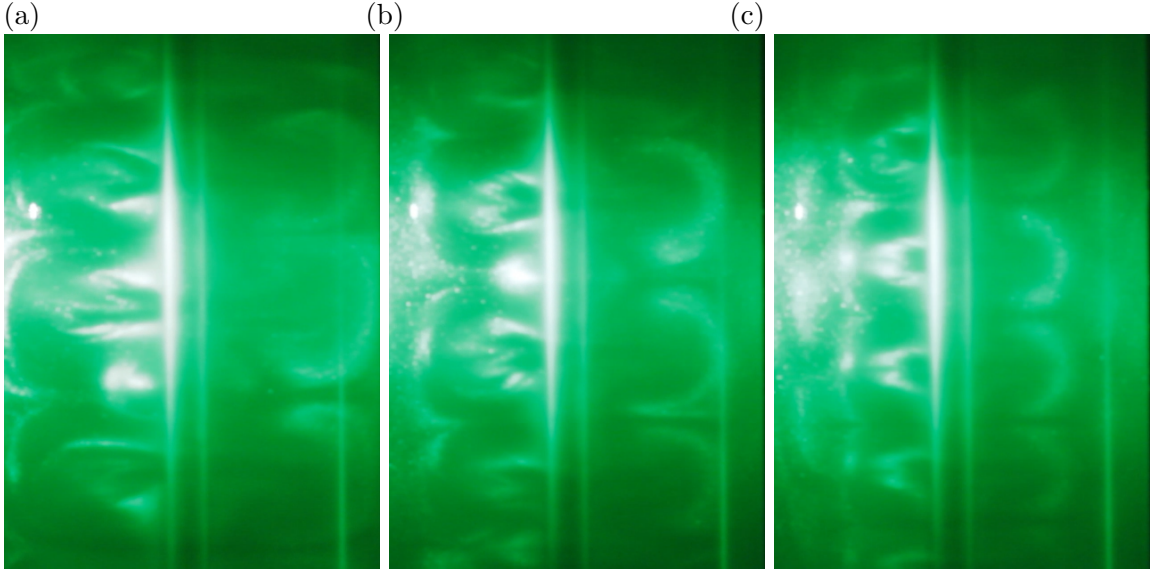


Figure 4.2: Images of meridional flow visualization for various Wavy Vortex flow situations, for $Re_s = 530$: (a) $\mu = -0.11$ Wavy Vortex flow, (b) $\mu = -0.043$ detached Wavy Vortex flow, (c) $\mu = -0.08$ detached Taylor Vortex flow.

gap width, as shown in figure 4.1(b). We are not able to describe the observed pattern by the classical laminar Taylor Vortex flow (TVF), as in contrast to the TVF, the observed pattern is not dominant with small scales at one point in time, but the outflow and inflow regions are irregular and unpredictable and travel in the axial direction, which leads to non-stationary patterns. Further, the patterns are not axially oscillating, so they can't be described by the known Wavy Vortex Flow (WVF) or Modulated WVF. We call this pattern an irregular Taylor Vortex Flow, as they appear similar to the TVF at instantaneous time (figure 4.1(b)), but then vary unsteadily through time. When the outer cylinder is set to rotate in the counter direction of the inner cylinder rotation, the in- and outflow regions are axially stabilized, and the classical laminar Taylor Vortex flow is observed as shown in figure 4.1(c) for rotation rates $-0.008 \leq \mu \leq -0.001$ and $500 \leq Re_s \leq 10^3$. Further, and when the outer cylinder is slightly co-rotated with the rotating inner cylinder ($\mu = +0.0036$), the stable laminar TVF is observed too (figure 4.1(a)). Although such patterns are just observed for a small range of shear Reynolds number $500 \leq Re_s \leq 600$, observing such patterns in the co-rotating regime is not expected. So it is clear, for the very low values Re_s , the slight rotation of the outer cylinder in both directions can stabilize the irregular laminar TVF and lead to the formation of the classical TVF.

4.2.2 Detached Taylor Vortex flow, Wavy Vortex Flow, and detached Wavy Vortex Flow

For the same low shear Reynolds number where the TVF is observed for $-0.008 \leq \mu \leq -0.001$, and by increasing the counter-rotation rate of the outer cylinder, the vortices start to oscillate axially, and the Wavy vortex flow is observed (figure 4.2(a)) for $-0.025 \leq \mu \leq -0.01$. For a further increase in the counter-rotation rate, the WVF detaches from the outer cylinder, due to the stabilization effect of the outer cylinder. The gradient of angular momentum drives centrifugal instability in the TC flow, so when only the outer cylinder is rotating, we have a

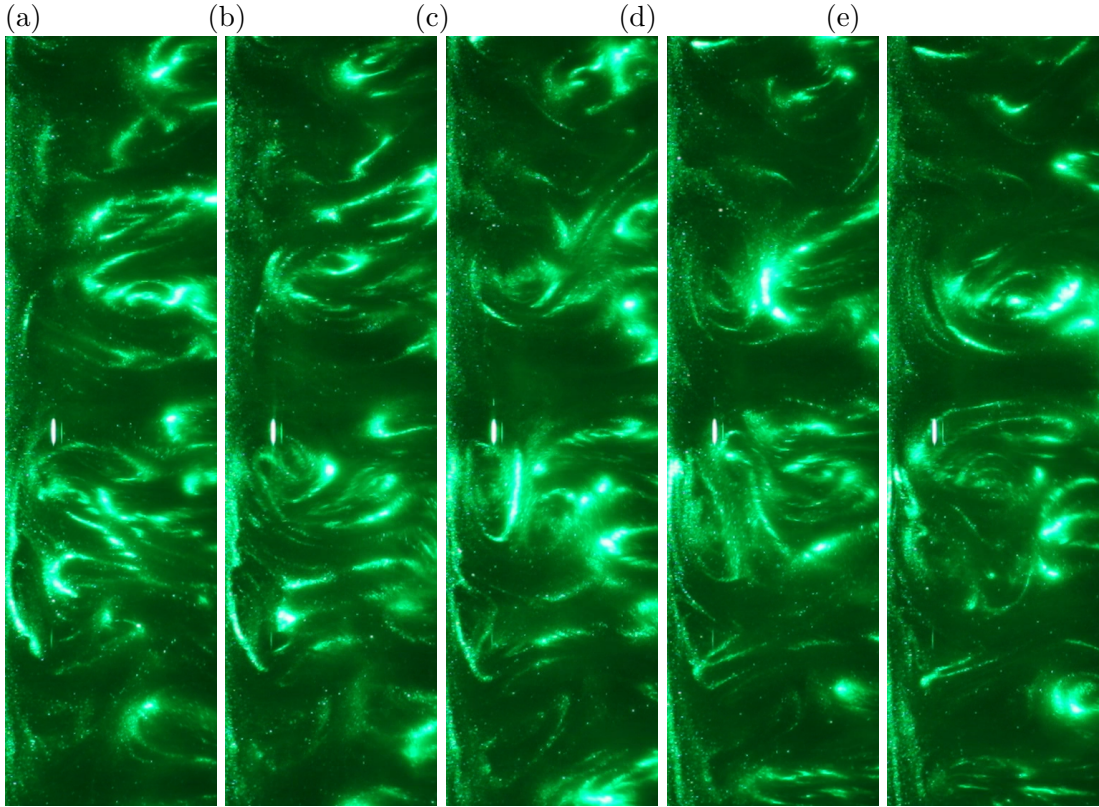


Figure 4.3: Sequence of meridional plane visualization of Turbulent Vortex flow at $Re_s = 3000$, $\mu = -0.01$ for time steps: (a) 0.0 sec, (b) 0.4 sec, (c) 0.8 sec, (d) 1.2 sec, (e) 1.6 sec. The inner cylinder wall is located at the right edge of the images, while the outer cylinder is located at the left edge.

positive gradient and the flow is centrifugally stable (Rayleigh-criterion), whereas when the inner cylinder is purely rotated, the gradient is negative and the flow is centrifugally unstable. In the case of both cylinders rotating, which is the case shown here, both the stable and unstable areas are found in the gap. Figure 4.2(b) shows how the WVF detaches from the outer cylinder for $\mu = -0.043$ and how the flow next to the outer cylinder is stabilized. For a higher outer cylinder rotation rate, $\mu = -0.08$, the stabilized area increases as the rotation and stabilization effect of the outer cylinder increase, but surprisingly, the patterns in the unstable area next to the inner cylinder are axially stabilized and look like the classical TVF without an axial wave, where such patterns are identified as detached TVF.

4.2.3 Turbulent Vortex flow

As the shear Reynolds number increases $Re_s \geq 2.5 \times 10^3$, the stationary patterns mostly vanish in the weak counter-rotating regime of $-0.01 \leq \mu \leq 0$, so the flow in the entire gap turns to be turbulent and different scale structures are observed. This turbulent small structure seems to feed large-scale vortices to grow, whereas strong Large-scale circulations appear over time in the gap, similar to the turbulent vortex flow observed in the larger radius ratio TC flows [18, 24, 36], but the here observed patterns are neither confined nor azimuthally and time stable. These huge turbulent vortices collapse over time as shown in figure 4.3, and the process of feeding a large-scale vortex from the small-scale turbulent structures is repeated elsewhere in the gap.

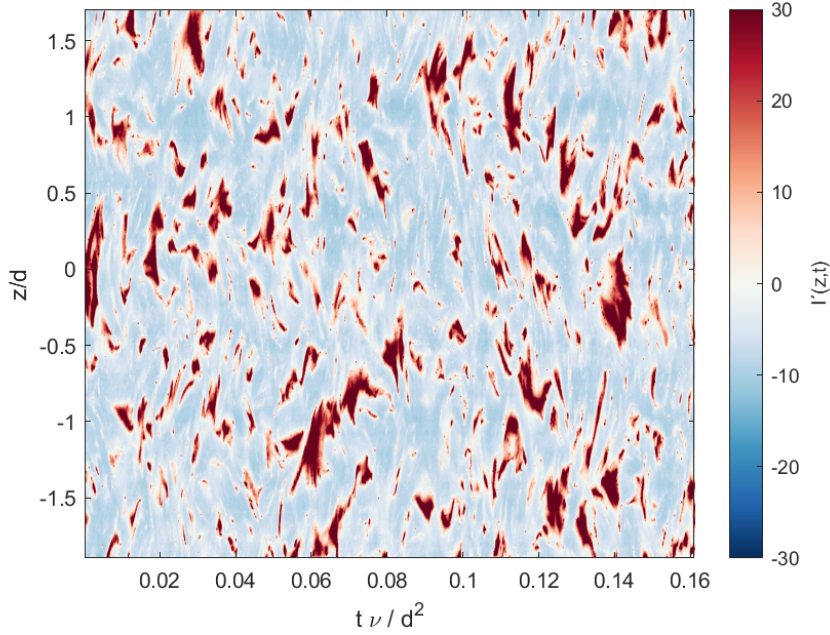


Figure 4.4: The spatial-temporal behavior of the light intensity fluctuation I' along the height of the central line. Here: turbulent spots are observed for $Re_S = 3000$ and $\mu = -0.03$.

4.2.4 Turbulent Spots and Bursts

For higher counter-rotation rates of $-0.06 \leq \mu \leq -0.01$ and for shear Reynolds numbers up to 5×10^3 , the stabilizing effect of the outer cylinder rotation increases and the flow in the gap is mostly laminar, but this laminar flow is penetrated by small-scale plumes forming close to the inner cylinder (figure 4.4). The small-scale plumes grow into isolated turbulent spots of motion and travel radially outward through the gap. When these turbulent spots approach the outer cylinder, they grow quickly in the axial-azimuthal direction, which reduces the spots' turbulent intensity. These turbulent spots are locally confined turbulent events surrounded by laminar flow, where finally this turbulent motion dwindles down and the flow is laminar again. From visual observation, these turbulent spots don't appear close to the top and end plates ($L/7 \sim 1.6d$ from the top and bottom), which is due to the end-plates effect, which induces flow and damps the turbulent motion. These results agree with the findings showing that the end plates effects are limited below $\sim 2d$ for flow in the centrifugal unstable regime [20], while they can grow to the entire gap in the centrifugal stable regime [128]. Further, in the axial central $5L/7$ of the flow axial domain, the spots are founded to happen at different axial heights irregularly and suddenly, and randomly spread through the gap. Such turbulent spots are investigated in the narrow gaps ($\eta = 0.871$) TC flow, where Borrero et al. [129] investigated the existence of turbulent patches in laminar flow.

As the shear Reynolds number increases, the probability of these turbulent spots increases, and these isolated turbulent spots transform into non-isolated turbulent structures that overlap and interact with one another. Thus, the flow becomes turbulent, which is driven by the occurrence of time-variant events of intense turbulence, which are identified as turbulent bursts (figure 4.5). By increasing the Re_s the turbulent bursts became more frequent and

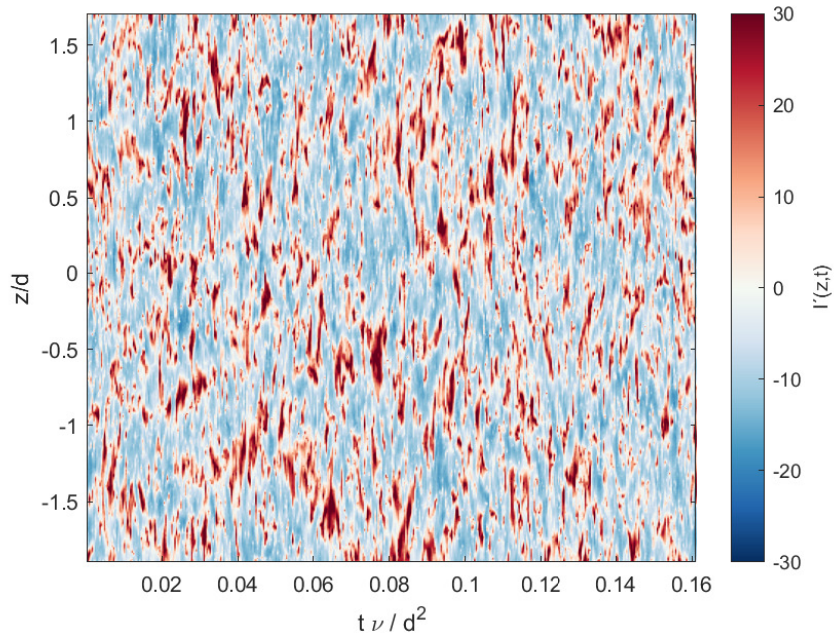


Figure 4.5: The spatial-temporal behavior of the light intensity fluctuation I' along the height of the central line. Here: turbulent spots are observed for $Re_S = 6000$ and $\mu = -0.03$.

even bigger. But surprisingly, by increasing the shear Reynolds number above a certain limit, the frequency of these patterns decreases, and the strong turbulent bursts get back to the weak turbulent burst flow observed before for a lower shear Reynolds number.

4.2.5 Axial Columnar Vortex

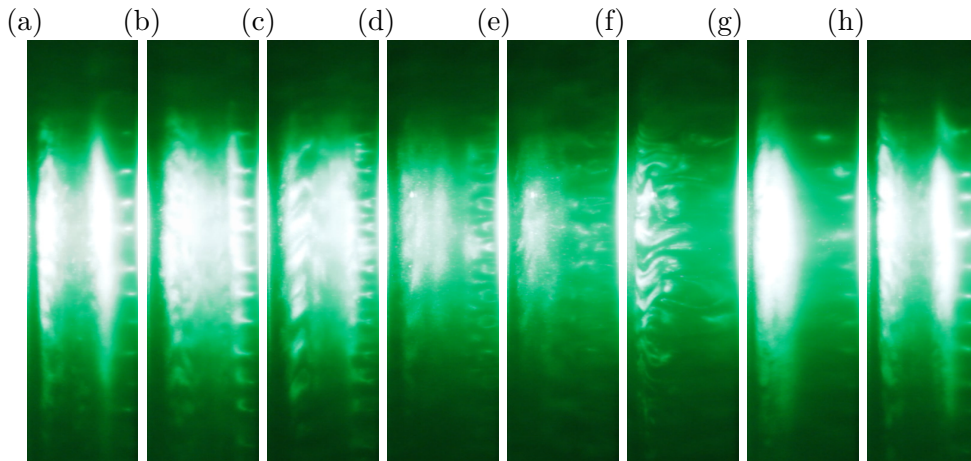


Figure 4.6: Sequence of meridional plane visualisation of Axial Columnar Vortex flow at $Re_S = 1650$, $\mu = -0.111$ for time steps: (a) 0.0 sec, (b) 0.2 sec, (c) 0.4 sec, (d) 0.6 sec, (e) 0.8 sec, (f) 1.0 sec, (g) 1.2 sec, (h) 1.4 sec. The inner cylinder wall is located at the right edge of the images, while the outer cylinder is located at the left edge.

The well-known mechanism for several large-scale circulations (e.g., TVF) to rise in the TC flow is that the system exhibits a radial outflow at one axial position, and then the fluid exhibits a radial inflow but at a different axial position due to the pressure gradient. But, in the currently studied TC flow geometry $\eta = 0.1$, a different behavior appears for very strong

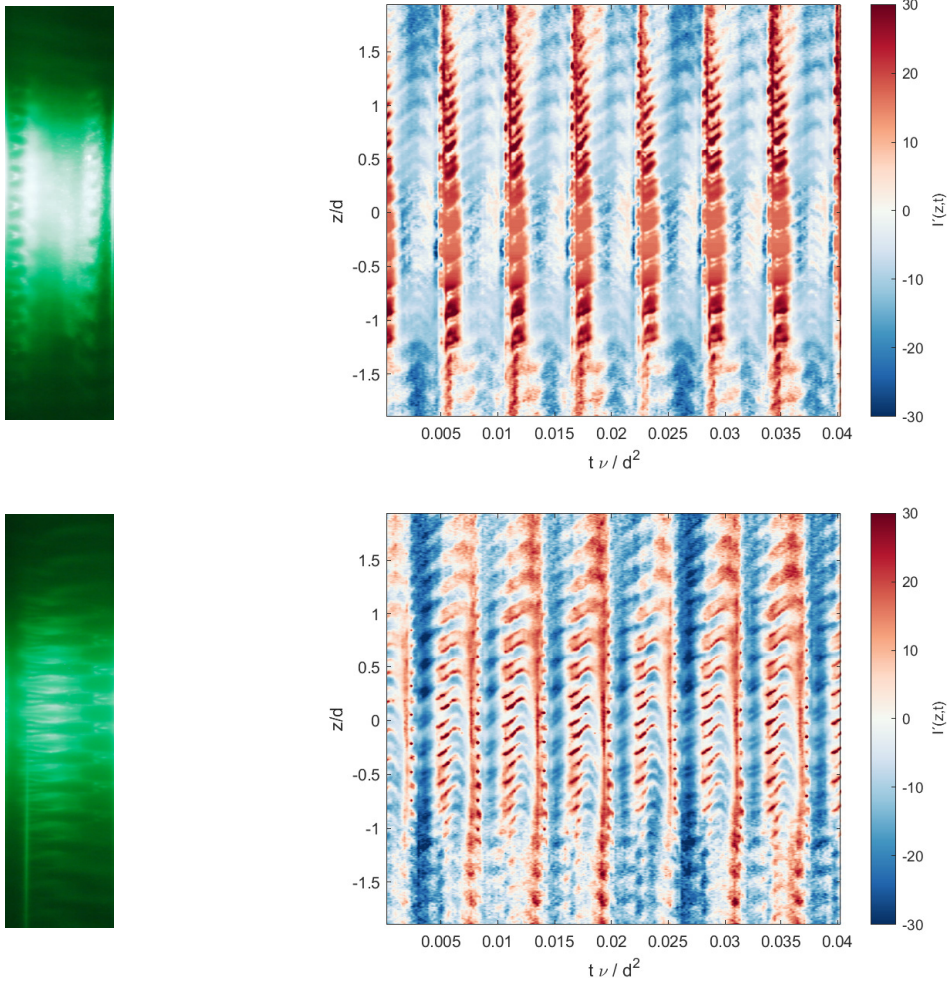


Figure 4.7: Meridional visualization image and spatial-temporal behavior of the Axial Columnar Vortex for $Re_S = 1680$ and $\mu = -0.133$. Top Figure left shows a snapshot for the pattern in the right gap side, and the bottom left shows a snapshot in the left gap side 1 sec later. Top right: Spatial-temporal behavior $5mm$ close to the outer cylinder to the right of the inner cylinder, and bottom right at location $5mm$ away on the left side from the inner cylinder corresponding to 0.08 of the gap width.

counter-rotation ratios $\mu \geq -0.06$. Due to the inner cylinder rotation, the flow next to it is accelerated, leading to radial outflow normal to the axis of rotation, at the entire height of the system. Further, when the radial out-flow reaches the outer cylinder, it is decelerated, and then an inflow takes place vertically aligned with the axis of rotation, forming with the outflow a single Axial Columnar Vortex (ACV) between the inner and outer cylinders as the sequence of meridional plane visualization images in figure 4.6 shows. The newly formed Axial Columnar Vortex starts then to rotate around the system with a fixed frequency, leading to an azimuthal mode of number 1. It is confirmed that these observed patterns are not harmonics with the system's rotation numbers, which could be caused by a slight misalignment of the Taylor-Couette apparatus. As in this case, for the same rotation ratio, the vortex speed increases linearly with the shear Reynolds number, but it also varies when μ is changed.

This kind of pattern can be clearly observed in the lab frame using global visualization, but in order to further present these patterns in the papers, meridional plane visualization is

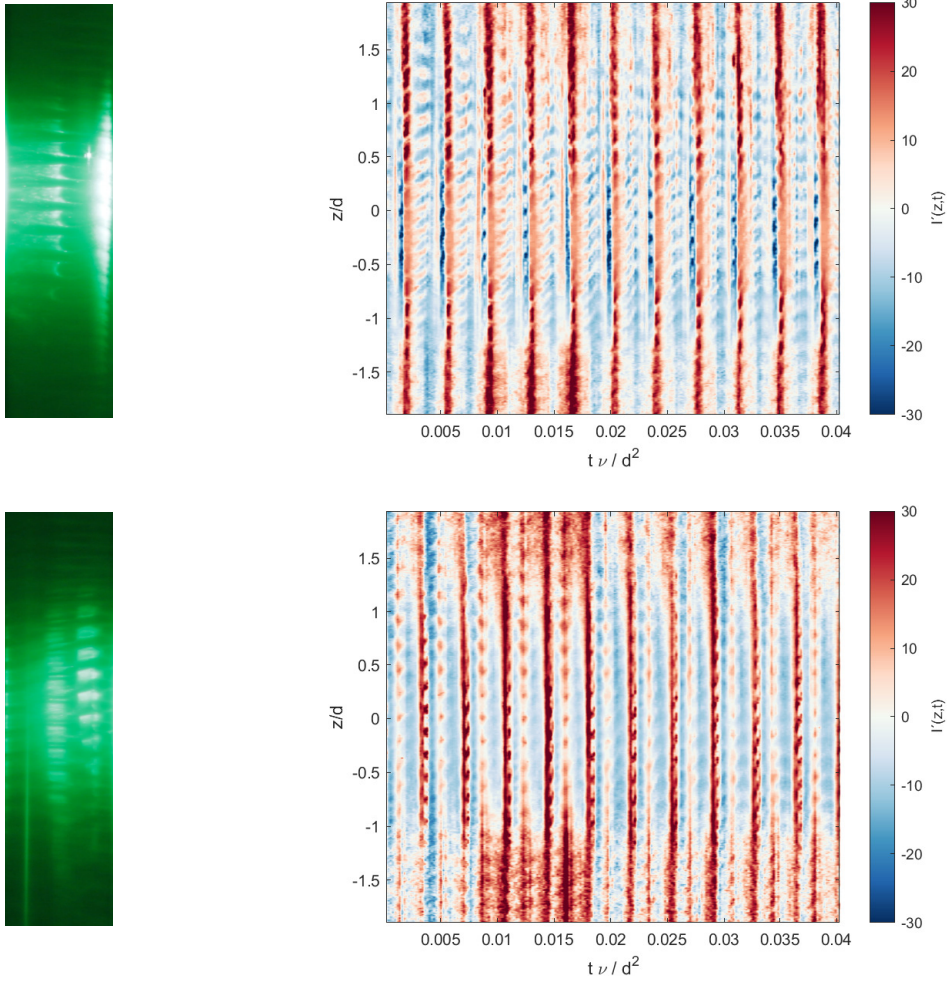


Figure 4.8: Meridional visualization image and spatial-temporal behavior of the Axial Columnar Vortex for $Re_S = 2250$ and $\mu = -0.133$. Top Figure left shows a snapshot of the pattern in the right gap side, and the bottom left shows a snapshot in the left gap side 0.48 sec later. Top right: Spatial-temporal behavior 5mm close to the outer cylinder to the right of the inner cylinder, and bottom right at location 5mm away on the left side from the inner cylinder corresponding to 0.08 of the gap width.

done, where the flow is visualized in the radial-axial plane and through the entire gap to the left and right of the inner cylinder, the same as in figure 4.1, and we looked at the flow inside the ACV. Figure 4.7 shows the spatial-temporal behavior at two positions, one to the left of the inner cylinder and next to the right. The first spatial-temporal plot shows the illumination of the particles at a distance of $0.08d = 5$ mm from the outer cylinder on the right side, while the second represents the behavior 5 mm from the inner cylinder to the left. The substructure close to the inner cylinder is strongly seen here, but much weaker next to the outer cylinder, with a remnant of the axial wave that can still be observed. Also, it can be observed from the figure how this vortex is rotating around the system, so when it appears on the cylinder's left side, it disappears from the right side, and vice versa. Furthermore, figure 4.8 shows how the vortex frequency increases by increasing the shear Reynolds number for a fixed rotation ratio. Here it is worth mentioning that, in narrow-gap TC flow $\eta = 0.917$, unsteady axially inclined vortical structures are observed for pure inner cylinder rotation [130], which appear

to have some similarity with the here observed ACV. But the main difference between the two observed structures is that the structures observed there are several unsteady inclined columnar vortices seen in a turbulent flow, while we observe a single quasi-stationary and axially aligned columnar vortex, which carries turbulent motion and alternates with a laminar backflow.

4.2.6 Helical Columnar Vortex

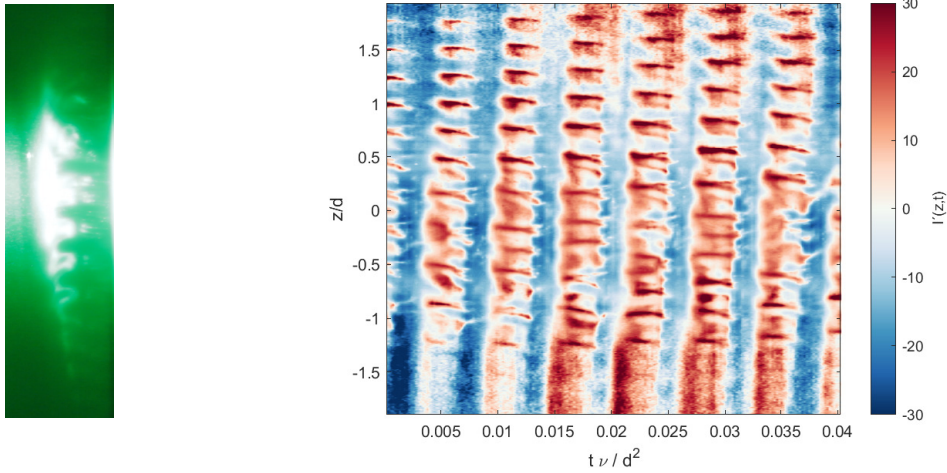


Figure 4.9: Meridional visualization image and spatial-temporal behavior of the Helical Columnar Vortex for $Re_S = 1440$ and $\mu = -0.2$ at a location 5 mm away from the inner cylinder corresponding to $0.08d$.

For further increases in the counter-rotating rates, and for a few cases where the Axial Columnar Vortex detaches from the outer cylinder and is then confined in the area next to the inner cylinder, the ACV misses its axial alignment with the axis of rotation and starts to become helical. Figure 4.9 shows a meridional visualization snapshot showing the helical shape of the vortex. Andereck et al. [18] had observed some spiral patterns in the TC geometry they studied, like spiral vortices, wavy spirals, and others; the here observed structure is not observed to be the same, but it seems to be observed only for very wide gaps in TC flows.

4.3 Regime diagram

In order to summarize the different observed patterns in this chapter for a very wide gap TC flow $\eta = 0.1$ and for $500 \leq 1.5 \times 10^4$ and a rotation ratio varying from $-0.0125 \leq \mu \leq 0$, figure 4.10 shows the phase space diagram of the different experiments done for this study. The observed structures are classified depending on the flow rotation ratio and Reynolds number; for the range of flow investigated in this chapter, we observed laminar as well as turbulent patterns, and they are all depicted in figure 4.10. In the figure, we call the turbulent bursts with low frequency "weak turbulence bursts", and the ones with high frequency "strong turbulence bursts".

It was evidenced by recent studies that multiple states and hysteresis are present in Taylor-Couette flow [132, 133, 134], which demonstrate the existence of multiple stable turbulent

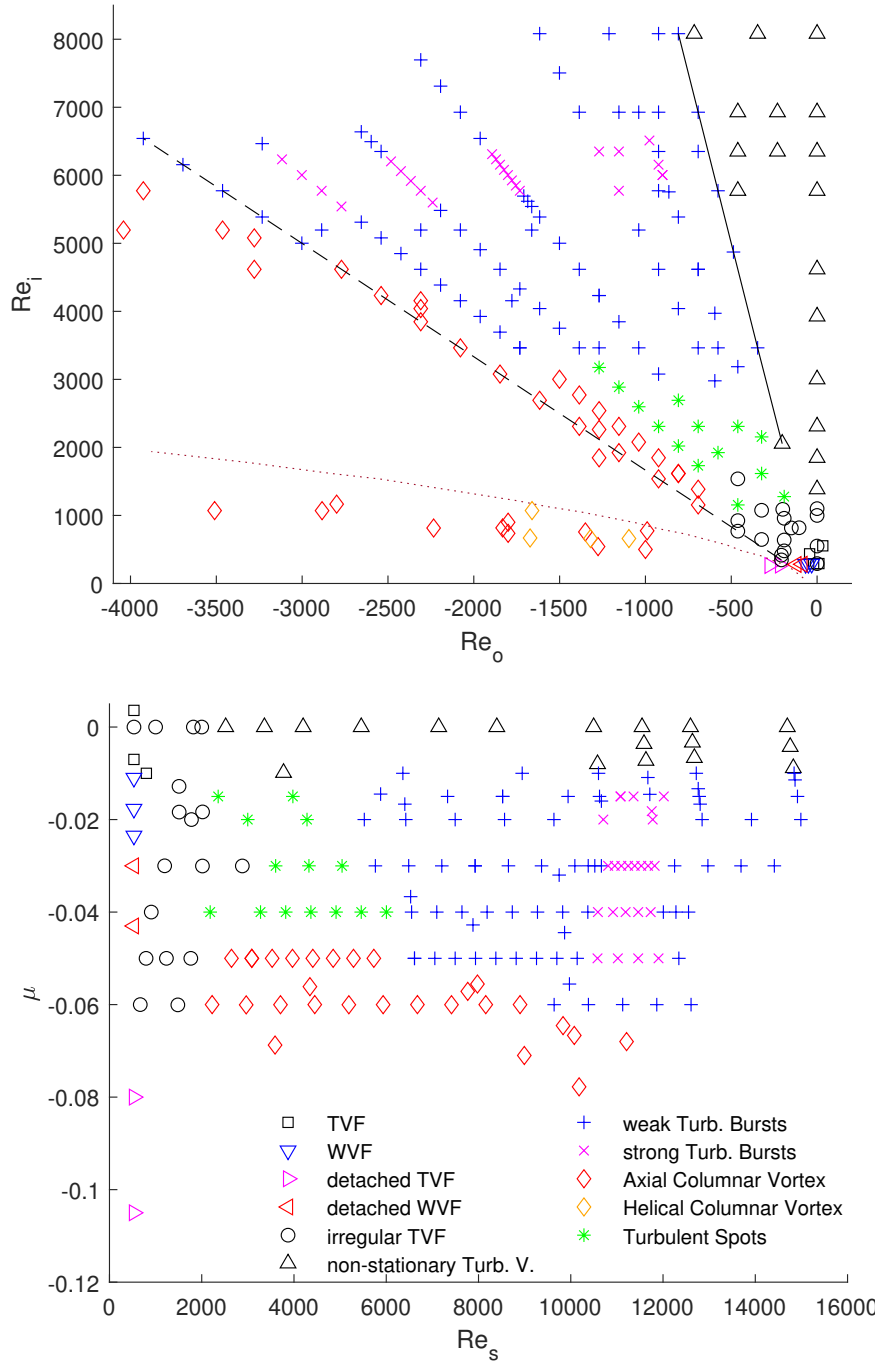


Figure 4.10: Regimes observed in flow between independently rotating cylinders at a radius ratio $\eta = 0.1$. Solid and dashed lines are for $\mu = -0.01$ and $\mu = -0.06$ respectively, and are drawn to guide the reader, the dotted line represents the stability line defined by Esser and Grossmann [131], considering the kinematic and viscous energy balance. Top: In representation of inner and outer Reynolds numbers (Re_i, Re_o). Bottom: representation using the shear Reynolds number (Re_s and the ratio of outer to inner angular velocity μ).

states in highly turbulent flows and their effect on the angular momentum transport. This study did not capture any hysteresis effects or multiple states, although different paths in the phase space were used to reach the desired rotation parameters. However, it should be noted that most flow patterns are non-stationary. Although the visualization method used can detect strong variations in the flow states, it is difficult to distinguish small changes in

axial wavelength. Therefore, we cannot rule out the possibility of multiple states existing. We suggest that due to the small inner cylinder radius, the flow's ability to show multiple states is reduced.

4.4 Conclusion

The different flow regimes in a very wide gap TC centrifugally unstable flow $\eta = 0.1$ are investigated in this chapter using visualization methods. The flow shows a clear dependence on both Re_s and μ . Some TC classical patterns appear in the flow. For very low co- and counter-rotation regimes and for $Re_s = 530$ the laminar classical TVF flow appears. For the same Re_s flow with pure inner cylinder rotation, the TVF is replaced by an irregular TVF, which varies axially through the apparatus unpredictably. At higher counter-rotating ratios, first laminar Wavy Vortex flow appears, and for further increases, the outer cylinder rotation stabilizes the flow next to it, and the TVF and WVF detach from the outer cylinder and the centrifugal unstable area is confined next to the inner cylinder. For higher shear Reynolds number flows, the transition of the flow to turbulence is observed, where for $-0.05 \leq \mu \leq -0.01$ turbulent spots appear, which disturb the laminar flow. Further increases in Re_s the frequency of these spots to increase, and turbulent bursts are then observed. A newly observed structure is investigated in this chapter, where an Axial Columnar Vortex between the inner and outer cylinders for $\mu \geq 0.06$ is observed. It is assumed that such flow pattern appears only in the very wide TC flow. Moreover, and for a few flow parameters, the ACV detaches from the outer cylinder, experiences an additional helicity, and turns into Helical Columnar Vortex flow, which is also a newly observed pattern in TC flows. For shear Reynolds number $Re_s \geq 2000$ and $0 < \mu \leq 0.012$, different turbulent flow structures appear in the flow with different scales, where the large scale structures rise and decay irregularly.

5

The turbulent flow with counter-rotating cylinders: Characteristics of the flow velocity field, and angular momentum transport.

In this chapter, the TC flow field features in the counter-rotating regime are investigated. Using high-speed Particle Image Velocimetry, the radial and the azimuthal velocity component in horizontal planes at different heights are measured for flows with different shear Reynolds numbers $20000 \leq Re_s \leq 1.31 \times 10^5$, and different rotation ratios $-0.06 \leq \mu \leq +0.008$. Moreover, the dependence of the angular momentum transport on the cylinder's rotation rate is discussed, and this dependence is further analyzed in order to study the physical explanation for the increase and decrease of the angular momentum transport at specific rotation ratios.

This chapter is organized as follows: in Section 5.1 the experimental set-up and the measurement procedure used for this study are presented. In Section 5.2 the flow field characteristics are analyzed, where the dependence of the flow velocities mean profiles on the shear Reynolds number and the rotation ratio are discussed. The position of the neutral line and the energy distribution is also studied in this section. In Section 7.3 the global response parameter, namely the angular momentum transport, is analyzed for the different studied parameters using different data analysis methods. This chapter ends with a conclusion in Section 7.4 which summarizes the main findings presented in this chapter.

The main results presented in this chapter except the results presented in 5.2.4 and 5.3.3, are part of the paper *Experimental investigation of turbulent counter-rotating Taylor-Couette flows for radius ratio $\eta = 0.1$* , by M. H. Hamede, S. Merbold and Ch. Egbers (2023), published in J. Fluid Mech. [78]. Note the text is mainly taken from the paper.

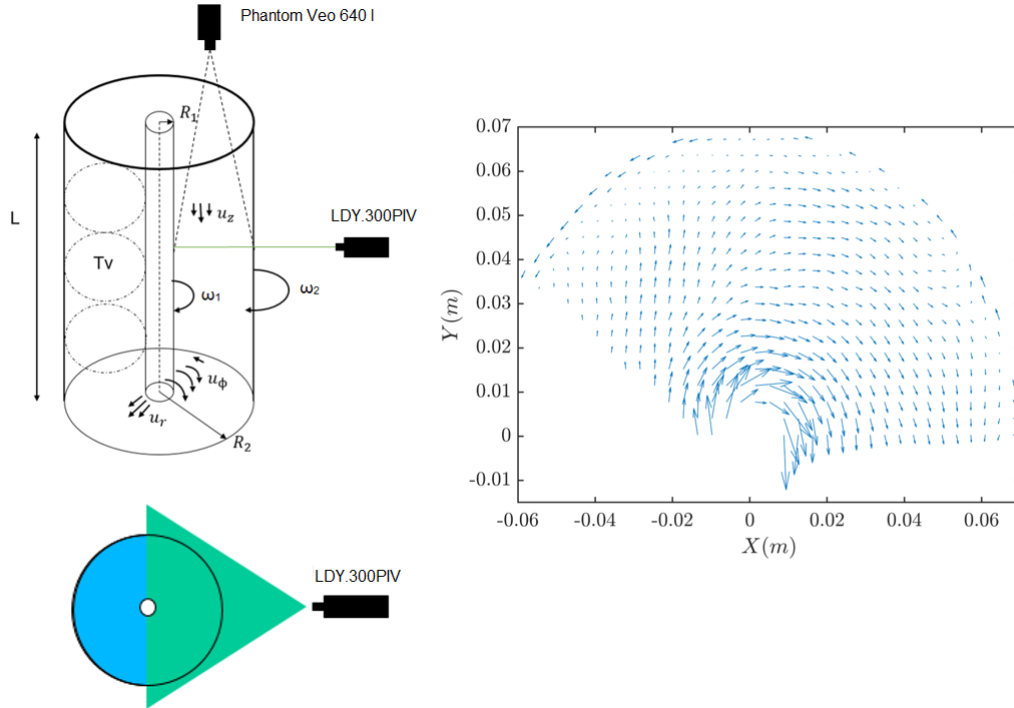
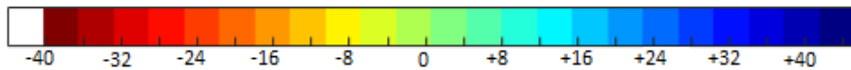


Figure 5.1: Left: Schematic of the TC apparatus with the PIV set-up, and the horizontal cross-section of the set-up with the horizontal laser sheet. Right: Mean velocity field in the azimuthal-radial plane at mid-height for $\mu = -0.007$ and $Re_s = 6.1 \times 10^4$ obtained using PIV. Every fourth vector in each row and column is plotted in this representation to improve readability.

5.1 Experimental set-up



$\Delta z(mm)$	40	28	16	0	-16	-28	-40
Scale factor (mpx^{-1}) $\times 10^{-5}$	7.139	7.316	7.505	7.750	7.993	8.177	8.378

Table 5.1: Scale factor at different heights. The colour map depicts the colours used to represent data at different heights. This representation is used in all sections of the current study.

The Top view TC - Cottbus (TvTCC) facility is used in the current study with $\eta = 0.1$ configuration. In a previous investigation using the same facility studying TC flow with different geometries $\eta = 0.357$ [36], the angular momentum transport was calculated by measuring the torque induced on the inner cylinder with the use of a torque sensor installed in the driving shaft. Unfortunately, the torque acting on the thin inner cylinder in this investigation is below the threshold for accurate measurement using this procedure ($< 2 \times 10^{-5}$ Nm). A second shaft-to-shaft torque sensor with higher sensitivity (Lorenz DR-3000) was used but did not give reliable results. Thus, the actual torque inside the $\eta = 0.1$ system is not able to be determined by the direct method, as done in the prior investigations.

The flow in the gap between both cylinders is restricted by two end plates fixed to the outer cylinders. Both the outer cylinder and the top end plate are made of acrylic glass,

enabling optical access to the flow in the gap. Figure 5.1 shows the PIV set-up used in this chapter. A Phantom VEO 640l (2560x1600 pixels) high-speed camera is mounted at the top of the apparatus, and an LDY.300PIV laser ($\lambda = 532$ nm, $P_0 = 15$ mJ) is placed beside the apparatus, the laser output is transported using a guiding arm, which generates a horizontal laser sheet through the gap as shown in the figure 5.1. The laser sheet's position is adjustable, allowing us to measure the flow velocities at different heights. This PIV set-up allows for measuring the radial (u_r) and azimuthal (u_ϕ) velocity components in the gap at different heights. Distilled water ($\nu(20^\circ C) = 10^{-6} \text{ m}^2 \text{ s}^{-1}$) is used as a working fluid. The fluid is seeded with silver-coated hollow glass spheres as tracer particles, with a mean diameter of $10 \mu\text{m}$, with Stokes number

$$St = \left(\frac{\rho_p}{\rho} - 1\right) \frac{d_p^2 u_s}{18\nu d} \quad (5.1)$$

assuming max speed of 2 m/s, $St = 1.7 \times 10^{-4}$, so $St \ll 1$. Furthermore, and considering the flow to be turbulent, the turbulent length scale $\eta_k = (\frac{\nu^3}{\epsilon})^{1/4}$ is calculated for $Re_s = 1.3 \times 10^5$, where according to [9]

$$\epsilon = \frac{2J_\omega \Delta\omega}{(r_2^2 - r_1^2)}. \quad (5.2)$$

As an assumption for the minimum length scale, a high turbulent angular momentum transport of $J_\omega = 100J_{lam}$ is estimated, with $J_{lam}^\omega = 2\nu r_1^2 r_2^2 (\omega_1 - \omega_2) / (r_2^2 - r_1^2)$. Hence, $\eta_k = 6 \times 10^{-5} \text{ m}$ is larger than the particle's mean diameter, confirming that they follow the flow precisely in all measured cases in this chapter.

We are aware of the weakness of two-dimensional (2-D) measurements in a three-dimensional (3-D) flow. But a full 3D measurement would first reduce the spatial resolution significantly [135], and add uncertainties from camera angle views. In addition, it will add calibration issues while capturing the flow through the cylindrical outer cylinder. For all the previously stated reasons, we choose to scan the volume in the third dimension to understand the axial dependence of the flow by measuring the flow in the horizontal ϕr plane at different heights. By changing the altitude of the horizontal laser sheet, the flow in the gap at different heights is measured. The measurements are done for heights between 40 mm above and 40 mm below the mid-height for $Re_s = 6.1 \times 10^4$ and 1.31×10^5 , and between 40 mm above and 90 mm below for $Re_s = 20000$. Figure 5.2(a) shows the parameters investigated in the current study. For the higher shear Reynolds number, the flow is measured at 21 different heights, with a distance of $\Delta z = 4 \text{ mm}$ between each height. While for lower Re_s , the measurements are done for 27 heights with $\Delta z = 5 \text{ mm}$ resulting in a longer range in z . Enlarging Δz is supported by previous flow visualizations, where the axial dependence is observed to be less. The camera is mounted at a fixed height, so by adjusting the height of the laser sheet, the camera lens needs to be refocused to capture the flow at the desired height. Refocusing the camera lens at each height leads to different spatial resolutions for the different heights, as shown in table 5.1.

For $Re_s = 20000$, the measurements are done for 7 seconds with 200 frames per second, which comes out with 1400 PIV images at each height. For the higher Re_s , the measurement time is increased to 10 seconds to better capture the temporal behavior of the flow, using the

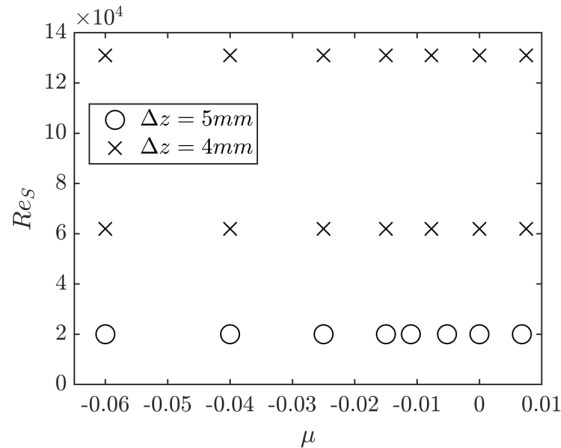


Figure 5.2: The investigated parameter space in terms of Re_s and μ .

same frame rate, which comes out with 2000 PIV images for each height. The single frame mode is used, as the time between every two consecutive images is $\Delta t = 0.005$ sec, which suits the displacement for the velocities of the experiment. Furthermore, the Kolmogorov micro time scale $\tau_K = (\nu/\epsilon)^{1/2}$ for the maximum investigated turbulent case $Re_s = 1.3 \times 10^5$, and by assuming a maximum $J_\omega = 25J_{lam}$ (c.f. figure 5.10), computes to $\tau_K = 0.00733$. As $\tau_K > \Delta t$, it is ensured that the measured data is time resolved. The PIV images are post-processed using LaVision Davis software. The velocities are calculated using an adaptive PIV algorithm, with the final interrogation area (IA) being 24×24 pixels with 50% overlap. The velocity data are transformed using MATLAB 2019b to a polar coordinate velocity (u_ϕ, u_r) and interpolated onto a polar grid of concentric cylinders of fixed radii r . After this interpolation, the data matrices at each instantaneous time are reorganized in such a way that all the data belonging to the same radial position are presented in one column, and for the different radial positions, the data has been presented in the same azimuthal domain.

The circumference of the inner cylinder is 10 times smaller than the outer cylinder. Thus, the spatial number of azimuthal samples in the radial position close to the inner cylinder is 10 times less than that for the radial position close to the outer cylinder. This can be a source of uncertainty for any statistical analysis, but the number of temporal samples (2000 images or 1400 images) for each measurement set can compensate for this uncertainty. Another source of uncertainty might be the calibration error. For the calibration, the same procedure used in [24] is used in the current study. For further details about the calibration procedure, the reader is referred to [101].

During the measurements, the fluid temperature rises up to 2 K, as every measurement set of 21 or 27 heights takes between 1.5 and 2 hours to be performed. During the measurements, the inner cylinder is rotating at high speed, which heats up the bearings and causes an increase in the fluid temperature. In order to solve this problem, the fluid temperature inside the gap is continuously measured using a temperature sensor, and for every rise in temperature, the velocity of the rotating cylinders is adjusted so that the dimensionless parameters (Re_s, μ) are guaranteed to be constant for every single measurement set.

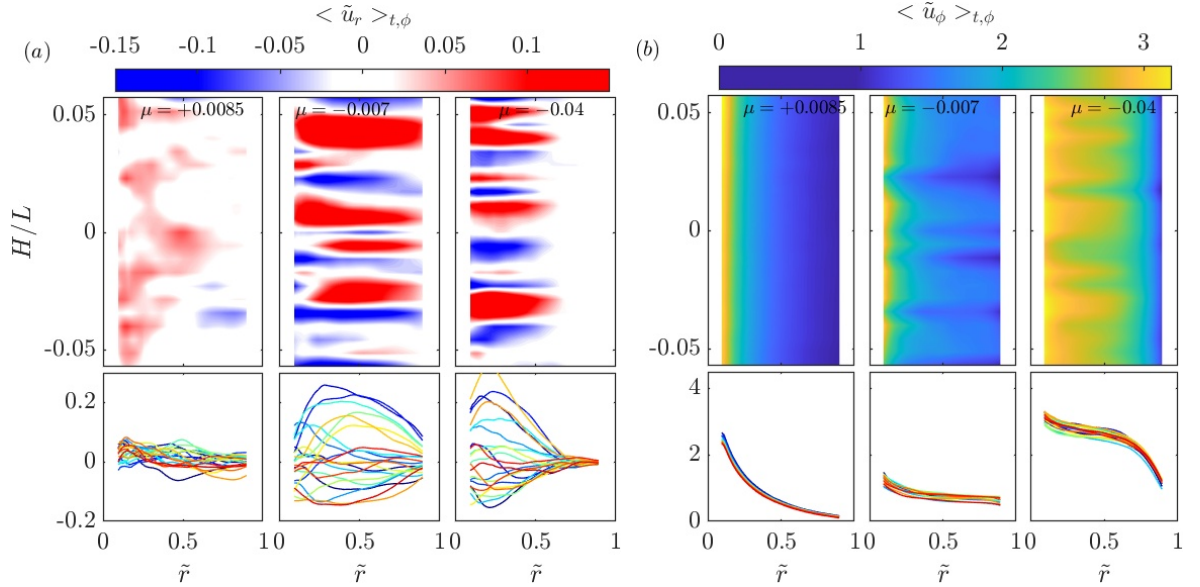


Figure 5.3: Contour plots and velocity profiles showing the dependence of the normalized temporally and azimuthally, (a) radial velocity \tilde{u}_r , (b) azimuthal velocity \tilde{u}_ϕ components. Profiles are plotted for 21 different heights for $Re_s = 6.1 \times 10^4$ and the rotation ratios $\mu = +0.0085, -0.007, -0.04$. Colours represent positions according to Table 5.1

5.2 Flow Field Features

5.2.1 Dependence of the flow structures on the rotation ratio.

Different flow parameters control the flow inside the TC apparatus; one of these main parameters is the rotation ratio $\mu = \omega_2/\omega_1$. Concerning the rotation ratio, the flow can be distinguished into three regimes: pure inner cylinder rotation ($\mu = 0$), counter-rotation ($\mu < 0$) and co-rotation ($\mu > 0$). Figure 5.3 shows the contour plots and velocity profiles for the azimuthally and temporally averaged normalized radial $\tilde{u}_r = u_r/u_s$, and azimuthal $\tilde{u}_\phi = (u_\phi - u_{\phi,2})/u_s$ velocities with

$$u_s = \frac{2}{1+\eta} |\eta u_{\phi,2} - u_{\phi,1}|, \quad u_{\phi,2} = \omega_2 r_2, \quad u_{\phi,1} = \omega_1 r_1 \quad (5.3)$$

for a shear Reynolds number $Re_s = 6.1 \times 10^4$ and rotation ratios $\mu = +0.0085, -0.007, -0.04$, for 21 different heights, 10 heights above the apparatus mid-height and 10 below.

The radial coordinate used in the different figures is the dimensionless gap position $\tilde{r} = (r - r_1)/(r_2 - r_1)$, so for $(r = r_1)$, $\tilde{r} = 0$ and, for $(r = r_2)$, $\tilde{r} = 1$. For $\mu = +0.0085$, where the outer cylinder co-rotates with the inner cylinder, the normalized time and azimuthally averaged radial velocity are mostly zero along all heights throughout the gap, with only a very weak outflow near the inner cylinder. On the other hand, the azimuthal velocity component changes noticeably with the radial position, where the velocity profile of the 21 height collapses into one line. Going to the second flow regime, the counter-rotating regime, and starting with the low counter-rotation $\mu = -0.007$, a significant difference compared with the previous case is observed, where the radial velocity shows a clear variation along the different heights, and

inflow and outflow regions exist. These inflow and outflow regions can be a fingerprint of a rotating pattern in the gap, like those observed by [24], but in the present case these regions are axially short measured in the radial dimension. The axial wavelength of classical and turbulent TV is usually in the order of $L \approx 2d$ (i.e. for $\eta = 0.5$ in [24]), while here we observe an axial wavelength of $L \approx 0.43d$. Thus, the observed flow structures are strongly elliptical, and in contrast to classical vortical patterns, they are better described as interlaced fingers of inflow and outflow. In these inflow and outflow regions, the angular momentum is transported strongly across the gap, as shown in section 5.3.1. For $\mu = -0.007$, the azimuthal velocity is nearly independent of the height, and like the previous case, the velocity profiles of the 21 height collapse into one line. However, the profiles show a small decrease near the inner cylinder and depict a flat profile with the smallest gradient in the bulk and near the outer cylinder. By increasing further the counter-rotation rate, the angular momentum induced by the outer cylinder stabilizes the flow near the outer cylinder (see figure 5.3, $\mu = -0.04$). Near the outer cylinder \tilde{u}_r is mostly zero, while close to the inner cylinder, it shows the same behavior as in the $\mu = -0.007$ case. In other words, the axial dependence of the profiles here is restricted to the inner part of the gap, where the magnitude of the radial velocity does not decrease compared with the $\mu = -0.007$ case. These results show a difference between the very wide gap TC flow studied here and the geometries studied previously, where [24] found, for $\eta = 0.5$, that the magnitude of the radial velocity component decreases significantly when the axial variation of the flow is limited near the inner cylinder. In contrast to the radial velocity, the azimuthal velocity shows a weak axial dependency in the bulk, but it varies near the inner and outer boundaries along the heights. The different flow regimes observed in the currently studied TC geometry are presented and discussed in detail in [19].

5.2.2 Averaged velocity profiles

Given the general overview of the dependence of the flow organization on the rotation rates in the previous section, and to better understand the influence of the rotation ratio μ and the shear Reynolds number (Re_s) on the flow, the temporal and spatial averaged (t, ϕ, z) radial profiles of the normalized angular velocity $\tilde{\omega} = (\omega - \omega_2)/(\omega_1 - \omega_2)$ with $\omega = u_\phi/r$, and the normalized angular momentum $\tilde{L} = (L - L_2)/(L_1 - L_2)$ with $L = r^2\omega = u_\phi r$ are analysed, where the angular velocity ω is the transported quantity in TC flow (see [9]).

As the scope of our study is to understand the behavior of the bulk, all profiles are studied for the radial positions in the range of $0.1 < \tilde{r} < 0.9$. The thin boundary layers at the cylinder walls are not well resolved while measuring the flow in the entire gap. The thickness of the boundary layers and the boundaries of the bulk are difficult to define. In particular for very wide gap geometries, a big difference between the thickness of the inner boundary layer (λ_i) and the outer boundary layer (λ_o) is expected, as estimated by [9], where they derived $\lambda_i/\lambda_o \approx \eta^3$ and, for $\eta = 0.1$, it computes to 10^{-3} . Also, the different measurements in this chapter are done for high shear Reynolds numbers, which reduces the size of the boundary layers additionally. For $\eta = 0.5$, [24] assumed that the effect of boundary layers is negligible in the radial positions between $0.1 \leq \tilde{r} \leq 0.9$ and, therefore, assumed this range to be fully dominated by the bulk flow. For the wider gap, even thinner boundary layers are expected,

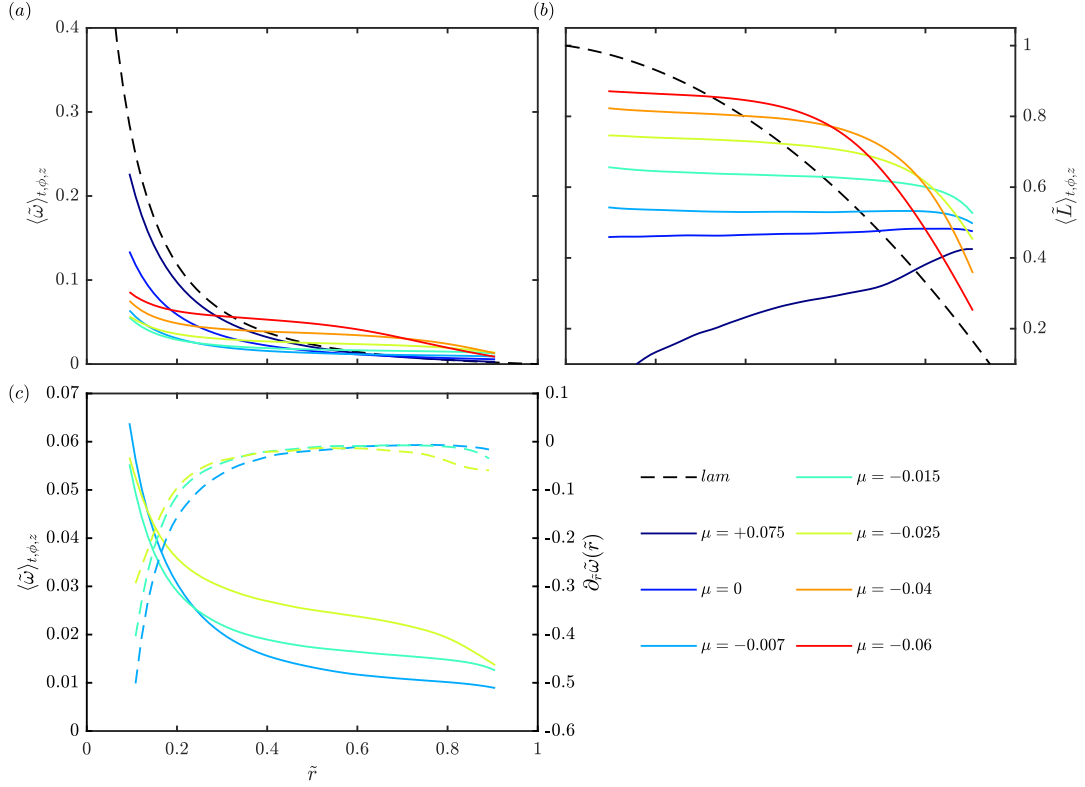


Figure 5.4: Radial Profiles of spatially and temporally averaged (t, ϕ, z) normalized angular velocity $\tilde{\omega}$ (a) and normalized angular momentum \tilde{L} (b) for $Re_s = 6.1 \times 10^4$ and different rotation ratios μ . The dashed line in (a,b) denotes the corresponding laminar profile (c.f. equations 5.6, 5.7). (c) Magnification for $\tilde{\omega}$ -profiles, and the radial gradient of $\tilde{\omega}(\tilde{r})$, for $\mu = -0.007, -0.015, -0.025$.

so it can be assumed that both the inner and outer boundary layers are not represented in the limits of $0.1 \leq \tilde{r} \leq 0.9$.

Analysing the dependency of $\omega(r)$ profiles on the driving parameters Re_s and μ is useful to understand how transport takes place in the flow. The profiles can be compared with the laminar circular Couette solution of the Navier-Stokes equation (for $\eta = 0.1$), which is given by

$$\omega_{lam}(r) = A + \frac{B}{r^2}, \quad L_{lam}(r) = Ar^2 + B \quad (5.4)$$

$$A = -\omega_1 \frac{\eta^2 - \mu}{1 - \eta^2}, \quad B = \omega_1 r_1^2 \frac{1 - \mu}{1 - \eta^2}. \quad (5.5)$$

The laminar profile is normalized like the measured profiles, so it becomes independent of the cylinder speeds: thus,

$$\tilde{\omega}_{lam}(r) = \frac{1}{1 - \eta^2} \left(\left(\frac{r_1}{r} \right)^2 - \eta^2 \right) \quad (5.6)$$

$$\tilde{L}_{lam}(r) = \frac{1}{1 - \eta^2} \left(1 - \left(\frac{r}{r_2} \right)^2 \right) \quad (5.7)$$

Finally, the influence of the rotation rate on the averaged flow properties is depicted in Figure 5.4. The temporal, azimuthal and axial averaged angular velocity profiles are given

5. The mean velocity field characteristics, and angular momentum transport.

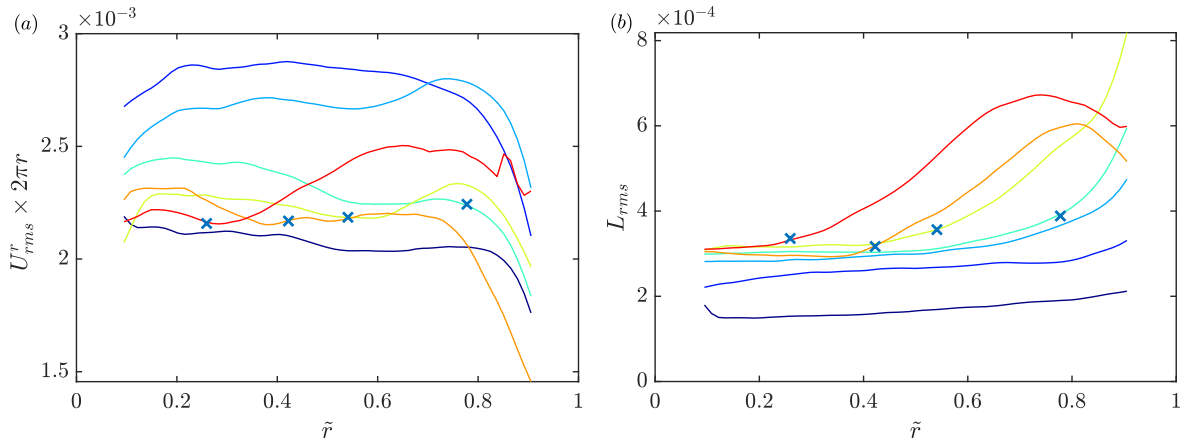


Figure 5.5: Radial profiles of spatially and temporally averaged (t, ϕ, z) root mean square (r.m.s.) of (a) the radial velocity fluctuation multiplied by $2\pi r$, and (b) angular momentum fluctuation, for different rotation ratios and $Re_s = 6.1 \times 10^4$. The crosses indicate the radial position of the neutral surface presented in figure 5.7. The legends used in this figure are the same as in figure 5.4.

in figure 5.4(a) for $Re_s = 6.1 \times 10^4$ and for the rotation ratio $-0.06 \leq \mu \leq +0.008$, where the laminar profile is also plotted for comparison. The profile related to the co-rotating regime approximately follows the laminar profile quite well, but the profiles deviate from the laminar profile for pure inner rotation and counter-rotation. The profiles tend to become flatter in the bulk flow until the gradient is lowest around $-0.015 \leq \mu \leq -0.007$. For higher counter-rotation, the profiles are shifted to higher $\tilde{\omega}$ near the inner boundaries.

Figure 5.4(b) shows the corresponding profiles of the normalized angular momentum (\tilde{L}) for the same driving parameters. In the presentation of \tilde{L} one has to consider that $(L_1 - L_2)$ differs a lot with μ , especially close to the Rayleigh stable area, where it tends to be zero, resulting in \tilde{L} being large. The behavior of the angular momentum across the gap for the co-rotation case shows a unique behavior compared with the other studied cases, where $\langle \tilde{L} \rangle_{t,\phi,z}$ has a positive slope varying through \tilde{r} . For weak counter-rotating cases, the profiles are flat in the bulk with different values, but as the counter-rotation increases, the flat radial profiles of $\langle \tilde{L} \rangle_{t,\phi,z}$ exhibit a strong negative slope starting from a specific radial position, and the position of this inflection point moves toward the inner part of the gap as the counter-rotation increases. The position of this inflection point can be related to the position of the neutral line, which will be discussed in detail in 5.2.3.

Figure 5.5 shows the radial profile of the fluctuation intensity, measured by the root mean square (r.m.s.), of the radial velocity multiplied by $2\pi r$ and the angular momentum (L) r.m.s. for different rotation ratios. The r.m.s. is calculated for the value $U = u - \langle u \rangle_t$. According to the incompressibility condition, a radial inflow or outflow decreases in magnitude with the circumference. We compensate for this for better readability of the graph by multiplying U_{rms}^r by $2\pi r$. Thus, in the case of a radially confined inflow and outflow region, where the mass flux in the radial direction is constant (like a large-scale circulation or time-dependent oscillations), the profile experiences a flat behavior and $2\pi r U_{rms}^r$ quantifies the strength of the radial fluctuations. Figure 5.5(a) shows these radial profiles of U_{rms}^r by $2\pi r$ for different

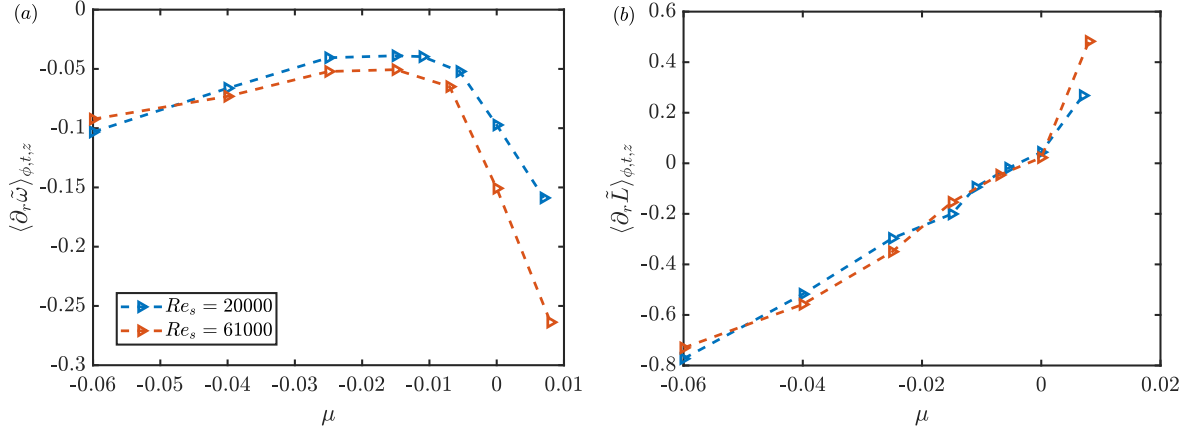


Figure 5.6: (a) Normalized radial gradient of angular velocity profiles as a function of μ , (b) Normalized radial gradient of angular momentum profiles as a function of μ . Blue and orange triangles represent the results of $Re_s = 20000$ and $Re_s = 6.1 \times 10^4$ for different rotation ratios, respectively

rotation ratios. For $\mu = +0.007, 0$ and -0.007 , the profile is almost flat in the bulk, whereas $\mu = 0$ and -0.007 experience higher values across the gap. For the stronger counter-rotating cases, the profiles show a different behavior, where the fluctuation profile experiences two different plateaus and a transition region in between. Inside the bulk flow close to the inner cylinder, the strength of the radial fluctuations quantified by $2\pi r U_{rms}^r$ is observed to be less compared with the strength of the radial fluctuations of the flow close to the outer cylinder. The radial position where the behavior changes from the inner region to the transient region coincides approximately with the neutral surface, as determined in figure 5.7 (the radial position where the azimuthal velocity vanishes). The same can be said about the angular momentum fluctuation (L_{rms}) shown in figure 5.5(b), where the profiles for $\mu = +0.007, 0$ and -0.007 are mostly flat in the bulk, while for higher counter-rotation ratios they are flat until they reach the radial position of the neutral velocity (no mean angular momentum). Furthermore, in the outer part of the gap the angular momentum fluctuation increases toward a strong maximum. At the cylinder walls, the fluctuation has to be zero due to the no-slip boundary condition.

To focus more on the counter-rotating regimes with low rotation ratio, where the angular momentum transport is expected to increase and achieve a maximum, and which will be proven and discussed in detail in 5.3.1, figure 5.4(c) shows the radial profile of $\langle \tilde{\omega} \rangle_{t,\phi,z}$ and $\partial_{\tilde{r}} \tilde{\omega}(\tilde{r})$ for $\mu = -0.007, -0.015$ and -0.025 to have a close look at the angular velocity gradient. All three cases show the lowest gradient in the centre of the bulk compared with the other cases, but for $\mu = -0.025$ case, a more negative slope is observed compared with both $\mu = -0.007$ and $\mu = -0.015$ cases, also, $\mu = -0.007$ has a clear increase in gradient in the inner region. Inspecting the radial profile of the radial gradient of $\tilde{\omega}(\tilde{r})$, one can clearly observe this low gradient in the bulk, where at $0.6 \leq \tilde{r} \leq 0.8$ the value of $\partial_{\tilde{r}} \tilde{\omega}(\tilde{r})$ for $\mu = -0.007$ and $\mu = -0.015$ is mostly zero, which means that at these radial positions $\langle \tilde{\omega} \rangle_{t,\phi,z}$ is constant.

To further quantify the smallest gradient of the $\langle \tilde{\omega} \rangle_{t,\phi,z}$ in the bulk, the gradient is calculated along $0.1 < \tilde{r} < 0.9$. The gradient is directly evaluated from the velocity profiles.

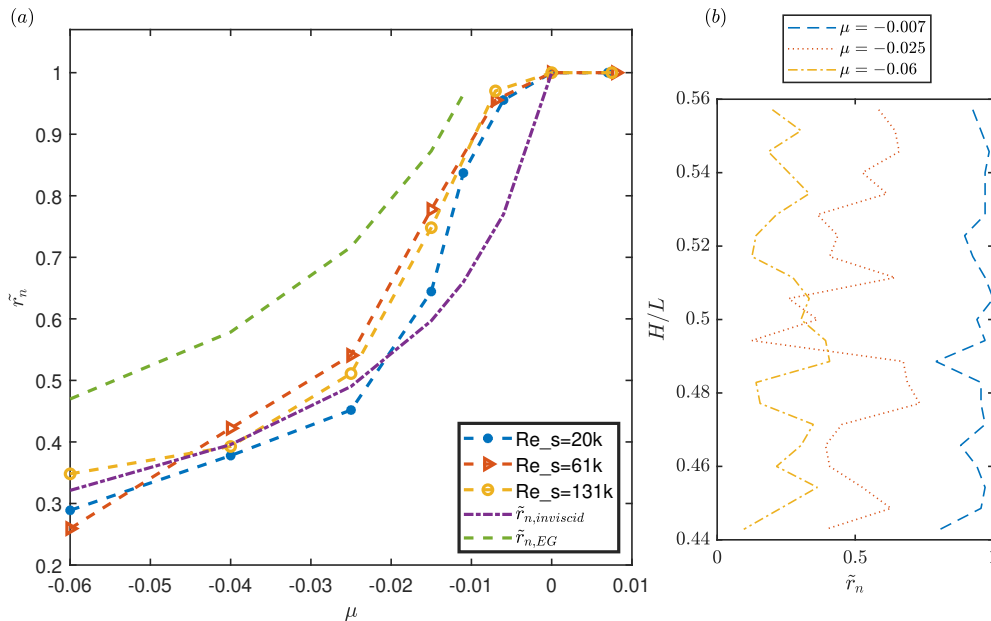


Figure 5.7: (a) Normalized neutral surface \tilde{r}_n as a function of the rotation ratio μ for $Re_s = 20000$ (blue), $Re_s = 6.1 \times 10^4$ (red) and $Re_s = 1.31 \times 10^5$ (yellow). (b) The radial position of the neutral surface at different heights for $Re_s = 6.1 \times 10^4$ and $\mu = -0.007, -0.025, -0.06$.

The normalized radial gradient of angular velocity shown in figure 5.6(a) is negative for all rotation ratios and for both Re_s . Both curves in the figure show the smallest value of gradient for $-0.02 \leq \mu \leq -0.007$, and the increase in gradient magnitude depends on the Re_s . Figure 5.6(b) shows the radial gradient of the $\langle \tilde{L} \rangle_{t, \phi, z}$ in the bulk, where also the $\langle \tilde{L} \rangle_{t, \phi, z}$ exhibits the smallest radial gradient for low counter-rotating cases. The two curves shown in both figures are related to two different experiments with different shear Reynolds numbers; however, both curves show the same behavior but with slightly different values. Thus, it is shown that the gradient values are more dependent on the rotation ratio than on the shear Reynolds number.

5.2.3 Neutral surface

The neutral surface is defined as the radial location in the gap where the azimuthal velocity component u_ϕ vanishes. The velocity profile and particularly the azimuthal velocity (u_ϕ) profile give access to finding the radial position of the neutral surface by detecting the position where the mean azimuthal velocity changes its direction (sign).

The neutral surface exists just for counter-rotating cases, and it coincides with the outer cylinder for pure inner cylinder rotation, while for the co-rotating cases, the neutral surface is not defined as both cylinders are rotating in the same direction. This surface indicates the division between the stable and unstable regions and implies a detachment of the unstable flow for any $\mu < 0$. In the stable region any perturbation to the azimuthal flow decay is directly damped by the mean azimuthal flow, where the radial position of the neutral surface (r_n) is defined according to [27] as

$$r_{n, inv}(\mu) = r_1 \sqrt{\frac{1 - \mu}{\eta^2 - \mu}}. \quad (5.8)$$

But experiments and viscous calculations show that large-scale circulation (LSC) patterns can extend beyond this neutral surface when counter-rotation sets in. [131] deduced from their stability calculation, a prediction for the vortex extension called $r_{n,EG}$, and that flow structures emerge in the neutral surface by a factor of $a(\eta)$

$$r_{n,EG}(\mu) = r_1 + a(\eta)(r_{n,inv} - r_1) \quad ; \quad a(\eta) = (1 - \eta) \left[\sqrt{\frac{(1 + \eta)^3}{2(1 + 3\eta)}} - \eta \right]^{-1}. \quad (5.9)$$

Due to the extension of the secondary flow to the outer cylinder wall, intermittency evolves, causing radial inhomogeneity inside the gap. The onset of the intermittency was used by [47] to predict the parameter of the torque maximum and was experimentally validated by [21] and [24] for $\eta = 0.5$, and [36] for $\eta = 0.357$. Figure 5.7(a) shows the position of the normalized neutral line for the three different shear Reynolds numbers, and for the different rotation ratios studied in the current study. The curves are depicted together with the two predictions introduced above. For the three curves shown in figure 5.7, it is clear that the neutral line does not exist for all experiments with $(0 \leq \mu)$ as mentioned above. The detachment of the neutral line from the outer cylinder started for the low counter-rotation cases. The position of the detachment point for the different Re_s did not converge with either of the two predictions, and this can be explained by the patterns, which do not fill the entire gap as they do in the observations by [24, 46, 132]. These results differ in the flow in the very wide gap ($\eta = 0.1$) in contrast to TC flow in narrower geometries. As an example, [24] and [47] showed that the detachment of the neutral line from the outer wall was well predicted by the prediction of [131] for $\eta = 0.5$ and $\eta = 0.71$ respectively. It is clear in the very wide gap geometry studied here that the detachment of the neutral line starts once the outer cylinder is set in counter-rotation. The outer cylinder radius is 10 times larger than the inner one in the TC geometry used in the current study; this can explain the ability of the outer cylinder rotation to stabilize the unstable fluid next to it once it is set to rotation, although at very low rates, as shown in 5.7(a) for $\mu = -0.0077$. For higher counter-rotating cases, the observed neutral position coincides with the prediction of the inviscid fluids.

Figure 5.7(b) shows how the position of the neutral surface depends on the height. Here the deviation of the neutral position with height is observed, which is caused by the difference in the secondary flow (u_r, u_z where only u_r is measured) between the different heights. Figure 5.3 shows the alternating strong inflow and outflow for the measured heights. Also from figure 5.7(b) it can be observed that the \tilde{r}_n profile has a certain kind of periodicity over the different heights for the presented rotation ratios. The variation of \tilde{r}_n along the different heights is the highest for $\mu = -0.025$. The low value of the variation of \tilde{r}_n for $\mu = -0.007$ can be returned to the fact that the neutral line is just beginning to detach, where in some heights it is shown that the position of the neutral line is still attached to the outer cylinder. For $\mu = -0.06$ small axial variation is also observed due to the stabilization effect of the rotation of the outer cylinder, so the unstable region is confined near the inner cylinder.

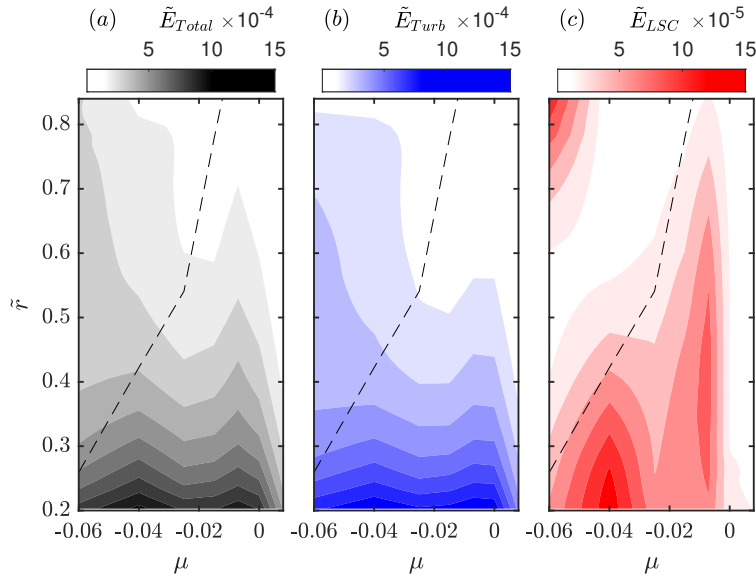


Figure 5.8: Contour plots of the axially, azimuthally and temporally averaged, normalized energy as a function of the normalized radius \tilde{r} and the rotation ratio μ at shear Reynolds number $Re_s = 6.1 \times 10^4$. The dashed line represents the radial position of the neutral line for the different μ

5.2.4 Energy distribution

To get a better understanding of the influence of the different parameters (Re_s and μ) on the flow, the kinetic energy is calculated and compared for the different cases. The flow is decomposed into Large scale and turbulent contributions according to [47]

$$\mathbf{u} = \langle \mathbf{u} \rangle_{\phi,t} + \mathbf{u}' = \bar{\mathbf{u}} + \mathbf{u}' \quad (5.10)$$

with u' the turbulent fluctuations and \bar{u} the temporal-averaged velocity. Using this decomposition, the averaged kinetic energy is calculated as follows:

$$E_{kin}(r) = \frac{1}{2} \langle \bar{u}_\phi^2 + \bar{u}_r^2 + \bar{u}_z^2 + u_\phi'^2 + u_r'^2 + u_z'^2 + 2u'_r \bar{u}_r + 2u'_\phi \bar{u}_\phi + 2u'_z \bar{u}_z \rangle_{t,\phi,z}. \quad (5.11)$$

The mixed terms vanish, in addition to the velocity axial component u_z which was not measured as the measurements in this study take place in the $r\phi$, so we have to neglect the u_z component (cf. [24, 136]). The term \bar{u}_ϕ represents the mean base flow in the gap, and it is the dominant term. To reveal the underlying flow structure, this energy portion is neglected, as done by [24]. The remaining terms from equation 5.11 can be decomposed into the two contributions, which are defined as the large-scale circulation energy E_{LSC} and the turbulent energy E_{Turb} :

$$E_{LSC}(r) : \frac{1}{2} \langle \bar{u}_r^2 \rangle_{t,\phi,z}, \quad E_{Turb}(r) : \frac{1}{2} \langle u_r'^2 + u_\phi'^2 \rangle_{t,\phi,z} \quad (5.12)$$

This averaged Energy are then normalized by the shear velocity energy E_s as $\tilde{E} = E/E_s$, with $E_s = u_s^2/2$.

The figures 5.8 and 5.9 show the contour plots of the values of both energy contributions as a function of the normalized radius \tilde{r} and rotation ratio μ for two different shear Reynolds

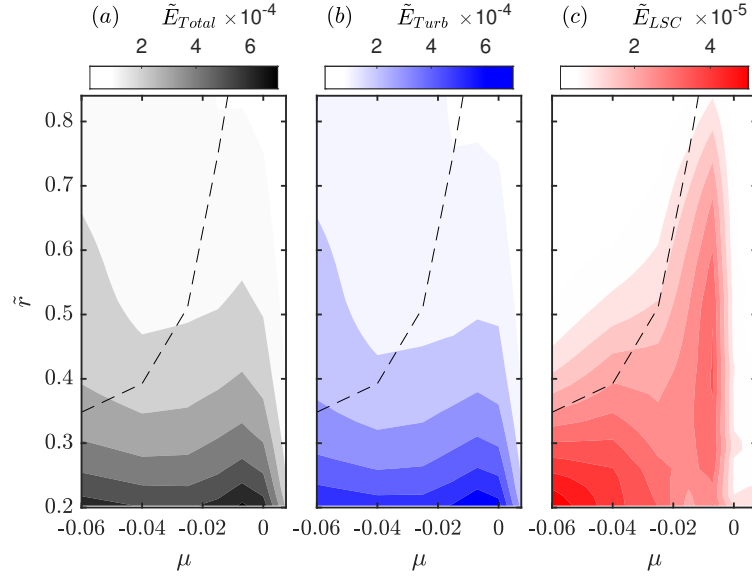


Figure 5.9: Contour plots of the axially, azimuthally and temporally averaged, normalized energy as a function of the normalized radius \tilde{r} and the rotation ratio μ at shear Reynolds number $Re_s = 1.31 \times 10^5$. The dashed line represents the radial position of the neutral line for the different μ .

number flows $Re_s = 6.1 \times 10^4$ and $Re_s = 1.31 \times 10^5$, respectively. The two contributions are summed to $E_{Total} = E_{LSC} + E_{Turb}$. In both figures, the dashed line is used to represent the radial position of the neutral line. For both shear Reynolds numbers, the same behavior is observed. Starting with LSC contribution, the energy is minimum for the co-rotating cases for both Re_s flows, then a small increase takes place for the pure inner cylinder rotating case ($\mu = 0$). The E_{LSC} shows a clear increase for the lowest counter-rotating case ($\mu = -0.007$), where it is observed that the high energy is distributed all over the inner region and the bulk, while it decreases in the outer region. For the higher counter-rotating cases, where the detachment of the neutral line from the outer cylinder starts, as one can observe from the dashed lines in the figures, the high E_{LSC} values were successfully maintained in the regions below the neutral line. E_{LSC} shows a maximum in magnitude at $\mu = -0.04$ for $Re_s = 6.1 \times 10^4$ and at $\mu = -0.06$ for $Re_s = 1.31 \times 10^5$. This high magnitude of energy can explain the high magnitude of the in-out flow of the radial velocity component u_r , as shown in figure 5.3 for $\mu = -0.4$, where this in-out flow is concentrated in the inner region. It is clear in all cases how E_{LSC} is the minimum above the neutral surface, as the flow in this region is stabilized by the outer cylinder rotation and the radial velocity reaches the minimum.

Similar to how E_{LSC} shows the same behavior for the different Re_s flows, the turbulent energy E_{Turb} shows the same behavior for $Re_s = 6.1 \times 10^4$ and $Re_s = 1.31 \times 10^5$ flows. But its behavior is completely different compared to E_{LSC} , where it varies slightly with respect to the different rotation rate; the higher values are always in the inner region while in the outer region we observe minimum values. The magnitude of the E_{Turb} decreases as the radial position gets farther from the inner region, but we can observe higher magnitudes for rotation ratios of $\mu \leq 0$.

It is clear from both figures that the E_{Turb} has the dominant contribution to the total energy E_{Total} compared with E_{LSC} , this dominance decreases as the shear Reynolds number

decreases, as can be observed from the color maps in both figures 5.8 and 5.9. So that for $Re_s = 6.1 \times 10^4$, although E_{Turb} still has the dominant contribution in E_{Total} , the ratio of E_{Turb}/E_{LSC} is less compared with that for $Re_s = 1.31 \times 10^5$. This change with respect to shear Reynolds number can be explained as: for low Re_s the u_r is less turbulent than for a higher shear Reynolds number, where it gets more turbulent, and this directly affects the E_{LSC} contribution to E_{Total} . Also, we can observe that the magnitude of the normalized averaged total \tilde{E}_{Total} energy decreases as the shear Reynolds number increases; this can be returned to the reason of neglecting the axial velocity u_z . So for lower shear Reynolds, the contribution of the axial velocity to the total energy in the system is less compared with the flow with higher Re_s , so we can assume that the error reflected from vanishing u_z in the energy equation is less influential for a lower shear Reynolds number as its contribution to the total energy is lesser.

5.3 Angular momentum transport

5.3.1 The Nusselt number

Beforehand, the flow field dependence on the different parameters, like the shear Reynolds number Re_s and the rotation ratio μ , is shown. In this section the angular momentum current J^ω is analysed in terms of the Nusselt number. The angular momentum transport is the conserved transport quantity in TC flow, and it is defined according to the Eckhardt–Grossmann–Lohse (EGL) [9] theory, by J_ω 1.2. At the cylinder walls, $\langle u_r \omega \rangle_{A(r),t}$ vanishes, and J^ω results from the friction exhibited to the walls and can be directly measured by the torque acting on the cylinders. In previous studies on various radius ratios, this has been determined by measuring the torque at the cylinders, while in this study the torque is too small for an accurate measurement system. In this chapter, J^ω is calculated using the velocity field measured by PIV. The measure of the angular momentum transport is then defined by the quasi-Nusselt number:

$$Nu_\omega = \frac{J^\omega}{J_{lam}^\omega} \quad (5.13)$$

where $J_{lam}^\omega = 2\nu r_1^2 r_2^2 (\omega_1 - \omega_2) / (r_2^2 - r_1^2)$ results from the laminar Couette solution 5.6.

According to the theory derived by EGL the transverse current of azimuthal motion J_ω is constant over all radii. Figure 5.10(a) shows the measured Nusselt number radial profiles $Nu_\omega(\tilde{r})$ for different rotation rates and $Re_s = 1.31 \times 10^5$ normalized by its radial average. It can be observed that the radial profiles in the radial range $\tilde{r} \in [0.2, 0.7]$ scatter around 1, in the limits between [0.85 1.15], which is considered to be in good agreement with the definition of the independence of the angular momentum flux on the radial position. Although the profiles are not exactly flat, it should be taken into consideration that these results are calculated from PIV measurements, where spatial resolution limitations always exist. It remains part of the uncertainty when studying the angular transport in this study that not all small scales are resolved. Another uncertainty is the instantaneous LSC, which is not covered by the current measurements and may also influence the results. However, an axial domain up to 2d

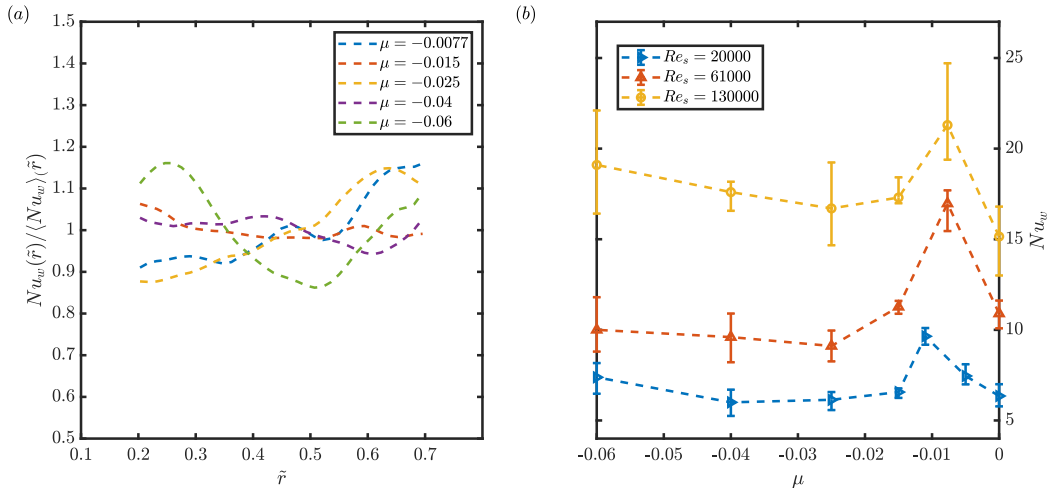


Figure 5.10: (a) The quotient of the Nusselt number radial profiles over its average in the radial range for different rotation rates μ , at a fixed shear Reynolds number $Re_S = 1.31 \times 10^5$. (b) The variation of the radial averaged Nusselt number Nu_{ω}^{Total} as a function of μ for different shear Reynolds numbers.

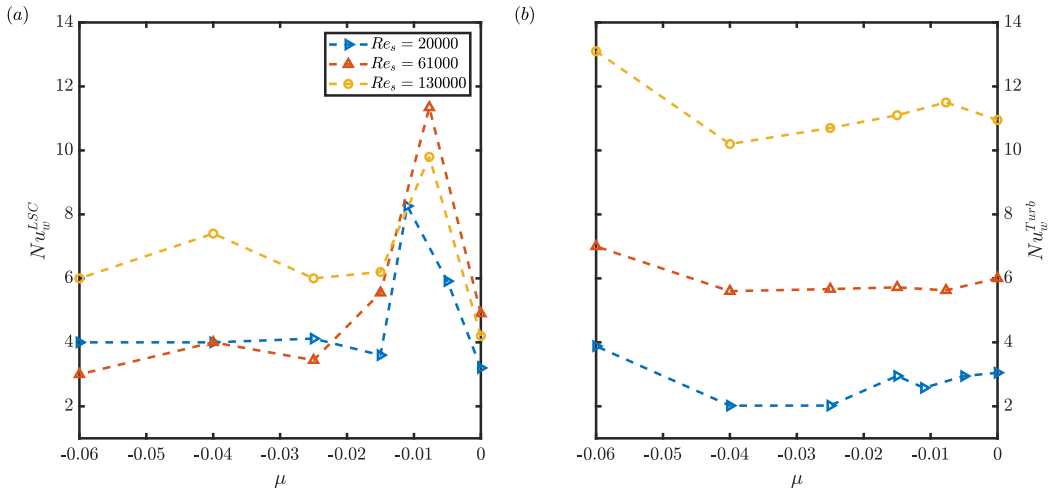


Figure 5.11: The Nusselt number Nu_{ω} is decomposed into its large-scale contribution (Nu_{ω}^{LSC}) and turbulent contribution (Nu_{ω}^{Turb}) (a) Radial averaged Nusselt number large-scale contribution (Nu_{ω}^{LSC}), (b) radial averaged Nusselt number turbulent contribution (Nu_{ω}^{Turb}) as a function of μ , for different shear Reynolds numbers.

5. The mean velocity field characteristics, and angular momentum transport.

is covered by our measurements, and figure 5.3 shows the existence of an LSC of size $\approx 0.43d$, which indicates that the axial dependence of the flow is mostly covered by our measurements, and it can be concluded that the influence of not covering the instantaneous LSC is small. To further improve the certainty of LSC, a 3-D measurement would be a solution. But besides the difficulty of collecting the necessary equipment for such measurement methods (several high-speed and highly resolved cameras and optical equipment plus a new high-power light source), the 3-D measurements reduce the resolution of small-scale fluctuations significantly and, as a result, reduce spatial resolution drastically ([135]). On the other hand, if a method is used to resolve small scales by the use of magnification, the LSC will not be covered. Taking all these factors into consideration and having a measurement method that covers the largest possible variety of flow scales, the angular momentum transport in this chapter is measured using a method already validated by [24] using the same TC facility but with a different radius ratio $\eta = 0.5$, where it shows very high accuracy. The Nu_ω is calculated at all gap radial positions, although the angular momentum transport can be calculated by measuring the azimuthal and radial velocities at a singular point, as done by [70] and [53] when studying the wide gap TC geometry $\eta = 0.35$, using the 2-D LDV method. But in order to enhance the certainty through statistics, the transport was calculated at the different gap radial positions and averaged across the bulk area. As close to the cylinder walls, the boundary layer will increase small-scale fluctuations induced in the shear, which are not resolved by the used method. Thus, an averaging interval of Nu_ω in the radial range $\tilde{r} \in [0.2, 0.7]$ is used to ensure higher accuracy.

The dependence of the Nusselt number Nu_ω on both the rotation ratio and the shear Reynolds number is studied in figure 5.10(b), where the variation of the radial averaged Nusselt number is plotted for three different Re_s values ($Re_s = 20000, 6.1 \times 10^4$ and 1.31×10^5) with respect to different rotation rates in the counter-rotating regime. The uncertainty bars in the figure show the maximum and minimum values of Nu_ω in the radial domain $0.2 < \tilde{r} < 0.7$, where $Nu_\omega(\tilde{r})$ is radially averaged. Using the measured Nu_ω a separation is defined, so the counter-rotating rates with $-0.012 \leq \mu \leq 0$ are named low counter-rotating regimes, $-0.025 \leq \mu \leq -0.015$ are named moderate counter-rotating regimes and, for $\mu \leq -0.04$, high counter-rotating regimes. However, when the low counter-rotating cases in the current study are compared with other studies with different radius ratios, we are not comparing the exact values of μ between both studies but we are comparing the different regimes according to the Nusselt behavior.

From the presented Nu_ω in figure 5.10(b), first a common behavior between the different studied cases with different Re_s is observed, where it is obvious that Nu_ω achieves its maximum value in the area of low counter-rotation. So for $Re_s = 20000$, the rotation ratio where the Nu_ω achieved its maximum value is determined at $\mu_{max} = -0.011$. While for $Re_s = 6.1 \times 10^4$ and $Re_s = 1.31 \times 10^5$, the maximum value of Nu_ω is determined at $\mu_{max} = -0.0075$. In this chapter, as the PIV measurements are used to calculate the Nusselt number, we are not able to calculate Nu_ω at very large range of μ so we can determine an exact value for μ_{max} . As an example, for $Re_s = 1.31 \times 10^5, 6.1 \times 10^4$ the flow in the low counter-rotating regime for rotation ratios $\mu = -0.0075, -0.015$ is measured, where it shows $\mu_{max} = -0.0075$.

For $Re_s = 20000$, and for the same regime, the rotation ratios $\mu = -0.006, -0.011, -0.015$ are measured, and it shows $\mu_{max} = -0.011$. So a general conclusion can be drawn from the studied cases, that μ_{max} is determined for rotation ratios between $-0.012 \leq \mu_{max} \leq -0.007$. From previous works like those done by Merbold et al. (2013) and Froitzheim et al. (2017) and then by Froitzheim et al. (2019b), the maximum μ_{max} was found to be $\mu_{max} = -0.2 \pm 0.02$ for $\eta = 0.5$ and $\mu_{max} = -0.123 \pm 0.03$ for $\eta = 0.357$, respectively, which showed that μ_{max} is shifted toward less counter-rotating values for wider gaps.

From previous works like those done by Merbold et al. [21] and Froitzheim et al. [24] and then by Froitzheim et al. (2019b) [36] the maximum μ_{max} was found to be $\mu_{max} = -0.2 \pm 0.02$ for $\eta = 0.5$ and $\mu_{max} = -0.123 \pm 0.03$ for $\eta = 0.357$, respectively, which showed that μ_{max} is shifted toward less counter-rotating values for wider gaps. The results of the current study support this idea too. Another observation is investigated here, which agrees with the results for $\eta = 0.5$ and $\eta = 0.357$, that at μ_{max} the normalized radial gradient angular velocity profiles achieve minimum through the bulk, as shown in figure 5.6(a), where it is clear for both curves related to $Re_s = 20000$ and $Re_s = 6.1 \times 10^4$ that the minimum gradient is in the area of $-0.0077 \leq \mu \leq -0.015$, where μ_{max} lies in this domain. The results show a common behavior with the previous studies done for narrower gaps, where they showed that as the counter-rotation is increased beyond the maximum $\mu < \mu_{max}$, the value of the Nusselt number decreases. This is explained by the fact that the rotation of the outer cylinder stabilizes the flow in the outer region, and the enhanced LSC cannot fill the entire gap width, so the transport is suppressed. But in huge contrast to the results achieved for $\eta \geq 0.357$, in the current study we observe from figure 5.10(b) that Nu_ω first decreases for $\mu < \mu_{max}$, but then it achieves a minimum μ_{min} , and by increasing the counter-rotation further $\mu < \mu_{min}$ the Nu_ω tends to increase again.

The results show a dependence between the position of μ_{min} and the shear Reynolds number. As Re_s increases, the position of μ_{min} shifts toward the low counter-rotating regime. So for $Re_s = 20000$, $\mu_{min} = -0.04$ is found, and for $Re_s = 6.1 \times 10^4$, $\mu_{min} = -0.025$, while for $Re_s = 1.31 \times 10^5$, μ_{min} can not be exactly determined. However, it is clear that it exists for $-0.025 < \mu < -0.015$. While μ_{max} is independent of Re_s , the minimum μ_{min} shows a clear dependence on the shear Reynolds number. As a conclusion, the angular momentum transport shows a maximum at low counter-rotating regimes, and a second maximum is expected for higher counter-rotating regimes, as at infinite counter-rotation one can assume a pure outer cylinder rotation with a low Nu_ω . This behavior is in contrast to what is reported for TC flows with $\eta \leq 0.9$ where the maximum of angular momentum transport is found at one defined rotation ratio, where it is accompanied by the strengthening of the large-scale structures, which is also the case here for the first maximum.

A similar double maxima behavior of the angular momentum transport observed for the currently studied TC geometry is observed on the extreme opposite side of the TC geometry, the very narrow gaps ($\eta > 0.91$) ([41, 42]) and the rotating plane Couette flow (RPC) ([43, 44]), where for such geometries, they reported the existence of two Nu_ω maxima at different rotation rates. The first maximum, or what they called “the broad peak”, was accompanied by the strengthening of the large-scale structures and a second maximum, “the narrow peak”,

5. The mean velocity field characteristics, and angular momentum transport.

which is a consequence of shear instabilities. The first maximum observed in all TC geometries ($0.1 \leq \eta \leq 0.98$) and RPC flows can be attributed to the same reason, the strengthening of the large-scale structures. But, concerning the second expected maximum observed in the current study for $\eta = 0.1$ and the narrow peak, it is hard to assume that both these peaks are a consequence of the same instability. In addition, [42] shows that as the driving of the system varies, the broad peak remains roughly at the same rotation ratio, which is in agreement with what is observed in the current study for the first Nu_w maximum. On the second hand, they show that the narrow peak position is dependent on the driving rate, which can also be the case for the second expected maximum. In this chapter, as it is observed here that μ_{min} is Re_s dependent, which can lead the position of the second maximum to be Re_s dependent too.

In order to further understand the behavior of the Nusselt number with the different parameters (Re_s and μ), the flow velocity field is decomposed according to [47] as shown in equation 5.10, and the decomposed velocity field is used in order to decompose the Nusselt number into two values, one related to the mean large-scale contribution (Nu_w^{LSC}) and the second related to the turbulent contribution (Nu_w^{Turb}). So that the Nusselt number reads

$$Nu_w = Nu_w^{LSC} + Nu_w^{Turb} \quad (5.14)$$

With

$$Nu_w^{Turb} = J_{lam}^{-1} \left\langle r^3 \langle u'_r \omega' \rangle_{A(r,t)} \right\rangle_r \quad (5.15)$$

$$Nu_w^{LSC} = J_{lam}^{-1} \left\langle r^3 \left(\langle \bar{u}_r \bar{\omega} \rangle_{A(r,t)} - \nu \partial_r \langle \bar{\omega} \rangle_{A(r,t)} \right) \right\rangle_r. \quad (5.16)$$

Where the mixed terms $\langle \bar{u}_r \omega' \rangle_{A(r,t)}$ and $\langle \bar{\omega}_r u'_r \rangle_{A(r,t)}$ vanish (cf. [24]). Also, $\partial_r \langle \omega' \rangle_{A(r,t)}$ vanishes as they are all linear in the deviation quantities [47].

In Figure 5.11 the variation of both contributions of the Nusselt number as a function of Re_s and μ is studied. Figure 5.11(a) shows the radial averaged Nusselt number large-scale contribution Nu_w^{LSC} as a function of μ and Re_s . For $Re_s = 20000, 6.1 \times 10^4$ and 1.31×10^5 , the Nu_w^{LSC} shows the highest value at μ_{max} (which is in agreement with the previous investigation ([24])), where the large-scale circulation enhances the angular momentum transport. Then Nu_w^{LSC} decreases for stronger counter-rotation as the detachment of the neutral line from the outer wall starts, so the circular patterns are more pushed toward the inner region of the gap, which leads to a decrease in the Nusselt number. Figure 5.11(a) shows that Nu_w^{LSC} decreases for $\mu < \mu_{max}$ until it reaches a level where the contribution of Nu_w^{LSC} varies weakly with the rotation rate and tends to be independent of the rotation rates. Figure 5.7(a) shows how the position of the neutral line changes for higher counter-rotating flows. These findings are in strong contrast to what is investigated for $\eta = 0.5$ and $\eta = 0.357$, where it is shown that Nu_w^{LSC} decreases for higher counter-rotating cases.

It is important to also understand the contribution of turbulence to global transport, quantified by the value Nu_w^{Turb} . Figure 5.11(b) shows the radial averaged turbulent contribution to the Nusselt number Nu_w^{Turb} as a function of μ and Re_s . The Nu_w^{Turb} shows a small variation in the values along the different low counter-rotating cases for constant

Re_s , but a clear increase for the high counter-rotation case. As a comparison between figure 5.11(a) and (b), for $Re_s = 20000$, it is shown that the contribution of Nu_ω^{LSC} in the Nu_ω^{Total} is dominant in contrast to Nu_ω^{Turb} , while for $Re_s = 6.1 \times 10^4$, the contributions are mostly equal and, finally, for $Re_s = 1.31 \times 10^5$, the contribution of Nu_ω^{Turb} has increased much more than that of Nu_ω^{LSC} . So it can be stated that as the shear Reynolds number increases, the intensity of the turbulent contribution in the flow increases strongly, while the Nu_ω^{LSC} is increasing only slightly with Re_s .

5.3.2 Spatial and temporal behavior of the shear stress

Figures 5.12, 5.13, and 5.14 show the space-time diagram of the shear stress component ωu_r , multiplied by r^3 and divided by J_{lam} for different rotation ratios in the $\phi - t$ plane for $Re_s = 6.1 \times 10^4$. For each rotation ratio, the space-time diagram is considered for the different measured axial positions, but as they show mostly the same behavior and for simplicity, one axial height is selected for representation, where the selected height $r^3(u_r, \omega)$ has the highest intensity compared with other heights. Understanding the spatial-temporal behavior will also give us the opportunity to compare and reveal the influence of the rotation ratio on the shear stress and angular momentum transport. The figures depict the contour plot of the space-time diagram at five radial positions distributed along the gap. The top subfigures belong to radial positions close to the inner cylinder, and the bottom sub-figures belong to radial positions close to the outer cylinder. It is noteworthy that the range of ϕ is kept constant for this representation, which has a strongly increasing circumferential length $r\phi$ as the radius increases.

Equation 1.2 can be separated into two terms: the first term represents the convective term $r^3 \langle u_r \omega \rangle_{A(r),t}$ and the second represents the viscous term $r^3 \nu \partial_r \langle \omega \rangle_{A(r),t}$. In the bulk flow where our analysis takes place, the convective term is the dominant term, as the contribution of the viscous term did not exceed 5% of the total J_ω in the bulk. For the stated reason, $r^3(u_r, \omega)$ is chosen for the comparison between the different experiments with different rotation ratios. Furthermore, $r^3(u_r, \omega)$ is divided by J_{lam} so the values can then be compared with the values in figure 5.10. The space-time evolution of $r^3(u_r, \omega)/J_{lam}$ is analysed in detail (figures 5.12, 5.13 and 5.14) as it is the main contributor to the Nu_ω when averaged over $\langle \rangle_{A(r),t}$, which is represented by the depiction in the $\phi - t$ plane.

From the underlying data, the effort is to study the existence of travelling patterns through the gap, and in the case of their existence, to see their intensity and the direction of propagation. Inspecting the time-space behavior leads to an understanding of how turbulent structures behave throughout the gap and quantifies the transported angular momentum. So for the shown figures, the red and blue spots are considered to be related to a propagating pattern, which can be a LSC down to a small-scale turbulent pattern that travels through the gap. Red patterns represent shear stresses that transport angular momentum outwards (positive), while blue patterns transport momentum in the opposite direction.

Starting with the pure inner cylinder rotating case, figure 5.12(a) shows the existence of propagating patterns with a short time scale. The last is deduced from the thickness of the red positive transporting patterns in the time axis, which is relatively small. The existence

5. The mean velocity field characteristics, and angular momentum transport.

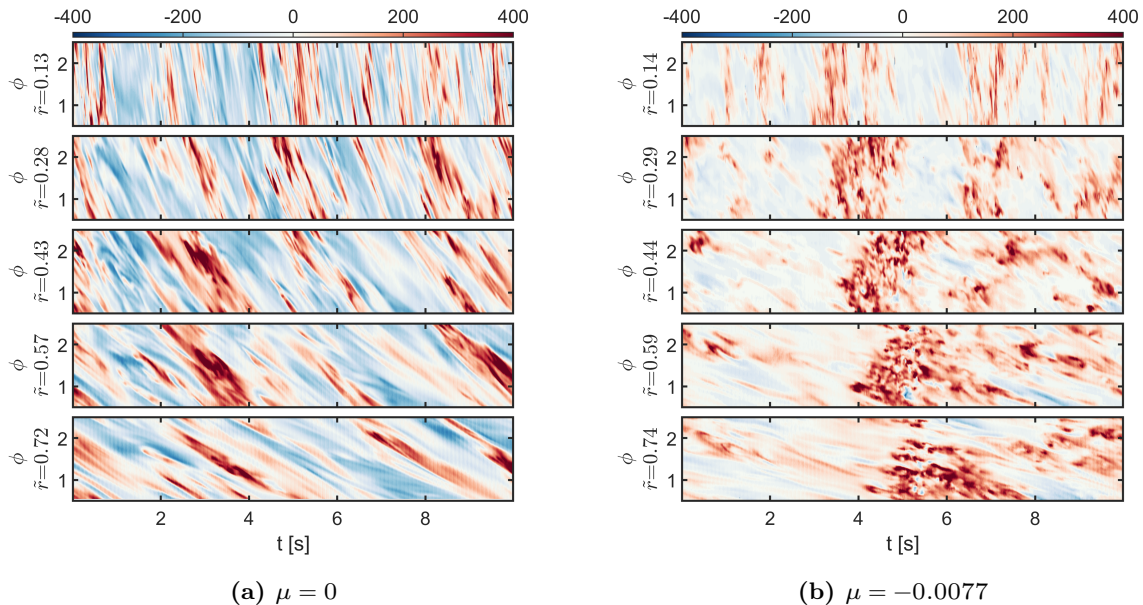


Figure 5.12: Contour plot showing the space-time diagram of $r^3(\omega u_r)/J_{lam}$ in the azimuthal-time plane, for five different radial positions, at a) $\Delta z = +12$ mm, b) $\Delta z = +4$ mm from apparatus mid-height, for $Re_s = 6.1 \times 10^4$ for pure inner cylinder and low counter-rotating cases. The top figure is a radial position close to the inner cylinder, and the bottom figure is close to the outer cylinder. Results are shown for (a) $\mu = 0$ and (b) $\mu = -0.0077$.

of these patterns with short lifetimes can explain the moderate contribution of Nu_ω^{LSC} in Nu_ω^{Total} shown in figure 5.11(a). When the outer cylinder is set to rotate slightly in the opposite direction of the inner cylinder rotation, different behavior is observed. The positive spots, which are related to the travelling patterns, appear in the flow, but with a longer lifetime than the one we detected for $\mu = 0$. Figure 5.12(b) shows the space-time diagram of $r^3(u_r \omega)$ for $\mu = -0.0077$, where the maximum Nusselt number is found (see Section 4). The patterns here can explain this maximum value of the Nusselt number. The existence of patterns with high intensity and long lifetime enhance the transport procedure of angular momentum, so that the Nu_ω^{LSC} contribution to Nu_ω^{Total} is the maximum at this rotation ratio compared with other rotation ratios. In contrast to $\mu = 0$, here the huge and long-lasting positive patterns increase the angular momentum transport, and fewer structures of negative transport can be identified.

By increasing the rotation rate of the outer cylinder in the counter direction, the patterns exist with a long lifetime, but in contrast to the $\mu = -0.0077$ case, the intensity of these patterns decreases. Figure 5.13(a) and (b), show the space-time diagram of $r^3(u_r \omega)$ at $\mu = -0.015$ and $\mu = -0.025$, respectively. Here it is observed how the intensity of these patterns decreases from $\mu = -0.0077$ to $\mu = -0.015$ and then decrease more for $\mu = -0.025$, especially in the radius position near the outer region, which is explained by the stabilizing effect of the outer cylinder rotation. The decrease of the pattern's intensity in these cases causes a decrease in the contribution of Nu_ω^{LSC} to Nu_ω^{Total} , which leads to a decrease in the total value of Nu_ω as shown in figure 5.10.

The dependence of the Nusselt number on the rotation ratio is studied in figures 5.10 and 5.11, where the results show an increase in the value of the Nusselt number for higher

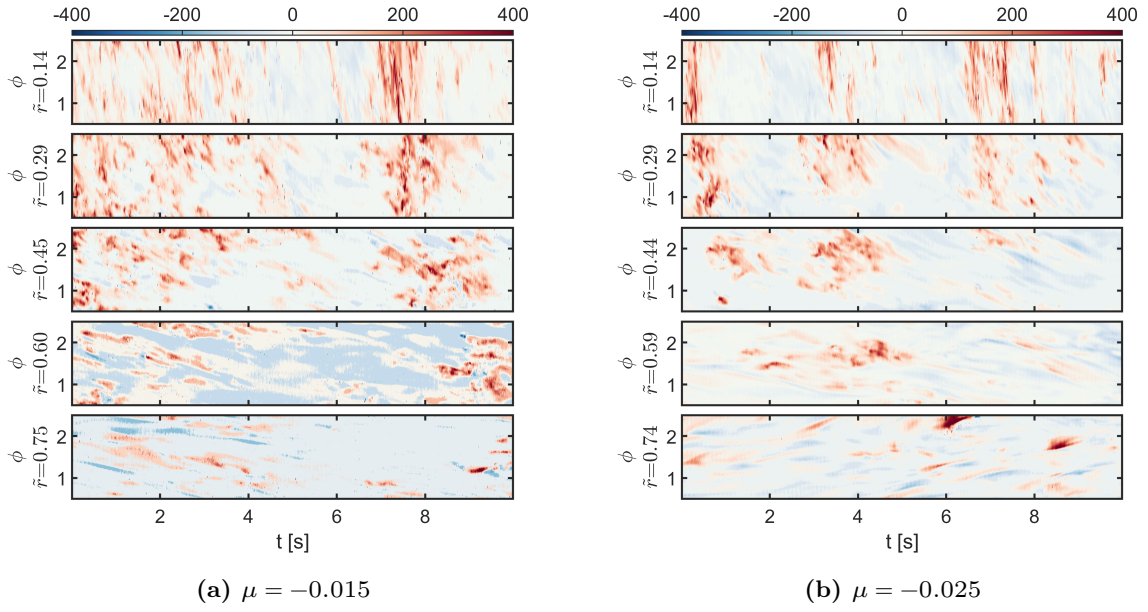


Figure 5.13: Contour plot showing the space-time diagram of $r^3(\omega u_r)/J_{lam}$ in the azimuthal-time plane for five different radial positions, at a) $\Delta z = 0$ mm, b) $\Delta z = +8$ mm from apparatus mid-height, for $Re_s = 6.1 \times 10^4$ for counter-rotating cases. The top figure is a radial position close to the inner cylinder, and the bottom figure is close to the outer cylinder. Results are shown for (a) $\mu = -0.015$ and (b) $\mu = -0.025$.

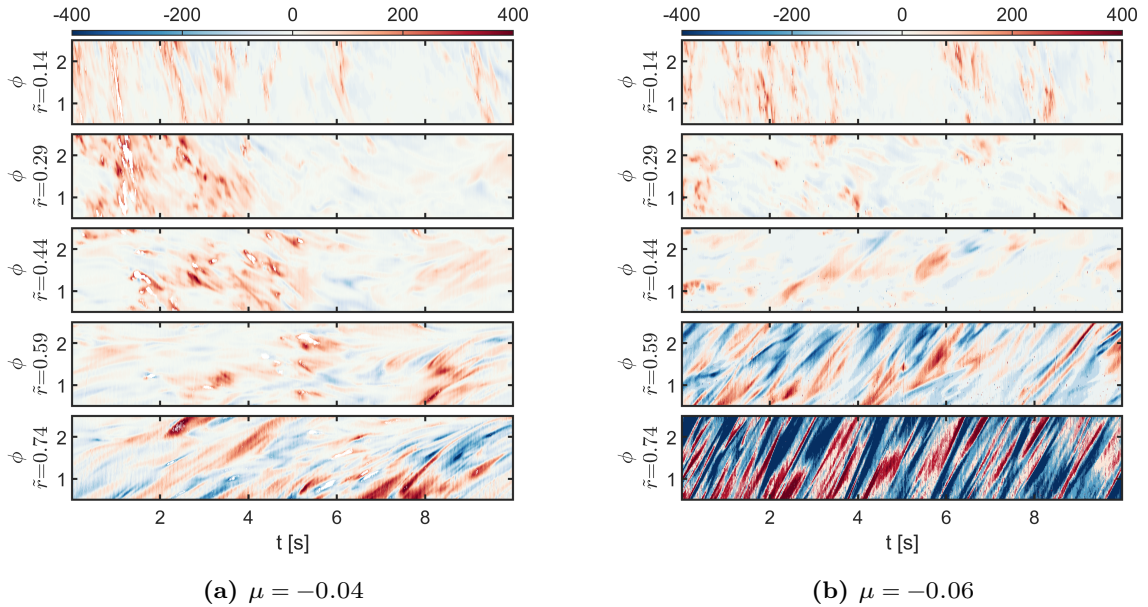


Figure 5.14: Contour plot showing the space-time diagram of $r^3(\omega u_r)/J_{lam}$ in the azimuthal-time plane for five different radial positions, at a) $\Delta z = +4$ mm, b) $\Delta z = +4$ mm from apparatus mid-height, for $Re_s = 6.1 \times 10^4$ for high counter-rotating cases. The top figure is a radial position close to the inner cylinder, and the bottom figure is close to the outer cylinder. Results are shown for (a) $\mu = -0.04$ and (b) $\mu = -0.06$.

5. The mean velocity field characteristics, and angular momentum transport.

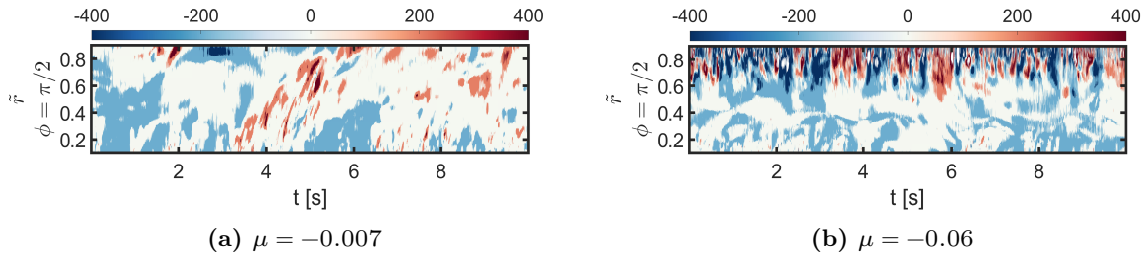


Figure 5.15: Contour plot showing the space-time diagram of $r^3(\omega u_r)/J_{lam}$ in the radial-time plane at a fixed azimuthal position $\phi = \pi/2$ for $Re_s = 6.1 \times 10^4$, for a) $\mu = -0.007$ and $\Delta z = +4\text{mm}$, and b) $\mu = -0.06$ and $\Delta z = +4\text{mm}$.

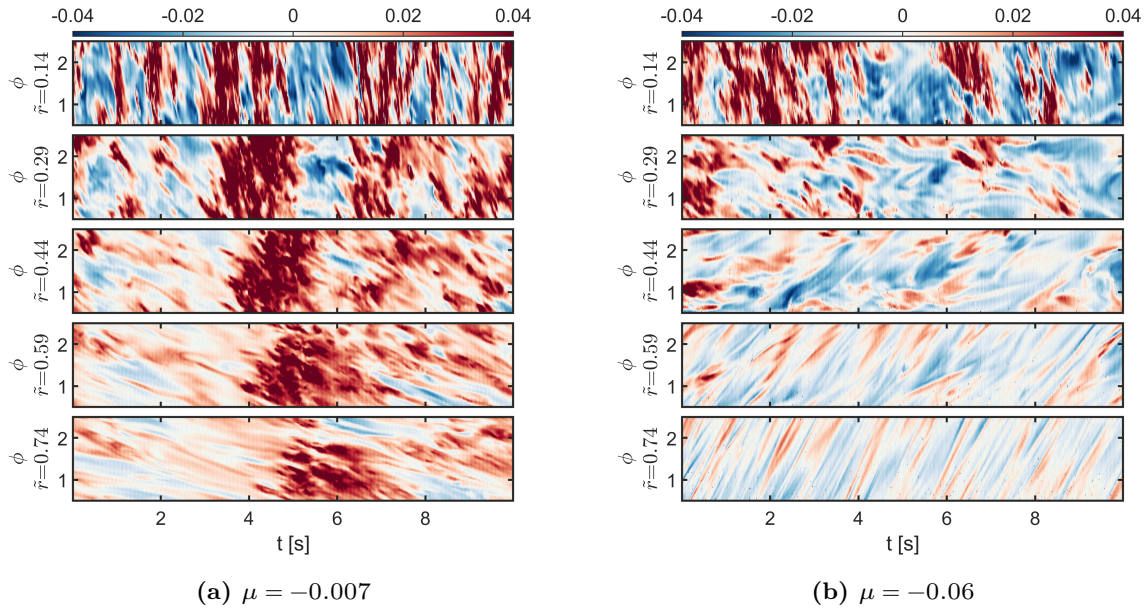


Figure 5.16: Contour plot showing the space-time diagram of the radial velocity U_r in the azimuthal-time plane for five different radial positions, at a) $\Delta z = +4\text{ mm}$, b) $\Delta z = +4\text{ mm}$ from apparatus mid-height, for $Re_s = 6.1 \times 10^4$ for a) $\mu = -0.007$ and b) $\mu = -0.06$. The colour map unit is m/sec.

counter-rotating cases. These results are not in agreement with those related to other TC flows with different radius ratios, like $\eta = 0.5$ and $\eta = 0.357$. Another difference between the currently studied geometry $\eta = 0.1$ and the previously studied geometry with higher radius ratios is the contribution of the Nu_ω^{LSC} to Nu_ω^{Total} , which did not vary with high values between the different high counter-rotating cases, in contrast to what was shown for $\eta = 0.5$ and $\eta = 0.357$ ([24] and [36]). The underlying flow phenomena can be inspected in figure 5.14, where the space-time diagram of $r^3(u_r\omega)/J_{lam}$ for $\mu = -0.04$ and $\mu = -0.06$ is presented. For the radial positions near the inner region, a similar behavior similar to $\mu = -0.015$ and $\mu = -0.025$ is observed, where the patterns with long lifetimes exist but with lower intensity. But the main difference appears in the radial positions near the outer cylinder, where small patterns with a short lifetime but high intensity appear. The intensity of these patterns increases as they go for higher counter-rotating cases. For $\mu = -0.04$, shown in figure 5.14(a), the patterns show lower intensity compared with the patterns shown 5.14(b) for $\mu = -0.06$. The existence of these patterns in the outer regions of the gap can explain why the contribution of Nu_ω^{LSC} did not decrease with increasing counter-rotation rate, while the intensity of the patterns in the inner region decreased.

In order to study the direction of these propagating patterns, figure 5.15 shows the space-time diagram of $r^3(\omega u_r)/J_{lam}$ for the lowest and highest counter-rotating rates in the $r-t$ plane at fixed azimuthal position. The figures are plotted for these two cases, as it is clear from figures 5.12, 5.13, and 5.14 that the patterns observed for $\mu = -0.007$ appear for all rotation ratios but with lower intensity, and the newly observed patterns in $\mu = -0.06$ also appear in $\mu = -0.04$ but with lower intensity. For $\mu = -0.007$, it is clear from figure 5.15(a) that the existing patterns, which are observed in the inner region for all studied rotation rates, are propagating from the inner cylinder toward the outer cylinder. While for $\mu = -0.06$, figure 5.15(b) shows the existence of two sets of patterns, the first set next to the inner cylinder but with low intensity that propagate radially outward, and another set of patterns near the outer cylinder that propagating inward. In addition, figure 5.16 shows the space-time plots for the radial velocity (U_r) at different radial positions and at a fixed height for both $\mu = -0.0077$ and $\mu = -0.06$. For $\mu = -0.077$, the radial velocity decreases in the direction toward the outer cylinder, or in other words, the propagating speed of the patterns decreases as they approach the outer cylinder. The same is observed for $\mu = -0.06$, but here the radial velocity did not vanish in the stable regions near the outer cylinder, although it exists with very low intensity, which means that the newly observed patterns near the outer cylinder travel with lower speed inward in comparison to the patterns propagating outward from the inner regions toward the central area.

To further study the characteristics of the propagating patterns, especially those observed near the cylinder walls, the spatial two-point auto-correlation coefficient of the azimuthal velocity fluctuation in the azimuthal direction is calculated, where it is defined according to ([137]) as

$$R_{\phi\phi}(r, z, \Delta\phi) = \frac{\langle u'_\phi(r, \phi, z, t)u'_\phi(r, \phi + \Delta\phi, z, t) \rangle_t}{\langle u'^2_\phi(r, \phi, z, t) \rangle_t} \quad (5.17)$$

5. The mean velocity field characteristics, and angular momentum transport.

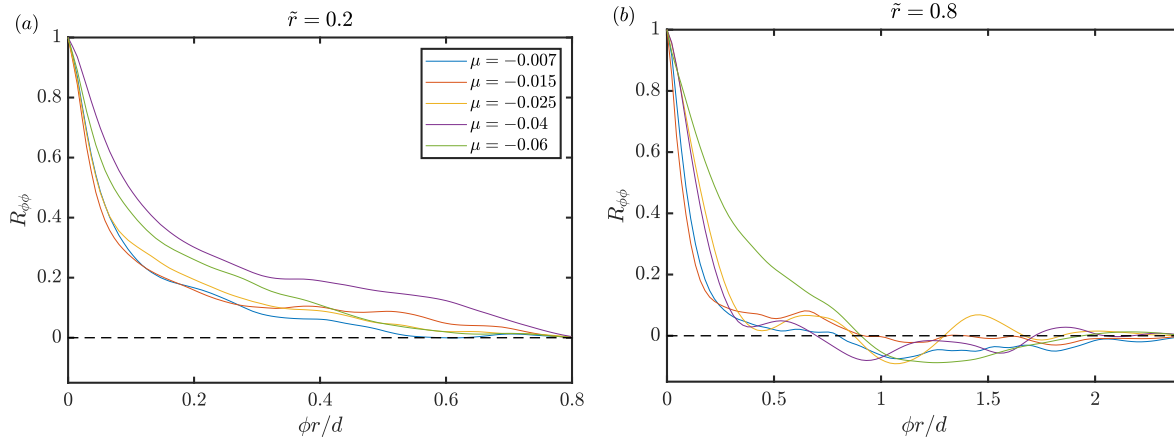


Figure 5.17: The spatial two-point auto-correlation coefficient of the azimuthal velocity fluctuation for different rotation ratios at the same axial height shown in figures 5.12, 5.13, and 5.14 for each, at a) $\tilde{r} = 0.2$ and b) $\tilde{r} = 0.8$.

with $\Delta\phi$ the azimuthal distance between every two correlated points. Figure 5.17 depicts the results for two radial positions, one next to the inner wall and the second next to the outer wall. For $\tilde{r} = 0.2$, figure 5.17(a) shows that the auto-correlation function monotonically decreases for all the counter-rotation cases shown in the figure. On the other hand, and for the radial position $\tilde{r} = 0.8$, figure 5.17(b) shows that the auto-correlation function for the different μ achieves minimums at different $\phi r/d$ values, which indicate the existence of azimuthal structure at this radial position with different sizes depending on the rotation ratio. For $\mu = -0.06$ the minimum is observed for $\phi r/d \approx 1.25$, which is interpreted as the size of the newly observed patterns.

These small-scale turbulent structures are formed in the outer cylinder shear layer and increase the transport in the outer part of the gap and so throughout the entire gap. Obviously, from figure 5.11(a) the contribution of Nu_{ω}^{Turb} increases by increasing the counter-rotation; this can explain why the value of the Nusselt number increases for high counter-rotation. But as our measurements are limited to $\mu = -0.06$, it is not possible to know if this increase will continue for higher counter-rotating cases and where the position of the second μ_{max} will be in the high counter-rotating rates, as theoretically, for very large μ , the flow should stabilize the fluid in the whole gap and the Nusselt number has to decrease to a value near 1.

The first maximum of the Nusselt number that appears in the low counter-rotating regimes is due to centrifugal instability, and this maximum is in agreement with the predicted torque maximum of the enhanced LSC theory predicted by [47]. The appearance of the second maximum at high counter-rotations is a new finding of this study, and the source of the high transport is connected to the strong turbulent structures inside the outer cylinder shear layer. From the observations of the flow structures, the existence of shear layer instability is assumed, which leads to increases in transport. Figure 5.10(b) shows that as Re_s increase, μ_{min} approaches more to μ_{max} , in other words, as the shear of the system increases, the shear instability can start earlier to contribute to the angular momentum transport for lower counter-rotating rates, and after that, it is observed how the Nu_{ω} starts to increase again. The mechanism by which these patterns are generated is still unclear to us. [138] investigated

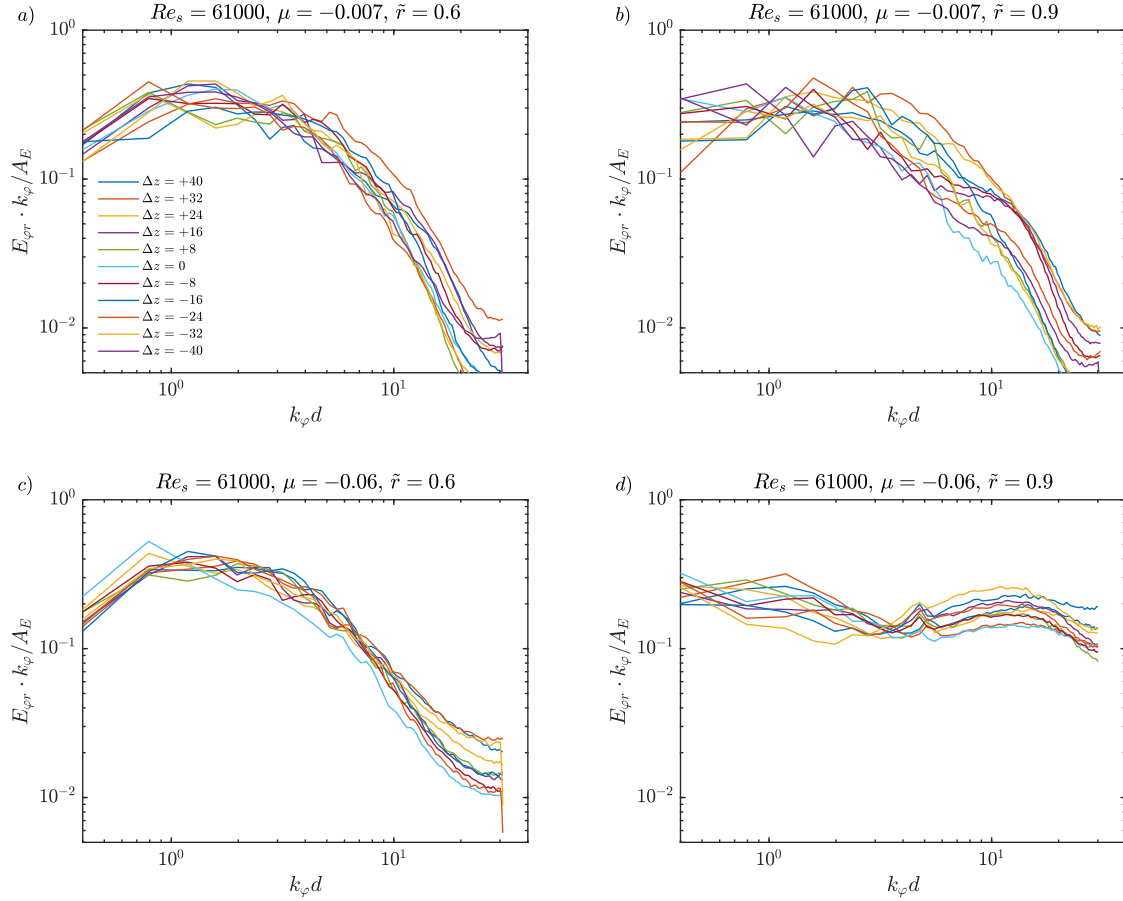


Figure 5.18: The pre-multiplied temporally averaged azimuthal energy co-spectra normalized by the area A_E below its graph. The profiles are shown for flows $Re_s = 6.1 \times 10^4$ at different heights. The profiles show results at: (a) $\mu = -0.007$ and $\tilde{r} = 0.6$, (b) $\mu = -0.007$ and $\tilde{r} = 0.9$, (c) $\mu = -0.06$ and $\tilde{r} = 0.6$, (d) $\mu = -0.06$ and $\tilde{r} = 0.6$.

the existence of modal structures near the outer cylinder for TC flow with $\eta = 0.2$. Where they mentioned that, because of the coherent structures on the inner cylinder's unstable side, the velocity disturbance could trigger Tollmien–Schlichting waves at the stable outer cylinder, resulting in these modal structures. It is not clear if the newly observed patterns from the current study are similar or not to these modal structures. Because of this a future study will concentrate on this aspect and investigate the reason and behavior of this shear layer instability in more detail at very strong counter-rotation.

5.3.3 Spatial spectral analysis

Figures 5.12, 5.13, 5.14 show the existence of propagating patterns whose strength, lifetime, and direction of propagation depend on the rotation ratio. For further information about the length scale of these propagating patterns, an analysis based on the spatial energy co-spectra is used. The azimuthal energy co-spectra are studied for the two velocity fluctuations, u'_r and u'_ϕ , at different fixed radial positions ($\tilde{r} = 0.4, 0.5, 0.6, 0.7, 0.8, 0.9$) and for $Re_s = 6.1 \times 10^4$ the different rotation ratios. The spatial co-spectra is studied at the different azimuthal points $n_\phi = \{0, 1, 2, \dots, N - 1\}$, spaced by the arc length interval

5. The mean velocity field characteristics, and angular momentum transport.

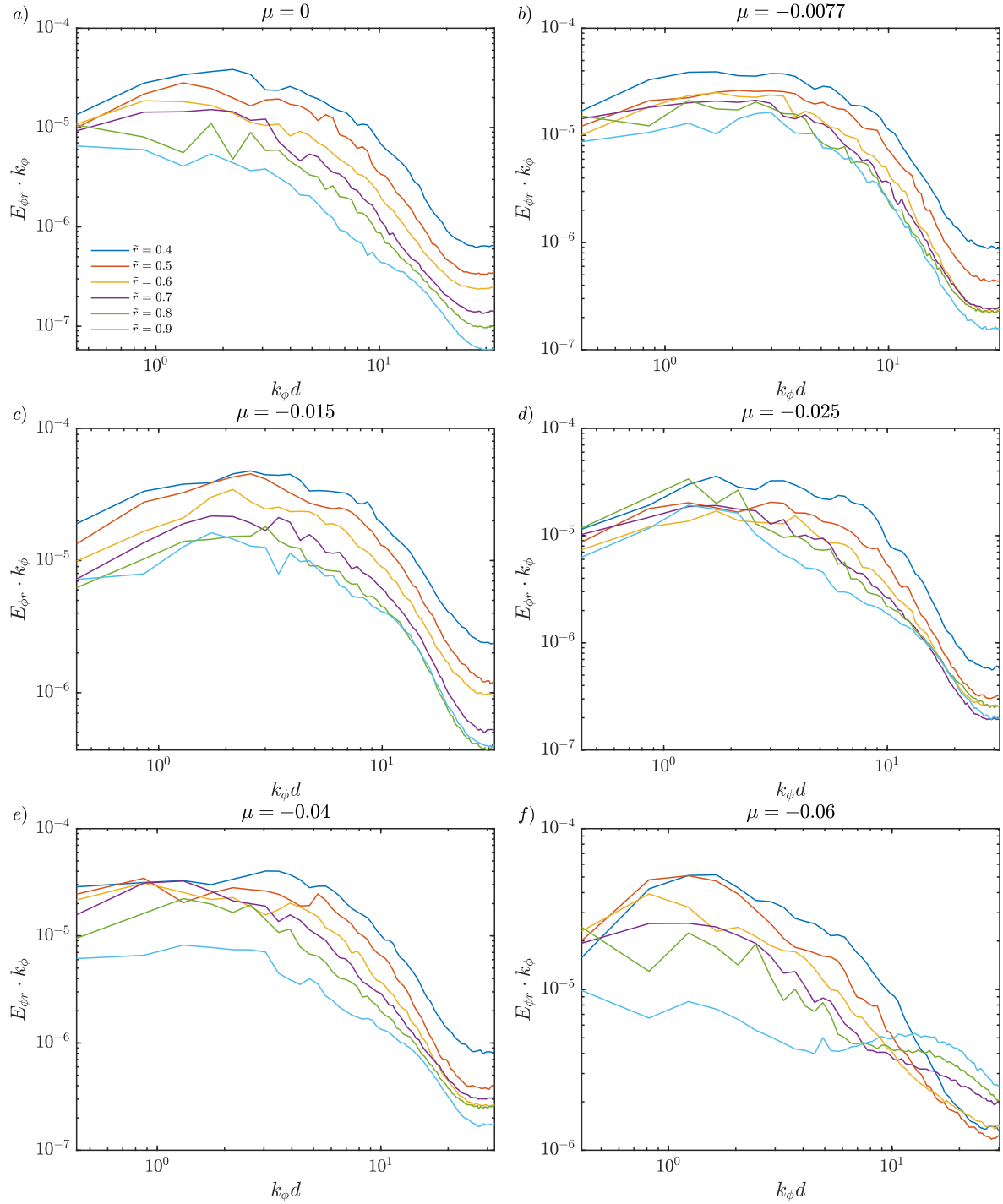


Figure 5.19: The pre-multiplied Temporally averaged azimuthal energy co-spectra for flow with $Re_s = 6.1 \times 10^4$ and different rotation ratios: a) $\mu = 0$, b) $\mu = -0.0077$, c) $\mu = -0.015$, d) $\mu = -0.025$, e) $\mu = -0.04$, and f) $\mu = -0.06$, at radial positions $\tilde{r} = 0.4, 0.5, 0.6, 0.7, 0.8, 0.9$. The profiles in each figure belong to the velocity fields at the same axial heights shown in figures 5.12, 5.13, 5.14.

$\Delta s = \Delta\phi r$. For further information about calculating the energy co-spectra and the wave number, please check Chapter 3, section azimuthal energy co-spectra. First, the dependence of the energy co-spectra profile on the axial height was discussed. Figure 6.6 shows the energy profile of the pre-multiplied spectra normalized by the area A_E below its graph with $A_E \approx (2\Delta s)^{-1} \sum_{n_\phi=0}^{N/2-1} [E_{r\phi}(k_\phi^{n_\phi}) + E_{r\phi}(k_\phi^{n_\phi+1})]$, for flows with $\mu = -0.0077$ and $\mu = -0.06$ at two different radial positions $\tilde{r} = 0.6$ and 0.9 , and at different heights. The figure shows that the energy co-spectra profile has a very weak dependence on the axial height and has mostly identical behavior through the different heights. Based on these results, we chose to study the profiles of the energy co-spectra at just one height for each rotation ratio and at the different radial positions. Where the chosen height is the same for each rotation ratio as the one used in figures 5.12, 5.13, and 5.14. Starting with the pure inner cylinder rotating case, the profiles show a pronounced maximum at $k_\phi d \approx 2.2$ for radial position $\tilde{r} = 0.4$, and the peak shifts to $k_\phi d \approx 1.5$ for radial positions next to the outer cylinder. So it can be seen that at this rotation ratio, the patterns appear to have relatively large scales at the different radial positions. For the counter-rotating cases and starting with $\mu_{max} = -0.0077$ a broad peak was observed at the different radial positions between $k_\phi d \approx 1.2$ and 4 , where it is a fingerprint of the existence of a variety of large-scale patterns at different radial positions. for $\mu = -0.015$ the same behavior appears but with a narrower peak between $k_\phi d \approx 1.5$ and 4 , the same for $\mu = -0.025$, although in this case it is observed that the profile at $\tilde{r} = 0.9$ deviates from the other profiles. For the higher counter-rotating profiles, this behavior of finding a clear peak at low wave numbers started to change, especially at the radial positions next to the outer cylinder. For $\mu = -0.06$, a double peak behavior appears next to the outer cylinder, so a peak is observed at $k_\phi d \approx 10.8$, indicating the existence of small-scale patterns, whereas the peak is observed for lower wave numbers for the radial positions next to the inner cylinder. We can assume that this peak at high wave numbers is related to the low lifetime inward propagating patterns that appear next to the outer cylinder in the high counter-rotating cases, and the peaks that appear for the different presented cases at the low wave number return to the long lifetime outward propagating patterns.

5.3.4 Quadrant analysis

For a better understanding of the patterns observed in the space-time plots, the quadrant map of the fluctuating components of u_r and ω is shown in figure 5.20. The quadrant analysis is a turbulence data-processing technique, and it has been applied over time in various experimental analyses, mainly in the investigation of turbulent shear flows ([139], [140]).

The fluctuations of two velocity components are scattered around their mean value and distributed into four quadrants considering their signs. In the current study, the pair of (ω', u_r') is represented. The numbering of quadrants is done counterclockwise starting with Q1 for both positive values of (ω', u_r') , Q2 with $\omega' < 0$ and $u_r' > 0$, Q3 with $\omega' < 0$ and $u_r' < 0$, and Q4 with $\omega' > 0$ and $u_r' < 0$. In figure 5.20 the data are contoured in terms of probability density, so the darkest zones in each plot correspond to the largest concentrations of instantaneous fluctuations for that position.

5. The mean velocity field characteristics, and angular momentum transport.

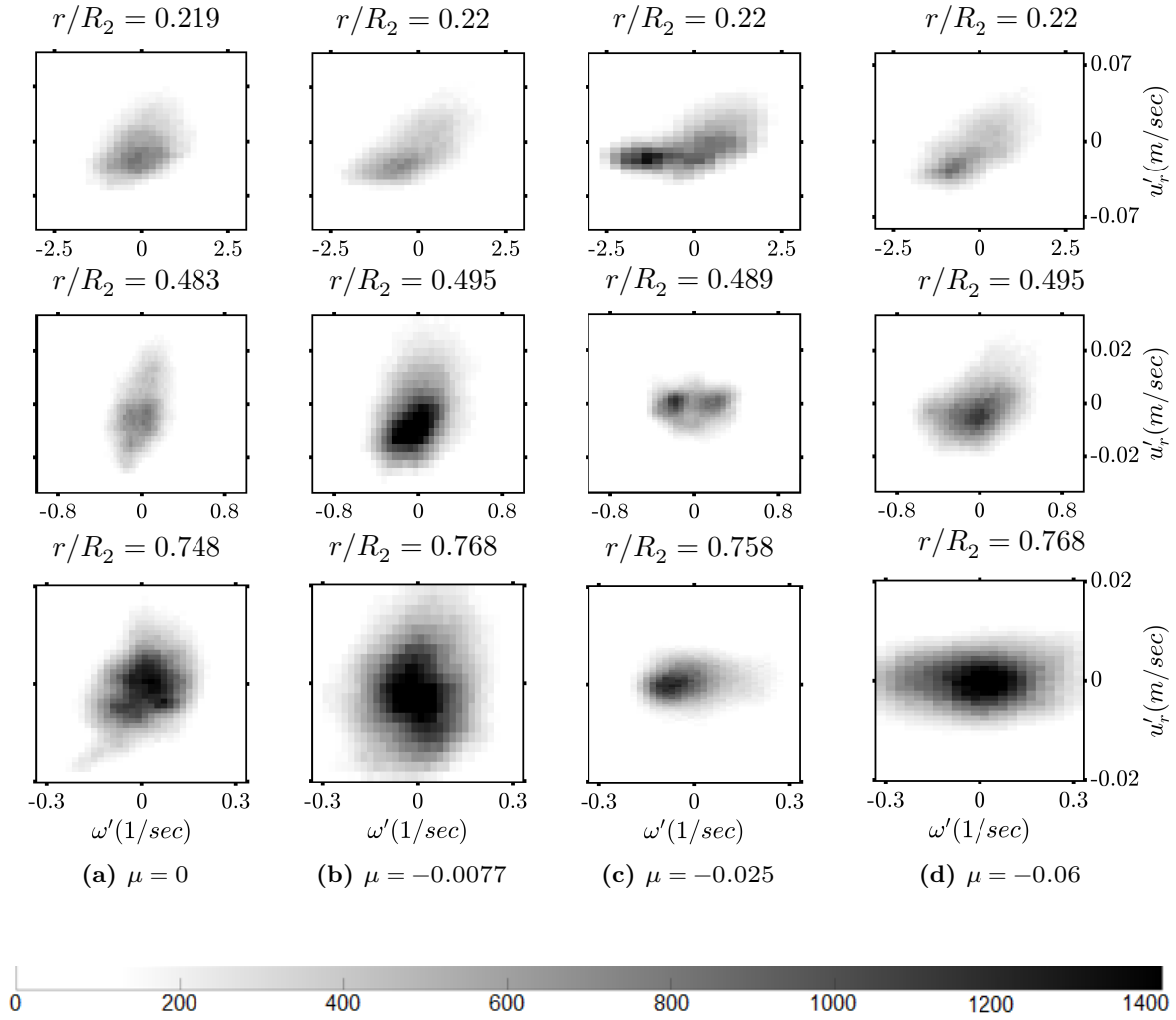


Figure 5.20: Joint PDFs of radial velocity fluctuations u'_r and angular velocity fluctuations ω' for the radial positions (top row) close to the inner cylinder (Figure 5.12-5.14, first row), (second row) centre of the gap (Figure 5.12-5.14, third row) and (bottom row) close to the outer cylinder (Figure 5.12-5.14 fifth row). Results are shown for the rotation rates (a) $\mu = 0$, (b) $\mu = -0.0077$, (c) $\mu = -0.025$ and (d) $\mu = -0.06$, for a shear Reynolds number of $Re_s = 6.1 \times 10^4$.

Figure 5.20 shows the quadrant map of (ω', u'_r) for different rotation rates at three different radial positions distributed in the inner gap region, middle of the gap and outer region. The velocities used for the current analysis belong to the same experiments used in figures 5.12, 5.13, and 5.14, with the same axial position and shear Reynolds number. In the inner regions (the figures at the top), the concentration of the distribution of (ω', u'_r) is mostly in $Q1$ and $Q3$ for the different rotation rates, so they form an oval-like shape in the diagonal direction, and they are the fingerprints of the patterns observed in the space-time figures that travel outward. In the middle of the gap, the behavior changes due to the different rotation rates. For $\mu = 0$ and $\mu = -0.0077$, the main concentration is still in $Q1$ and $Q3$, but the difference compared with the inner regions is that the value of (ω', u'_r) decreases and the direction of the oval shape is observed to rotate towards the y axis. These observations are still a figure print of the outward patterns, although with lower intensities than those observed in the inner region, in agreement with what is observed in the space-time plots. For $\mu = -0.025$, two highly concentrated black dots appear in the regions $Q1$ and $Q2$. The appearance of these two spots in these regions is a sign of the existence of inward and outward patterns, although with very low intensities, as the values of ω' and u'_r are very low. This can explain why, at this counter-rotation rate, the behavior changes. This is seen at $\mu = -0.06$, where the same behavior is observed but with higher values of ω' and u'_r . In the outer regions (the figures in the bottom), for $\mu = 0$, the oval shape of the black spots in $Q1$ and $Q3$ still exists, however, with much lower values of ω' and u'_r . But for $\mu = -0.0077$, the main concentration is also in $Q1$ and $Q3$, while some black spots appears in $Q2$ and $Q4$, where these spots are in agreement with the very light blue spots that appear in figure 5.12(b) at the same radial position, which is a fingerprint of the existence of very weak patterns travelling inward. For higher counter-rotations $\mu = -0.025$ and $\mu = -0.06$, the appearance of the black spots in $Q2$ and $Q4$ increases, which further explains the existence of the patterns that travel inward and how the intensity of this pattern increases as the rotation rate of the outer cylinder in the counter direction is increased. Another important observation from the figures related to the outer region of the gap is that where it is seen for $\mu = 0$ and $\mu = -0.0077$, the ω' and u'_r are more distributed along the y axis, which represents the radial velocity with low angular momentum fluctuations. But, for $\mu = -0.025$ and $\mu = -0.06$, different behavior is observed, where the fluctuating velocities are more distributed along the x axis, which represents the angular momentum fluctuations, with low radial velocity fluctuations. These results can support the conclusion derived from the space-time plots, where it is concluded that the shear layer instability has a high contribution to the angular momentum transport in the high counter-rotating regimes.

5.4 Conclusion

In this chapter, the turbulent counter-rotating TC flow was investigated for different shear Reynolds number values between 20000 and 1.31×10^5 . The azimuthal and radial velocity components were measured at different cylinder heights using high-speed PIV. The particle images were captured at 200 frames per second, ensuring that the data was time resolved. This study gives the opportunity to understand the physics of the flow in a very wide gap TC

5. The mean velocity field characteristics, and angular momentum transport.

geometry that has rarely been studied before. The flow in this geometry shows some common behaviors compared with the TC flows in different geometries with larger radius ratios and some different behaviors.

The dependence of the flow field on the different rotation ratios was studied first, where it was noted that the radial component is strongly height dependent, while the azimuthal component is weakly dependent. Until today, it was not clear whether a LSC exists in the wide gaps for $\eta < 0.14$ ([9]), as here the circumferential length of the inner cylinder is smaller than the gap width, especially for high shear Reynolds numbers and turbulent flow. In the current study the existence of the LSC for $\eta = 0.1$ was proven. Although they are not represented as classical Taylor vortices, their form is strongly elliptical with a high axial wave number.

The radial velocity component achieved different inflow and outflow regions through the different heights, so they were described as interlaced fingers from inflow and outflow. Also, by decreasing the μ for higher counter-rotating rates, it was observed that the radial velocity component mostly vanishes near the outer cylinder but still exists with high magnitudes in the inner region. The angular velocity and angular momentum profiles in the bulk were investigated, finding the smallest radial gradient of angular velocity for low counter-rotating rates of $-0.007 < \mu < -0.02$, where μ_{max} lies in this interval. These findings are in good agreement with those of [46] and [136]. Other findings contradict these studies, as it was found in the current study for the newly investigated geometry that the start of the neutral line detachment from the outer cylinder wall did not coincide with μ_{max} but the detachment started for the lowest counter-rotating rate before reaching μ_{max} . Furthermore, except for very strong counter-rotating rates, both theoretical predictions of [131] and [27] were unable to predict the position of the neutral surface, in which case our findings agree with [27] prediction. The earliest observed detachment of the neutral line was explained by the high curvature of the system, which allows the outer cylinder to stabilize the flow next to it at very low counter-rotating rates.

The kinetic energy was decomposed into two components: the large-scale circulation's contribution and the turbulent one. For highly turbulent flows ($Re_s > 50000$) we found that the turbulent contribution is dominant compared with the large-scale circulation contribution. Although the E_{LSC} still contributes to the total energy, it does so very weakly, and this contribution decreases with increasing the shear Reynolds number. This dominance of E_{Turb} increases with the shear Reynolds number. Also, we discovered that E_{LSC} has high values throughout the entire gap for μ_{max} , but the highest values of E_{LSC} appear in the higher counter-rotation case in the inner regions, where the value drops in the bulk after that. Total energy displays both maximums, one for μ_{max} and the other for the highest counter-rotating case.

The angular momentum transport is quantified from the velocity fields, and the resulting quasi-Nusselt number shows its highest values for the different studied shear Reynolds numbers at the low counter-rotation regions, so μ_{max} was found for $-0.007 < \mu < -0.012$. The value of Nu_ω decreases for higher counter-rotation and achieved μ_{min} and tends to increase again for decreasing μ , where it is expected to achieve a second maximum. The value of the first

μ_{max} shows independence in the shear Reynolds number, while the values of μ_{min} were shifted toward high counter-rotation rates as the shear Reynolds number decreased.

For further information and in order to understand the Nu_ω double maxima behavior with the advantage of a time-resolved measurement, the space-time behavior of the velocity field at different rotation rates was analyzed. For all the counter-rotating cases studied, patterns that travel radially outward through the gap were observed, and the intensity and lifetime of these patterns show a clear dependence on the rotation ratio. When compared with the other studied cases, these patterns appeared to have the highest intensity and longest lifetime for μ_{max} . Another set of patterns was found for the high counter-rotating cases, but in contrast to the previously mentioned patterns, these patterns just appear in the region next to the outer cylinder and propagate inward through the gap. The existence of these inwardly propagating patterns at high counter-rotating rates can explain the increase in angular momentum transport there, where we expect a second maximum for higher counter-rotating rates. It was clear that the first maximum of Nu_ω is due to centrifugal instability, and this is explained by the patterns traveling outwards through the gap. The increase of angular momentum transport for even higher counter-rotations was counterintuitive, but from our observations of the flow structures, especially the inward traveling patterns, the existence of a shear layer instability is assumed, which causes the increase in the angular momentum transport.

In order to understand more the behavior shown in the space-time figures, the fluctuating component of u'_r and ω' were analysed using the quadrant method, where they show a good agreement with the space-time plots. They show the existence of inward patterns in the outer region of the gap for high counter-rotating ratios. A conclusion can be derived here: that those patterns are a source of convective terms and, thus, are the reason for the increase in Nusselt number. The figures show that the magnitude of the angular velocity fluctuations increased in the regions near the outer cylinder for high-counter rotating cases. This observation supports our assumption of the existence of a shear layer instability responsible for the increase in angular momentum transport in the high counter-rotating cases.

6

Transition to the ultimate turbulent flow regime for flows with a stationary outer cylinder.

In this chapter, the dependence of the flow global response on the shear Reynolds number for a very wide gap TC configuration $\eta = 0.1$ is studied. The study is extended to flows up to $Re_s = 1.31 \times 10^5$, in a pure inner cylinder rotation regime, where the outer cylinder is kept stationary. The radial and azimuthal velocities of the flow are measured at different heights using a high-speed particle image velocimetry (Hs-PIV). In addition, direct torque measurements are conducted for very low shear Reynolds number flows. Indeed, one of the goals of this study is to find the critical shear Reynolds number ($Re_{s,c}$) where the flow is transformed to the ultimate regime. This is done by calculating the effective scaling between the shear Reynolds number and the Nusselt number, assuming the scaling exponent 0.76 ± 0.08 to be the signifier of this transition. The flow properties are studied and compared for the cases before and after the transition, and the angular momentum transport is quantified.

This chapter is organized as follows: in Section 6.1 the experimental setup and the measurement procedure are described. In Section 6.2 the angular momentum scaling is presented. In Section 6.3 the flow regimes and velocity mean profiles are discussed. In Section 6.4 the flow field scale behavior is analyzed by the use of the azimuthal energy temporal and spatial co-spectra. The dominant flow-field dynamic modes are presented in Section 6.5. This chapter ends with a conclusion in Section 6.6.

The main results presented in this chapter except the results presented in 6.5 are part of the paper *Transition to the ultimate Turbulent regime in a very wide gap Taylor-Couette flow ($\eta = 0.1$) with a stationary outer cylinder*, by M. H. Hamede, S. Merbold and Ch. Egbers (2023), published in *Europhys. Lett.* [79]. Note the text is mainly taken from the paper.

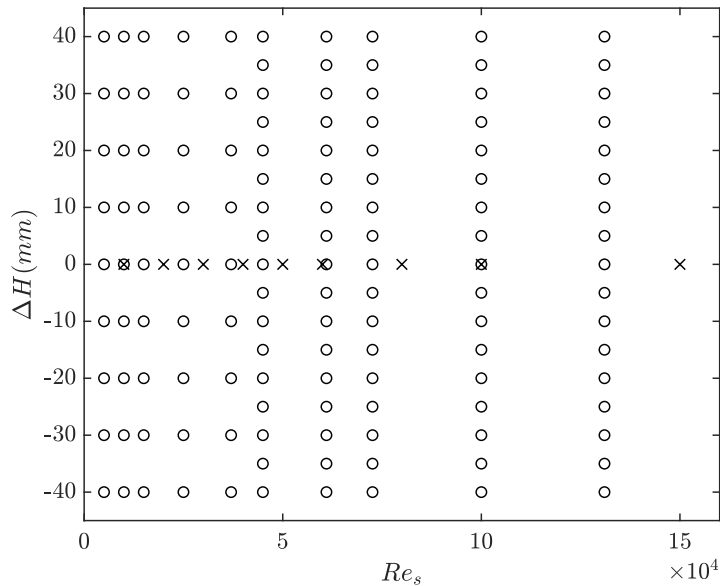


Figure 6.1: The investigated parameter space in terms of Re_s and μ . The crosses denote the measurement sets with 8000 PIV images, while the circles denote the measurement sets with 2000 PIV images.

6.1 Experimental setup and measurement procedure

In this chapter, two different measurement techniques are used to evaluate the angular momentum transport. The first technique uses a shaft-to-shaft torque sensor in order to measure the torque applied to the inner cylinder. This enables the calculation of the angular momentum transport. For this purpose, a Lorenz DR-3000 shaft-to-shaft torque sensor is used, which has a measurement range of up to ± 0.1 Nm and an accuracy of 0.05%. Unfortunately, the torque sensor could only be used for a few experiments up to a shear Reynolds number of 7000 as the accuracy of the system did not give reliable values until it entirely broke. As it was not possible to rectify this system, further direct torque measurements could not be obtained. In order to calculate the angular momentum transport for higher Re_s flows, the radial and azimuthal velocities are measured using HS-PIV at different levels of height. The measurements are conducted in the axial range between ± 40 mm starting from the apparatus mid-height, with an axial distance between the two consecutive measured planes of $\Delta z = 10$ mm for experiments up to $Re_s \leq 3.7 \times 10^4$, and $\Delta z = 5$ mm for flows with higher Re_s . Changing the axial distance between the measured planes was motivated by the visualization performed by Merbold et al. [19], where it shows less flow axial dependence for $Re_s \leq 3.7 \times 10^4$ than for higher Re_s . At each height, the flow field was recorded for 10 seconds with an acquisition frequency of 200 frames per second (fps) providing 2000 PIV images. The authors refer to chapter 3 for additional information about the measurement and calibration procedures. After measuring the velocities and using eq.1.2, the angular momentum transport is calculated in terms of the Nusselt number. By definition, the angular momentum flux J^ω is a conserved quantity over the different gap radial positions, as shown by [9], so the value of J^ω is constant at the different radial positions through the gap. In this work, the J^ω radial profile shows

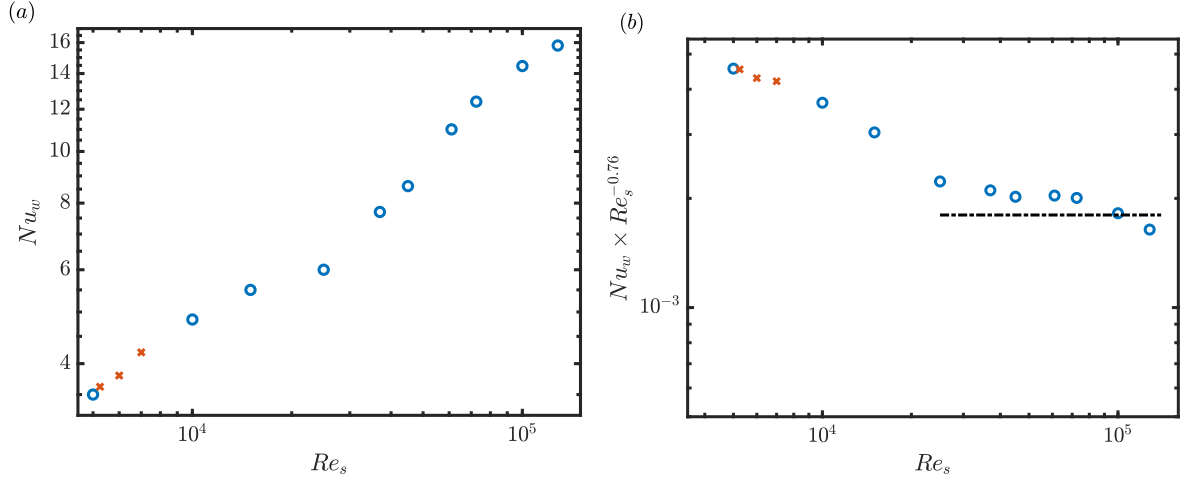


Figure 6.2: (a) The radial averaged quasi-Nusselt number as a function of shear Reynolds number for outer cylinder at rest. The blue circles represent the values calculated from the measured velocity field using HS-PIV, while the orange crosses represent the values obtained using direct torque measurements. (b) The compensated Nusselt number $Nu_w Re_s^{-0.76}$ as function of shear Reynolds number. The dash-dotted line is used to guide the eye to $Nu_w \sim Re_s^{0.76}$.

mostly a flat behavior in the bulk for $\tilde{r} = (r - r_1)(r_2 - r_1) \in [0.3, 0.7]$. This was a resulting fact of the limitations of the PIV technique to temporarily and spatially scales, especially close to the wall-bounded shear flow. Furthermore, taking into consideration the minor axial dependence of the observed flow [19], and for more detailed temporal analysis, additional measurement sets are conducted at one single height (the mid-height of the apparatus) for the same rotation ratio $\mu = 0$ and different Re_s for 40 seconds, resulting in 8000 PIV images. Hence, it is considered that most of the different flow structures with different scales pass through this axial position and are covered by the velocity measurements. These measurement sets are used to perform a spectral analysis of the energy distribution over the different flow scales. The investigated parameteric spaces are shown in figure 6.1 .

6.2 Angular momentum scaling

The angular momentum transport is studied for different Re_s flows with pure inner cylinder rotation. Figure 6.2(a) shows the variation of Nu_w with respect to Re_s , the uncertainty bars in the figure show the maximum and minimum values of Nu_w in the radial domain $0.3 < \tilde{r} < 0.7$, where $Nu_w(\tilde{r})$ is radially averaged. In addition, an increase in the angular momentum transport is noted in terms of in Nu_w , with shear Reynolds number Re_s . Figure 6.2(b) presents the value of Nu_w compensated with $Re_s^{-0.76}$ and given for the different Re_s values. The experimental data suggest that for $Re_{s,cr} = 2.5 \times 10^4$ a transition is achieved in the scaling exponent to 0.76, which is a sign of the flow transition from the classical turbulent regime (where the flow in the bulk is turbulent but laminar in the boundary layers) to the ultimate turbulent regime (both the bulk and boundary layers are turbulent) [96, 52, 21].

6. Flow transition to the ultimate turbulent flow regime

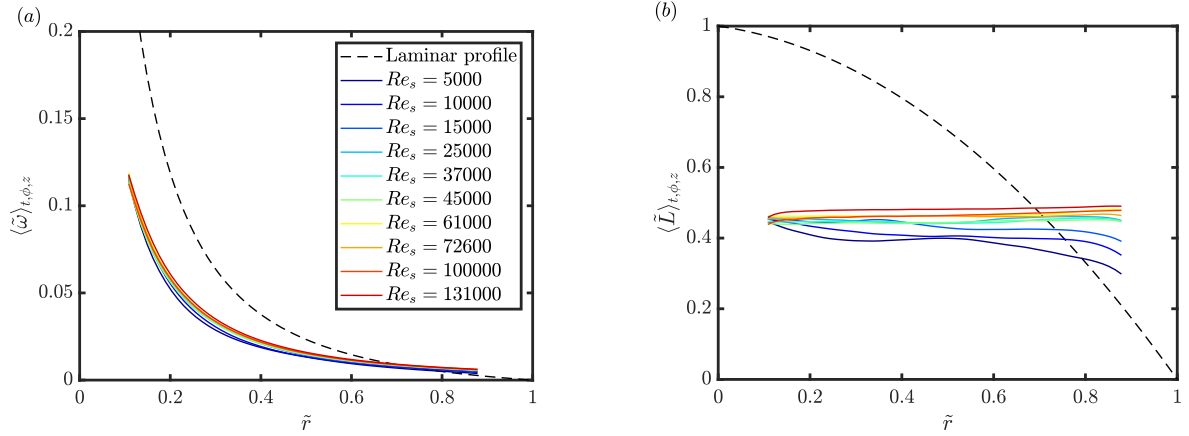


Figure 6.3: The radial profiles of spatially and temporally averaged (t, ϕ, z) normalized, (a) angular velocity, (b) angular momentum, for different shear Reynolds numbers and fixed rotation ratio $\mu = 0$. The dashed line denotes the corresponding laminar profile $\tilde{\omega}_{lam}(r) = \frac{1}{1-\eta^2} \left(\left(\frac{r_1}{r} \right)^2 - \eta^2 \right)$, and $\tilde{L}_{lam}(r) = \frac{1}{1-\eta^2} \left(1 - \left(\frac{r}{r_2} \right)^2 \right)$. Both figures use the same color legends.

6.3 Flow regimes and velocity profiles

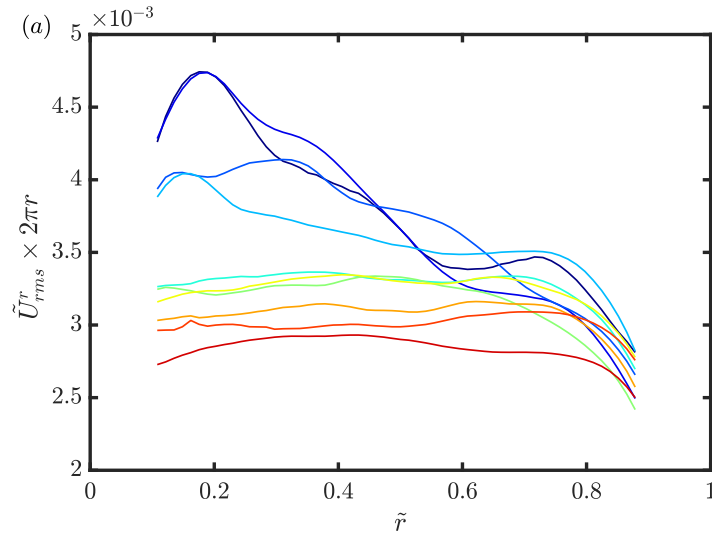


Figure 6.4: Radial profiles of the of spatially and temporally averaged (t, ϕ, z) root-mean-square of the normalized radial velocity fluctuation $\tilde{U}_{rms}^r = U_{rms}^r/u_s$, with $u_s = 2|u_\phi, 2 - u_\phi, 1|/1 + \eta$ the shear velocity, multiplied by $2\pi r$ for different shear Reynolds number and for pure inner cylinder rotation regime. The legends used in this figure are the same as in figure 6.3.

In order to study how the increase of the shear Reynolds number influences the general flow behavior, in particular when the flow achieves a transition from the classical to the ultimate regimes, the flow velocity profiles are studied. Figure 6.3 shows the radial profiles of spatially and temporally averaged (t, ϕ, z) , angular velocity ($\omega = u_\phi/r$) and angular momentum ($L = u_\phi r$). The profiles in the figure are presented in their normalized form, defined as $\tilde{\omega} = \omega/\omega_1$ and $\tilde{L} = L/L_1$. Figure 6.3(a) shows the profiles of the angular velocities which show a weak dependence on the shear Reynolds number and tend to mostly collapse to one point. Although a small deviation from this trend is observed in the area $\tilde{r} \in [0.15, 0.4]$ for flows with $Re_s < Re_{s,cr}$ that are defined by the classical turbulent regime. This deviation decreases

as Re_s approaches to $Re_{s,cr}$. In contrast to the angular velocity, the angular momentum is more likely to show a distinct dependence on Re_s . Figure 6.3(b) shows the radial profile of $\langle \tilde{L} \rangle$, where the profiles belong to two different regimes with different behavior. For $Re_s \geq Re_{s,cr}$ the profiles are mostly flat through the gap, while for $Re_s < Re_{s,cr}$ the profile shows large variations in the boundaries with a flat behavior in the middle. Here, this variation in the boundaries decreases as Re_s approaches to $Re_{s,cr}$. The deviation from the flat profile, especially near the cylinder walls, is more pronounced near the outer cylinder, as shown in figure 6.3(b). It is expected that these deviations are due to bursting or plume injection. The origin of this deviation is further discussed below using spectral analysis. In addition, for $Re_s > Re_{s,cr}$ the value of $\tilde{L} \approx 0.5$ was observed in the bulk of the gap. This value was also found by Froitzheim et al. [36] for $\eta = 0.357$ and $Re_s \geq Re_{s,cr}$, where the transition to the ultimate regime was observed, which is in agreement with our finding. The $\tilde{L} \approx 0.5$ value corresponds to $(L_1 + L_2)/2$, which indicates that the angular momentum is well-mixed [41]. To understand the secondary flow and its contribution to the angular momentum transport, it is important to study the behavior of the wall-normal velocity (u_r) fluctuations, the component in which the angular momentum is advected. By definition, the spatial-temporal average of this component is zero, so the spatial-temporal fluctuations of the radial inflow and outflow are of interest. The intensity of these fluctuations is quantified by the root-mean-square of the radial volume flux per height $2\pi r u'$ with u' the velocity fluctuation component: $u'(r, \phi, t) = u(r, \phi, t) - \langle u(r, \phi, t) \rangle_t$. Figure 6.4 depicts the radial profile of the axially averaged azimuthal and temporal root-mean-square of the radial velocity fluctuations defined as $U_{rms}^r = \langle \sigma_{t,\phi}(u'_r(\phi, r, t, z)) \rangle_z$ for different Re_s . The presented profiles are normalized by the shear velocity $u_s = (2/(1 + \eta))|u_{\phi,2} - u_{\phi,1}|$ in order to compensate for the shear driven. As a radial velocity decreases radially due to increasing circumference and incompressibility, the local results are given in volume flux per cylinder height so that \tilde{U}_{rms}^r profiles are multiplied by $2\pi r$. Similar to the angular momentum profiles, the profiles show a change in behavior at the transition to the ultimate regime $Re_s > Re_{s,cr}$. For $Re_s \leq Re_{s,cr}$ the radial fluctuations are strong at radial positions close to the inner cylinder and decrease outwards. The highest relative in- and outflow can be observed for the lowest presented Re_s . For the ultimate regime, the profiles are mostly flat across the bulk with small variations towards the boundaries, with the weakest relative in- and outflow fluctuations for the highest Re_s observed.

6.4 Azimuthal energy spatial and temporal co-spectra

Another flow feature that distinguishes the ultimate from the classical turbulent regime is the scaling behavior of the various turbulent structures in the flow. In this study, the spatial and temporal energy co-spectra are used to analyse the length scales of different flow structures. The energy co-spectra are studied for two velocity fluctuations u'_r and u'_ϕ , at different fixed radial positions ($\tilde{r} = 0.35, 0.4, 0.5, 0.6, 0.7, 0.8, \text{ and } 0.9$). The spatial co-spectra are studied at the different azimuthal points $n_\phi = \{0, 1, 2, \dots, N - 1\}$, spaced by the arc length interval $\Delta s = \Delta \phi r$. The temporal co-spectra are studied at different temporal positions, spaced by the sampling frequency of 200/sec.

6. Flow transition to the ultimate turbulent flow regime

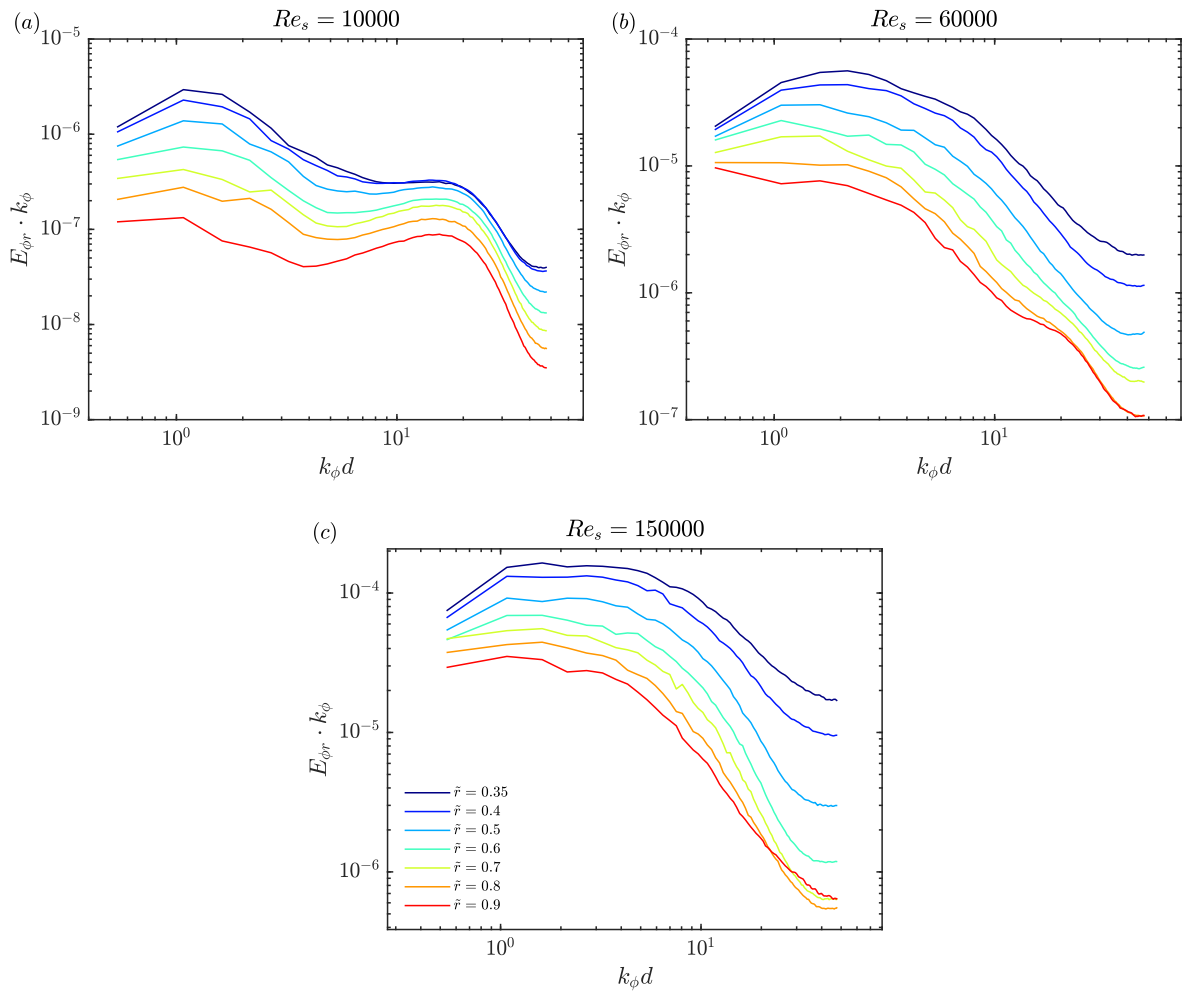


Figure 6.5: The pre-multiplied azimuthal energy co-spectra at the different radial positions and at the apparatus midheight for: (a) $Re_s = 10^4$, (b) $Re_s = 6 \times 10^4$, and (c) $Re_s = 1.5 \times 10^5$. The energy co-spectra were calculated for the given axial and radial position through the different azimuthal points at each time step, and then averaged over the different time steps and presented in this figure.

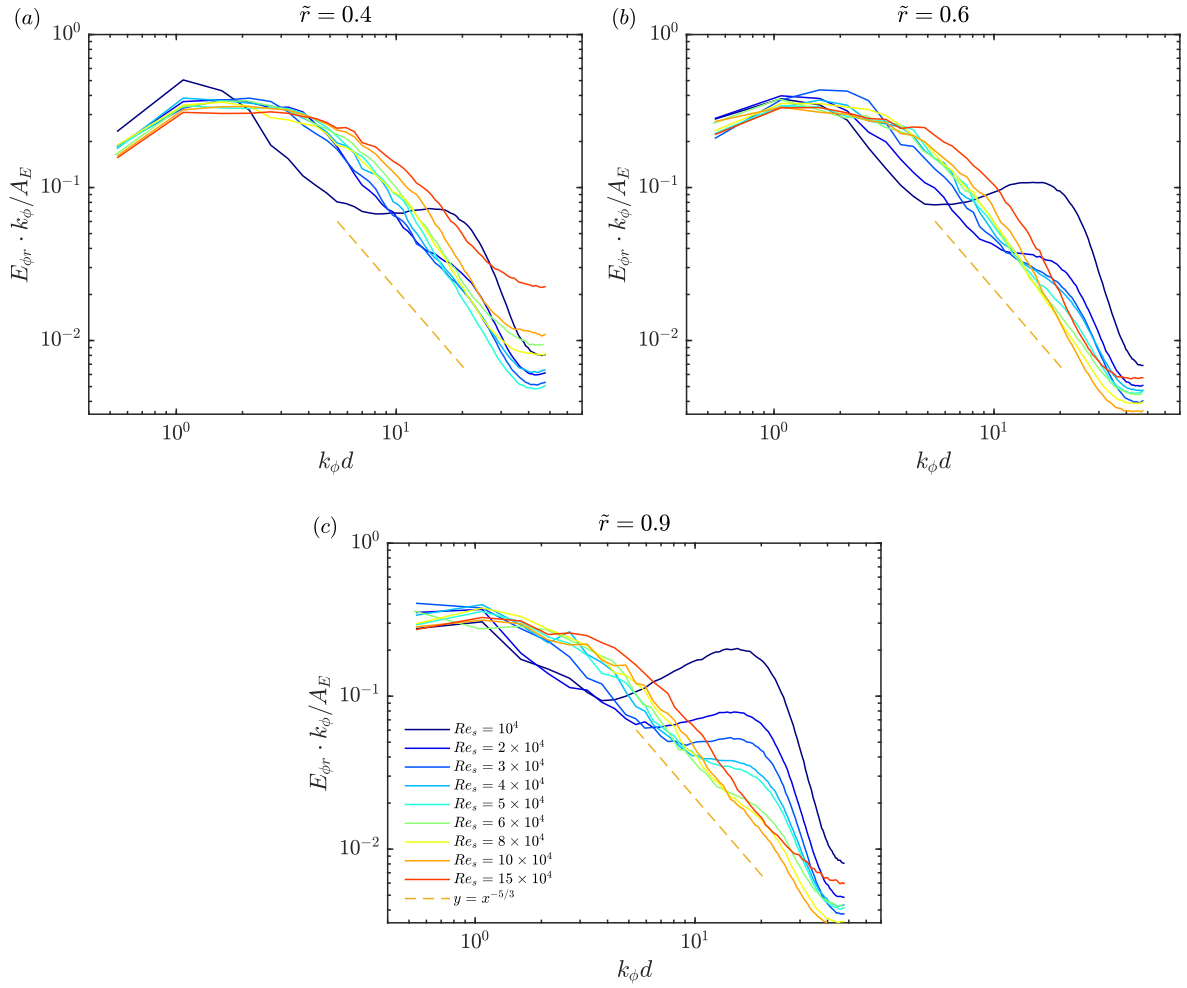


Figure 6.6: The pre-multiplied Temporally averaged azimuthal energy co-spectra normalized by the area A_E below its graph. The profiles are shown for flows with different Re_s at fix radial positions : (a) $\tilde{r} = 0.4$, (b) $\tilde{r} = 0.6$, (c) $\tilde{r} = 0.9$. The energy co-spectra were calculated for the given axial and radial position through the different azimuthal points at each time step, and then averaged over the different time steps and presented in this figure.

The discrete spatial FFT ($U'_r(n_\phi)$ and $U'_\phi(n_\phi)$) of both velocity components fluctuations (u'_r and u'_ϕ) are calculated to evaluate the azimuthal energy co-spectra $E_{r\phi}$ by using the algorithm presented in Press et al.[118]. For the spatial co-spectra, the wave number vector is defined by $k_\phi^{n_\phi} = (\Delta s)^{-1} n_\phi / N$. The spatial energy co-spectra is calculated for each time step and then averaged over the 8000 snapshots for each presented case. In order to enable the comparison of the co-spectra between the different Re_s cases, the co-spectra are normalized based on the trapezoidal integration method by the area A_E below its graph with $A_E \approx (2\Delta s)^{-1} \sum_{n_\phi=0}^{N/2-1} [E_{r\phi}(k_\phi^{n_\phi}) + E_{r\phi}(k_\phi^{n_\phi+1})]$.

In figures 6.5 and 6.6 shows the co-spectral energy profiles multiplied by the wave number vector k_ϕ and the pre-multiplied temporally averaged azimuthal energy co-spectra shown for different Re_s at different radial positions. First, it needs to be said that the measurements cover one third of the gap's azimuthal length, resulting in an arc size at radial positions $\tilde{r} \leq 0.35$ smaller than the gap width. Hence, the results are given for radial positions $\tilde{r} \geq 0.35$, to prevent under-resolved spectral profiles.

6. Flow transition to the ultimate turbulent flow regime

For the classical turbulent regime, figure 6.5(a) shows the pre-multiplied energy co-spectra for $Re_s = 10^4$ at different radial positions. The different curves belonging to different radial positions are showing majorly the same behavior with some variations across the gap. A clear peak is observed at a large wavelength $k_\phi d \approx 15.5$ and refers to the amplification of small-scale structures that dominate the flow. The amplitude of these peaks decreases closer to the outer cylinder. These small-scale patterns can be described by structures that exhibit from the outer cylinder boundary layer. For larger wave numbers the spectral energy decays strongly for all radial positions. A second peak is observed for $k_\phi d \approx 1.2$ indicating patterns of large-scale circulation that tend to approximately fill the whole gap. For $Re_s = 6 \times 10^4$ flows in the ultimate turbulent regime the pre-multiplied energy co-spectra profiles show different behavior. No further peaks at large wave numbers are observed; either they no longer exist or they are shifted toward large wave numbers above the measured range. The large-scale peak still exists, but is shifted to $k_\phi d \approx 2.2$ for all radial positions except $\tilde{r} = 0.9$ where no clear peak is observed. Thus, the energy is distributed more homogeneously compared to the classical turbulent regime case and the co-spectra show a negative slope for $k_\phi d \geq 7$ scaled by $y = x^{-5/3}$ at almost all radial positions. By remaining in the ultimate turbulent regime, figure 6.5(c) shows the pre-multiplied energy co-spectra for $Re_s = 1.5 \times 10^5$ where no peaks are observed for small scales. However, one broad peak is observed for larger scales for all radial positions and is increasing broader with the radial position approaching the outer cylinder. The peak can indicate different structures with different large scales in the flow that are all shorter than the gap width. It is clear from the presented profiles, and in contrast to $Re_s = 6 \times 10^4$, that the energy decay rate is dependent on the radial position. For the radial positions closer to the outer cylinder, a stronger energy decay is observed.

The pre-multiplied energy co-spectra for the different flows with different Re_s is presented in figure 6.6(a-c) at three radial positions $\tilde{r} = 0.4, 0.6,$ and 0.9 . At these selected positions, the flow was classified into three groups according to the co-spectral shape. The first is the classical regime, where the energy achieves two peaks, one related to small-scale and the other to large-scale structures. The amplitude of the first peak related to the small structures decreases as Re_s approaches $Re_{s,cr}$. The second group is the ultimate regime with $3 \times 10^4 \leq Re_s < 8 \times 10^4$, and the third is the ultimate regime with $Re_s \geq 8 \times 10^4$. The main distinction between the second and third groups is that the third has a wider peak for low wave numbers indicating larger developed turbulence with high energetic patterns and a broad range of large sizes. Furthermore, the energy decaying rate at larger wave numbers shows a radial dependence for the third group, but not for the second.

To understand the temporal behavior of the flow for the different studied parameters, the temporal co-spectra profiles are presented in figure 6.7 for flows with different Re_s at different radial positions. The azimuthal energy co-spectra is calculated at each azimuthal step $\Delta\phi$ and averaged over the different azimuthal points. Furthermore, in order to reduce the noise that is related to the inner cylinder's rotation without altering the profile shape, the profiles in figure 6.7 are smoothed using a sliding median method. The presented profiles consist of 4000 points, and the smoothing was done in intervals of 70 points. Using the same group classification presented above, figure 6.7 (a) shows the flow in the classical regime which

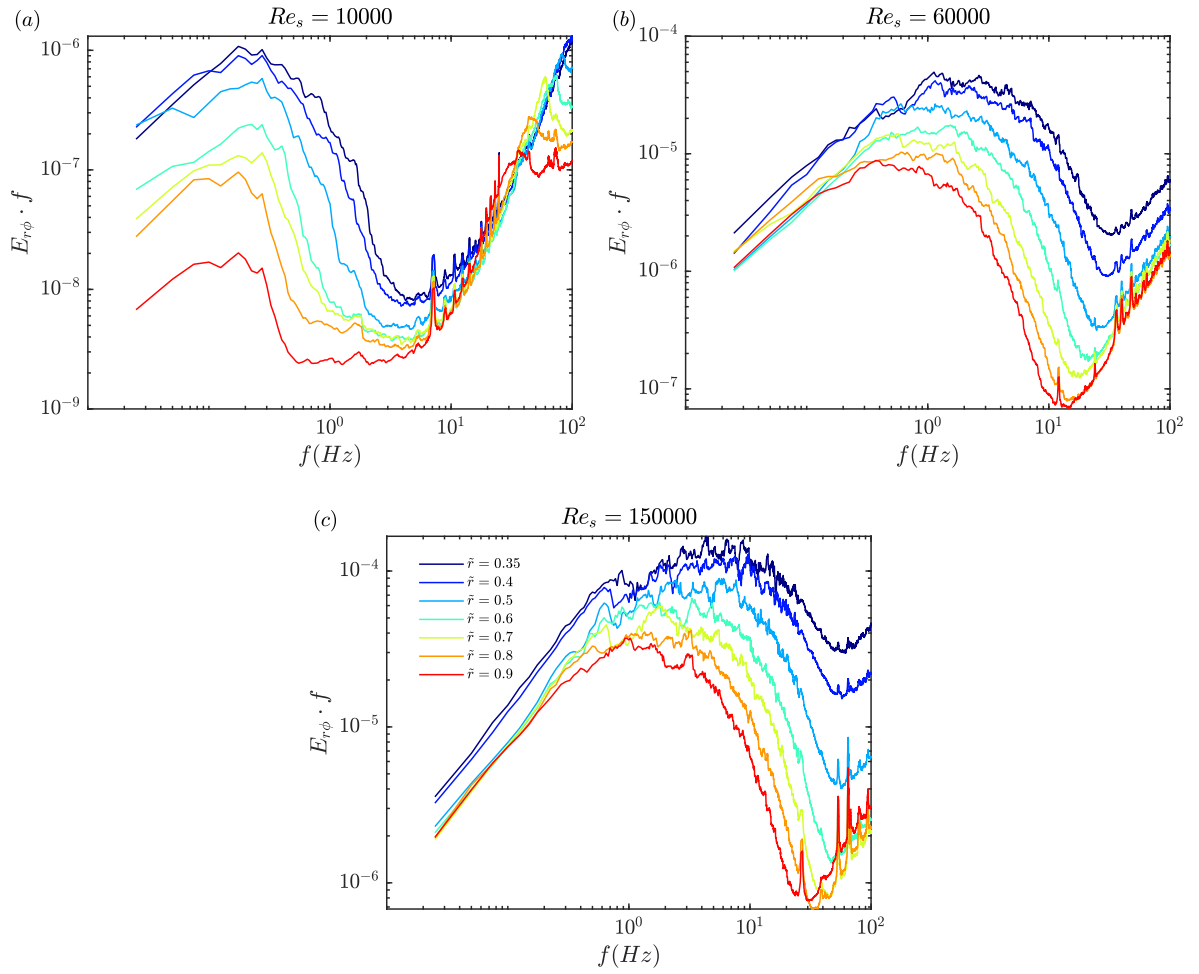


Figure 6.7: The pre-multiplied azimuthal energy temporal co-spectra for the measured velocity field at the apparatus midheight and different radial positions for flow with: (a) $Re_s = 10^4$, (b) $Re_s = 6 \times 10^4$, and (c) $Re_s = 1.5 \times 10^5$. The energy co-spectra were calculated for the given axial, radial, and azimuthal positions along the different time steps, and then averaged over the different azimuthal points.

6. Flow transition to the ultimate turbulent flow regime

achieves a first peak at a small frequency $\approx 0.1\text{Hz}$, with a frequency peak being independent of the radial position, although the energy decreases as we approach the outer cylinder. The energy decreases for larger frequencies and reaches a broad minimum where it tends to increase again for the highest frequency. It can be assumed from the figure that the first peak with low frequencies is related to large-scale patterns ($k_\phi d \approx 1.2$) that fill the whole gap, as the frequency of the peak is independent of the radial position. The second peak seems to be dependent on the radial positions and is assumed to be related to the small-scale structures ($k_\phi d \approx 15.5$). The second group shows the flow is in the ultimate regime but with low Re_s . The profiles in figure 6.7 (b) show a relatively broad peak for frequencies between 1 and 7 Hz. This can be explained by the variety of patterns with different scales explained above. For the third group in figure 6.7(c) mostly the same behavior is observed, but the broad peak in frequency is extended to higher frequencies up to 10 Hz. The broad spatial and temporal spectral profiles peak in this group are result of the development of the turbulence, so different patterns with a broad variety of sizes and frequencies appear in the flow.

6.5 Dynamic Mode Decomposition (DMD)

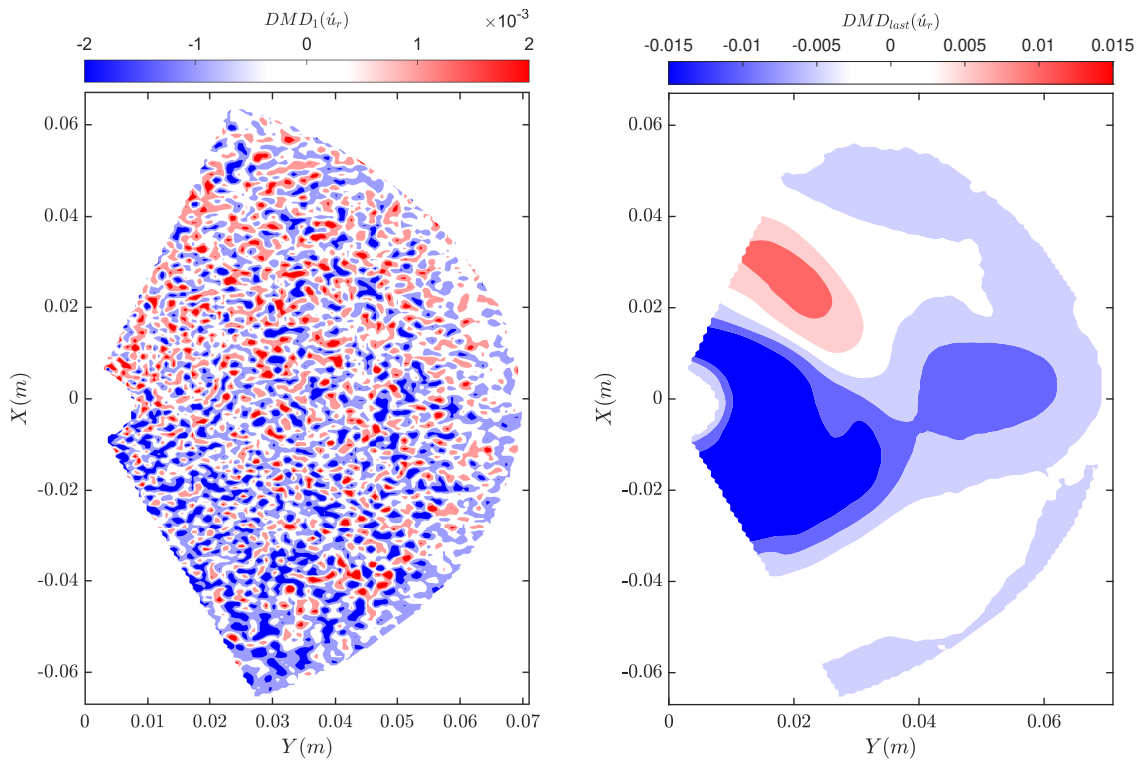


Figure 6.8: Visualization of the DMD modes of the radial velocity component fluctuation for $Re_s = 10000$ and $\mu = 0$. (a) Shows the captured DMD mode with the highest decay rate, and (b) shows the DMD mode with the lowest decay rate.

The spatial and temporal co-spectral analysis presented in figures 6.5, 6.6, and 6.7 shows the existence of flow structures with a variety of spatial and temporal scales. In order to capture and extract the flow spatio-temporal patterns, the Dynamic Mode Decomposition (DMD)

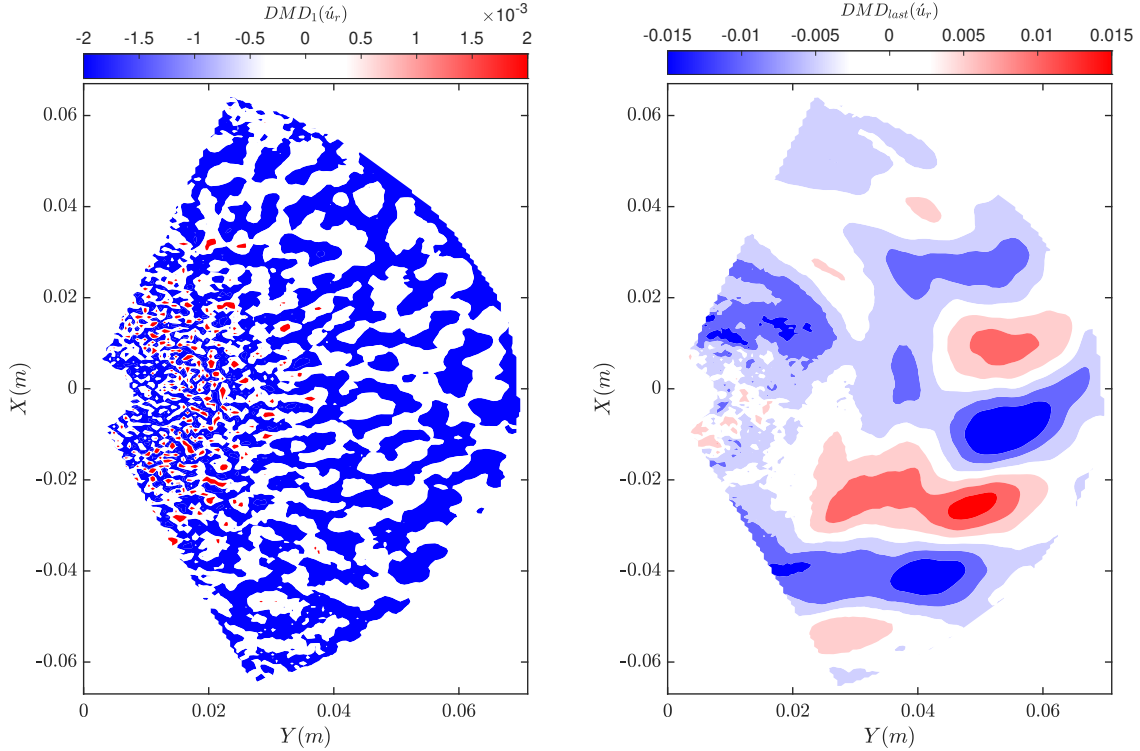


Figure 6.9: Visualization of the DMD modes of the radial velocity component fluctuation for $Re_s = 150000$ and $\mu = 0$. (a) Shows the captured DMD mode with the highest decay rate, and (b) shows the DMD mode with the lowest decay rate.

method is used. The DMD can be considered a great combination of spatial dimensionality-reduction techniques, such as the proper orthogonal decomposition (POD), and the Fourier transforms in time. This leads to associating the correlated spatial modes with a temporal frequency and a growth/decay rate. The different DMD modes can be classified using both the mode amplitude and the mode growth/decay rate. In this chapter, the different DMD modes of the radial velocity component are calculated using the method explained in Chapter 3. The modes were computed for the 8000 PIV images, which leads to having 8000 modes, and then they were filtered by getting rid of all modes having frequencies higher than the sampling rate frequency $f = 200\text{Hz}$. Here, the growth/decay rate is used to assort the different modes.

Figures 6.8 and 6.9 show two different shear Reynolds number flows, the DMD mode with the lowest and highest decay rates. Because the figure coordinate axes are presented in real units, the representation illustrated in these figures can provide us with the real approximate size of the mode in addition to the temporal information of the mode. Starting with the flow in the classical regime, figure 6.8 shows the DMD modes with the highest and lowest decay rates for $Re_s = 10^4$. For the captured DMD mode with the highest decay mode, it is observed to have a small-scale vortical structure that appears through the whole gap; the frequency of this mode is 66 Hz. This frequency was already observed in figure 6.7(a), where for the radial positions $\tilde{r} \geq 0.5$ the temporal co-spectra achieves a maximum at $f \approx 60$ Hz, where the here observed results agreed that this peak is related to the small-scale patterns. For the second presented mode with the lowest decay rate shown in figure 6.8(b), a single large-scale

vortex-like structure is observed that mostly fills the whole gap with a mode frequency of 0.244 Hz. These results are in agreement with what was presented in figures 6.5(a) and 6.7(a), where from the first we observe the existence of a large-scale pattern that fulfills the whole gap and from the second we observe a peak value for the energy co-spectra at $f \approx 0.2\text{Hz}$ which is approximately equal to the mode frequency. Moving to the ultimate regime, figure 6.8 shows the DMD modes with the highest and lowest decay rates for $Re_s = 1.5 \times 10^5$. In contrast to what was observed in the classical regime, the small-scale patterns are still observed for the mode with the highest decay rate, but they are more restricted to the area next to the inner cylinder, having a mode frequency of 64.65 Hz. The results observed here can't be compared to the results obtained from the spectral analysis, as the spectral analysis didn't cover the radial positions where these modes appear. In the second mode with the lowest decay rate, presented in figure 6.9(b), a relatively large-scale vortical-like structure appears with a mode frequency of 11.2 Hz and a spatial size smaller than the gap width (d). However, the structures that appeared in the azimuthal domain presented seem not to have an identical size. These findings are consistent with the findings in figure 6.5(c), where we observed the presence of relatively large-scale structures with a range of large sizes but smaller than the gap width. From the temporal aspect, the mode frequency didn't match the peak observed in the temporal energy co-spectra profiles, except for radial position $\tilde{r} = 0.35$.

6.6 Conclusion

In this chapter, the angular momentum transport in a very wide gap $\eta = 0.1$ Taylor-Couette flow was quantified for a set of shear Reynolds number flows. A scaling relation is found between the Nusslet number and the shear Reynold number and is defined by $Nu_\omega \sim Re_s^{0.76}$ for $Re_s \geq 2.5 \times 10^4$. This effective scaling is a measure of the transition from the classical to the ultimate turbulent regime. In addition, the angular velocity is measured and shows mostly the same behavior in both classical and turbulent regimes. In contrast, the angular momentum profiles show a clear dependence on Re_s . For the ultimate flow regime, the profiles show flat behavior in the bulk, while for the classical flow regime, they show high variation in the regions next to the inner and outer cylinders. The latest behavior of the profiles in the classical regime are returned to the injection of small structures into both cylinders. Moreover, the spectral analysis of the flow in the classical regime reveals the presence of highly energetic small-scale structures with large frequencies, and large-scale structures having the size of the gap width with small frequency. However, only highly energetic large-scale structures with a broad variety of moderate frequencies are observed in the ultimate regime, having smaller sizes than the large-scale structures investigated in the classical regime. Further, these results were confirmed using DMD.

7

The flow stability in the co-rotating regime.

In this chapter, the flow in the co-rotating regime is studied. When talking about flow in the co-rotating regime, it is important to separate between two flow states: the centrifugally stable flow for a rotation ratio of $\mu > \eta^2$ and the centrifugally unstable flow for $\mu < \eta^2$ as already explained in the first chapter of the thesis. The current chapter investigates the flow with $5 \times 10^4 \leq Re_s \leq 9 \times 10^4$ and $+0.005 \leq \mu \leq 0.04$ using two different methods: flow visualization, and velocity measurements for the radial and azimuthal components at different axial positions, using high-speed Particle Image velocimetry (HS-PIV). The here investigated rotation ratio ranges between $1.4 \leq q \leq 2$, where q is a new parameter defined when studying the TC flow in the co-rotating regime, and the value of $q = 3/2$ returns to the flow having a Keplerian azimuthal angular velocity profile.

This chapter is organized as follows: in Section 7.1 the flow measurement methods used to investigate the flow behavior in the co-rotating regime are presented. In Section 7.2 the flow regimes investigated by the use of the flow visualization are discussed. The angular velocity and radial velocity profiles measured by HS-PIV are presented and discussed in Section 7.3. This chapter ends with a conclusion in Section 7.4.

7.1 Flow measurement methods

The experimental apparatus used to investigate the flow in the co-rotating regime is the same one used in the previous chapters studying the counter-rotating and the pure rotating inner cylinder regimes ($\eta = 0.1$, $\Gamma = 11.11$). To investigate the flow in the co-rotating regime, the flow visualization method is used first, which provides a general view of the flow's global behavior. The first visualization arrangement described in chapter 3 is used in this chapter. Two continuous lasers placed exactly opposite to each other with respect to the inner cylinder emit a monochromatic beam at wavelength 532 nm (green beam), producing a quasi-2D

7. The flow stability in the co-rotating regime.

laser sheet with a maximum thickness of 1 mm. This arrangement allows observing the flow dynamics in the radial-axial (meridional) plane. The distilled water is used as a working fluid, giving the ability to reach flows with a relatively high shear Reynolds number. The fluid is seeded by tracing particles as explained in Chapter 3. In addition to the flow visualization, the radial and azimuthal velocity components were measured at different heights using HS-PIV, and following the same PIV measurement procedure explained in Chapter 3. The flow visualization shows that the flow in the co-rotating regime had less axial dependence compared to the flow in the counter-rotating regime. Due to this observation, the flow is measured over 13 different heights, 4 above the apparatus midheight and 8 below, with an axial distance of $\Delta z = 10$ mm between each two consecutive measured heights. The measurements were conducted for 10 seconds at each height, resulting in 2000 PIV images. The results in this chapter belong to the flow of $5 \times 10^4 \leq Re_s \leq 9 \times 10^4$, and $+0.005 \leq \mu \leq 0.04$.

7.2 Flow visualization

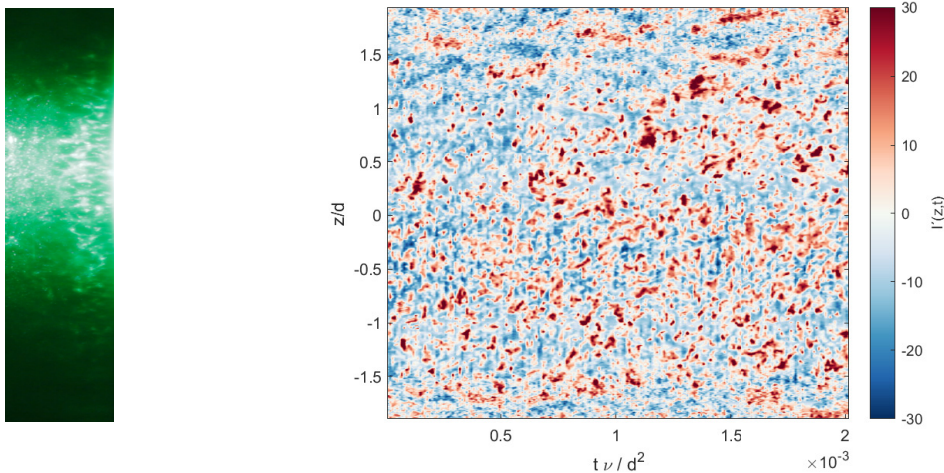


Figure 7.1: Meridional visualization image, where the left edge of the image corresponds to the outer cylinder wall and the right to the inner cylinder wall, and spatial-temporal behavior of the flow for $Re_s = 5 \times 10^4$ and $\mu = +0.01$ at a location 5 mm away from the inner cylinder corresponding to $0.08d$.

According to the Rayleigh criterion, the flow is centrifugally stable for $\mu > \eta^2$, which yields for the here studied geometry $\mu > 0.01$. For these rotation rates, the flow is expected to be stable without any hydrodynamic disturbances. Figure 7.1 shows a meridional visualization image at an instantaneous time for the flow to the left of the inner cylinder. From the presented image, it is clear that the flow is not fully stable, especially in the region next to the inner cylinder. In addition, the temporal behavior of the flow is shown to analyze flow disturbances. To do this, the light intensity I is analyzed in terms of the light intensity fluctuations, at an axial line 5 mm away from the inner cylinder. Then, $I'(z, t)$ is plotted in a space-time plot to demonstrate the temporal evolution of the flow. The space-time plots in figure 7.1 show the existence of different axially confined events with short lifetimes. These small-scale events are first observed next to the inner cylinder, where they grow into isolated

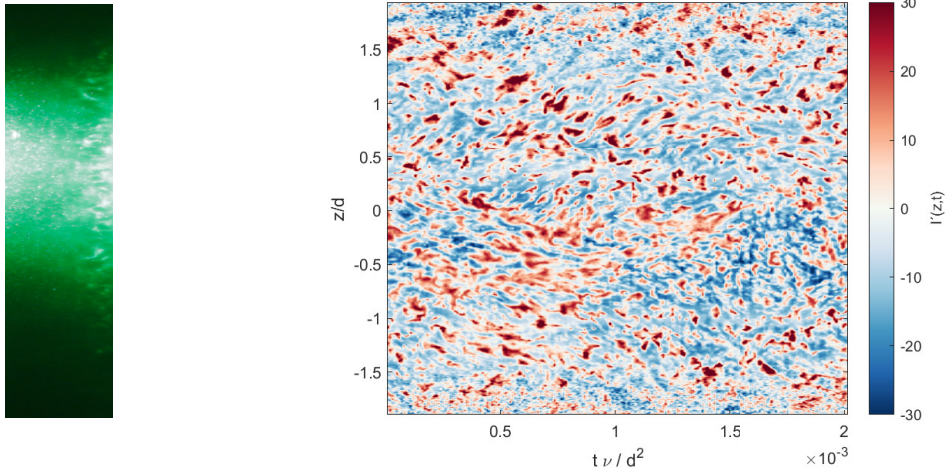


Figure 7.2: Meridional visualization image, where the left edge of the image corresponds to the outer cylinder wall and the right to the inner cylinder wall, and spatial-temporal behavior of the flow for $Re_S = 5 \times 10^4$ and $\mu = +0.02$ at a location 5 mm away from the inner cylinder corresponding to $0.08d$.

turbulent spots of motion, and then travel radially outward through the gap. This pattern resembles the turbulent spots discussed in Chapter 4, which appear in the high counter rotation flow $-0.06 \leq \mu \leq -0.01$ for shear Reynolds numbers up to 5×10^3 . As it is clear from the meridional visualization image shown in figure 7.1 the flow next to the outer cylinder is mostly stable. Although this stable flow region is penetrated by these turbulent spots, the laminar flow surrounding these spots in this region damps down this turbulent motion, and this turbulent spot doesn't succeed in disturbing the flow in this region. Visual observation reveals that these turbulent spots occur at irregular axial heights, but they are weaker, and the stable flow region extends more in the gap to axial positions near the top and bottom plates ($\sim 2d$ from the top and bottom), which is due to the end-plates effect, which induces flow and dampens the turbulent motion. By increasing the co-rotating ratio as shown in figure 7.2 up to $\mu = 0.02$ the same behavior is still observed, but in contrast to the previous case, the stable laminar flow region is extended more through the gap and the disturbed region is more restricted next to the inner cylinder. For $\mu = +0.03$ as shown in figure 7.3, although the stable region area is mostly extended through the whole gap, the disturbed area is still observed for a very limited region next to the inner cylinder, and turbulent spots are no longer able to penetrate through this area so long, but they are damped down before reaching the midgap.

When talking about the flow in the co-rotating regime, the end plates effect is always under discussion, especially since it can grow to the entire gap in the centrifugal stable flow [128]. However, the geometry of the system plays a big role in limiting this effect, so one can expect less effect for systems with a high aspect ratio [45]. In this study, the system used has an aspect ratio of $\Gamma = 11.1$ which is considered high and comparable to the system used in the Paoletti et al. study [71], where they expect no end plate effect in the apparatus mid-area. Also, Nordsiek et al. [74] argue that the angular momentum transport in the centrifugally stable regime (in particular the quasi-keplerian regime) is axially transported and is due to

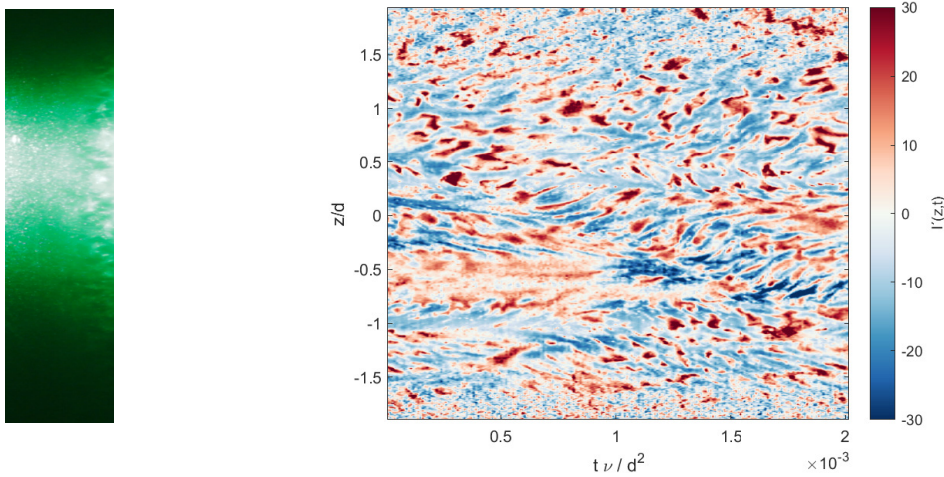


Figure 7.3: Meridional visualization image, where the left edge of the image corresponds to the outer cylinder wall and the right to the inner cylinder wall, and spatial-temporal behavior of the flow for $Re_s = 5 \times 10^4$ and $\mu = +0.03$ at a location 5 mm away from the inner cylinder corresponding to $0.08d$.

the end plates effect. But in the observed flow behavior, we didn't observe any dominant axial flow, and the observed turbulent spots have a confined, limited axial motion. So it can be concluded that the disturbed flow near the inner cylinder is not due to the end plates effect.

7.3 Velocity Profiles

For a more detailed study, the radial and azimuthal velocities of the flow are measured at different heights, as explained in Section 1. The measurements cover the axial area $-1.26d \leq \Delta z \leq +0.65d$, where it was investigated in Section 2 that the flow in this axial area is not affected by the end plate effects. Figure 7.4 shows the averaged normalized angular velocity profile for the different studied cases. The two figures return to different shear Reynolds number flows, but it is clear that the profiles in both figures are mostly identical. This identical profile behavior of the normalized quantities is a fingerprint of the very weak dependence of the flow field's general behavior on the driving rate. The result can be another piece of evidence that the flow in the investigated area is not affected by the end plate effects, as it was shown that by increasing the shear Reynolds number the end plate effects decrease [70, 71], but here we didn't observe any difference.

All profiles presented in figure 7.4 show a monotonic decrease with respect to r , which is expected behavior. But what is not expected is that the angular velocity profiles deviate from the angular velocity laminar predicted profile for flows with rotation ratios $\mu > 0.01$, although the flow is centrifugally stable for these parameters. The deviation reaches its maximum in the mid-gap, while next to the outer cylinder, the profiles reunite again. The deviation of the profiles from the laminar predicted profiles is evidence that flows are not stable for $0.08 \leq \mu \leq 0.04$ for the investigated Re_s flows. These results are returned to the observed turbulent spots in the previous section, where such turbulent spots can disturb the flow. Further, the mean radial velocity profiles for $\mu = 0.015$ and 0.025 and $Re_s = 6 \times 10^4$ are shown

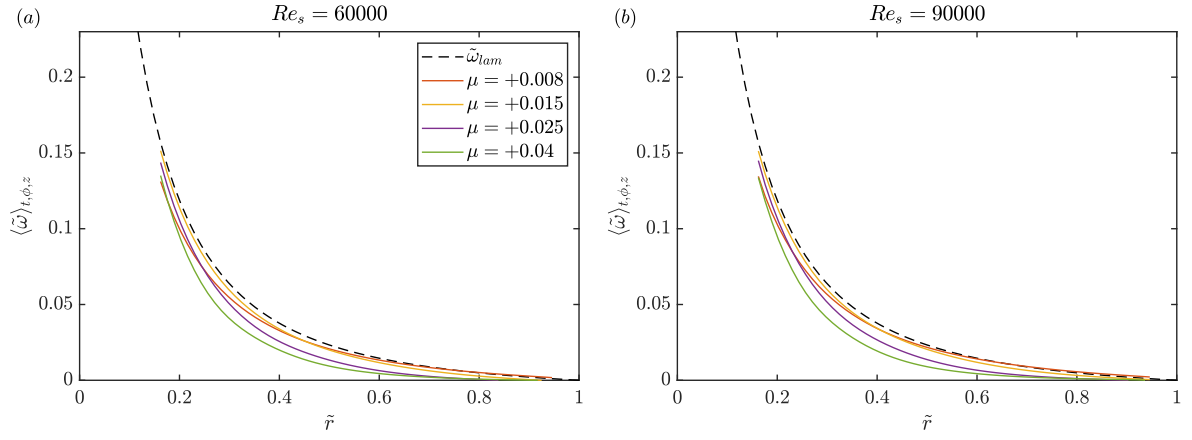


Figure 7.4: Radial Profiles of spatially and temporally averaged (t, ϕ, z) normalized angular velocity $\tilde{\omega}$ for flows with rotation ratio $0.008 \leq \mu \leq 0.04$ for (a) $Re_s = 6 \times 10^4$, (b) $Re_s = 9 \times 10^4$. The dashed line in both figures represents the normalized laminar prediction of the angular velocity

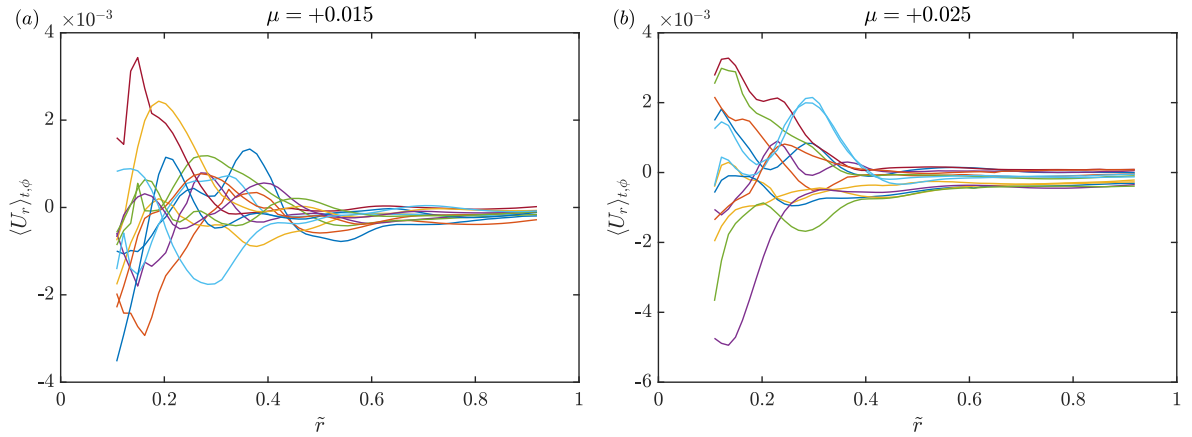


Figure 7.5: Radial Profiles of azimuthal and temporally averaged (t, ϕ) radial velocity (U_r) for $Re_s = 6 \times 10^4$ for (a) $\mu = +0.015$, (b) $\mu = +0.025$. The profiles are shown for at the 13 measured heights.

7. The flow stability in the co-rotating regime.

in figure 7.5 for the different measured heights. The profiles show what was already observed from the visualization results. High radial velocity next to the inner cylinder appears, while the velocity mostly vanishes next to the outer cylinder. As μ increases, the very low radial velocity region extends more toward the inner cylinder as shown in figure 7.5(b). Unfortunately, these results are not enough to calculate the angular momentum transport using eq . ?? as done in chapters 5 and 6. This is due to the extremely low radial velocity values near the outer cylinder, where the used measurement method was unable to resolve these scales. Although we can trust the J_ω values near the inner cylinder area, the J_ω profile through the entire gap will not follow its definition of conserved overall gap radial positions, so our argument will be weak.

7.4 Conclusion

This chapter investigated the flow in the co-rotating regime for rotation ratios up to $\mu = 0.04$ and the shear Reynolds number in the range $5 \times 10^4 \leq Re_s \leq 9 \times 10^4$. The flow visualization, in addition to the planar HS-PIV was used. The flow visualization in the radial-axial plane shows the existence of axially confined turbulent spots, which travel outward through the gap and penetrate the stable flow region next to the outer cylinder before it is damped down. The existence of these patterns was investigated for flow with rotation ratios up to $\mu = 0.03$. Further, the azimuthal and radial velocity profiles were measured using HS-PIV at different heights. The angular velocity profiles for $Re_s = 6 \times 10^4$ and 9×10^4 show a clear deviation from the angular velocity laminar predicted profile for $+0.008 \leq \mu \leq 0.04$, which is clear evidence that the flow is not laminar and is disturbed.



Conclusion

In this thesis, we conducted an experimental investigation of the Taylor-Couette (TC) flow in a very-wide gap geometry ($\eta = 0.1$). The study involved a parametric study of different shear Reynolds numbers ranging from 530 to 1.5×10^5 , along with various rotation ratios between -0.06 and $+0.04$. The flow was studied in the three different rotating regimes, each one separately: the counter-rotating, pure inner cylinder rotating and co-rotating regimes. For the last, the current study covers both the centrifugal stable region $0 < \mu < +0.01$ and the centrifugal unstable $+0.01 \leq \mu \leq +0.04$ cases. In the first stage of this work, we concerned ourselves with the exploration and characterization of the TC flow in a geometry that was rarely studied before this work, while in the second stage, we compared the flow behavior observed in our investigation with that studied in previous works for TC flow in narrower gap geometries.

The experimental investigation presented in this thesis was carried out in the top-view Taylor-Couette Cottbus (TvTCC) facility. The TvTCC is distinguished by its flexible geometry, which allows the inner cylinder to be changed. The TC flow was studied previously utilizing the same facility but for different radius ratios $\eta = 0.5$ [133, 24], and $\eta = 0.357$ [36]. For the current study, the TvTCC underwent modifications to minimize vibrations in the system when the cylinders rotate at their maximum speeds by rebuilding the TC system over a heavy-weight steel table. The 7 mm radius inner cylinder used here was specially designed and produced from steel C55, so the used thin shaft can have a high resistance against torsion and axial bending when rotating at a maximum speed of 2300 rpm. For some studied parameters, it was necessary to rotate the outer cylinder at very low speeds (between 2 and 10 rpm) and for others at higher speeds (up to 250 rpm). To do so and to reduce the rotation velocity fluctuation, two different motors were used to run the outer cylinder, the first running the cylinder at a maximum speed of 500 rpm and the second at 100 rpm. Furthermore, all seals and bearings were incorporated into the system to minimize friction between the cylinders while they were rotating. The working fluid temperature inside the gap was monitored using a type K Thermocouple sensor ($-50 + 300^\circ\text{C}, \pm 1.5\%$), connected to the fluid in the gap

8. Conclusion

through the bottom plate. To maintain constant studied parameters (Re_s and μ), the rotation speed of the cylinders was adjusted if the fluid temperature rose. Within this study, beside the distilled water, the M 5, 10, and 20 silicone oils with $\nu(@25^\circ C) = 5.402, 10.34, \text{ and } 19.95$ respectively, were used as working fluids. By using fluids with different kinematic viscosities, we could investigate a wider range of flow parameters.

The TVTCC facility is featured by its transparent outer cylinder and top plate, which enable clear observation of the fluid in the gap. Various optical techniques were used to investigate the flow characteristics in this thesis. First, visualization method was used to study the different flow patterns in the fluid with the use of kalliroscope particles, which were added to the fluid to make the flow patterns visible under spotted light. Two different configurations of light sources were used for this technique. The first gave a global view of the fluid by installing two high-energy LED lamps at the top and bottom, directing light toward the apparatus mid-height. The second allowed for tracking of flow patterns in the radial-axial plane by installing two lasers facing each other, symmetrically placed with respect to the inner cylinder, each producing a vertical laser sheet with a thickness of 1mm. The flow was recorded using different cameras with varying frame rates, which were always positioned facing the bright side of the fluid.

In addition to the visualization methods and exploiting the transparent top plate, the flow field was quantitatively studied using High-Speed Particle Image Velocimetry (HS-PIV). The radial and azimuthal velocity components were measured at different horizontal planes through the top plate by installing the high-speed VEO 640 Phantom camera above the top plate and moving the horizontal laser sheet axially. The axial distance between the measured horizontal planes was dependent on the flow axial dependence provided by the visualization results and varied between $4 \text{ mm} \leq \Delta z \leq 10 \text{ mm}$. The velocity measurements were conducted in the axial range from $1.64d$ to $2d$, on the apparatus's mid-height. Although we were aware of the limitations of 2D measurements in a 3D flow, a full 3D measurement, in addition to its logistic complexity, would reduce the spatial resolution significantly [135]. In addition, the currently used velocity measurement method was already demonstrated to have high accuracy in a previous TC flow study conducted in the same TC facility but with a different inner cylinder [24]. Another weakness of the 2D measurement that was taken into consideration is the instantaneous Large-scale circulation (LSC), which cannot be covered by our measurements and may influence the results, but our measurements cover an axial domain up to $2d$ and show the existence of LSC of size $\approx 0.43d$ which indicates that the flow axial dependence is mostly covered by our measurements and the influence of not covering the instantaneous LSC to our results is minimal. The single frame mode was used, with an acquisition frequency of 200 Hz, which suits the fluid displacement in the different studied parameters. The measured data was ensured to be time-resolved, where the Kolmogorov micro timescale $\tau_k = 0.00733$ was calculated to be larger than the time between every two consecutive images ($\Delta t = 0.005 \text{ sec}$) in the case of the most turbulent flow. The measurements were conducted for varying durations between 7 and 40 sec, depending on the studied case. The calibration of the measured velocities was done by fitting two concentric circles to the observed cylinder walls in one instantaneous PIV image. This calibration was repeated for

each measured height, computing different scale factors at each height. To check for calibration accuracy, a measurement set for solid body flow was done, and the measured velocities were compared to the theoretically predicted ones, which showed a maximum measurement error of 1 % in the inner region of the gap and 0.3 % in the outer region.

After providing an overview of the Taylor-Couette flow's historical background and the current state of research in Chapter 1, Chapter 2 presents a theoretical description of the phenomenon. Chapter 3 then explicitly describes and explains the used experimental setup, measurement techniques and data analysis methods used in this thesis. The results of this thesis were presented and analyzed in Chapters 4–7.

Chapter 4 focused on investigating and presenting the different flow patterns observed in counter-rotating regime with $-0.125 \leq \mu \leq 0$, and different Reynolds numbers, ranging between $530 \leq Re_s \leq 1.5 \times 10^4$, using visualization techniques. The question was always raised: do the classical Taylor Vortex flow and the other classical patterns appear in the very wide gap TC flow? In this chapter, we answered yes! For flow with $Re_s \leq 530$ and low counter and surprisingly co-rotating rates, the laminar Taylor vortices (TV) appear. For the same shearing rates and higher counter-rotating rates, the TV turns to be wavy, and for a further increase in the counter-rotating rates, the wavy TV is restabilized again and detaches from the outer cylinder. Due to the stabilizing effect of the outer cylinder, the flow in the gap is mostly laminar for $800 \leq Re_s \leq 5 \times 10^3$ and relatively high counter-rotating rates of $-0.06 \leq \mu \leq -0.01$. This laminar flow was penetrated by small-scale plumes that formed close to the inner cylinder and destabilized the flow locally, resulting in locally isolated turbulent spots. As the system's driving rates increase, the repetition rate of these spots increases, and they are switched to non-isolated turbulent structures we identify as turbulent bursts, which overlap and interact with each other and destabilize the entire flow. As the driving rates increased, the frequency and size of the bursts also increased, but surprisingly, increasing the Re_s over a certain limit decreased the frequency of these patterns again. For higher counter-rotating rates $\mu \geq -0.06$ a novel pattern appears, which we assumed just existed in the very wide gap TC flow. The radial inflow and outflow, vertically aligned with the rotation axis, formed a single Axial Columnar Vortex (ACV) between the cylinders, which rotated around the system with a fixed frequency, leading to an azimuthal mode of number 1. For further higher counter-rotating rates, the ACV detaches from the outer cylinder, loses its axial alignment, becomes helical, and the Helical Columnar Vortex appears. All investigated patterns are summarized in figure 4.10.

The influence of the rotation ratio, specifically in the counter-rotating regime, on the velocity field behavior and the flow global response was studied in Chapter 5 for flows with $Re_s = 2 \times 10^4$, 6.1×10^4 and 1.31×10^5 , and $-0.06 \leq \mu \leq 0$. This study revealed significant axial dependency in the flow field for the different investigated parameters. The radial velocity component achieved different inflow and outflow regions through the different axial positions, where oval-like vortical patterns with an axial size of approximately $0.43d$ appeared. These cortical patterns mostly fulfilled the whole gap for $\mu = -0.077$. For higher counter-rotating rates, the radial velocity largely vanishes next to the outer cylinder, and the observed vortical patterns are found to have a smaller axial size and are restricted to the area next to the inner

8. Conclusion

cylinder. The stabilizing effect of the outer cylinder rotation, which leads to damping down the radial velocity in the gap outer region, appears once it is set to counter-rotate, where the so-called “neutral line“ detaches from the outer cylinder wall for the lowest counter-rotating rates $\mu > \mu_{max}$. The detachment of the neutral surface observed in this study doesn't follow the different theoretical predictions proposed in [27, 131], although TC flows in narrower gaps [24, 36] did follow these predictions. These results reveal the effect of the system's curvature, so the minimum rotation of the outer cylinder can stabilize the centrifugally unstable flow in the region next to its wall. Moreover, the angular momentum fluctuation L_{rms} radial profiles show a clear change from the inner region to the transient region, which coincides approximately with the neutral surface, where it strongly increases in the regions next to the outer cylinder. To study the strengthening of the observed patterns, the flow kinetic energy is studied, where the energy was decomposed into two components, the large-scale circulation (E_{LSC}) contribution and the turbulent one (E_{Turb}). The results show a high value for (E_{LSC}) at the different radial positions for $\mu = -0.0077$. Furthermore, the angular momentum transport dependence on the rotation ratio was studied, and presented in terms of the quasi-Nusselt number in analogy to the heat transport in the Rayleigh–Bénard flow. For the three investigated Re_s flows, the quasi-Nusselt number achieved a maximum value for low counter-rotating rates $-0.011 \leq \mu_{max} \leq -0.0077$, where for this specific rotation rates the large-scale patterns were founded to fulfill the whole gap. At μ_{max} a very low radial gradient of $\langle \omega \rangle_{\phi,z,t}$ profile through the gap was investigated, which reflects the effective mixing of the angular momentum. However, the angular momentum transport decreases from its maximum for higher counter-rotating rates, until it reaches a minimum value μ_{min} and then tends to increase again for higher counter-rotating rates ($\mu_{min} \geq \mu$) where a second maximum is expected. In contrast to μ_{max} observed at the low counter-rotating rates, the position of μ_{min} shows a clear dependence on the shear Reynolds number. The decomposition of the Nusselt number into turbulent and LSC contributions shows a maximum for the first at high rotating ratios and for the second at μ_{max} . It was obvious that the first Nu_ω maximum is a result of the strengthening of the LSC which fills the whole gap, but the reason behind the second expected maximum was not clear until the space-time behavior of the flow was studied. The flow space-time behavior shows for high counter-rotating rates $\mu \geq -0.025$ the existence of short-life time patterns in the radial region next to the outer cylinder, propagating inward from the outer cylinder toward the inner one, with increasing intensity as the counter-rotating rates increase. These newly observed patterns at high counter-rotating rates enhance the angular momentum transport, and a second maximum in the transport mechanism has to be expected. Furthermore, the spatial-spectral analysis shows that these observed patterns have small scales, and it was assumed that these patterns are generated due to a shear layer instability next to the outer cylinder wall.

Chapter 6 focuses on the effective scaling of angular momentum transport with the shearing rate for flows with a stationary outer cylinder. As expected, the Nusselt number increases with the shear Reynolds number, but a transition in the scaling relation between Nu_ω and Re_s was observed for a sufficient shearing rate. For $Re_s \geq 2.5 \times 10^4$, the scaling relation $Nu_\omega \sim Re_s^{-0.76}$ was found. The transition in the effective scaling reflects a transition in the

flow state, as the computed exponent -0.76 in this study was used to reveal a transition from the classical to the ultimate turbulent regime [52, 21, 23]. The flow velocity field reflects this transition from classical to the ultimate turbulent regime. The angular momentum radial profiles for $Re_s \geq 2.5 \times 10^4$ show mostly flat profiles in the bulk, with $\langle \tilde{L} \rangle_{t,\phi,z} = 0.5$, which corresponds to $(L_1 + L_2)/2$, indicating a mixing of angular momentum in the bulk. In contrast, profiles in the classical regime show high variation through the bulk. Another flow feature distinguishing the ultimate regime from the classical turbulent regime is the flow structure's behavior, examined through spatial and temporal azimuthal energy co-spectra profiles. In the classical regime, small-scale structures with high frequencies were observed, in addition to large-scale structures with low frequencies mostly occupying the whole gap, while only a broad variety of large-scale patterns were observed with moderate frequencies in the ultimate regime. These results were further confirmed using Dynamic Mode Decomposition (DMD) for the flow in both regimes. Additionally, the DMD results show that the small-scale patterns observed in the classical regime have very high decay rates in contrast to the large-scale ones, which are mostly temporal-stable structures. These results help in understanding the relation between these two sets of patterns so that the small-scale patterns, which are frequently generated, feed and help strengthen the large-scale structures.

The flow stability in the co-rotating regime was studied in Chapter 7, with a special focus on the centrifugally stable flow. Using both flow visualization and velocity measurements, the flow was investigated for $Re_s = 5 \times 10^4$, 6×10^4 and 9×10^4 , for $+0.01 \leq \mu \leq +0.04$. The flow visualization in the radial-axial plane shows a clear division in the flow behavior inside the gap for all studied rotation rates, where the flow next to the outer cylinder is stable, unlike the disturbed flow next to the inner cylinder. In the disturbed flow region, turbulent isolated confined patterns were observed, which are generated next to the inner cylinder and travel radially inward. These turbulent spots disturb the region next to the inner cylinder and penetrate the outer stable area before damping down. By increasing the rotation ratio, the stable area extends further toward the inner cylinder, but a small area of disturbed flow still appears next to the outer cylinder. Furthermore, the velocity measurements show a clear deviation for the $\langle \tilde{\omega} \rangle_{t,\phi,z}$ profile from the theoretically predicted laminar profile ($\tilde{\omega}_{lam}$) for all the studied parameters, confirming that the centrifugally stable flow is not laminar. The chapter's findings can be viewed as an effort to address the contentious problem of momentum transport brought on by hydrodynamic instability in quasi-Keplerian flows; although it is an incomplete one, it can be considered a first step.

8.1 Open questions and future work

Although the results of this thesis have answered many questions that were raised before about the very wide gap TC flow in which is rarely studied before this study, they have also raised new questions. One of the most pressing questions is related to the newly observed patterns next to the outer cylinder for high counter-rotating rates. These patterns enhance angular momentum transport, and it was assumed that they were generated due to shear layer instability. However, further investigation is needed to confirm this assumption. The plan is to conduct velocity measurements focusing on the outer cylinder wall to magnify the small-scale

8. Conclusion

flow structures and resolve all flow scales in that area. Additionally, measurements are needed to explore the flow in the very high counter-rotating regime, as current experimental findings indicate the existence of a second angular momentum maxima in this flow regime, without specifying its position. Moreover, the flow velocity field was measured within this study for high-shear Reynolds number flows ($Re_s \geq 20000$). But the flow visualization demonstrates the presence of fascinating flow patterns for ($Re_s \leq 15000$)(see Chapter 4). Different flow patterns emerged from the analyzed flow regimes, where we suppose that these occur only in the very wide gap TC flow (e.g. Axial Columnar and helical Vortex). However, the mechanism responsible for these instabilities remains an open question. A detailed time-resolved PIV of the radial and azimuthal velocities at the different axial positions for these specific flow parameters is planned for future work.

Regarding the flow in the co-rotating regime, particularly the centrifugally stable flow, the results found are preliminary, and further investigation, possibly direct torque measurement, is needed for more conclusive validation. Measuring the angular momentum transport by direct torque measurement or another velocity measurement technique that can capture flow at small scales is crucial to drawing a conclusion about the ability of hydrodynamic instabilities to transport momentum in quasi-Keplerian flows.

References

- [1] L. F. Richardson. “The supply of energy from and to atmospheric eddies.” In: *Proc. R. Soc. London Ser. A* 97 (1920), pp. 354–373.
- [2] A. N. Kolmogorov. “The local structure of turbulence in incompressible viscous fluid for very large Reynolds numbers.” In: *Dokl. Akad. Nauk SSSR*. 30 (1941), pp. 9–13.
- [3] A. N. Kolmogorov. “On degeneration (decay) of isotropic turbulence in incompressible viscous liquid”. In: *Dokl. Akad. Nauk SSSR*. 31 (1941), pp. 538–540.
- [4] A. N. Kolmogorov. “Dissipation of energy in locally isotropic turbulence.” In: *Dokl. Akad. Nauk SSSR*. 32 (1941), pp. 16–18.
- [5] Mark Buchanan. “This Physics Breakthrough Could Help Save the World.” In: *Bloomberg, Europe Edition* (2018).
- [6] G. Brethouwer, P. Billant, E. Lindborg, and J-M Chomaz. “Scaling analysis and simulation of strongly stratified turbulent flows.” In: *J. Fluid Mech.* 585 (2007), pp. 343–368.
- [7] G. Rüdiger, M. Schultz, F. Stefani, and R. Hollerbach. “Magnetorotational instability in Taylor-Couette flows between cylinders with finite electrical conductivity.” In: *Geophysical and astrophysical fluid Dynamics* 112.4 (2018), pp. 301–320.
- [8] B. Dubrulle, O. Dauchot, F. Daviaud, P.-Y. Longaretti, D. Richard, and J.-P. Zahn. “Stability and turbulent transport in Taylor-Couette flow from analysis of experimental data.” In: *Phys. Fluid* 17 (2005), pp. 118–149.
- [9] B. Eckardt, S. Grossmann, and D. Lohse. “Torque scaling in turbulent Taylor-Couette flow between independently rotating cylinders.” In: *J. Fluid Mech.* 581 (2007), p. 095103.
- [10] Russell J Donnelly. “Taylor–Couette flow: the early days.” In: *Phys. Today* (44) 11 (1991), pp. 32–39.
- [11] I. Newton. “Mathematical Principles”. In: *Florian Cajori, University Of California Press*. (1946), p. 385.
- [12] G. G. Stokes. “Mathematical and Physical papers.” In: *Cambridge university press, England* 1 (1880), p. 102.
- [13] M. Margules. “Ueber die Bestimmung der Reibungs- und Gleitungscoefficienten aus ebenen Bewegungen einer Flüssigkeit.” In: *Sitzungsberichte der Kgl. Akademie der Wissenschaften in Wien* 83 (1881), pp. 588–602.

REFERENCES

- [14] A. Mallock. “Determination of the viscosity of water.” In: *The Royal society* 45 (1888), pp. 126–132.
- [15] M. Couette. “Etudes sur le frottement des liquides.” In: *Doctoral dissertation* (1888).
- [16] G. I. Taylor. “Stability of a viscous liquid contained between two rotating cylinders.” In: *Phil. trans. Roy. Soc. London* 223 (1923).
- [17] S. Chandrasekhar. “Hydrodynamic and Hydromagnetic stability.” In: *Clarendon, Oxford* (1961).
- [18] C. D. Andereck, S. S. Liu, and H. L. Swinney. “Flow regimes in a circular Couette system with independently rotating cylinders”. In: *J. Fluid Mech.* 83 (1986), pp. 155–164.
- [19] S. Merbold, M. H. Hamede, A. Froitzheim, and Ch. Egbers. “Flow regimes in a very wide-gap Taylor-Couette flow with counter-rotating cylinders”. In: *Philosophical transaction A* (2023). DOI: 10.1098/rsta.2022.0113.
- [20] D. P. M. VanGils, S. G. Huisman, C. Sun, and D. Lohse. “Optimal Taylor-Couette turbulence.” In: *J. Fluid Mech.* 706 (2012), pp. 118–149.
- [21] S. Merbold, H. J. Brauckmann, and C. Egbers. “Torque measurements and numerical determination in differentially rotating wide gap Taylor-Couette flow.” In: *Physical Review* 87 (2013), p. 023014.
- [22] R. Ostilla-Monico, R. J. A. M. Stevens, S. Grossmann, R. Verzicco, and D. Lohse. “Optimal Taylor-Couette: transition to turbulence”. In: *J. Fluid Mech.* 719 (2013), pp. 14–46.
- [23] R. Ostilla-Monico, E. P. van Der Poel, R. Verzicco, S. Grossmann, and D. Lohse. “Exploring the phase diagram of fully turbulent Taylor-Couette flow”. In: *J. Fluid Mech.* 761 (2014b), pp. 1–26.
- [24] A. Froitzheim, S. Merbold, and C. Egbers. “Velocity profiles, flow structures and scalings in a wide-gap turbulent Taylor-Couette flow.” In: *J. Fluid Mech.* 831 (2017), pp. 330–357.
- [25] R. C. DiPrima and H. L. Swinney. “Hydrodynamic Instabilities and the transition to Turbulence”. In: *Topics in Applied Physics* 45 (1985), pp. 139–180.
- [26] G. I. Taylor. “Stability of a viscous liquid contained between two rotating cylinders.” In: *Phil. Trans. R. Soc. Lond. A* 223 (1923), p. 289.
- [27] S. Chandrasekhar. “Hydrodynamic and Hydromagnetic Stability”. In: *1st edn. Clarendo* (1961).
- [28] S. Dong and X. Zheng. “Direct numerical simulation of spiral turbulence.” In: *J. Fluid Mech.* 668 (2011), pp. 150–173.
- [29] M. A. Razzak, B. C. Khoo, and K. B. Lua. “Numerical study on wide gap Taylor-Couette flow with flow transition”. In: *phys. Fluids* 31 (2019), p. 113606.
- [30] J. L. Synge. “On the stability of a viscous liquid between rotating coaxial cylinders”. In: *phys. Fluids* 167 (1938), pp. 250–256.

-
- [31] T. T. Lim, Y. T. Chew, and Q. Xiao. “A new flow regime in a Taylor-Couette flow”. In: *phys. Fluids* 10 (1998), p. 3233.
- [32] D. Coles. “Transition in circular Couette flow.” In: *J. Fluid Mech.* 25 (1965), p. 513.
- [33] C. D. Andereck, R. Dickman, and H. L. Swinney . “New flows in a circular Couette system with co-rotating cylinders”. In: *The Physics of Fluids* 26 (1983), p. 1395.
- [34] S. Altmeyer, Ch. Hoffmann, M. Heise, J. Abshagen, A. Pinter, M. Lücke, and G. Pfister. “End wall effects on the transitions between Taylor vortices and spiral vortices”. In: *Phys. Rev. E* 81 (2010), p. 066313.
- [35] S. Altmeyer, Ch. Hoffmann, and M. Lücke. “Islands of instability for growth of spiral vortices in the Taylor-Couette system with and without axial through flow”. In: *Phys. Rev. E* 84 (2011), p. 046308.
- [36] A. Froitzheim, S. Merbold, R. Ostilla-Monico, and C. Egbers. “Angular momentum transport and flow organization in Taylor-Couette flow at radius ratio of $\eta = 0.357$.” In: *Phys. Rev.* 4 (2019), p. 084605.
- [37] P. Bradshaw. “The analogy between streamline curvature and buoyancy in turbulent shear flow.” In: *J. Fluid Mech.* 36 (1969), pp. 117–191.
- [38] B. Dubrulle and F. Hersant. “Momentum transport and torque scaling in Taylor-Couette flow from an analogy with turbulent convection.” In: *Eur. Phys. J. B.* 26 (2002), pp. 379–386.
- [39] F. H. Busse. “The Twins of Turbulence Research.” In: *Physics* 5 (2012), p. 4.
- [40] B. Eckhardt, S. Grossmann, and D. Lohse. “Fluxes and energy dissipation in thermal convection and shear flows.” In: *Europhys. Lett.* 78 (2007), pp. 1–6.
- [41] H. J. Brauckmann, M. Salewski, and B. Eckhardt. “Momentum transport in Taylor–Couette flow with vanishing curvature”. In: *J. Fluid Mech.* 790 (2016), pp. 419–452.
- [42] R. Ezeta, F. Sacco, D. Bakhuis, S. G. Huisman, R. Ostilla-Mónico, R. Verzicco, C. Sun, and D. Lohse. “Double maxima of angular momentum transport in small gap $\eta = 0.91$ Taylor–Couette turbulence”. In: *J. Fluid Mech.* 900 (2020), A23.
- [43] M. Salewski and B. Eckhardt. “Turbulent states in plane Couette flow with rotation”. In: *Physics of Fluids* 27 (2015), p. 045109.
- [44] T. Kawata and P. H. Alfredsson. “Turbulent rotating plane Couette flow: Reynolds and rotation number dependency of flow structure and momentum transport.” In: *Phys. Rev. Fluids* 1 (2016), p. 034402.
- [45] M. S. Paoletti and D. P. Lathrop. “Angular momentum transport in turbulent flow between independently rotating cylinders.” In: *Phys. Rev.* 106 (2011), p. 024501.
- [46] R. Ostilla-Monico, S. G. Huisman, T. J. G. Janninik, D. P. M. van Gils, R. Verzicco, S. Grossmann, and D. Lohse. “Optimal Taylor-Couette flow: radius ratio dependence.” In: *J. Fluid Mech.* 747 (2014a), pp. 1–29.
- [47] H. J. Brauckmann and B. Eckhardt. “Intermittent boundary layers and torque maxima in Taylor-Couette flow”. In: *Physical Review* 87 (2013), p. 033004.

REFERENCES

- [48] F. Wendt. “Turbulente Strömungen zwischen zwei rotierenden konaxialen Zylindern.” In: *Ingenieur-Archiv volume 4* (1933), pp. 577–595.
- [49] D. P. Lathrop, J. Fineberg, and H. L. Swinney. “Transition to shear-driven turbulence in Couette-Taylor flow.” In: *Phys. Rev. A* 46 (1992), p. 6390.
- [50] G. S. Lewis and H. L. Swinney. “Velocity structure functions, scaling, and transitions in high-Reynolds-number Couette-Taylor flow.” In: *Phys. Rev. E* 59 (1999), p. 5457.
- [51] D. P. M. van Gils, S. G. Huisman, G. Bruggert, C. Sun, and D. Lohse. “Torque Scaling in Turbulent Taylor-Couette Flow with Co- and Counterrotating Cylinders”. In: *Physical Review Letters* 106 (2011), p. 024502.
- [52] S. G. Huisman, D. P. M. van Gils, S. Grossmann, C. Sun, and D. Lohse. “Ultimate Turbulent Taylor-Couette Flow.” In: *Physical Review Letters* 108 (2012), p. 024501.
- [53] M. J. Burin, E. Schartman, and H. Ji. “Local measurements of turbulent angular momentum transport in circular Couette flow”. In: *Experiments in Fluids*. 48 (2010), pp. 763–769.
- [54] R. H. Kraichnan. “Turbulent thermal convection at arbitrary Prandtl number.” In: *Phys. Fluids* 5 (1962), pp. 1374–1389.
- [55] S. Grossmann and D. Lohse. “Logarithmic temperature profiles in the ultimate regime of the thermal convection”. In: *Phys. Fluids*. 24 (2012), p. 125103.
- [56] G. P. King, Y. Li, W. Lee, and H. L. Swinney. “Wave speeds in wavy Taylor-vortex flow.” In: *J. Fluid Mech.* 141 (1984), pp. 365–390.
- [57] P. S. Marcus. “Simulation of Taylor-Couette flow. Part 2. Numerical results for wavy-vortex flow with one travelling wave.” In: *J. Fluid Mech.* 146 (1984), pp. 65–113.
- [58] L. Prandtl. “über Flüssigkeitsbewegung bei sehr kleiner Reibung.” In: *Verhandlungen des III. Internationalen Mathematiker Kongresses, Heidelberg* (1905), pp. 485–491.
- [59] H. Blasius. “Grenschichten in Flüssigkeiten mit Kleiner Reibung.” In: *Zeitschrift für Angewandte Mathematik und Physik* 56 (1908), pp. 1–37.
- [60] S. G. Huisman, S. Scharnowski, Ch. Cierpka, Ch. J. Kähler, D. Lohse, and C. Sun. “Logarithmic Boundary Layers in Strong Taylor-Couette Turbulence.” In: *Physical Review Letters* 110 (2013), p. 264501.
- [61] S. Grossmann, D. Lohse, and C. Sun. “Velocity profiles in strongly turbulent Taylor-Couette flow.” In: *Phys. Fluids* 26 (2014), p. 025114.
- [62] R. Ostilla-Mónico, E. P. Van Der Poel, R. Verzicco, S. Grossmann, and D. Lohse. “Boundary layer dynamics at the transition between the classical and the ultimate regime of Taylor-Couette flow.” In: *Phys. of Fluids* 26 (2014), p. 015114.
- [63] G. Ahlers, E. Bodenschatz, D. Funfschilling, S. Grossmann, X. He, D. Lohse, R. J. A. M. Stevens, and R. Verzicco. “Logarithmic Temperature Profiles in Turbulent Rayleigh-Bénard Convection.” In: *Physical Review Letters* 109 (2012), p. 114501.
- [64] L. Rayleigh. “On the dynamics of revolving fluids”. In: *Proc. R. Soc. Lond. A* 54 (1917), pp. 93–148.

-
- [65] S. Fromang and G. Lesur. “Angular momentum transport in accretion disks: a hydrodynamical perspective.” In: *EAS Publications Series* 82 (2017), pp. 391–413.
- [66] E. Schartman, H. Ji, and M.J. Burin. “Development of a Couette-Taylor flow device with active minimization of secondary circulation”. In: *Rev. Sci. Instruments* 80 (2009), p. 024501.
- [67] H. Ji and S. Balbus. “Angular momentum transport in astrophysics and in the lab”. In: *Phys. Today* 66(8) (2013), p. 27.
- [68] E. Schartman, H. Ji, M.J. Burin, and J. Goodman. “Stability of quasi-Keplerian shear flow in a laboratory experiment”. In: *Astron. Astrophys.* A94 (2012), p. 543.
- [69] M. Avila. “Stability and Angular-Momentum Transport of Fluid Flows between Corotating Cylinders.” In: *Physical Review Letters* 108 (2012), p. 124501.
- [70] H. Ji, M.J. Burin, E. Schartman, and J. Goodman. “Hydrodynamic turbulence cannot transport angular momentum effectively in astrophysical disks.” In: *Nature* 444 (2006), pp. 343–346.
- [71] M.S. Paoletti, D.P.M. van Gils, B. Dubrulle, C. Sun, D. Lohse, and D.P. Lathrop. “Angular momentum transport and turbulence in laboratory models of Keplerian flows.” In: *Astron. Astrophys.* 547 (2012), A64.
- [72] B. Dubrulle, L. Marié, C. Normand, D. Richard, F. Hersant, and J.-P. Zahn. “An hydrodynamic shear instability in stratified disks.” In: *Astronomy and Astrophysics* 429 (2004), pp. 1–13.
- [73] R. Ostilla-Mónico, R. Verzicco, S. Grossmann, and D. Lohse. “Turbulence decay towards the linearly stable regime of Taylor–Couette flow”. In: *J. Fluid Mech.* 748 (2014), R3.
- [74] F. Nordsiek, S. G. Huisman, R. C. A. van der Veen, C. Sun, and D. Lohse and D. P. Lathrop. “Azimuthal velocity profiles in Rayleigh-stable Taylor-Couette flow and implied axial angular momentum transport”. In: *J. Fluid Mech.* 774 (2015), pp. 342–362.
- [75] H. Görtler. “On the Three-Dimensional Instability of Laminar Boundary Layers on Concave Walls”. In: *NACA TM 1375*. (1954).
- [76] W. S. Saric. “GÖRTLER VORTICES”. In: *The Annual Review of Fluid Mechanics* 26 (1994), pp. 379–409.
- [77] M. H. Hamede, S. Merbold, and Ch. Egbers. “Experimental method for investigating the formation of flow patterns in a very wide gap Taylor-Couette flow ($\eta= 0.1$).” In: *Technisches Messen* 90(5) (2023), pp. 332–339.
- [78] M. H. Hamede, S. Merbold, and Ch. Egbers. “Experimental investigation of turbulent counter-rotating Taylor–Couette flows for radius ratio $\eta= 0.1$.” In: *J. Fluid Mech.* 964 (2023), A36.
- [79] M. H. Hamede, S. Merbold, and Ch. Egbers. “Transition to the ultimate turbulent regime in a very wide gap Taylor-Couette flow ($\eta= 0.1$) with a stationary outer cylinder.” In: *Europhys. Lett.* 143 (2023), p. 23001.

REFERENCES

- [80] J. H. Spurk and N. Aksel. “Fluid Mechanics.” In: *2nd ed. Berlin Heidelberg: Springer* ISBN: 978-3-540-73536-6 (2008), p. 5.
- [81] H. L. Swinney and J. P. Gollub. “Hydrodynamic Instabilities and the Transition to Turbulence.” In: *2nd ed. Springer* (1985).
- [82] W.H. Reid P.G. Drazin. “Hydrodynamic stability.” In: *NASA STI/Recon Technical Report A*, 82 (1981).
- [83] P.G. Drazin. “Introduction to hydrodynamic stability.” In: *Cambridge university press* 32 (2002).
- [84] I.M. Cohen P.K. Kundu. “Fluid mechanics.” In: *Elsevier* (2001).
- [85] D. J. Tritton. “A visualization of the wall region in turbulent flow.” In: *Oxford science Publications* second Edition (1987), pp. 226–227.
- [86] P. K. Kundu and I. M. Cohen. “Fluid Mechanics.” In: *Elsevier Science* second Edition (2002), pp. 574–577.
- [87] D. Coles and C. Van Atta. “Measured distortion of a laminar circular couette flow by end effects.” In: *J. Fluid Mech.* 25(2) (1966), pp. 513–521.
- [88] S. Shionoya. “Flow regimes between two independently rotating cylinders.” In: *Proc. 19th Turbulence Symposium* (1987), pp. 177–181.
- [89] G. Ahlers, S. Grossmann, and D. Lohse. “Heat transfer and large scale dynamics in turbulent Rayleigh-Bénard convection”. In: *Rev. Mod. Phys.* 81 (2009), p. 503.
- [90] D. Borrero-Echeverry, M.F. Schatz, and R. Tagg. “Transient turbulence in Taylor-Couette flow”. In: *Phys. Rev. E* 81 (2010), p. 025301.
- [91] K. Avila and B. Hof. “High-precision Taylor-Couette experiment to study subcritical transitions and the role of boundary conditions and size effects”. In: *Rev. in Sci. Instr.* 065106 (2013).
- [92] K. Avila, D. Moxey, A. de Lozar, M. Avila, D. Barkley, and B. Hof. “The Onset of Turbulence in Pipe Flow”. In: *Science* 333 (2011), pp. 192–196.
- [93] A. Prigent. and O. Dauchot. “Visualization of a Taylor–Couette flow avoiding parasitic reflections.” In: *Physics of Fluids* 12 (2000), p. 2688.
- [94] F. Ravelet, R. Delfos, and J. Westerweel. “Influence of global rotation and Reynolds number on the large-scale features of a turbulent Taylor–Couette flow.” In: *Physics of Fluids* 22 (2010), p. 055103.
- [95] K. Avila and B. Hof. “High-precision Taylor-Couette experiment to study subcritical transitions and the role of boundary conditions and size effects”. In: *Rev. Sci. Instruments* 84 (2013), p. 065106.
- [96] D. P. M. van Gils, G. W. Bruggert, D. P. Lathrop, C. Sun, and D. Lohse. “The Twente turbulent Taylor–Couette (T^3C) facility: Strongly turbulent (multiphase) flow between two independently rotating cylinders”. In: *Rev. Sci. Instrument* 82 (2011), p. 025105.

-
- [97] E. Schartman, H. Ji, and M. J. Burin. “Development of a Couette–Taylor flow device with active minimization of secondary circulation”. In: *Rev. Sci. Instruments* 80 (2009), p. 024501.
- [98] E. Schartman, H. Ji, M. J. Burin, and J. Goodman. “Stability of quasi-Keplerian shear flow in a laboratory experiment”. In: *Astron. Astrophys.* 543 (2012), A94.
- [99] M. S. Paoletti and D. P. Lathrop. “Angular Momentum Transport in Turbulent Flow between Independently Rotating Cylinders.” In: *Phys. Rev. Lett.* 106 (2011), p. 024501.
- [100] S. G. Huisman, R. C. A. van der Veen, G. W. H. Bruggert, D Lohse, and C Sun. “The boiling Twente Taylor-Couette (BTTC) facility: Temperature controlled turbulent flow between independently rotating, coaxial cylinders.” In: *Rev. Sci. Instruments* 86 (2015), p. 065108.
- [101] A. Froitzheim. “Angular momentum transport and pattern formation in medium- and wide-gap turbulent Taylor-Couette flow: An experimental study.” In: *Cuvillier Verlag, Göttingen* ISBN 978-3-7369-7073-1 (2019), PhD thesis BTU Cottbus–Senftenberg.
- [102] C. Tropea, L. Alexander, and L. Yarin. “Handbook of Experimental Fluid Mechanics”. In: *Berlin Heidelberg:Springer* ISBN: 978-3-540-25141-5 (2007).
- [103] O. Reynolds. “An Experimental Investigation of the Circumstances Which Determine Whether the Motion of Water Shall Be Direct or Sinuous, and of the Law of Resistance in Parallel Channels”. In: *Phil. trans. Roy. Soc. London* 174 (1883), pp. 935–982.
- [104] D. Coles. “Transition in circular Couette flow”. In: *J. Fluid Mech.* 21 (1965), pp. 385–425.
- [105] J-M. Chomaz. “Terra Bulla, the influence of Yves Couder on the emerging domain of arts and physics sciences.” In: *Comptes Rendus. Mécanique* 348 (2020), pp. 447–456.
- [106] M. van Dyke. “An album of fluid motion”. In: *Stanford, California: The Parabolic Press* (1982).
- [107] C. D. Andereck, S.S. Liu, and H. L. Swinney. “Flow regimes in a circular Couette system with independently rotating cylinders”. In: *J. Fluid Mech.* 164 (1986), pp. 155–183.
- [108] T. T. Lim, Y. T. Chew, and Q. Xiao. “A new flow regime in a Taylor-Couette flow”. In: *Phys. Fluids* 10 (1998), p. 3233.
- [109] D. Borrero-Echeverry, M. F. Schatz, and R. Tagg. “Transient turbulence in Taylor-Couette flow”. In: *Phys. Rev. E* 81 (2010), p. 025301.
- [110] D. J. Burin and C. J. Czarnocki. “Subcritical transition and spiral turbulence in circular Couette flow”. In: *J. Fluid Mech.* 709 (2012), pp. 106–122.
- [111] B. Martínez-Arias, J. Peixinho, O. Crumeyrolle, and I. Mutabazi. “Effect of the number of vortices on the torque scaling in Taylor–Couette flow”. In: *J. Fluid Mech.* 748 (2014), pp. 756–767.
- [112] A. Barcilon and J. Brindley. “Organized structures in turbulent Taylor-Couette flow”. In: *J. Fluid Mech.* 143 (1984), pp. 429–449.

REFERENCES

- [113] N. Abcha, N. Latrache, F. Dumouchel, and I. Motabazi. “Qualitative relation between reflected light intensity by kalliroscope flakes and velocity field in the Couette-Taylor system”. In: *Exp. Fluids* 45 (2008).
- [114] G. Gauthier, P. Gondret, and M. Rabaud. “Motions of anisotropic particles: Application to visualization of three-dimensional flows”. In: *Phys. Fluids* 10 (1998), pp. 2147–2154.
- [115] A. Mallock. “Experiments on fluid viscosity.” In: *Phil. Trans. Roy. Soc. Lond.* A187 (1896), pp. 41–56.
- [116] F. Wendt. “Turbulente Strömungen zwischen zwei rotierenden koaxialen Zylindern”. In: *Ing. Arch.* 4 (1933), p. 577.
- [117] R. J. M. Bastiaans. “Cross-correlation PIV : theory, implementation and accuracy.” In: *EUT reports* 99 (1993), W–001.
- [118] W. H. Press, S. A. Teukolsky, W. T. Vetterling, and B. P. Flannery. “Numerical recipes. The Art of scientific computing”. In: *Cambridge University Press* 3rd Edition (2007), p. 653. ISSN: ISBN:978-0-521-88068-8.
- [119] J. M. Wallace, R. S. Brodkey, and H. Eckelmann. “The wall region in turbulent shear flow.” In: *J. Fluid Mech.* 54 (1972), pp. 39–48.
- [120] E. R. Corino and R. S. Brodkey. “A visualization of the wall region in turbulent flow.” In: *J. Fluid Mech.* 37 (1969), pp. 1–30.
- [121] P. J. Schmid and J. Sesterhenn. “Dynamic mode decomposition of numerical and experimental data.” In: *Bull. Am. Phys. Soc.* (2008), pp. 53–102.
- [122] P. J. Schmid. “Dynamic mode decomposition of numerical and experimental data.” In: *J. Fluid Mech.* 656 (2010), pp. 5–28.
- [123] C. W. ROWLEY, I. MEZIĆ, S. BAGHERI, P. SCHLATTER, and D. S. HENNINGSON. “Spectral analysis of nonlinear flows.” In: *J. Fluid Mech.* 641 (2009), pp. 115–127.
- [124] I. MEZIĆ. “Analysis of Fluid Flows via Spectral Properties of the Koopman Operator.” In: *Annual Review of Fluid Mechanics* 45 (2013), pp. 357–378.
- [125] J. N. Kutz, S. I. Brunton, B. W. Brunton, and J. L. Proctor. “Dynamic Mode Decomposition: Data-Driven Modeling of Complex Systems”. In: *Society for Industrial and Applied Mathematics Philadelphia* (2016).
- [126] J. H. Tu, C. W. Rowley, D. M. Luchtenburg, S. L. Brunton, and J. N. Kutz. “On dynamic mode decomposition: Theory and applications.” In: *Journal of Computational Dynamics* 1(2) (2014), pp. 391–421.
- [127] B. Martínez-Arias and J. Peixinho. “Torque in Taylor–Couette flow of viscoelastic polymer solutions 2017.” In: *Journal of Non-Newtonian Fluid Mechanics* 247 (2017), pp. 221–228.
- [128] R. Hollerbach and A. Fournier. “End-effects in rapidly rotating cylindrical Taylor-Couette flow.” In: *AIP Conference Proceedings* 733 (2005), pp. 114–121.
- [129] D. Borrero-Echeverry, M. F. Schatz, and R. Tagg. “Transient turbulence in Taylor-Couette flow.” In: *Phys. Rev. E* 81 (2010), p. 025301.

-
- [130] S. Tokgöz, G.E. Elsinga, R. Delfos, and J. Westerweel. “Large-scale structure transitions in turbulent Taylor-Couette flow”. In: *J. Fluid Mech.* 903 (2020), A45.
- [131] A. Esser and S. Grossmann. “Analytical expression for Taylor-Couette stability border”. In: *phys. Fluids* 8 (1996), pp. 1814–1819.
- [132] S. G. Huisman, R. C. A. van Gils, C. Sun, and D. Lohse. “Multiple states in highly turbulent Taylor-Couette flow”. In: *Nat. Commun.* 5 (2014), p. 3820.
- [133] R. C. A. van der Veen, S. G. Huisman, S. Merbold, U. Harlander, C. Egbers, D. Lohse, and C. Sun. “Taylor–Couette turbulence at radius ratio: scaling, flow structures and plumes.” In: *J. Fluid Mech.* 799 (2016), pp. 334–351.
- [134] M. Gul, G. E. Elsinga, and J. Westerweel. “Experimental investigation of torque hysteresis behaviour of Taylor–Couette Flow”. In: *J. Fluid Mech.* 836 (2018), pp. 635–648.
- [135] S. Tokgöz, G. E. Elsinga, R. Delfos, and J. Westerweel. “Spatial resolution and dissipation rate estimation in Taylor-Couette flow for tomographic PIV”. In: *Experiments in fluids* 53 (2012), pp. 561–583.
- [136] A. Froitzheim, R. Ezeta, S. G. Huisman, S. Merbold, C. Sun, D. Lohse, and C. Egbers. “Statistics, plumes and azimuthally travelling waves in ultimate Taylor-Couette turbulent vortices.” In: *J. Fluid Mech.* 876 (2019), pp. 733–765.
- [137] S. Dong. “Turbulent flow between counter-rotating concentric cylinders: a direct numerical simulation study”. In: *J. Fluid Mech.* 615 (2016), pp. 371–399.
- [138] R. Tanaka, T. Kawata, and T. Tsukahara. “DNS of Taylor–Couette flow between counter-rotating cylinders at small radius ratio”. In: *Int. J. Adv. Eng. Sci. Appl. Math* 10(2) (2018), pp. 159–170.
- [139] J. M. Wallace. “Quadrant Analysis in Turbulence Research: History and Evolution”. In: *The Annual Review of Fluid Mechanics* 58 (2016), pp. 48–131.
- [140] G. Hasanuzzaman, S. Merbold, C. Cuvier, V. Motuz, J.-M. Foucaut, and C. Egbers. “Experimental investigation of turbulent boundary layers at high Reynolds number with uniform blowing, part I: statistics.” In: *Journal of Turbulence* (2020), pp. 129–165.